Variability and Black Hole Mass in Active Galactic Nuclei

JESSICA SKELTON

Institute for Astronomy
School of Physics

University of Edinburgh
Doctor of Philosophy

December 2005

Abstract

This thesis explores the links between variability both in X-rays and optical continuum flux and the mass of the central black hole in active galactic nuclei (AGN). The relationships between black hole mass, the mass of the host galaxy spheroid and the emission-line velocity widths are also investigated.

Optical observations of a sample of narrow-line and classical broad-line Seyfert 1 galaxies are presented. Off-nuclear spectra of the bulge were used to obtain the line-of-sight stellar velocity dispersion (σ_*). Nuclear spectra were used to remove residual nuclear emission from the bulge spectra and to calculate single-epoch virial black hole mass estimates. The two samples were augmented using objects taken from the literature.

The width of the [O III] 5007Å line was found to be a poor estimator of σ_* for NLS1s. The ratio $\sigma_{\rm FWHM}/\sigma_*$ was strongly correlated with σ_*, suggesting that the NLR only traces the bulge potential well for galaxies with very massive bulges. It was not clear that $\sigma_{\rm FWHM}$ provided a better estimate of σ_* for higher-luminosity objects. Only a poor correlation with Eddington ratio was found; however, uncertainties in the estimation of the Eddington ratio make it difficult to assess the significance of this result.

A comparison of σ_* for both NLS1s and BLS1s was made. The two distributions were not consistent with being drawn from the same parent population, leading to the conclusion that narrow permitted lines in NLS1s are not due solely to orientation effects. NLS1s were found to be consistent with the relationship between $M_{\rm BH}$ and σ_* established for inactive galaxies and broad-line AGN. No evidence that soft X-ray selected NLS1s lie preferentially off this relationship was found, although the available sample was small.

The optical flux variability of the least-luminous known Seyfert 1 galaxy, NGC 4395, has been a matter of controversy, with a number of apparently contradictory reports. Optical spectroscopic observations of NGC 4395 are presented, during which the nucleus was monitored every half-hour over the course of three nights. The continuum emission varied by ~35 per cent over the course of three nights, and marginal evidence for greater variability in the blue continuum than the red was found. A number of diagnostic checks were performed on the data in order to constrain any systematic or aperture effects. No correlations were found that adequately explained the observed variability, leading to the conclusion that real intrinsic variability of the nuclear source has been observed. No simultaneous variability was measured in the broad Hβ line, although given the difficulty in deblending the broad and narrow components it is difficult to comment on the significance of this result.

The observed short time-scale continuum variability is consistent with NGC 4395 having an intermediate-mass ($\sim 10^5 \mathrm{M}_\odot$) central supermassive black hole, rather than a very low accretion rate. Comparison with the Seyfert 1 galaxy NGC 5548 shows that the observed variability seems to scale with black hole mass in roughly the manner expected in accretion models. However the absolute timescale of variability differs by several orders of magnitude from that expected in simple accretion disc models in both cases.

An investigation was made of the relationship between hard (2-10 keV) X-ray variability and both X-ray luminosity (L_{X}) and M_{BH}. For objects with secure mass estimates, it was not possible to determine which of these was the primary correlation. However, when high and low accretion-rate objects were included the correlation with L_{X} was found to be very poor, while the M_{BH} correlation was still good.

Declaration

I declare that this thesis is not substantially the same as any that I have submitted for a degree or diploma or other qualification at any other University. I further state that no part of my thesis has already been or is being concurrently submitted for any such degree, diploma or other qualification.

This thesis is the outcome of my own work except where specifically indicated in the text.

Jessica Skelton
Edinburgh,
July 7, 2006

Acknowledgements

It's a strange feeling to be sitting here at the end of my PhD still struggling to write the first page. It's been a bit of a rollercoaster. No, wait, that's not right - the 'down' bits are fun on a rollercoaster. Perhaps it's more like a long hike, complete with sunshine, rain, fog (lots of fog) and the occasional blizzard. Like many hikes, there's a warm and comfortable pub at the end. None of this would have been possible without the support, friendship and frequent kicks-up-the-backside from a long list of people. This is where I attempt to thank you all, but I'm bound to miss a few. Don't hold it against me. Please.

First of all, I have to thank my supervisors Andy Lawrence, Omar Almaini and Ross McLure, for giving me this opportunity in the first place and for all of their subsequent support. For help with the velocity dispersion analysis and for allowing me use of his stellar template spectra I extend grateful thanks to Tommaso Treu at the University of California, Santa Barbara, and also to Roeland van der Marel for providing the original code. Gratitude and thanks must also go to John Peacock and Alan Heavens for their suggestions and advice.

I'd like to thank my examiners, Philip Best and Kirpal Nandra, for making me feel as though I earned this.

Huge thanks must go to all the students and friends at the ROE without whom the last three-and-a-bit years would have been unbearable. There are more than I can list here, but a particular mention must to go to Emma, Rachel, Michael and Miller, for proving that no matter how badly I felt things were going, there was always someone worse off than me! Cheers to Tom and Matt, for all the geekiness and fun, and to Niall, for all the football-related trivia. Many thanks to Martin for all the beer and help with job-hunting. Olivia gets a special mention for putting up with all the rants. In no

particular order, Caz, Emma Rigby, Rita, Barney, Anita, Michele, Eric, Ben, Mairi and Morag have always provided friendship and drinking buddies whenever required. Finally, here's to the Pear Tree and KB pub quiz teams, without whom no Monday or Tuesday night would be complete!

Of course, none of this would have been possible without the emotional (and financial!) support of my family. No matter what direction I've chosen to take my life, they've always been there. So, my final salutation goes to Mum, Grandma, Jools, Ross, James, Josie, Simon and Annie, for everything.

Jessica Skelton
Edinburgh
July 2006

For Peter Michael Skelton

Contents

CHAPTER 1

Introduction

The recent discovery that black holes appear to be ubiquitous at the centres of nearby normal, quiescent galaxies has provided powerful support for the black hole – accretion disc model for active galactic nuclei. Previously, this model was founded primarily on indirect arguments from the luminosities and size-scales inferred from observations. However, there was no concrete proof that the prerequisite ingredient in this model - the central supermassive black hole - actually existed anywhere in nature.

This situation has now changed dramatically. The advent of adaptive-optics techniques in optical astronomy has allowed the proper motions of stars close to the Galactic centre to be determined with a high degree of precision, and the conclusions are clear; the observed velocities can only be produced if the object that the stars are orbiting is a black hole, with a mass a few million times that of the Sun. This, together with observations of other local galaxies has provided clear evidence that not only can supermassive black holes exist, but that in fact they appear to be a normal product of galaxy formation and subsequent evolution.

Now that a plausible model exists it is naturally important to test its exact nature. Modern astronomy has given us extremely sensitive tools with which to observe the properties of active galaxies across the entire electromagnetic spectrum. A common characteristic of active galactic nuclei (AGN) is variation of the continuum emission

in the X-ray, ultraviolet and optical bands. Since this emission is purported to arise from the accretion disc surrounding the black hole, detailed variability studies can in principle tell us a great deal about the physical structure and size-scales of this region.

In this thesis I undertake a detailed study of the relationship between the mass of the central black hole and the time-scales and amplitude of variability, primarily in the X-ray and optical wavebands. The motivation for this is twofold; firstly, it is necessary to understand exactly from where the variable emission arises, in terms of distance from the central black hole. Secondly, if it were possible to determine a direct relationship between either variability amplitude or timescale and black hole mass, it would provide a potentially powerful technique for determining black hole masses and accretion rates in more distant active galaxies where current estimation techniques are difficult if not impossible. I also investigate the properties of the peculiar class of AGN known as narrow-line Seyfert 1s. As the result of several studies undertaken over the last few years, it has been postulated that these could be 'young' AGN in which the black hole is still growing rapidly. I attempt to verify this conclusion using new observations of samples of narrow- and broad-line Seyfert 1 AGN.

This introduction explains the scientific background behind this project and gives an overview of the position of current research into AGN physics. I begin with a brief overview of some of the salient observational properties of AGN, justifying the confidence - or lack thereof - with which we can view the black hole – accretion disc AGN paradigm. In Section 1.2 I discuss the mounting evidence in favour of the existence of black holes in the centres of galaxies, including relationships between galaxy and black hole properties and how these can be used to infer black hole masses. Section 1.3 summarises the variability properties of AGN in the optical and X-ray wavebands, plus the problems that these properties pose for our AGN models. Finally I outline the specific areas that this project has covered.

1.1 Multiwavelength properties of AGN

One of the intriguing properties of active galaxies is the range of wavelengths over which significant levels of flux can be detected. Even with a varied stellar population a typical galaxy emits the bulk of its radiation over a single decade in frequency,

which can be well-characterised by a superposition of blackbody spectra. AGN, however, show substantial emission at wavelengths from radio up to hard X-rays. Often the emission is consistent with nonthermal emission mechanisms such as synchrotron radiation or Compton scattering, and hence a common technique is to fit power-law models of the form $F_\nu \propto \nu^\alpha$, where α is the spectral index and F_ν is the flux density at frequency ν. Typical values of α for AGN are between zero and unity (Elvis et al. 1994), leading to a common description of AGN as flat-spectrum sources.

The strongest feature in AGN spectral energy distributions is a strong, broad feature known as the *big blue bump* (BBB). This dominates the continuum spectrum for wavelengths below 4000Å, and possibly extends all the way to the soft X-ray regime (0.1–2 keV) (Elvis et al. 1994). Qualitatively the slope and turnover of the BBB resemble the predicted thermal emission from simple accretion disc models (Shakura & Sunyaev 1973), and therefore this was initially thought to be thermal emission from the disc itself. However, observations of a sample of AGN (Malkan 1983) found that the turnover in all of the objects was very similar, implying a fairly uniform maximum temperature in all the discs. Other observations showed that there was considerable emission at wavelengths shortward of the UV turnover, which required much higher temperatures and highly super-Eddington accretion rates (Bechtold et al. 1987). One possible solution to this is that the opacity due to electron scattering is more significant than in simple disc models (Czerny & Elvis 1987). Including opacity effects predicts a less extreme turnover in frequency, allowing for the significant UV and soft X-ray excesses that are observed in many objects. In addition, a higher temperature would be required for the object to radiate at the same luminosity, implying less super-Eddington accretion rates.

The advent over the last two decades of space-based X-ray observatories with good sensitivity and pointing accuracy has enabled AGN to be studied at this wavelength regime in detail. Significant X-ray flux is a defining characteristic of all AGN; for instance, per unit volume more X-ray-emitting Seyfert 1 galaxies have been discovered than in any other wavelength band (Danese et al. 1986), and the X-ray luminosity represents a significant fraction of the bolometric luminosity in most AGN, typically contributing between $5 - 40$ per cent (Ward et al. 1987). Power-law fits to AGN hard

X-ray spectra (2–20 keV) show that the average photon index Γ (related to the spectral index by $\Gamma = \alpha + 1$) is closely distributed around $\Gamma = 1.7$ (Awaki 1991). However, power-law fits to spectra in the softer X-ray bands produce a wide range of slopes (Wilkes & Elvis 1987). Generally the soft X-ray spectrum steepens to give the soft X-ray excess (possibly the high-energy manifestation of the BBB), one possible interpretation for which is that it is associated with thermal emission from the innermost regions of the accretion disc (Arnaud et al. 1985; Pounds et al. 1986; Czerny & Elvis 1987). However such explanations find it difficult to explain the breadth of the excess emission, which extends from the optical/UV through to X-rays.

At harder X-ray energies, an excess over the power-law continuum is seen above 10 keV (Nandra et al. 1991). Guilbert & Rees (1988) showed that reprocessed X-ray emission reflected off a slab of relatively cold material would produce features of this kind. This 10 keV 'reflection hump' would require that the accretion disc was illuminated by a strong X-ray source from above, leading to a model in which the X-ray emission is produced by a corona of hot material around the disc (Pounds et al. 1990; George & Fabian 1991). Most of the hard X-ray flux is absorbed by the disc, but a small percentage ($\sim$10 per cent) is reflected back to the observer via Compton scattering. Spectroscopic X-ray observations using *EXOSAT* and *Ginga* found that spectral X-ray features are a common feature of Seyfert nuclei (see e.g. Nandra et al. 1989; Pounds et al. 1989). In particular, an emission line at 6.4 keV corresponding to Kα emission from iron is observed in many Seyfert 1 spectra (Mushotzky et al. 1993). The intensity of these lines was much higher than was expected from the relatively metal-poor intergalactic medium in the line-of-sight to the AGN. The profile shapes and equivalent widths of this feature suggested that the emitting material subtended a large solid angle as seen from the source of the hard X-ray flux. This was seen as further supporting evidence for the reprocessing scenario, and also suggested that more than one source of nuclear emission was required to account for the observed spectral components. Simultaneous UV and X-ray monitoring of the variability of the Seyfert 1 galaxy NGC 5548 showed that the UV and X-ray variations over time-scales of days to weeks were correlated with almost no time lag (Clavel et al. 1992), which is consistent with the hypothesis that the UV variations in the disc are directly caused by the

absorbed X-ray flux from a surrounding corona rather than from the disc itself.

If a part of the X-ray flux originates in a region close to the central black hole, then this would also be expected to leave an imprint on the emission line profiles. Further study of the 6.4 keV iron lines using the *Advanced Satellite for Cosmology and Astrophysics* (*ASCA*), which had much improved sensitivity and spectral resolution, found that it was possible to resolve the Kα line (Fabian et al. 1994). Dramatic evidence for an origin close to the black hole came from observations of MCG -6-30-15 (Tanaka et al. 1995) and NGC 4151 (Yaqoob et al. 1995). The measured widths of the iron lines implied gas velocities $\gtrsim 100,000$ km s^{-1} and the profiles were strongly skewed, with an extremely broad red tail. This was strong evidence in favour of a gravitationally redshifted source (Fabian et al. 1995).

In addition to X-ray lines, strong optical emission lines are a characteristic of most AGN. In Type-1 AGN, permitted lines such as the Lyman and Balmer series from hydrogen show strong broad wings with widths corresponding to $2,000$ to $\sim 10,000$ km s^{-1}, in addition to much narrower core components. The speeds implied by these line widths are much higher than would be expected if the gas were moving in the gravitational potential of a normal galaxy bulge. Such high velocities can only occur quite close to the black hole, in clouds of relatively dense material whose constituents are ionized by emission from the central engine. This is the *broad-line region* (BLR). These broad wings are not seen in Type-2 AGN (Seyfert 2s and radio galaxies), and this is one of the foundations of the unification scheme for AGN; in Type-2 AGN, the BLR is obscured by a torus of dusty material (Lawrence & Elvis 1982; Antonucci 1983; Lawrence 1991).

Forbidden lines are also seen in AGN spectra, and since these lines are only observed from rarefied gas in which the probability of collisional de-excitation is much reduced, these cannot arise from the dense environment of the BLR. This is confirmed by the widths of the forbidden lines, which are considerably narrower than those of the permitted lines ($200 \lesssim \mathrm{FWHM} \lesssim 1,500$ km s^{-1}). These narrow lines are observed in both Type-1 and Type-2 AGN, suggesting an origin much further from the central engine in the *narrow-line region* (NLR), which is not obscured by the dusty torus. The NLR is spatially extended and can therefore can provide a valuable probe of the inner

regions of the AGN as it is sometimes resolved in observations, whereas the BLR and accretion disc are unresolved with even space-based telescopes.

1.2 Supermassive black holes in AGN

1.2.1 Early considerations

Early arguments for the existence of supermassive black holes at the centre of AGN focussed on the size and mass constraints imposed by variability considerations and the Eddington limit. In order for a source to vary coherently, the entire region must be causally connected, and this means that the minimum time-scale for variability is determined by the light travel time. Observations of the variability of AGN can therefore give us information on the sizes of the emission regions, using the relation

$$R \lesssim c T_{\rm cr} \tag{1.1}$$

where $T_{\rm cr}$ is the time-scale for variability and represents the time taken for a photon to traverse the region of interest, which has radius R, and c is the speed of light. The optical continuum of a typical Seyfert 1 galaxy varies by a factor of 20-50 per cent over a time-scale of several months, constraining the optical emission region to be significantly less than a light-year in size, and early studies confirmed that smaller but still significant variations could occur over a few days (Smith & Hoffleit 1963). The mass required to produce a given observed luminosity can be calculated using the Eddington limit, at which the gravitational force on a proton (mass $m_{\rm p}$) exceeds the outward force due to radiation pressure, giving

$$M_{\rm Edd} \geq \frac{\sigma_{\rm e} L}{4\pi G c m_{\rm p}} \tag{1.2}$$

where $M_{\rm Edd}$ is the Eddington mass, L is the luminosity of the source, $\sigma_{\rm e}$ is the Thomson cross-section for electron scattering and other symbols take their usual meanings. The variability of AGN is a fundamental part of the central black hole model because it constrains the maximum size that the central region can take, while the Eddington limit gives the minimum mass required to produce the observed luminosity.

When AGN were first discovered, it was thought that the mechanism necessary to produce such a large luminosity from a small region must be nuclear fusion. However,

when attempting to construct models for AGN based on the liberation of energy by this method, it was realised that the masses required possessed sufficient gravitational potential energy for the emission to have arisen as a result of gravitational contraction (Salpeter 1964; Lynden-Bell 1978). The black hole paradigm neatly explained many of the observed AGN properties and the general acceptance of the accreting black hole model came before any observational proof of the existence of black holes existed. Early stellar-dynamical black hole searches (Sargent et al. 1978; Young et al. 1978) found evidence for a possible $4 \times 10^9 M_\odot$ black hole at the centre of M87, although this discovery was based on the assumption that the stellar velocity dispersion was isotropic, an assumption that is not necessarily true for elliptical galaxies like M87 (Illingworth 1977; Binney 1978). However, these papers were seminal and set the field in motion.

The most convincing candidate for a supermassive black hole lies at the centre of the Milky Way. Evidence for this arose with the discovery of a compact radio source that showed nonthermal emission signatures in the region of Sgr A* (Lo et al. 1975). For many years the data used to estimate the mass at the centre of the Galaxy were sparse because of the need to use stars that were bright enough to be individually resolved (Ghez 1998; Kormendy 2003). Recent technological improvements such as adaptive optics and CCD spectroscopy have enabled the resolution of a cluster of stars surrounding Sgr A* (Gezari et al. 2002). The stars in this cluster move fast enough that we can observe their proper motions, providing a direct measure of the velocity dispersion, giving a mass for the central black hole of $(2.6 \pm 0.2) \times 10^6 M_\odot$. Other measurements from observations of 17 proper-motion stars (Ghez et al. 2005) give the slightly larger, but still comparable, mass of $M_{\rm BH} = (3.7 \pm 0.2) \times 10^6 M_\odot$. These measurements of stellar orbits constrain the central mass to exist inside such a small radius that plausible alternatives to black holes, such as large clusters brown dwarfs or stellar remnants, are ruled out by astrophysical constraints (Maoz 1995, 1998).

Another convincing case for a supermassive black hole in a nearby galaxy comes from observations of a water maser disc in NGC 4258 (Miyoshi et al. 1995). Spectroscopic observations showed that the emitting gas moved in near-Keplerian orbits with line-of-sight velocities of $\sim$1000 km s^{-1} centred around the systemic velocity of

the galaxy. The slight deviation from Keplerian motion is consistently explained if the gas lies in a slightly warped thin disc (Herrnstein et al. 1996). The central mass implied by the position and velocity data is $3.8 \times 10^7 M_\odot$ (Herrnstein et al. 2005), and radio observations showed that the maser emission is emitted from an annular disc extending from 0.17 to 0.28 pc from the central mass (Miyoshi et al. 1995). As for the Milky Way, the central mass is constrained to lie within such a small volume that alternatives to black holes are ruled out. These two objects remain the only objects for which this can be stated with confidence.

1.2.2 Measuring black hole masses in nearby galaxies

If observed cosmological evolution of quasars holds true, and AGN were many times more numerous at $z \simeq 2$ than they are now, then the remnants of dead AGN should be found in a high proportion of local early-type galaxies (Kormendy & Gebhardt 2001). The search for supermassive black holes in AGN is hindered by the luminosity of the nucleus, but in local normal galaxies the search should be much easier since the central stellar population is resolved for galaxies as distant as the Virgo cluster using the *Hubble Space Telescope* (*HST*). Initially it was thought that the brightness profiles of galaxies could be used to constrain black hole masses. In particular, it was thought that a bright central cusp of stars in the gravitational sphere of influence of the black hole could provide an observational signature of a central supermassive black hole (see e.g. Young et al. 1978; Fabbiano et al. 1994). However, observations of the galaxy M33 (Kormendy & McClure 1993) and of the globular cluster M15 (Lauer et al. 1991) found that although these objects had high central densities and 'cuspy' brightness profiles there was no evidence for a central black hole in either.

Stellar-kinematical black hole mass searches involve observing the brightness profile, systemic velocity and velocity dispersion of a galaxy. The observed values for these quantities are the projected values along the line-of-sight. To retrieve the true unprojected values a set of model kinematics are used to calculate model spectra along the line of sight, which are then convolved with the instrument point spread function. The observed model spectrum is then iterated until it agrees with the data (Kormendy 1988a,b; Dressler & Richstone 1988). If the implied mass-to-light (M/L) ratio rises

rapidly towards the centre of the galaxy, then this is evidence (although not conclusive proof) for the presence of a black hole.

Stellar-dynamical searches can be confused by anisotropic stellar orbits (e.g. Duncan & Wheeler 1980). In many cases, gas dynamics can be used to provide central mass estimates, by assuming Keplerian orbits. Searches using the dynamics of the central stars in galaxies are often more accurate than those using gas dynamics, because gas is easily perturbed from pure Keplerian orbits by local events such as supernovae or strong winds from the AGN. However, gas-dynamical searches do allow the central regions of the galaxy to be probed. Therefore for galaxies close enough for the nuclear stellar region to be resolved gas-dynamical searches can strengthen the case for a central black hole, as in the case of M87 (Harms et al. 1994; van der Marel 1994).

As the search methods using stellar kinematics and gas dynamics improved and the number of provisional black hole detections increased, it became obvious that there was a strong correlation between the mass of the black hole and the mass of the bulge component of the host galaxy, obtained from measurements of the bulge luminosity $L_{\rm Bulge}$ (Kormendy & Richstone 1995). Observations of a sample of 36 local galaxies strengthened this correlation, giving a black hole-to-bulge mass ratio of around 0.005 (Magorrian et al. 1998). This relationship had a large scatter ($\simeq 0.5$ dex), which consequently limited its usefulness when it came to estimating black hole masses. Some results suggested that the $M_{\rm BH} - L_{\rm Bulge}$ relations differed for active and inactive galaxies (Wandel 1999). Follow-up work by McLure & Dunlop (2001) and Laor (2001) showed that the bulge masses for AGN were consistent with the same $M_{\rm BH} - L_{\rm Bulge}$ relationship as for normal galaxies, and that the previous results of Wandel (1999) were a result of the difficulties in obtaining accurate measurements of the bulge luminosities in AGN. Black hole mass estimates were obtained from broad line widths and continuum luminosity measurements for a large sample of active and inactive galaxies with good bulge luminosity measurements (McLure & Dunlop 2002), confirming that active and inactive galaxies followed the same bulge luminosity–black hole mass relationship over several decades in black hole mass, and furthermore that it was possible to reduce the scatter in the relation to less than 0.4 dex (see Figure 1.1).

Using a sample of galaxies with well-determined black hole masses and velocity

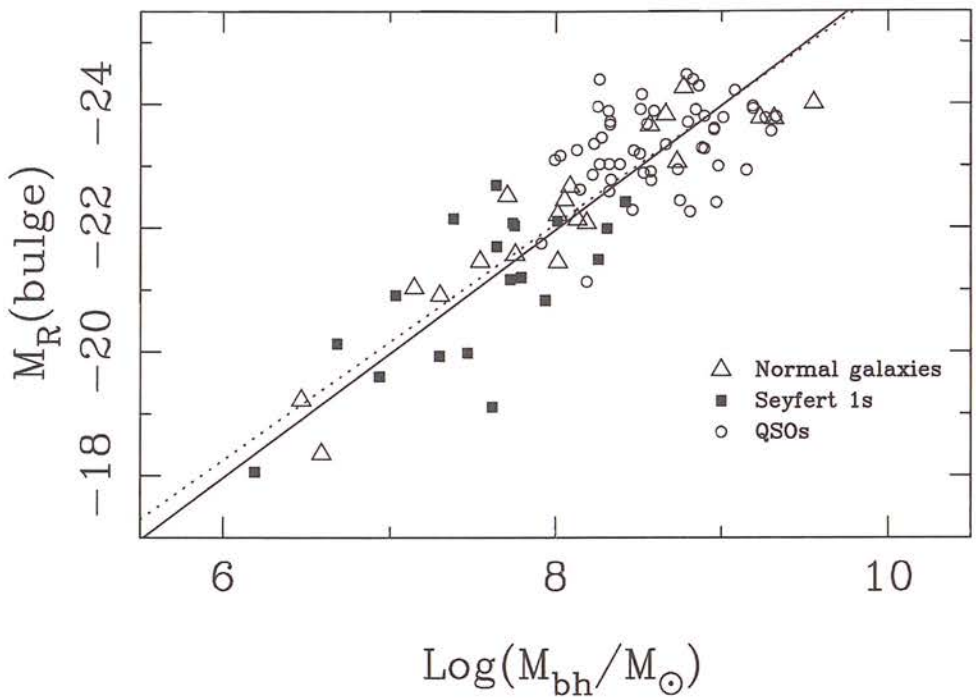

Figure 1.1: The relation between the absolute R-band magnitude versus the black hole mass for the sample of 72 AGN and 18 normal galaxies from McLure & Dunlop (2002). The formal best-fitting line (solid line) and best-fitting linear relation (dotted line). Figure from McLure & Dunlop (2002).

dispersion measurements from either stellar kinematics or gas dynamics, a strong correlation was found between the velocity dispersion σ_* of the stars in the bulge and the mass of the black hole (Gebhardt et al. 2000a; Ferrarese & Merritt 2000). This correlation was discovered independently by the two groups, and the best-fitting relation between the stellar velocity dispersion σ_* and black hole mass $M_{\rm BH}$ given by each differed significantly. Tremaine et al. (2002) argue that this difference results from a systematic difference in the way the velocity dispersions were calculated. The best-fitting relationship adopted by Tremaine et al. (2002) from a sample of 31 galaxies is given in Equation 1.3

$$\log\left(\frac{M_{\rm BH}}{M_\odot}\right) = (8.13 \pm 0.06) + (4.02 \pm 0.32)\log\left(\frac{\sigma}{\sigma_0}\right) \tag{1.3}$$

where σ is the measured velocity dispersion relative to a reference value $\sigma_0 = 200$ km s^{-1}.

1.2.3 Mass-estimation methods for AGN

Velocity dispersions and bulge masses

The velocity dispersion–black hole mass relation can be used to estimate the black hole masses in AGN as well as normal galaxies. The advantages of this method are that the velocity dispersion is reasonably easy to obtain using ground-based spectroscopy, at least for local AGN. Also, the implied intrinsic scatter in the relationship is zero, if the uncertainties arise solely from measurement errors, so that in principle it provides a good constraint on black hole masses.

One disadvantage is that unlike some other methods, the velocity dispersion is based on fitting to stellar absorption lines, and as such does not probe the innermost regions of the active nucleus. Therefore any mass estimate derived this way is an upper limit to the true black hole mass. Also, this analysis is only applicable to fairly local, low-luminosity AGN. Since the technique relies upon being able to resolve the spheroidal component of the host galaxy, the smallest angular diameter possible is restricted to an arcsecond or so using ground-based spectroscopy. In addition to this, the need to resolve the stellar absorption lines on top of the non-thermal AGN continuum means that this analysis for the most luminous quasars is ruled out even if high-resolution spectroscopy were available.

The correlation between black hole mass and bulge luminosity is extremely useful in that it means that we can measure black hole masses in luminous AGN, providing that we can deconvolve the nuclear and host galaxy components. This includes radio-loud quasars and other galaxies for which velocity dispersion analysis is difficult or impossible. Obtaining the bulge luminosity is difficult, because frequently the low surface brightness of the host galaxy is completely masked by the high-luminosity quasar nucleus. Therefore a modelling technique needs to be used that allows the successful decomposition of the nuclear and host galaxy light. This means that the point spread function of the optical system needs to be accurately modelled, which can be done by taking a number of exposures of a standard star using different integration times, to allow a point-spread function with high dynamic range in both the core and wings to be constructed.

Reverberation mapping

The two methods listed so far utilise the properties of the AGN host galaxy to determine the mass of the central engine. This is the only way of determining central black hole masses in the majority of inactive galaxies, since there are very few galaxies for which it is possible to resolve the motions of gas in the inner regions of galaxies (one of the rare examples is the maser emission in NGC 4258 discussed previously). In this respect, AGN provide us with one crucial advantage over inactive galaxies, in that the strong continuum and line emission from the nucleus is observable. As a consequence, a great deal of time and endeavour (and money) has been applied to the problem of relating the nuclear emission properties to the gas motions and hence the black hole mass.

Reverberation mapping utilises variability in both the optical continuum and broad-line emission to constrain the size and shape of the broad-line region in the active nucleus (Blandford & McKee 1982). The flux and the line profiles of the broad optical emission lines are both observed to vary over time-scales of days or longer, and this variability follows similar variations in the continuum flux with a small (10-30 d) time lag. This means that the BLR clouds must be optically thick and close to the nucleus, and that since the flux variations seem to be correlated with the *optical* continuum emission, this implies that the optical continuum closely follows variations in the continuum responsible for the ionization of the emission lines (Peterson 2001). These are photons with energies greater than the hydrogen ionization potential of 13.6 eV, which are not normally observable due to absorption. Using the line width to obtain an estimate of the velocity of the broad-line emitting gas, the mass of the central engine is then obtained by assuming that the gas is gravitationally bound and that the virial mass can be calculated from the emission-line data using

$$M_{\rm BH} \sim \frac{v^2 R_{\rm BLR}}{G} \tag{1.4}$$

The size of the broad-line region, $R_{\rm BLR}$, is measured by observing the response of the emission line to the driving continuum variations. This lag is assumed to arise entirely as a result of the light travel time between the accretion disc and the broad-line clouds, which implies that the central emitting source is much smaller than the BLR and that the relationship between the ionizing continuum and the observed continuum is a

simple one (Peterson 1993). It is also assumed that the response of the clouds to the ionizing continuum is near-instantaneous. The relationship between the light curve and the emission-line intensity $I(t)$ is then given by

$$I(t) = \int \Psi(\tau) L(t - \tau) d\tau \tag{1.5}$$

where the function $\Psi(\tau)$ is the transfer function (Blandford & McKee 1982). This is known as the transfer equation. That is, fluctuations in the continuum luminosity $L(t)$ predict fluctuations in the line luminosity at later times through a convolution with the transfer function.

The transfer function is obviously highly dependent upon the geometry of the BLR, the viewing angle and also the line emissivity. Since data from AGN monitoring campaigns are almost never regularly sampled, the transfer function is determined from maximum-entropy methods (MEM) rather than through Fourier transform analysis (Horne et al. 1991; Krolik et al. 1991; Peterson et al. 1993). The amplitude of the transfer function tells how much matter there is (and how sensitive its line output is to continuum variations) at a radius $r \sim c\tau$. The few monitoring experiments of good enough quality to allow the determination of the transfer function indicate that there is significant response over a range of lags and presumably a comparable range in radius (Krolik et al. 1991). This means that the characteristic radius of the BLR that we get from the lag measurements is weighted by the line emissivity, which is the energy radiated in the line per unit volume caused by changes in the continuum flux (Peterson 1993).

Line widths are commonly quantified in two ways. The first is to measure the full-width at half-maximum (FWHM) of the broad emission line in each of the spectra used for the time-series analysis and calculate the mean FWHM for these data. The second is to use the spectra from the time-series analysis to create a root-mean-square (rms) spectrum defined as

$$\sigma(\lambda) = \left\{ \frac{1}{(N-1)} \sum_{i=1}^{N} [f_i(\lambda) - \bar{f}(\lambda)]^2 \right\}^{0.5} \tag{1.6}$$

where $\bar{f}(\lambda)$ is the average of the N spectra (Kaspi et al. 2000). The line FWHM is then measured from the rms spectrum. The advantage of this method is that it characterises

the variable part of the emission line while excluding constant features such as the narrow core component and Galactic absorption (Peterson et al. 1998). The width of the rms line profile then gives the velocity dispersion in the varying part of the gas.

One of the biggest potential uncertainties in the reverberation mapping method is the assumption that the motions of the line-emitting gas are gravitationally bound. There is no real *a priori* reason why this should be true; line velocities could be due to outflows or disc winds. One test of this is to check whether the characteristic velocities vary as $r^{1/2}$. If the ionization of the BLR is stratified, then different emission lines are emitted at different distances away from the central source. Typically, different lines also have different line widths. If the dynamics of the BLR really are gravity-dominated, then the Keplerian relation in Equation 1.4 should give the same value when measured using different ionization species. This comparison was attempted by Wandel et al. (1999) with the data from one of the best-studied AGN, NGC 5548. They found that the different ionization species did give the same value for the virial mass, within the not-inconsiderable errors (see Figure 1.2). However, this is not conclusive proof of gravity-dominated dynamics, since other models such as radiation pressure-driven outflows make the same prediction (Krolik 2001). Some support for gravity-dominated dynamics does come from the agreement between the masses inferred from the bulge velocity dispersions of Gebhardt et al. (2000a) and Ferrarese & Merritt (2000) with the reverberation masses of Wandel et al. (1999).

If we assume that the BLR cloud motions are dominated by gravity, then it is necessary to determine the exact geometry of the BLR and the shape and inclination of the cloud orbits within it. The most common way of determining $R_{\rm BLR}$ comes from cross-correlating the line and continuum flux (Wandel et al. 1999; Kaspi et al. 2000). However, accurately determining the cross-correlation function requires knowledge of the power spectrum of the continuum fluctuations and ideally calculation of the power spectrum requires an infinite time-series of observations. Obviously, this is not possible in reality and so the power spectrum is calculated via a discrete Fourier transform (DFT). If there are too few data points in the DFT analysis, this can lead to inferred mass estimates that are too small, because the range of time-scales sampled is less than the radial extent of the BLR (Krolik 2001). In addition, if the sampling inter-

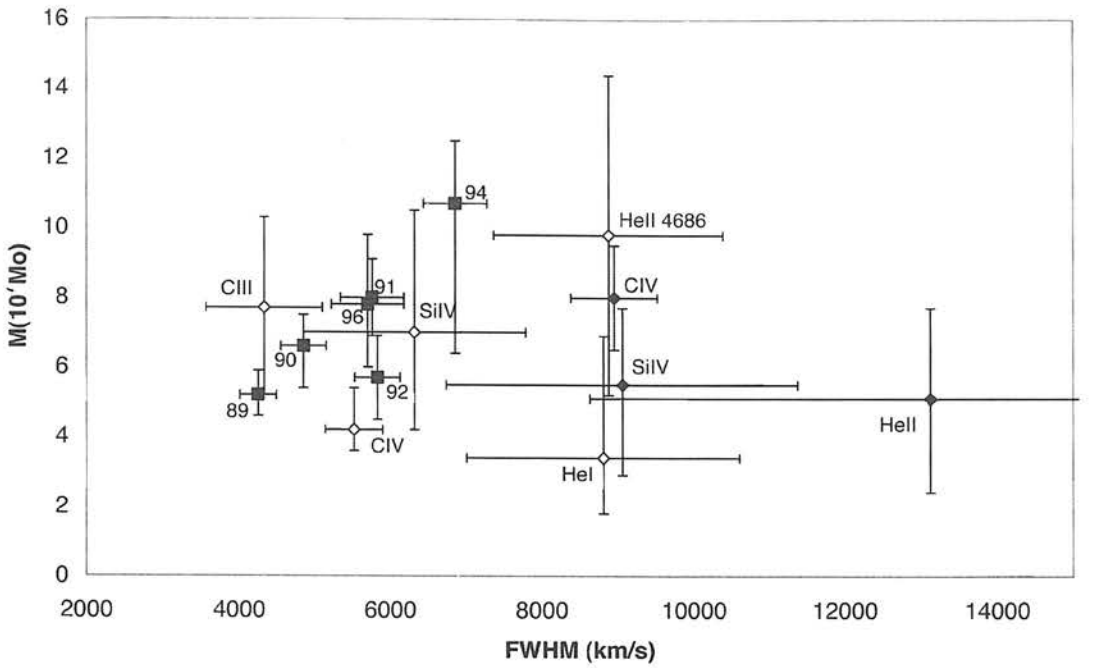

Figure 1.2: Virial mass of NGC 5548 vs. FWHM for Hβ (filled squares) for six observing periods from 1989 to 1996, plus five other ionization species determined from monitoring campaigns from 1989 to 1993. Figure from Wandel et al. (1999).

val does not correspond to the characteristic variability time-scale of the continuum, then this can also bias the results.

The lag time will depend on the distance of the line-emitting gas from the origin of the continuum emission, particularly if the gas is radially extended. The reverberation mapping studies that have allowed detailed studies of the transfer function suggest that the BLR emission originates from a region that can span a wide range in radius, possibly an order of magnitude or more (Krolik et al. 1991; Done & Krolik 1996; Ulrich & Horne 1996). Whether the line-emitting regions radiate isotropically will also have an effect on the response function inferred from observation (Krolik 2001). Anisotropic emission could introduce bias to the mass measurement if, for instance, more emission is seen from regions on the far side of the central mass. In this case, the lag time that is measured will be greater than is the true case because of the greater light travel time, implying a larger radius (and hence mass) than corresponds to reality. Accurate recovery of the transfer function therefore requires a monitoring campaign that spans a broad range of time-scales so that the size and extent of the BLR can be determined.

This information could then be used to ensure that the proper sampling time-scales and number of data points are used when calculating the fluctuation power spectrum.

In order to determine the precise relationship between the velocity $v_{\rm FWHM}$ as measured from the emission line widths and the virialized velocity v in Equation 1.4 it is necessary to know the constant of proportionality between them. This is not trivial. In the simple case where the BLR clouds are circular and in a single plane at radius r and with inclination angle i, then the mean line-of-sight velocity is given by $v_{\rm los}^2 = GM \sin^2 i/2r$ and $v^2/v_{\rm los}^2 = 2/\sin^2 i$, and then $v_{\rm FWHM} \simeq 2.355 v_{\rm los}$ if the line profile is Gaussian. Another possibility is that the orbits are isotropic, in which case it becomes necessary to know the orbital shapes (Krolik 2001). A detailed study of Seyfert 1 galaxies with both reverberation mapping estimates and estimates from velocity dispersions showed that the data were best fitted using a model in which the line-emitting gas has a flattened disc-like geometry rather than random orbits (McLure & Dunlop 2002).

Clearly, there are a number of potential pitfalls and uncertainties associated with reverberation mapping. However, the usefulness of a mass-estimation technique that uses the observed properties of the innermost regions of the AGN means that this is still a powerful tool. Accurate reverberation mapping requires AGN monitoring campaigns over many years in order to successfully measure the time lag, broad-line widths and variability power spectrum.

Photoionization modelling

An alternative method of estimating the virial mass is based on estimating the size of the BLR using photoionization theory, and using the emission-line width as an indicator of the line-of-sight velocity dispersion. This method only assumes that the gas is gravitationally bound and does not rely on the specific geometry of the BLR as does reverberation mapping. The simplest method is to use line ratios to determine the density of the line-emitting gas and its ionization parameter U, given by

$$U = \frac{Q}{4\pi r^2 n_{\rm e} c} \tag{1.7}$$

where

$$Q = \int \frac{L_\nu}{h\nu} d\nu \tag{1.8}$$

is the number of ionizing photons and n_e is the electron number density. The ionization parameter can then be re-written as

$$U = \frac{L_{\rm ion}}{4\pi r^2 \bar{E} n_e c} \tag{1.9}$$

where $L_{\rm ion}$ is the ionizing luminosity and $\bar{E} = L_{\rm ion}/Q$ is the average energy of an ionizing photon. Therefore if it is possible to estimate the ionizing luminosity, Equation 1.9 can be rearranged to estimate the distance of the ionized gas from the ionizing source

$$R_{\rm ph} = \left(\frac{L_{\rm ion}}{4\pi U \bar{E} n_e c} \right)^{1/2} \tag{1.10}$$

This implies that we can estimate the virial mass using

$$M_{\rm ph} \simeq \frac{v^2 R_{\rm ph}}{G} = K v^2_{\rm FWHM} \left(\frac{L_{\rm ion}}{U n_e \bar{E}} \right)^{1/2} \tag{1.11}$$

where

$$K = \frac{f_k}{G\sqrt{4\pi c}} \tag{1.12}$$

and $v^2_{\rm FWHM}$ is obtained from the FWHM of the broad line. The factor f_k relates the actual velocity dispersion to the projected radial velocity deduced from the Doppler broadening, and parametrizes the fact that the the inclination of the orbits of the broad-line gas and the specific geometry of the region are unknown.

Again, as for reverberation mapping, the principal problem with this method is whether the BLR cloud motions are dominated by gravity or by winds or outflows, and the considerations regarding this matter discussed previously also apply here. Another problem is estimating the ionizing luminosity. As a zeroth-order estimate it can be assumed that it is proportional to the optical luminosity, and try and determine the proportionality constant using a sample with a mass estimate derived from another method, such as reverberation mapping. Kaspi et al. (2000) found a correlation between the monochromatic luminosity at 5100Å and the size of the BLR, which is now the most common method for determining the size of the BLR in photoionization modelling. This result gives a relation between the radius of the BLR and the luminosity of $R_{\rm ph} \propto L^{0.7}$, where naively we would expect $R_{\rm ph} \propto L^{0.5}$ from Equation 1.11. However, subsequent results have suggested that $R_{\rm ph}$ is consistent with the $L^{0.5}$ relation (Peterson et al. 2000; McLure & Jarvis 2002).

1.3 AGN variability

A defining characteristic of AGN is variability of the emission in the optical, UV and X-ray bands (Mushotzky et al. 1993). Since we now have the facilities to monitor AGN over long periods of time this is a major field of study. Typically an AGN will vary by about 10 per cent in the optical over a time-scale of a few years (with the exception of Optically Violently Variable objects); however, the most extreme variability is observed in X-rays, where variations of $\sim$2 are seen over time-scales of the order of hours to days, suggesting that the X-rays come from the innermost regions of the central engine.

Most AGN show little optical or UV variability on time-scales as short as days but many, such as the Seyfert 1 galaxy NGC 5548 (Peterson et al. 2002), show dramatic variations on time-scales of the order of weeks or months, with the UV continuum showing more variability than the optical.

1.3.1 X-ray variability

Long-look X-ray observations using *EXOSAT* allowed analysis of the X-ray variability of AGN for the first time (Lawrence et al. 1987). The variability at all energies was found to be stochastic, with no characteristic frequencies indicative of regular processes such as rotation that could explain the observed variations. It was found in a sample of 11 AGN that all showed red-noise variability, so that the power density spectrum (PDS) contained more power at low frequencies (Lawrence & Papadakis 1993). In order to characterise the intrinsic source variability, Lawrence & Papadakis measured the fractional rms variability seen from each source. However, because the variability of any source displaying red-noise characteristics will depend on the length of the observation, the shape of the PDS must also be known. Power-law fits were modelled to each spectrum, with the weighted mean power-law index given by the relation

$$P(\nu) \propto \nu^{-1.55\pm0.09} \tag{1.13}$$

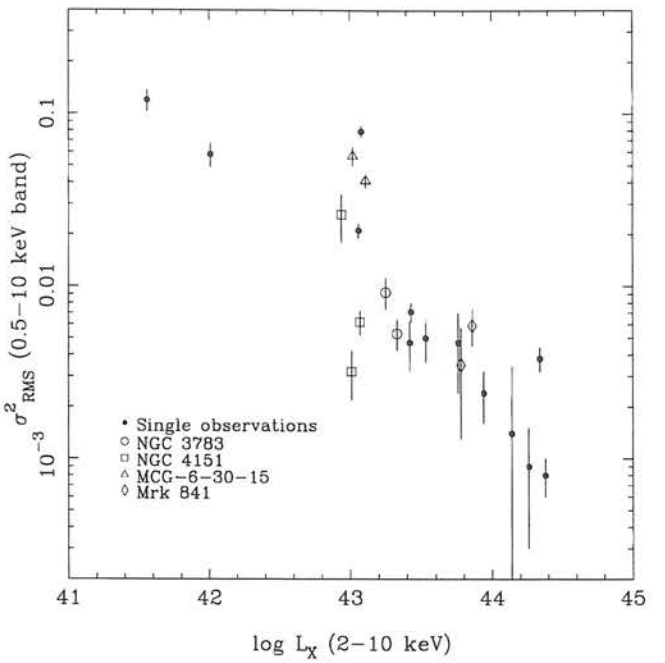

Figure 1.3: Results from Nandra et al. (1997) showing the relationship between excess variance $\sigma^2_{\rm rms}$ and X-ray luminosity $L_{\rm X}$ for a sample of 17 AGN. Data from Nandra et al. (1997).

In addition to this, a strong correlation between the amplitude of variations A and the X-ray luminosity $L_{\rm X}$ of the source was found, of the form

$$A \propto L_{\rm X}^{0.53\pm0.05} \tag{1.14}$$

This result was confirmed from the observations of 17 AGN using *ASCA* (Nandra et al. 1997), where the excess variance $\sigma^2_{\rm rms}$ was used to determine the average X-ray variability for each source, above that expected from statistical fluctuations in the background level. The results are shown in Figure 1.3. Nandra et al. (1997) found that short time-scale X-ray variability was very common in AGN, with some objects showing evidence for 'ultrarapid' variability on time-scales of seconds. The amplitude of variability was often greater in the soft band (0.5–2.0 keV) than in the harder 2–10 keV band. The general trend in X-ray continuum variability for AGN has been found to be a softening of the 2–10 keV spectrum with increasing source luminosity (Mushotzky et al. 1993).

However, there are classes of AGN that do *not* follow the relationship between X-ray variability and luminosity seen in local AGN. One such group is the narrow-line Seyfert 1 galaxies (NLS1s), investigated in detail in Chapters 2 and 3. Narrow-

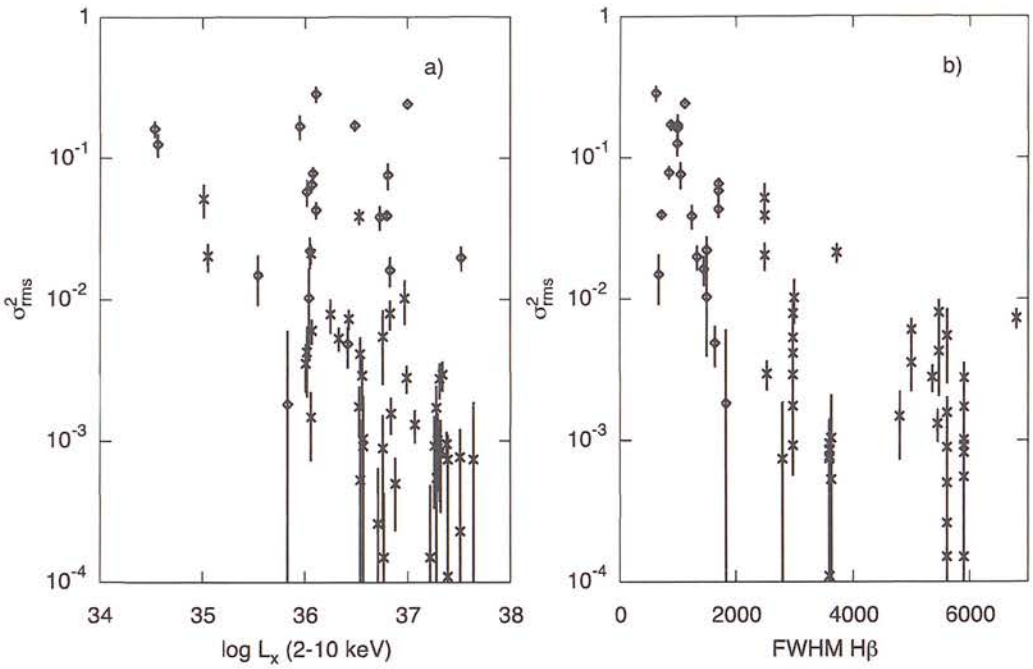

Figure 1.4: Results from Turner et al. (1999) showing the relationship between (a) excess variance $\sigma^2_{\rm rms}$ and X-ray luminosity $L_{\rm X}$ (in log W) and (b) $\sigma^2_{\rm rms}$ and FWHM of the Hβ line for a sample of broad-line Seyfert 1s (crosses) and narrow-line Seyfert 1s (open diamonds). Data from Turner et al. (1999).

line Seyfert 1 galaxies are AGN that show the same properties as classical broad-line Seyfert 1s, with comparable bolometric luminosities, but the widths of the permitted lines from the BLR are only slightly wider than the narrow forbidden lines. *ASCA* observations of 36 Seyfert galaxies covering the full range of permitted-line widths were analysed to see whether the observed variability-luminosity relation held when NLS1s were included in the sample (Turner et al. 1999). The excess variances for all the galaxies in the sample were calculated, and while a significant correlation remained, the scatter was much greater than that seen in the sample of Nandra et al. (1997). This suggested that the excess variance had a strong dependence on the width of the permitted lines in addition to the dependence on luminosity. When the excess variance was plotted against FWHM of Hβ a strong correlation was observed, shown in Figure 1.4.

Another class of AGN also violate the variability–luminosity relationship. The X-ray variability of a sample of 13 AGN with X-ray luminosities $\lesssim 10^{34}$ W was studied

by Ptak et al. (1998). These low-luminosity AGN (LLAGN) as a class showed generally much lower-amplitude variability than predicted from the variability–luminosity relationship. It is thought that this could be because the geometry of the accretion disc is different for LLAGN than for more luminous sources. One possible difference is that while the accretion disc for normal AGN is thought to be geometrically thin and optically thick, the accretion discs in LLAGN are not thin and have a much lower radiative efficiency. In this case heat would be transferred through the disc by advection, in an *advection-dominated accretion flow* (ADAF). The advection causes the disc to heat and thicken vertically (Narayan & Yi 1995). The resulting almost-spherical accretion flow is optically thin (Rees et al. 1982; Abramowicz et al. 1995). In the case of ADAFs, it is the accretion flow that produces the X-ray emission, whereas for a thin disc the most likely scenario is inverse-Compton scattering of UV photons in a corona above the disc. The low efficiency of the radiation mechanism means that the radiative area is much larger, and so the time required to respond to changes in accretion rate (if this is what drives the variability) is likely to be between several to tens of kiloseconds, depending on whether the characteristic time-scale corresponds to light or sound travel-time (Ptak et al. 1998). Therefore little or no variability would be expected on the time-scales probed by the *ASCA* observations.

Studies of high-redshift AGN have previously been undertaken to see whether the variability–luminosity relation holds further back in AGN evolution. Archival *ROSAT* observations were analysed using a maximum-likelihood technique to determine limits to the intrinsic variability of 86 AGN spanning a wide range of redshift (Almaini et al. 2000). The maximum-likelihood technique was used because the sources were too faint to obtain using the power density spectrum, with each source then divided by its mean flux to obtain the fractional variability. Although the results showed that only a small number of AGN showed individual evidence for variability, it is possible that a significant fraction of all AGN would show variability given sufficient signal-to-noise as the maximum-likelihood technique suggested that the average variability of the ensemble was above zero. When the fractional variability was plotted against the X-ray luminosity, the data showed an apparent minimum with an upturn toward higher luminosities. The data were split into local and distant AGN samples, with

the local AGN showing the clear correlation between variability and luminosity described in previous studies. The high-redshift AGN, however, showed no evidence for the same correlation, and in fact there was the suggestion that the high luminosity high-redshift sources were more variable in X-rays than their low-redshift counterparts. This analysis was repeated on a larger sample of 156 AGN from the deep *ROSAT* survey (Manners et al. 2002). These AGN were combined into ensembles in order to obtain meaningful Gaussian statistics and the variability amplitudes were normalised to reduce the effect of red-noise on the results. Again, a clear correlation between variability and X-ray luminosity was observed, and a power-law fit to the AGN with $z < 2$ gave a value close to that found for local AGN. The upturn in variability for AGN with $z > 2$ was again found as in Almaini et al. (2000) and could not be explained as a consequence of the known trend in variability with luminosity.

1.3.2 Optical and UV variability

Optical variability was one of the first recognised properties of quasi-stellar objects (Matthews & Sandage 1963; Smith & Hoffleit 1963), prior to their classification as AGN, and was one of the early arguments used for a small emitting region (see Section 1.2.1). The first objects to be clearly identified as optically variable were what are now known as blazars or optically violent variables (OVVs), for which the optical variability is thought to arise from Doppler beaming from a jet viewed face-on. Optical variability of Seyfert galaxies was not discovered until later (Fitch et al. 1967). As with the X-ray variability, the optical and UV variations are stochastic with no characteristic time-scales; therefore, for the AGN for which the optical variability has been quantified, the most common way of characterising the variability is to use the mean fractional variation (Peterson 2001)

$$F_{\rm var} = \frac{\sqrt{\sigma^2 - \bar{\delta^2}}}{\bar{f}} \tag{1.15}$$

where σ^2 is the flux variance, $\bar{\delta^2}$ is the mean-square uncertainty in the fluxes and $\bar{f}$ is the mean flux over all observations. This is the same as the excess variance used to characterise the X-ray variability, and the differences between the nomenclature are historical.

The best-studied object in the optical and UV is the Seyfert 1 galaxy NGC 5548; therefore it is useful to discuss it in detail here as its properties are the same as for other Seyfert 1s, but they are perhaps better understood thanks to the wealth of data made available by the AGN Watch project[1], a collaborative effort designed to allow the determination of the geometry of the BLR in AGN via reverberation mapping. NGC 5548 was chosen due to its low redshift ($z = 0.0172$) and long history of strong optical and UV variability (Gregory et al. 1982; Peterson et al. 1990). The nucleus of NGC 5548 was observed every four days for eight months using the *International Ultraviolet Explorer* (*IUE*) in order to characterise the variability of the UV continuum and emission lines (Clavel et al. 1991). The study found significant variability in both the continuum and in emission lines spanning a wide range of ionization states, with the variability amplitude decreasing with increasing wavelength. There was no lag between variations in the different wavelength bands, meaning that the continuum emission was much bluer when brighter; however, it was not clear how much of this was due to contamination by stellar emission from the host galaxy. For the emission lines, the highest ionization species appeared to show the strongest variability, almost as strong as the continuum fluctuations whose maximum fractional variability was $F_{\rm var} = 0.30$ in the 1350Å band (Clavel et al. 1991). The regular sampling interval of the *IUE* observations also permitted the shape of the ionizing continuum to be derived, and also the determination of the fluctuation power spectrum (Krolik et al. 1991). As for the X-ray variability studies, the PDS for the UV variability showed red-noise characteristics. The slope of the PDS was steep ($\alpha \sim 2 - 3$), with most of the power at time-scales of $\sim$1 yr.

Contemporaneous optical variability studies of NGC 5548 were performed alongside the *IUE* observations. The observations initally spanned a 10-month period (Peterson et al. 1991), but were continued over the following 13 years to allow the optical variability to be characterised over long time-scales (Peterson et al. 2002). The optical study utilised observations at many different telescopes and was less regularly-sampled than the UV data-set. Significant variability was again observed both in the continuum and in the Hβ broad emission line, but with lower fractional variability

[1]See the AGN Watch website at http://www-astronomy.mps.ohio-state.edu/ agnwatch/

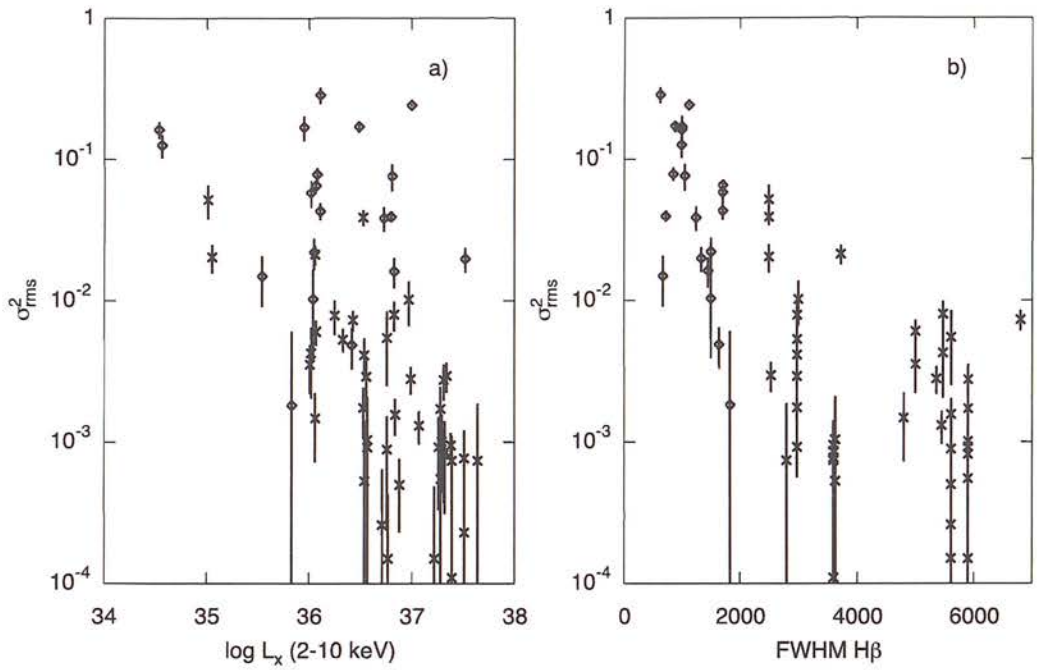

Figure 1.4: Results from Turner et al. (1999) showing the relationship between (a) excess variance $\sigma^2_{\rm rms}$ and X-ray luminosity $L_{\rm X}$ (in log W) and (b) $\sigma^2_{\rm rms}$ and FWHM of the Hβ line for a sample of broad-line Seyfert 1s (crosses) and narrow-line Seyfert 1s (open diamonds). Data from Turner et al. (1999).

line Seyfert 1 galaxies are AGN that show the same properties as classical broad-line Seyfert 1s, with comparable bolometric luminosities, but the widths of the permitted lines from the BLR are only slightly wider than the narrow forbidden lines. *ASCA* observations of 36 Seyfert galaxies covering the full range of permitted-line widths were analysed to see whether the observed variability-luminosity relation held when NLS1s were included in the sample (Turner et al. 1999). The excess variances for all the galaxies in the sample were calculated, and while a significant correlation remained, the scatter was much greater than that seen in the sample of Nandra et al. (1997). This suggested that the excess variance had a strong dependence on the width of the permitted lines in addition to the dependence on luminosity. When the excess variance was plotted against FWHM of Hβ a strong correlation was observed, shown in Figure 1.4.

Another class of AGN also violate the variability–luminosity relationship. The X-ray variability of a sample of 13 AGN with X-ray luminosities $\lesssim 10^{34}$ W was studied

by Ptak et al. (1998). These low-luminosity AGN (LLAGN) as a class showed generally much lower-amplitude variability than predicted from the variability–luminosity relationship. It is thought that this could be because the geometry of the accretion disc is different for LLAGN than for more luminous sources. One possible difference is that while the accretion disc for normal AGN is thought to be geometrically thin and optically thick, the accretion discs in LLAGN are not thin and have a much lower radiative efficiency. In this case heat would be transferred through the disc by advection, in an *advection-dominated accretion flow* (ADAF). The advection causes the disc to heat and thicken vertically (Narayan & Yi 1995). The resulting almost-spherical accretion flow is optically thin (Rees et al. 1982; Abramowicz et al. 1995). In the case of ADAFs, it is the accretion flow that produces the X-ray emission, whereas for a thin disc the most likely scenario is inverse-Compton scattering of UV photons in a corona above the disc. The low efficiency of the radiation mechanism means that the radiative area is much larger, and so the time required to respond to changes in accretion rate (if this is what drives the variability) is likely to be between several to tens of kiloseconds, depending on whether the characteristic time-scale corresponds to light or sound travel-time (Ptak et al. 1998). Therefore little or no variability would be expected on the time-scales probed by the *ASCA* observations.

Studies of high-redshift AGN have previously been undertaken to see whether the variability–luminosity relation holds further back in AGN evolution. Archival *ROSAT* observations were analysed using a maximum-likelihood technique to determine limits to the intrinsic variability of 86 AGN spanning a wide range of redshift (Almaini et al. 2000). The maximum-likelihood technique was used because the sources were too faint to obtain using the power density spectrum, with each source then divided by its mean flux to obtain the fractional variability. Although the results showed that only a small number of AGN showed individual evidence for variability, it is possible that a significant fraction of all AGN would show variability given sufficient signal-to-noise as the maximum-likelihood technique suggested that the average variability of the ensemble was above zero. When the fractional variability was plotted against the X-ray luminosity, the data showed an apparent minimum with an upturn toward higher luminosities. The data were split into local and distant AGN samples, with

the luminous AGN with masses between $10^7 - 10^9 M_\odot$. The properties of this particular AGN, discussed in detail in Chapter 4, make it ideal for testing our expectations of AGN variability.

The optical variability of this object has proven the subject of some controversy, and so a monitoring of the nucleus was undertaken on several consecutive nights in order to determine whether it was in fact optically variable. Chapter 4 discusses the data analysis and results, and I describe the detection of optical variability in NGC 4395 and the precautions that were taken to ensure that the observed variability was not an artifact of the reduction process. The optical properties of NGC 4395 are compared with NGC 5548, and I show that the variability time-scales for the two objects are consistent with a simple scaling relationship with black hole mass between the two. Absolute variability time-scales are compared with the predictions from a simple accretion disc model and are found to be inconsistent, as for other Seyfert 1 galaxies.

1.4.3 Investigating X-ray variability and black hole mass in AGN

Although a good correlation between X-ray variability and luminosity is seen for local broad-line Seyfert 1s, the fact that this is destroyed when NLS1s and LLAGN are included in the sample suggests that another parameter is driving either the variability amplitude or time-scale. One possibility is that the primary parameter is the mass of the black hole, as is discussed for the optical variability in NGC 4395 and NGC 5548. In this study, the correlations between $\sigma^2_{\rm NXS}$ with luminosity or $M_{\rm BH}$ are discussed first for objects that have mass estimates from reverberation mapping, which are potentially the most secure. This is followed with an investigation of the relationships when the putative extreme accretion rate objects (NLS1s and LLAGN) are included in the sample. In the latter case the correlation with luminosity is very poor, confirming the results of previous authors. The correlation with mass is still good when the objects with less-accurate mass measurements are included, indicating that this parameter is an important driver of the X-ray variability amplitude. The implications of this result are discussed with respect to several models of X-ray variability.

CHAPTER 2

NLS1 Reduction and Analysis

2.1 Introduction

Narrow-line Seyfert 1 galaxies (NLS1s) are a peculiar subclass of AGN first isolated by Osterbrock & Pogge (1985), after the discovery of abnormally narrow permitted lines in Mrk 359 (Davidson & Kinman 1978). These objects have permitted lines only slightly broader than the forbidden lines such as [O III]; Seyfert 1s are generally defined as NLS1s if they have FWHM H$\beta \lesssim 2000$ km s^{-1} and if the flux ratio [O III]/H$\beta < 3$ applies, to distinguish them from Seyfert 2s. A larger proportion of bright soft X-ray AGN are found to be NLS1s than are found in optical samples. Generally about 15 per cent of optically-selected AGN are found to be NLS1s using the above criteria (Osterbrock & Pogge 1987), whereas on average some 40 per cent of soft X-ray selected AGN are NLS1s (Grupe et al. 1998, 1999; Edelson et al. 1999). However, this does not appear to be the case for samples of AGN selected using their hard X-ray spectra (Fischer et al. 1998). Many NLS1s also show fast high-amplitude X-ray variability (Nandra et al. 1997; Turner et al. 1999), as outlined in Chapter 1. In addition to this, NLS1s display other properties that distinguish them from classical Seyfert 1s. Most NLS1s show strong Fe II emission (Osterbrock & Pogge 1985), a weak big blue bump (Pounds et al. 1987), steep soft X-ray spectra (Boller et al. 1996) and bright IR emission (Moran et al. 1996).

The physical nature of NLS1s that leads to the above phenomena is not currently understood. There are several possible explanations for the narrow permitted lines, which also provide explanations for the other observed properties to a greater or lesser extent. One possibility is that the BLR is partially covered, such that the highest-velocity clouds are obscured from the line-of-sight. Seyfert 1 and 2 galaxies are already known to be different in their polarization properties (see e.g. Antonucci 1983), arguing for two (or more) separate scattering regions whose observational effects vary depending on the orientation of the nucleus to the line-of-sight. If the inner part of the BLR is obscured in NLS1s, then the inner region could be visible in the form of a broad component of polarized flux in the permitted lines. However, a study by Smith et al. (2002) found that there was no evidence that the NLS1 broad lines were broader in polarized flux than in total flux, and furthermore that the (admittedly small) sample of NLS1s were no different in their polarization properties than normal Seyfert 1s, arguing against this interpretation.

Alternatively, formation of BLR clouds close to the active nucleus could be hindered in some way, so that we see only clouds further away from the central black hole with lower velocities. Reverberation mapping studies (e.g. Wandel et al. 1999; Kaspi et al. 2000) have included a number of NLS1s and narrow-line QSOs, allowing a relative study of the radii of their BLRs to be undertaken (Peterson et al. 2000). It was found that NLS1s (with the exception of NGC 4051) lie on the same relation between $R_{\rm BLR}$ and the monochromatic luminosity at 5100Å found by Kaspi et al. (2000), and hence it is unlikely that abnormally large BLRs are responsible for the unusual properties of NLS1s.

The third possibility is that the axis of the BLR in NLS1s is preferentially aligned close to the line-of-sight. In this case, the geometry of the BLR is required to be disc-like, and then the line-of-sight velocities in the disc are reduced as a result of inclination effects. The studies of NLS1 soft X-ray spectra by Boller et al. (1996) showed that NLS1s generally have steeper soft X-ray spectra than normal BLS1s, and that Seyfert galaxies with FWHM H$\beta \gtrsim 3000$ km s^{-1} and soft X-ray photon index $\Gamma > 3$ seemed to be discriminated against in nature. This could happen if either NLS1s had much stronger soft X-ray excesses relative to their optical and IR spectra, with normal-

strength hard X-ray tails, or if the soft X-ray excess was similar in strength to normal Seyfert 1s, but the hard X-ray tail was markedly weaker. If the former were true, then relatively large soft X-ray excesses could occur if a geometrically-thick accretion disc were viewed along its polar axis (Madau 1988), or alternatively if a thin disc were viewed edge-on (Laor & Netzer 1989; Netzer 1989). However if NLS1s have weak hard X-ray tails their properties are more difficult to explain using primarily geometric arguments (Boller et al. 1996).

Finally, the current favoured model is that the central black holes in NLS1s are systematically smaller than in normal Seyfert 1s for a given luminosity. This would require that the accretion rate in NLS1s is close to the Eddington limit in order to explain the luminosities of these objects, which are generally very similar to normal broad-line Seyfert 1s (BLS1s). In this case the BLR is located at the same absolute radius as for a BLS1 of the same luminosity, but at a much larger multiple of the Schwarzschild radius, which gives rise to the narrower broad-line widths. Mathur (2000) proposed that NLS1s could be low-luminosity analogues to the high-luminosity distant quasars, in which the black hole is thought to be in an 'active-growth' phase.

Clues to the nature of NLS1s could be found by studying the relationship between the central black hole and the properties of the host galaxy. A good correlation exists for inactive galaxies between the central black hole mass ($M_{\rm BH}$) and the stellar velocity dispersion σ_* of the bulge component of the host galaxy (Gebhardt et al. 2000a; Ferrarese & Merritt 2000), although the slope of the relation is a subject of some debate. A similar correlation exists between $M_{\rm BH}$ and the blue luminosity ($L_{\rm Bulge}$) of the host galaxy bulge (Kormendy & Richstone 1995; Magorrian et al. 1998), from which the $M_{\rm BH} - L_{\rm Bulge}$ relation was found to be equivalent to a simple proportionality between $M_{\rm BH}$ and the mass of the bulge ($M_{\rm Bulge}$). Initially it was thought that the former correlation was tighter than the latter, with the $M_{\rm BH} - \sigma_*$ correlation being consistent with zero intrinsic scatter within the measurement errors. However a subsequent study of the $M_{\rm BH} - M_{\rm Bulge}$ relationship by McLure & Dunlop (2002) found that the scatter in this correlation could be reduced to a level comparable with that of the $M_{\rm BH} - \sigma_*$ relation if the black hole mass estimates came from reliable stellar dynamical methods alone and if the bulge luminosities were calculated using nuclear–host galaxy decom-

position techniques and the superior resolution of *HST*.

The same correlations have been shown to apply to AGN also. Initially, a study by Wandel (1999) found that Seyfert 1s had a lower $M_{\rm BH}/M_{\rm Bulge}$ ratio than normal inactive galaxies; however, subsequent analysis found this not to be the case and that Seyfert galaxies do follow the same $M_{\rm BH} - M_{\rm Bulge}$ relation as inactive galaxies (Wandel 2002). This result was supported by the findings from other studies (McLure & Dunlop 2001; Laor 2001). Seyfert 1s were also shown to lie on the $M_{\rm BH} - \sigma_*$ relation by Gebhardt et al. (2000b), whose initial study included a sample of 7 Seyfert 1s that had black hole mass estimates from reverberation mapping studies and previously published velocity dispersions.

The question of whether NLS1s also lie on either the $M_{\rm BH} - M_{\rm Bulge}$ or $M_{\rm BH} - \sigma_*$ correlations remains a subject of some controversy. Mathur et al. (2001) estimated black hole masses, bulge masses and stellar velocity dispersions for a sample of 11 NLS1s and 4 NL quasars. The black hole masses were calculated by fitting the spectral energy distributions (SEDs) with an accretion disc and corona model proposed by Witt et al. (1997), and the bulge magnitudes were estimated from ground-based absolute magnitudes corrected for emission from the nucleus, rather than via nuclear–host galaxy decomposition. The stellar velocity dispersions were calculated using [O III] FWHM/2.35 rather than stellar absorption lines, as the latter are often difficult to observe for NLS1s as a result of strong Fe II emission in the wavelength regions of interest. They found that the narrow-line objects followed neither the $M_{\rm BH} - M_{\rm Bulge}$ or $M_{\rm BH} - \sigma_*$ relations. A subsequent study of a larger sample of both normal Seyfert 1s and NLS1s (Grupe & Mathur 2004) found again that NLS1s lie below the $M_{\rm BH} - \sigma_*$ relation, a conclusion confirmed by Bian & Zhao (2004), who analysed a sample of 150 NLS1s from the Sloan Digital Sky Survey (SDSS) Early Data Release. However, a study of 59 NLS1s (Wang & Lu 2001) observed spectroscopically by Véron-Cetty et al. (2001) determined that NLS1s do conform to the $M_{\rm BH} - \sigma_*$ relation, but with more scatter. A recent study by Botte et al. (2004) found that NLS1s lie on the $M_{\rm BH} - M_{\rm Bulge}$ relation but below the $M_{\rm BH} - \sigma_*$ relation; however, a in a subsequent paper (Botte et al. 2005) using stellar velocity dispersions obtained from stellar absorption lines they cast doubt on the validity of the latter result, and find that NLS1s follow the same relations

as other AGN and inactive galaxies.

Crucially, one thing that all the above studies of the $M_{\rm BH} - \sigma_*$ relation have in common (with the exception of Botte et al. (2005)) is their use of $\sigma_{\rm FWHM}$=[O III] FWHM/2.35 as a proxy for the stellar velocity dispersion. It is not certain that this provides an accurate determination of σ_* for objects such as NLS1s. Indeed Botte et al. (2005) studied both σ_* from the Ca II triplet at ~ 8550Å and from $\sigma_{\rm FWHM}$ and found that $\sigma_{\rm FWHM}$ overestimated the true stellar velocity dispersion for NLS1s. This result is confirmed in the much larger study of 1749 Seyfert 2s from the SDSS by Greene & Ho (2005). This study found that for massive galaxies with large values of σ_*, $\sigma_{\rm FWHM}$ provided a good estimate of the true stellar velocity dispersion, whereas for less massive galaxies with smaller σ_*, $\sigma_{\rm FWHM}$ provides a systematically poorer estimate of σ_*. This corresponds to a trend with $M_{\rm BH}$ as a result of the $M_{\rm BH} - \sigma_*$ relation. They also found a strong correlation between the Eddington ratio $L/L_{\rm Edd}$ and the suitability of $\sigma_{\rm FWHM}$ as an estimate for σ_*, and determined that for high Eddington-ratio objects such as NLS1s, $\sigma_{\rm FWHM}$ may overestimate σ_* by as much as $0.2 - 0.3$ dex. When they corrected the Grupe & Mathur (2004) velocity dispersions using their derived values, they found that the conclusion that NLS1s do not follow the $M_{\rm BH} - \sigma_*$ relation was no longer statistically valid.

This study has several aims. Firstly, it is necessary to determine whether $\sigma_{\rm FWHM}$ is a good estimator of σ_* for NLS1s, as implied by the investigations of Greene & Ho (2005) and Botte et al. (2005). Secondly, are the black holes in NLS1s systematically smaller than BLS1s, or are the unusual properties of the former due to inclination effects? The question of whether NLS1s lie on the $M_{\rm BH} - \sigma_*$ relation is also addressed. If they do not, then it provides powerful support for the paradigm of NLS1s as local, low-luminosity analogues to high-redshift QSOs as proposed by Mathur (2000). Finally, can the extreme X-ray properties of NLS1s be explained using a scaling relation between the amplitude of the X-ray variability and the black hole masses? As mentioned in Chapter 1, NLS1s deviate from the relationship seen between $\sigma^2_{\rm NXS}$ and $L_{\rm X}$ for local AGN. Could it be that the underlying parameter driving the variability amplitude is in fact the mass of the black hole rather than the luminosity, or is it some combination of the two?

To achieve the aims set out above, a sample of NLS1s and BLS1s was observed using moderate-resolution spectroscopy in order to obtain as many new stellar velocity measurements as possible. In addition to this, samples of both NLS1s and BLS1s were taken from the literature in order that meaningful statistical interpretations of the results could be attempted. The remainder of this Chapter explains in detail the observing and reduction procedures and the fitting methods utilised to extract the stellar velocity dispersion information. The following Chapter combines these new results with the literature values and discusses the properties of the two samples, and the X-ray variability properties of NLS1s and BLS1s are compared in Chapter 5.

2.2 Data Acquisition

Long-slit spectroscopic observations of a sample of 9 NLS1s and 13 BLS1s were obtained during three separate observing runs. Two of these used the 4.2-m *William Herschel Telescope* (*WHT*) at the Roque de los Muchachos Observatory on the island of La Palma. The first of these took place from 4-6 October 2002 and was performed by R. McLure. The second was performed by the author and O. Almaini on 24-25 July 2003. The third set of observations were obtained by R. McLure using the 3.5-m *New Technology Telescope* (*NTT*) at the European Southern Observatory (ESO) at La Silla, Chilé. The NLS1 objects were selected to be those low-redshift objects with good X-ray variability data in the literature. The BLS1 sample objects were predominantly objects for which no velocity dispersion information had previously been obtained. Some objects that already had good quality velocity dispersion measurements in the literature were included to act as controls and checks during the analysis.

For the *WHT* observations the ISIS double-beam spectrograph was used to obtain medium-resolution spectra of the regions including the Mg *b* feature at ~ 5170Å and the Ca II triplet feature (rest-frame wavelengths 8498.06, 8542.14 and 8662.17Å). The EEV12 4096×2048 and MARCONI2 4611×2048 pixel CCD detectors were used for the blue and red arm detectors respectively, with the R1200 gratings giving dispersions of 0.23Å pixel^{-1} for each arm. An order-blocking filter was used (RG630) with the red-arm grating to prevent contamination by second-order blue continuum emission from the Seyfert nucleus. For the October 2002 observations, the central wavelengths for the

blue and red spectrographs were 5175Å and 8525Å, each with an unvignetted spectral range of $\sim$ 800Å. For the July 2003 observations, the central wavelengths were varied depending on the redshifts of the objects, ensuring that the desired spectral regions were always centred on the regions of the chips with the least vignetting. A 1 arcsec slit width was used for all observations, giving velocity resolutions of $\sim$41 km s^{-1} and $\sim$21 km s^{-1} for the blue and red spectra.

The red-arm detector of the ESO Multi-Mode Instrument (EMMI) was used for the *NTT* observations. EMMI uses 2 2048×4096 pixel MIT/LL CCDs with 15-μm pixels. During these observations, the pixels were binned $2\times$ along both detector axes, giving a spatial scale of 0.33 arcsec pixel^{-1}. Grating 7 was used giving a dispersion of 0.41Å pixel^{-1}, centred on 5001Å with a wavelength covereage of 1300Å. Again, a 1 arcsec slit was used for all observations, giving a velocity resolution of $\sim$50 km s^{-1}.

Obtaining stellar velocity dispersions for AGN is often difficult, since stellar absorption features suffer severe contamination from nuclear AGN light. This is a particular problem for NLS1s, which often show strong Fe II multiplets centred on 4570, 5190 and 5300Å, and also the Ca II triplet in emission. This can make it difficult or impossible to detect the stellar features in these spectral regions. So an observing strategy was constructed that would minimize the contribution from the active nucleus. Initial studies of the $M_{\rm BH}$–σ_* relation by Gebhardt et al. (2000a) found that the stellar velocity dispersion did not deviate much within an aperture radius up to $2R_e$, where R_e is the effective radius of the bulge and is the radius within which half of the luminosity of the bulge is emitted. Therefore it was decided to obtain spectra offset by 1 arcsec from the AGN position in order to minimise the nuclear contribution while remaining within the predicted effective radii of the galaxies in the sample. Several offset spectra were obtained for each galaxy. This allowed the positioning of the slit on either side of the nucleus so that any disc contribution could be quantified via observable asymmetries in the absorption features. Nuclear spectra were also taken to facilitate the measurement of nuclear properties (specifically Hβ linewidths, 5100Å continuum luminosities and [OIII] 5007Å linewidths and luminosities). It was hoped that the nuclear spectra would also allow the modelling and subtraction of any residual nuclear contamination in the offset spectra. Exposure times varied between $6,000-14,000$ s in

total for the offset spectra and between $600 - 1,200$ s for the nuclear spectra. A log of observations is presented in Table 2.1. In the cases of two of the BLS1s (NGC 6814 and NGC 7450), only nuclear spectra were obtained since these objects already had reliable σ_* values in the literature (Nelson & Whittle 1995). The slit was always positioned at the parallactic angle to minimize light losses due to differential atmospheric refraction, which can be a particular problem in the blue regions of the spectrum. Spectra of photometric standard stars were also taken to allow flux-calibration of the nuclear spectra.

2.3 Data Reduction

All data reduction was performed using the Image Reduction and Analysis Facility (IRAF). In this and subsequent sections, all IRAF commands and routines will be distinguished by small caps.

The first procedure is to remove the bias pedestal. This is an arbitrary voltage added to the detector chip to ensure that the number of counts in a pixel is never negative as a result of statistical fluctuations. This eliminates the requirement for a signed bit, thus doubling the digital saturation level and enabling much longer integration times. To remove this, a large number of bias 'exposures' were taken with the detector shutter closed and a zero integration time. This gave an instantaneous reading of the bias level and allowed any gradients and variations across the detector chip to be quantified. The bias exposures were averaged to remove any purely statistical fluctuations or radiation events and then this averaged frame was subtracted from each two-dimensional image.

Following this it was necessary to flat-field each exposure; that is, correct each image for the variations in the gain of individual detector pixels. The gain is the conversion factor between the number of photoelectrons per pixel produced by incident photons and the number of digital counts that this produces. To correct for the gain variations a number of exposures of a tungsten lamp were obtained prior to and after each observing session. In the case of the ISIS red-arm spectrograph, lamp exposures were obtained between each object observation to allow the correction of severe interference fringe effects that occur redward of 8000Å in this detector. For

Table 2.1: Log of observations. Columns (1), (2) and (3) list the object name, AGN type and redshift (listed in order of RA). Telescope/instrument is given in column (4). The total exposure time for each object for the offset and nuclear spectra are given in columns (5) and (6) respectively.

Object	Type	z	Telescope/ Instrument	Exp (s) Offset	Exp (s) Nucleus
Mrk 335	NLS1	0.0258	WHT/ISIS	6000	600
I Zw 1	NLS1	0.0611	WHT/ISIS	5400	600
Mrk 359	NLS1	0.0178	WHT/ISIS	9000	600
IRAS 13224-3809	NLS1	0.0667	NTT/EMMI	7200	600
MCG -6-30-15	NLS1	0.0077	NTT/EMMI	7200	600
Mrk 493	NLS1	0.0313	WHT/ISIS	9000	600
IRAS 17020+4544	NLS1	0.0604	WHT/ISIS	9000	600
Kaz 163	NLS1	0.0630	WHT/ISIS	9000	600
Akn 564	NLS1	0.0247	WHT/ISIS	6000	600
E12-G21	BLS1	0.0300	NTT/EMMI	8370	600
NGC 526A	BLS1	0.0191	NTT/EMMI	9000	600
IRAS 03450+0055	BLS1	0.0310	WHT/ISIS	5400	600
3C 120	BLS1	0.0330	WHT/ISIS	12000	1200
Mrk 79	BLS1	0.0222	WHT/ISIS	6600	600
E141-G55	BLS1	0.0360	NTT/EMMI	14000	1200
NGC 6814	BLS1	0.0052	NTT/EMMI	...	900
NGC 6860	BLS1	0.0149	NTT/EMMI	7200	600
Mrk 509	BLS1	0.0344	WHT/ISIS	5400	600
Mrk 509			NTT/EMMI	7200	600
PG 2130+099	BLQ	0.0630	WHT/ISIS	4932	600
NGC 7213	BLS1	0.0060	NTT/EMMI	7200	600
3C 445	BLS1	0.0562	WHT/ISIS	7200	900
3C 445			NTT/EMMI	7200	600
NGC 7450	BLS1	0.0106	NTT/EMMI	...	1200
NGC 7469	BLS1	0.0163	WHT/ISIS	6000	600

Figure 2.1: An ISIS red-arm tungsten lamp exposure, demonstrating the severe fringing effects that occur at near-IR wavelengths.

the blue-arm ISIS observations and the EMMI observations the lamp exposures were median-averaged to produce a single image for each night, whereas for the ISIS red-arm observations each image was flat-fielded using the lamp exposure taken immediately beforehand. Before this could be done, the wavelength-dependent structure resulting from the tungsten lamp itself was removed by summing the CCD columns along the spatial axis and then fitting a cubic spline function of a sufficiently high order that the large-scale structure from the lamp was removed while preserving any small-scale features peculiar to the object spectrum itself. It was particularly important when flat-fielding the ISIS red-arm data not to fit the interference fringes in the process. The object spectra were then flat-fielded by dividing by the normalized flat-field exposures.

Interference fringes in CCD spectra occur as a result of an effect similar to thin-film interference. In order to achieve high sensitivity, CCDs for astronomical uses are back-illuminated, so that photons do not have to travel through intervening layers of circuitry to reach the light-sensitive substrate. In addition to this, to improve sensitivity at the blue end of the spectrum the silicon substrate must be thinned to reduce the probability of recombination of the higher-energy photoelectrons. However, at wavelengths longer than about 7000Å the chip becomes semi-transparent to incoming radiation, resulting in multiple internal reflections between the front and back of the chip. These rays can then interfere either constructively or destructively, resulting in a fringing pattern that depends on the wavelength and also the spatial position on the chip. A representative ISIS red-arm lamp exposure is shown in Figure 2.1 to demonstrate this effect.

In order to remove the interference fringes from the object spectra, special care was taken during the observing procedure. During the observations, the target was nodded up and down the slit by 5 arcsec to ensure that a different part of the chip was sampled for each observation. As indicated, a tungsten lamp exposure was taken immediately prior to each observation and after normalization this was scaled and then subtracted from the object spectrum. When the object spectra were later combined, any remaining interference effects cancelled each other out as they arose from different regions on the chip.

As a result of the optics of the ISIS double-beam spectrograph, both arms of the spectrometer suffer severely from vignetting effects. In order to correct this, spectra were taken of the twilight sky in both the evening and morning on each night of observations. The sky frames were used to correct the vignetting rather than the lamp frames because in the case of the sky frames the light path through the instrument optics was the same as that for the object spectra. The sky frames were combined and flat-fielded and then binned along the dispersion axis. The rows in each bin were then summed and a cubic spline function fitted along the spatial axis to determine the illumination gradient. The object spectra were then divided through by the resulting normalized frame. Bias-correction, flat fielding and the vignetting correction were all applied using the IRAF task CCDPROC.

The next step in the reduction process is to convert the dispersion axis from a pixel scale to a wavelength scale. In the case of long-slit data, it is necessary to perform this stage prior to subtracting the sky background and extracting a one-dimensional spectrum. The detector optics introduce geometrical distortions along the slit direction that it is necessary to correct prior to any further reduction stages. This is important in the case of the red-arm ISIS spectra which have a great many sky emission lines that require accurate removal. To achieve this a number of exposures were taken of an arc lamp using the same instrumental set-up (slit width and central wavelength) as for the object observations. The respective lamps used were either CuNe-CuAr or HeAr for the *WHT* or *NTT* observations. In each comparison lamp spectrum, the strongest unblended emission lines were manually identified with their associated wavelengths for one image section (a few columns wide to improve the S/N of the weaker lines).

The task IDENTIFY was then used to fit a smooth, single-valued function along the dispersion axis, and then this process was repeated automatically every few pixels along the spatial axis using REIDENTIFY to obtain dispersion solutions all the way along the slit. The emission line identifications were then used to fit two-dimensional functions to wavelength as a function of column and row number using FITCOORDS, which were then used to perform the geometrical corrections using TRANSFORM. The dispersion scale of each nuclear spectrum or photometric standard star was mapped to a linear wavelength scale with a constant wavelength-interval per pixel. In the case of the offset spectra a logarithmic wavelength scale was used, giving a constant velocity interval per pixel.

Once the wavelength-calibration had been completed and the geometric distortions corrected, cosmic rays and radiation events were removed and the sky background was subtracted by fitting low-order (typically order 2 – 3) cubic spline functions along the spatial axis. A one-dimensional spectrum was then extracted from each image using APALL. As a result of differential refraction (and also partly because the grating is not precisely aligned with the dispersion axis of the CCD) the blue and red ends do not fall on the same part of the chip. Therefore to extract the spectrum a number of rows at a point along the dispersion axis were summed and the centre of the spectral profile found. The precise number of lines was dependent on the visibility of the spectrum in the two-dimensional image. The centre of the profile was then found automatically every 5 or 10 rows and plotted as a function of dispersion, and a low-order polynomial was fitted through the points. An aperture spanning the profile centre was set, and the one-dimensional spectrum was extracted by summing the pixels within this aperture using the trace determined above. The size of the aperture depended on the individual spectrum. A 3-pixel aperture was used for all nuclear spectra, to minimize the contribution from the host galaxy. For the offset spectra, the aperture size was determined predominantly by the redshift of the object, in order to remain within the effective radius of the bulge. Since only the nuclear spectra were to be flux-calibrated, 3-pixel spectra of the photometric standard stars were extracted also.

To flux-calibrate the nuclear spectra, a sensitivity function mapping the change

in sensitivity of the detector as a function of wavelength was constructed using the extracted standard stars and then applied to each nuclear spectrum. A correction for atmospheric extinction was applied to each object, using the standard extinction curve for La Palma. No separate extinction curve was available for the La Silla observatory, so the La Palma extinction curve was also used for these objects. The extinction curve was shifted depending on the conditions for each night using the extinction magnitudes determined nightly by the Carlsberg Meridian Telescope (CMT)[1]. A correction for Galactic extinction was also made using the tabulated values from NED[2], using the reddening maps determined by Schlegel et al. (1998). The absolute flux calibration is expected to have an accuracy of $20 - 30$ per cent. No extinction correction or flux-calibration was applied to the offset spectra. The final reduced, extracted offset blue ISIS and EMMI spectra, and red ISIS spectra, are shown in Figures 2.2, 2.3, 2.4, 2.5 and 2.6.

2.4 Spectrum preparation

To prepare the reduced galaxy spectra, both the blue and red spectra were truncated to minimize the effect of any telluric absorption features or nuclear emission lines, leaving just the spectral regions of interest. During wavelength calibration, the spectra were binned logarithmically in wavelength to ensure a constant velocity interval per pixel. The setup of the ISIS instrument means that the spectra are oversampled, allowing $2\times$ binning of the dispersion axis to improve the S/N of the fainter objects (for the objects where this was applied, the binning-up was done early in the reduction process). The stellar templates were prepared in the following manner; first, the wavelength resolution of the galaxy spectra was determined by fitting Gaussian functions to unresolved lines in the comparison lamp spectra. The resolution as a function of wavelength was then determined, and the stellar template spectra broadened to this resolution using Gaussians whose width was the difference in quadrature between the instrumental resolution and the resolution of the stellar templates. In the case of the

[1]The CMT is operated jointly by the Copenhagen University Observatory, the Institute for Astronomy, Cambridge and the Real Instituto y Observatorio de la Armada en San Fernando.

[2]NASA Extragalactic Database. NED is operated by the Jet Propulsion Laboratory, California Institute of Technology, under contract with the National Aeronautics and Space Administration.

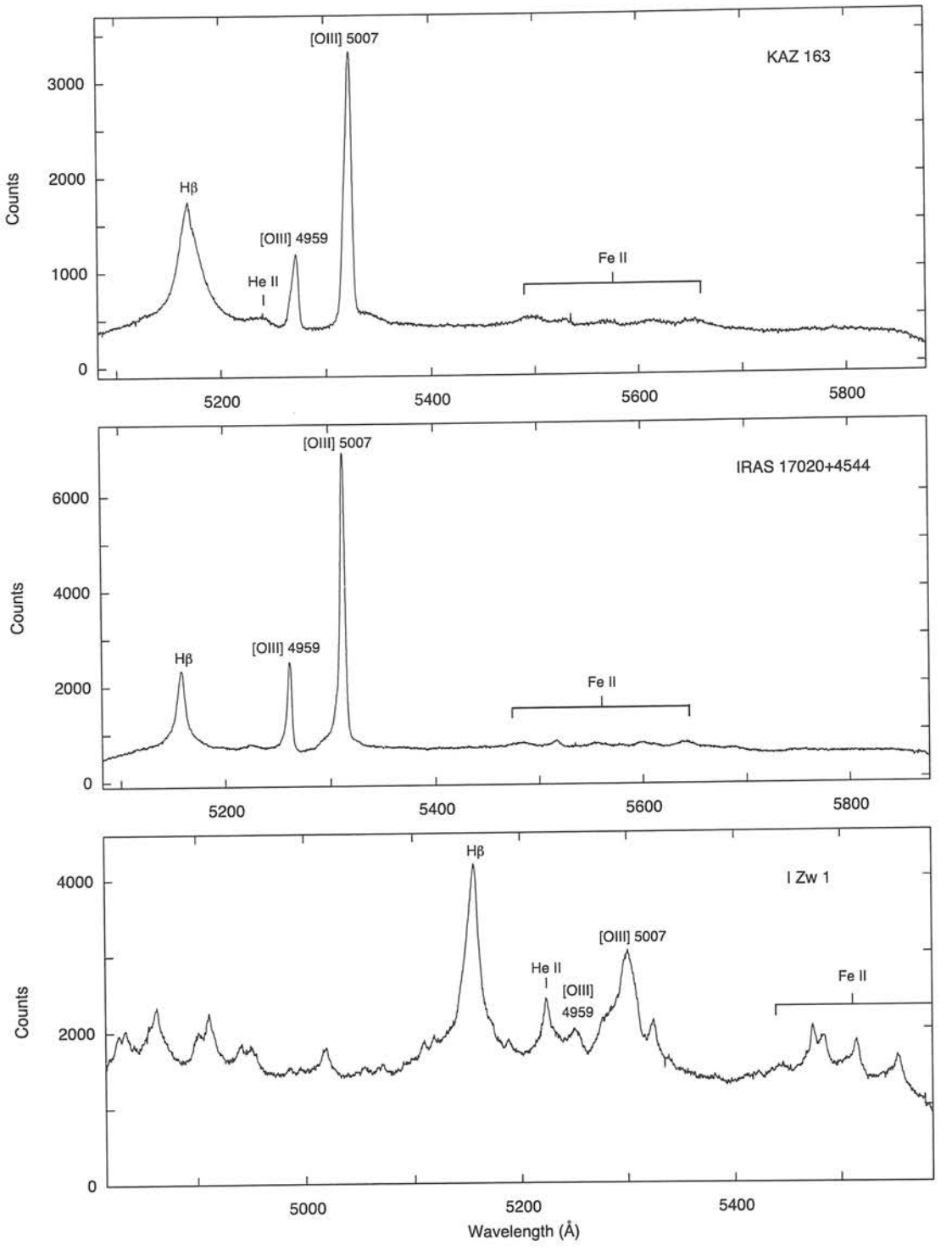

Figure 2.2: Blue offset spectra for the NLS1 sample observed with the ISIS blue-arm spectrograph. Spectra are shown in the observed frame and prominent emission/absorption lines are marked.

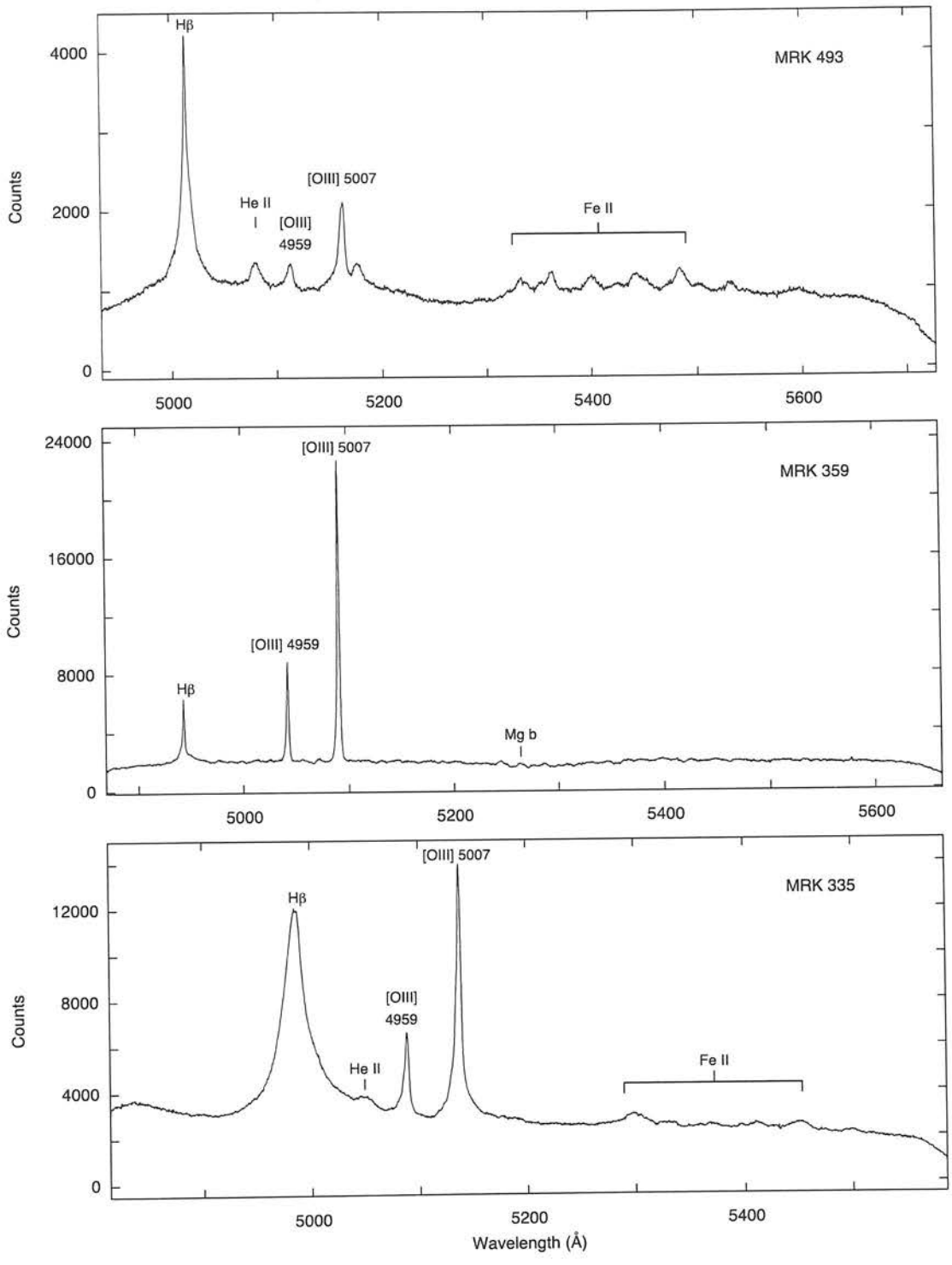

Figure 2.2: -*Continued*

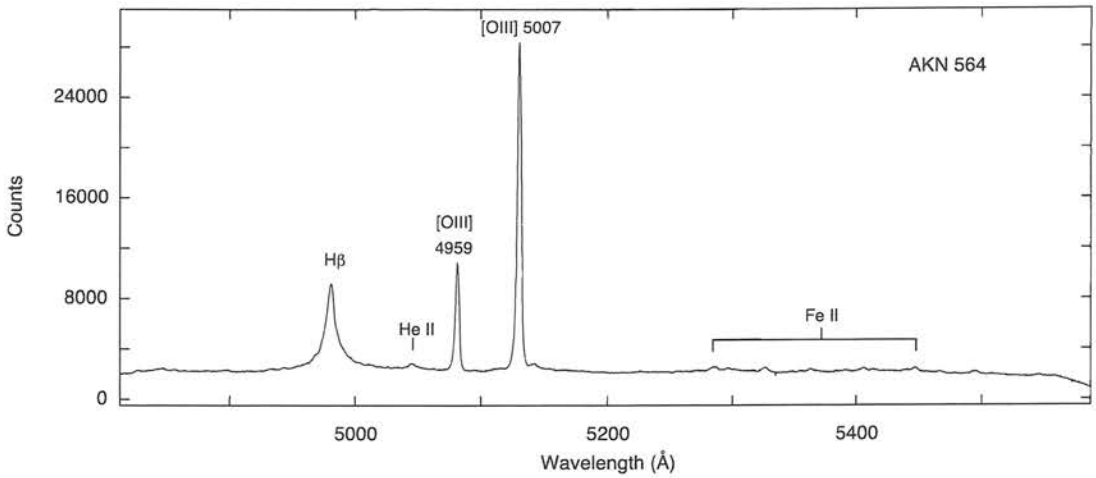

Figure 2.2: *-Continued*

red-arm ISIS spectra, the instrumental resolution was greater than that of the stellar templates. For these cases, the stellar template spectra were simply resampled onto a finer grid. Since the widths of the galaxy absorption features were likely to be significantly larger than the ISIS instrumental resolution, this was not expected to be a problem.

To subtract off the nuclear contribution, the (non-flux-calibrated) nuclear spectra were truncated to the same wavelength limits as the offset galaxy spectra, and polynomial functions fitted to the continuum. Gaussian functions were fitted to the emission lines and then added to the continuum fit to give a noise-free model of the nuclear emission. It would have been preferable to use the nuclear spectra themselves, but the S/N was often insufficient for this purpose. The nuclear model was then scaled to the intensities of the emission lines in the offset spectrum, and then the scaled model was subtracted off.

2.5 Gaussian velocity profile fitting

The Gauss-Hermite Pixel Fitting software developed by van der Marel (1994) was used to derive the bulge stellar velocity dispersion by comparing the galaxy spectrum with a library of stellar template spectra. This method is more useful for AGN spectra than techniques that involve Fourier-fitting, as it allows the masking of residual emission

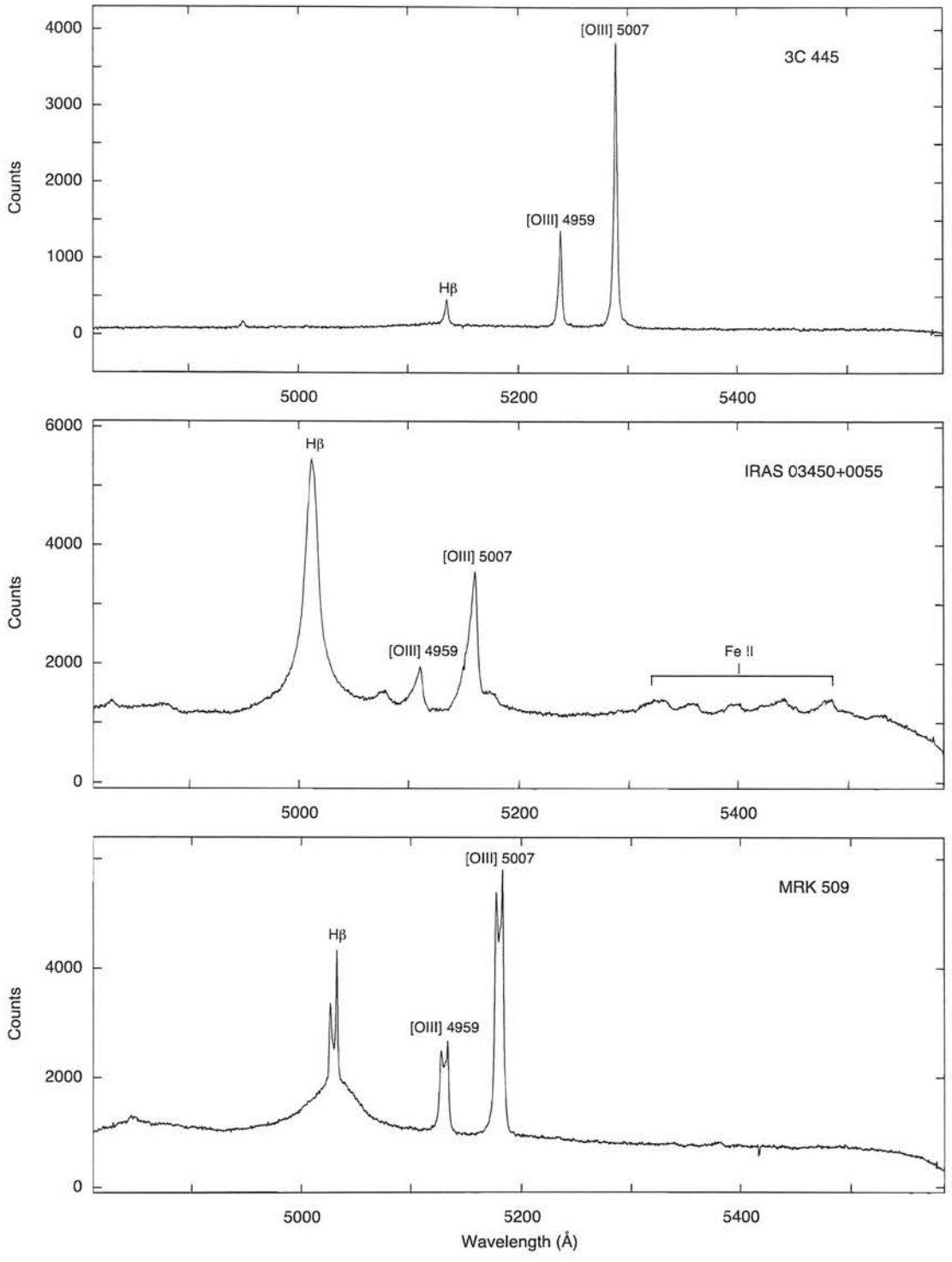

Figure 2.3: Blue offset spectra for the BLS1 sample observed with the ISIS blue-arm spectrograph. Spectra are shown in the observed frame and prominent emission/absorption lines are marked.

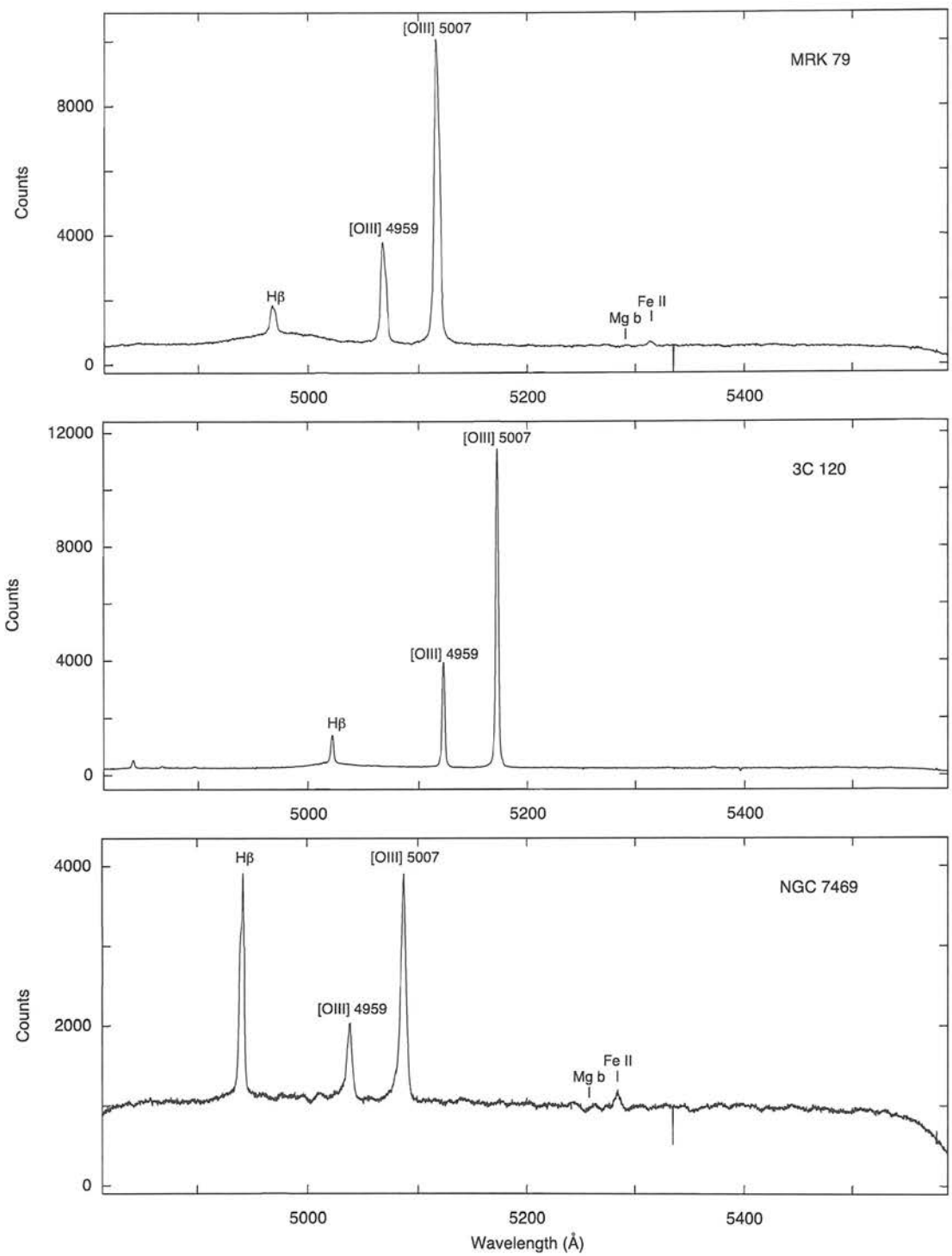

Figure 2.3: -*Continued*

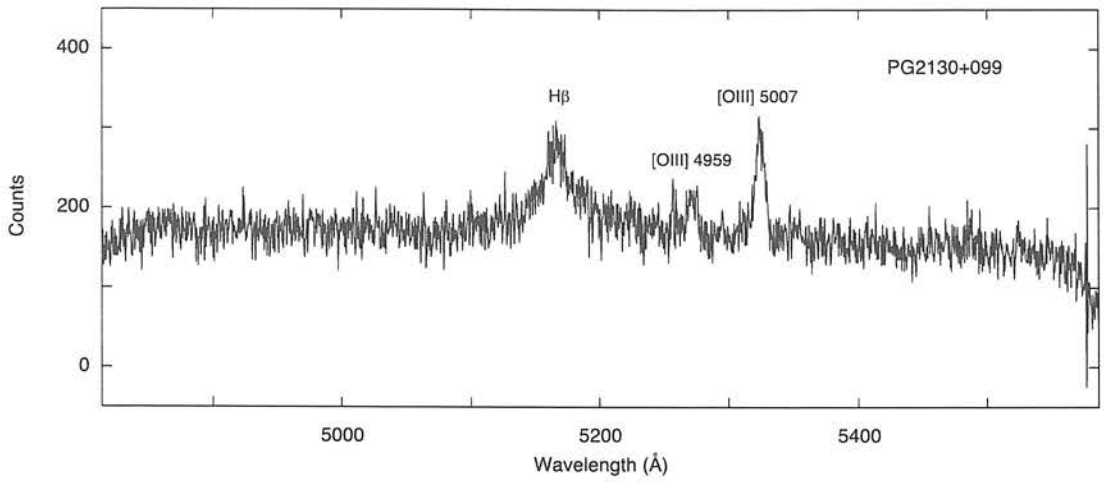

Figure 2.3: *-Continued*

Table 2.2: Stellar template stars used in the Gauss-Hermite pixel fitting process.

Star ID	Type	V	$E(B-V)$
HR4	G5III	5.55	0.893
HR14	K2III	6.07	1.380
HR19	K0III	6.23	0.970
HR22	G9III	5.53	1.045
HR40	G0III	6.30	0.650
HR60	G8III	5.74	0.880
HR224	K4III	4.43	1.500
HR279	G7III	5.61	0.970

lines or bad pixels that may remain after the subtraction of any nuclear component or sky lines. This method assumes that the galaxy spectrum is a convolution of the stellar spectrum with a broadening function representing the true velocity dispersion of the stellar population. The fitting routine convolves the template spectrum with a series of parametrized velocity profiles. These profiles are then compared with the prepared galaxy spectrum and the best-fitting parameters and errors are determined by χ^2-minimization. The stellar template stars were obtained from Treu et al. (2004). These are spectra of G-K giant stars obtained with the Echelle Spectrograph and Imager (ESI) on the *W. M. Keck-II* telescope, which has a similar resolution to ISIS. The stellar template spectral types, optical colours and magnitudes are given in Table 2.2.

To fit the prepared data, a polynomial function was fitted to the continuum of each

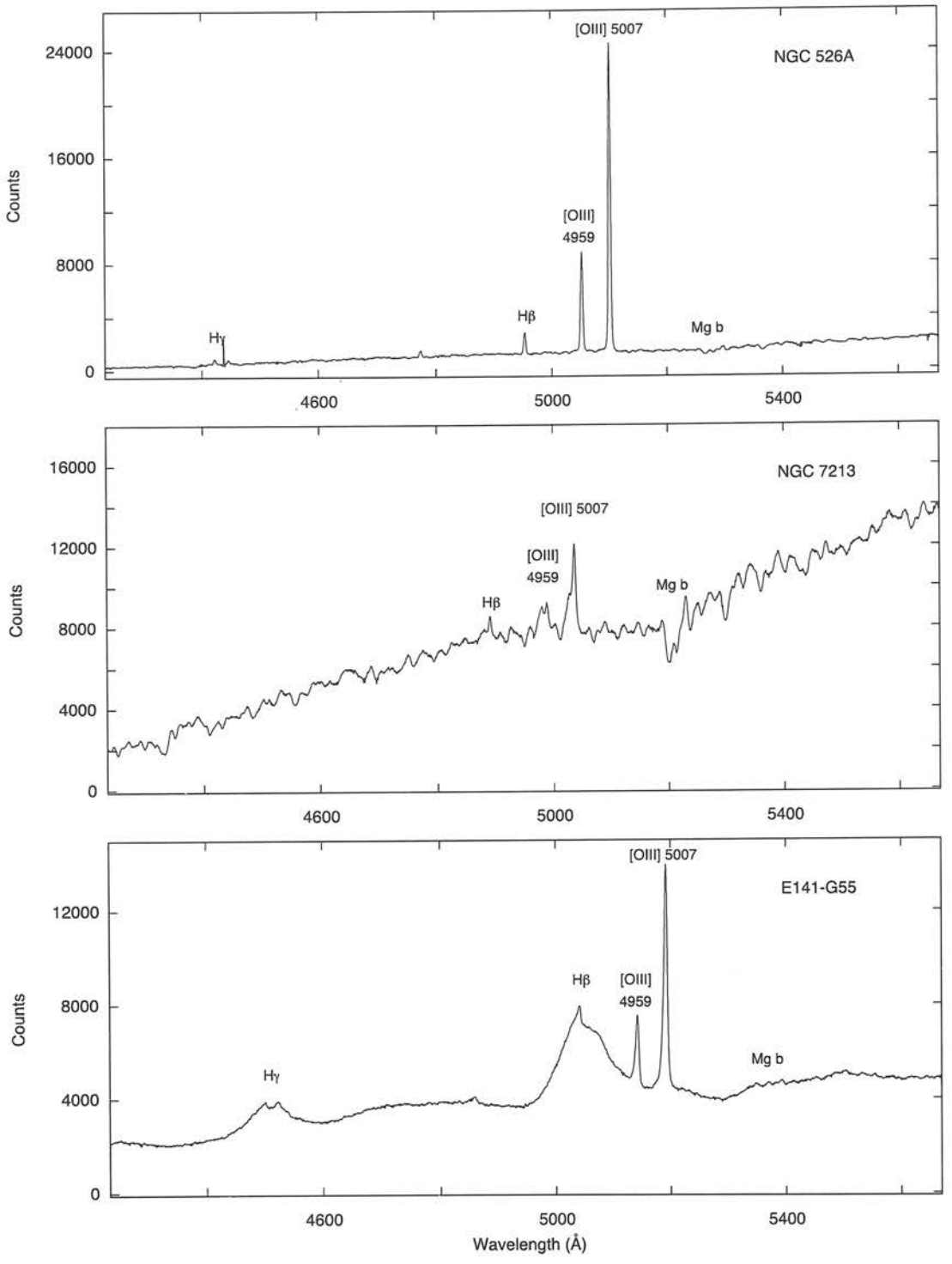

Figure 2.4: Offset spectra for the entire sample of BLS1s and NLS1s observed using the EMMI spectrograph with *NTT*. Spectra are shown in the observed frame and prominent emission/absorption lines are marked.

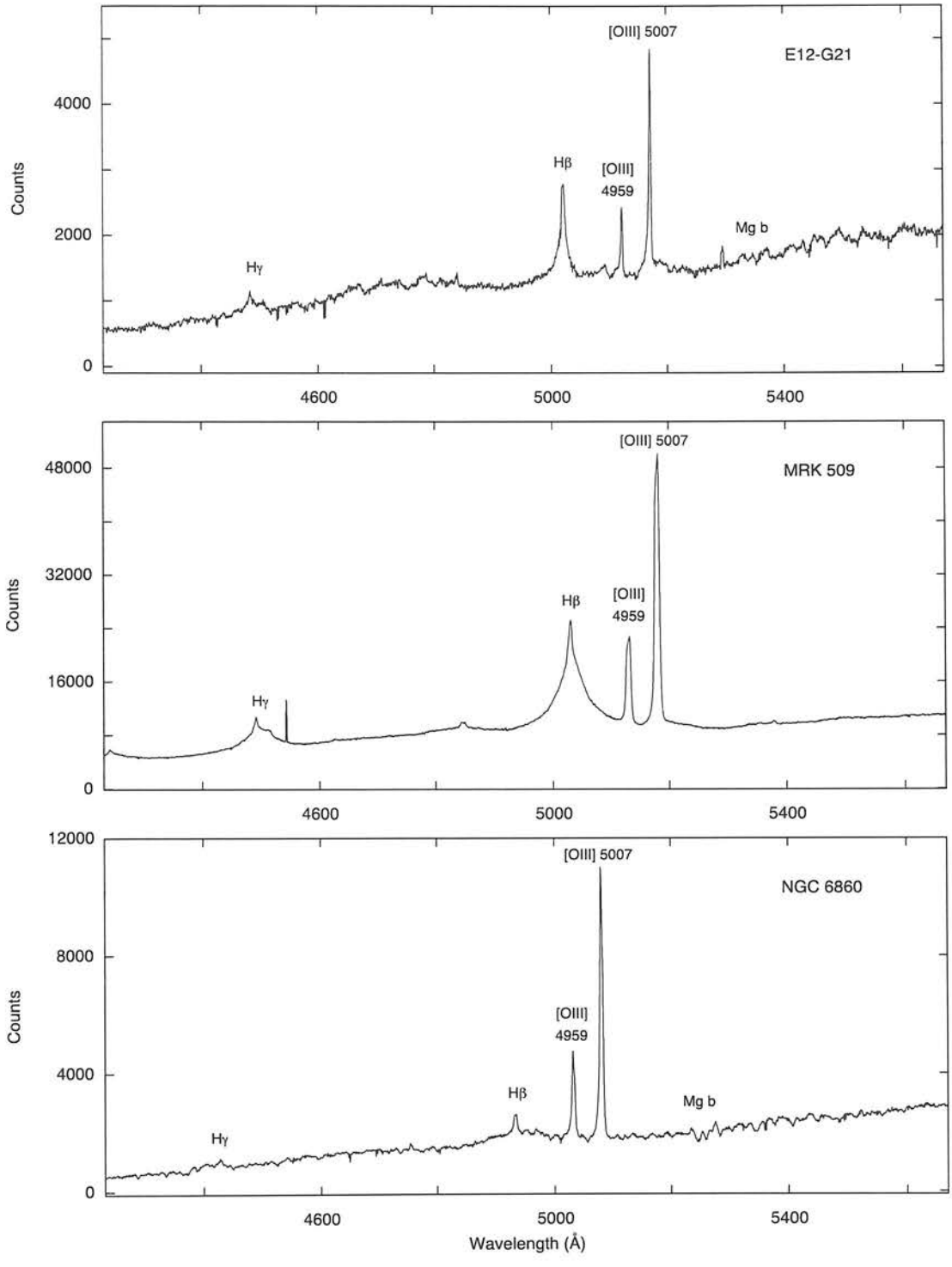

Figure 2.4: *-Continued*

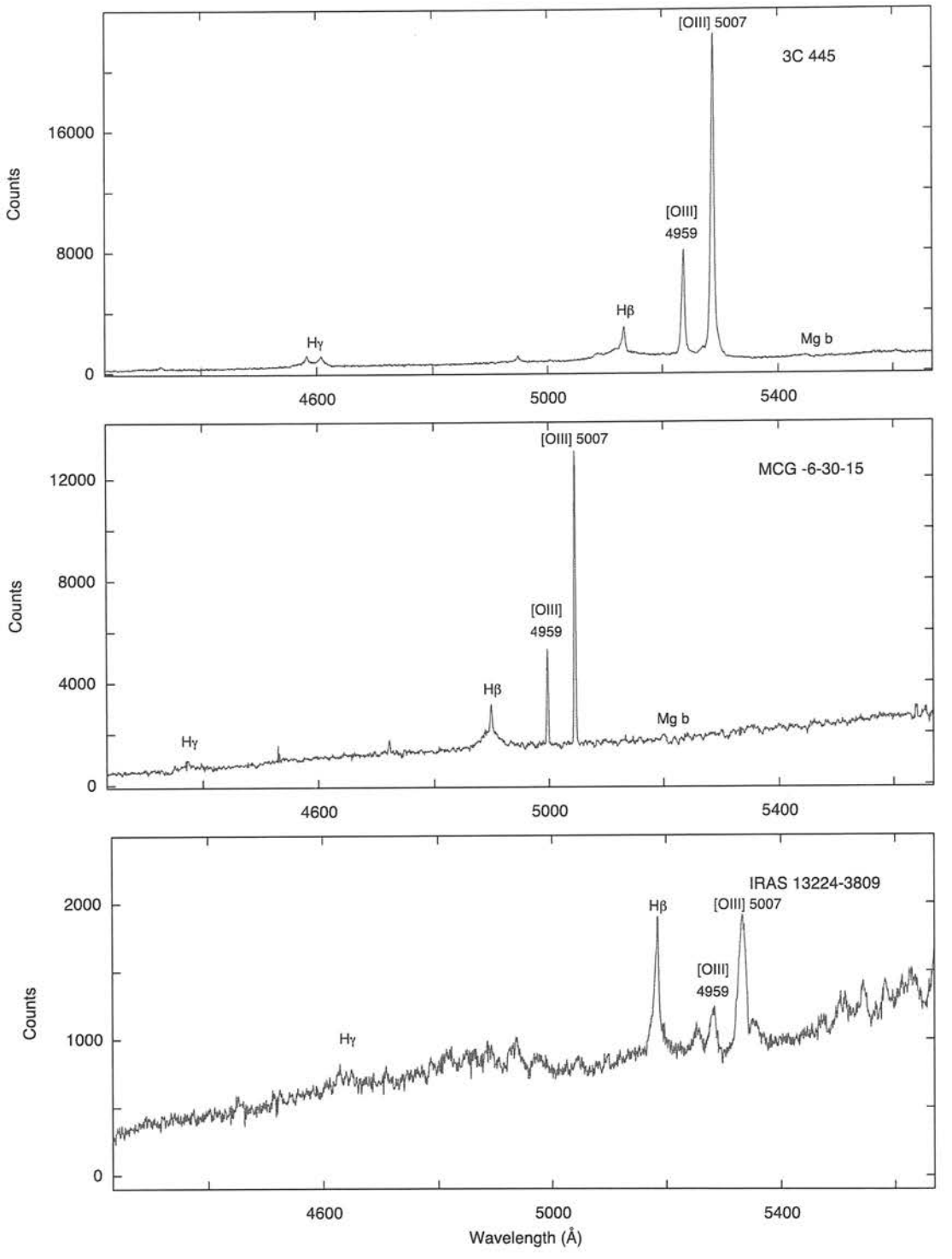

Figure 2.4: -*Continued*

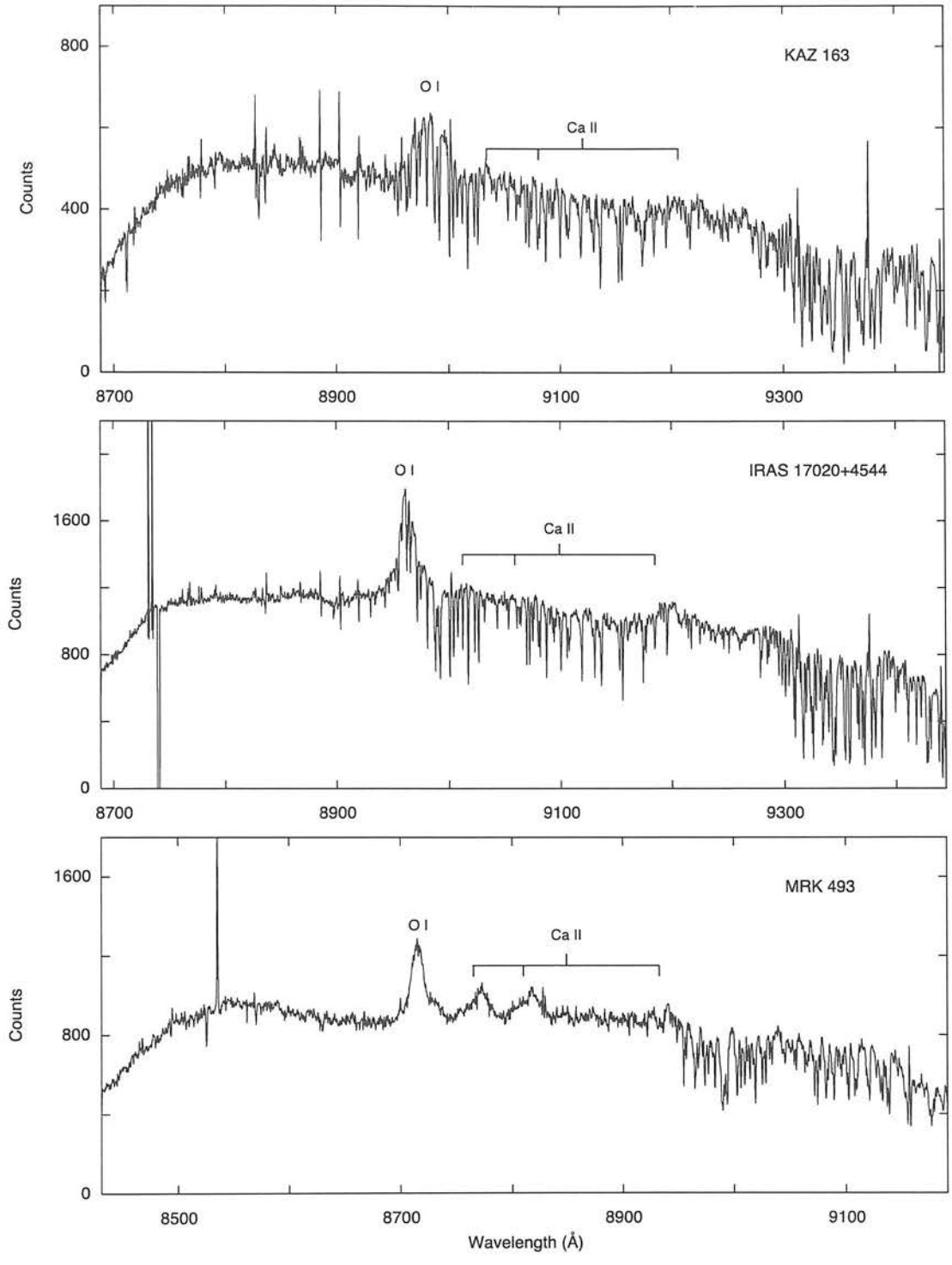

Figure 2.5: Red offset spectra for the NLS1 sample observed with the ISIS red-arm spectrograph. Spectra are shown in the observed frame and prominent emission/absorption lines are marked. Note the presence of significant sky absorption in the region of interest for the higher-redshift objects.

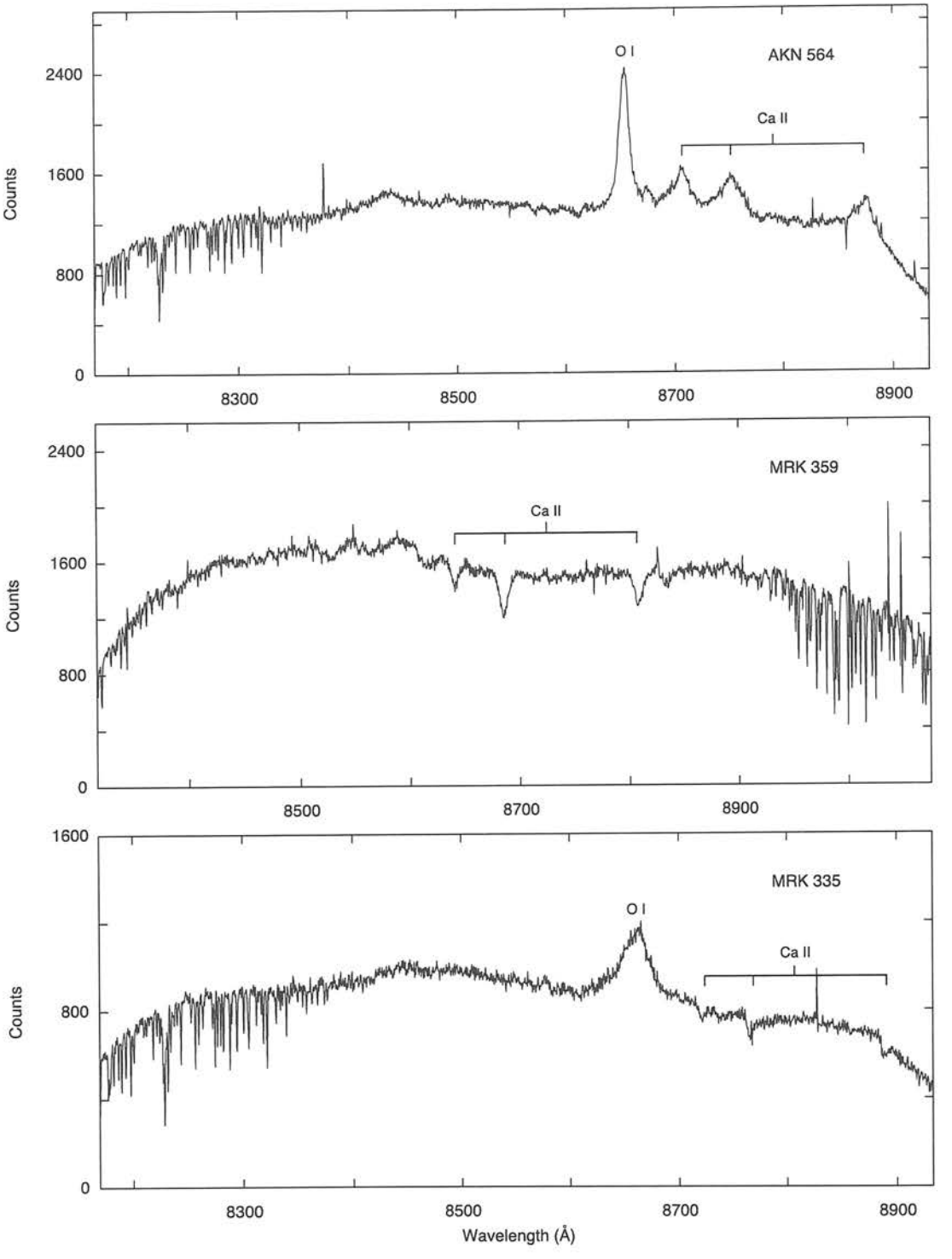

Figure 2.5: -*Continued*

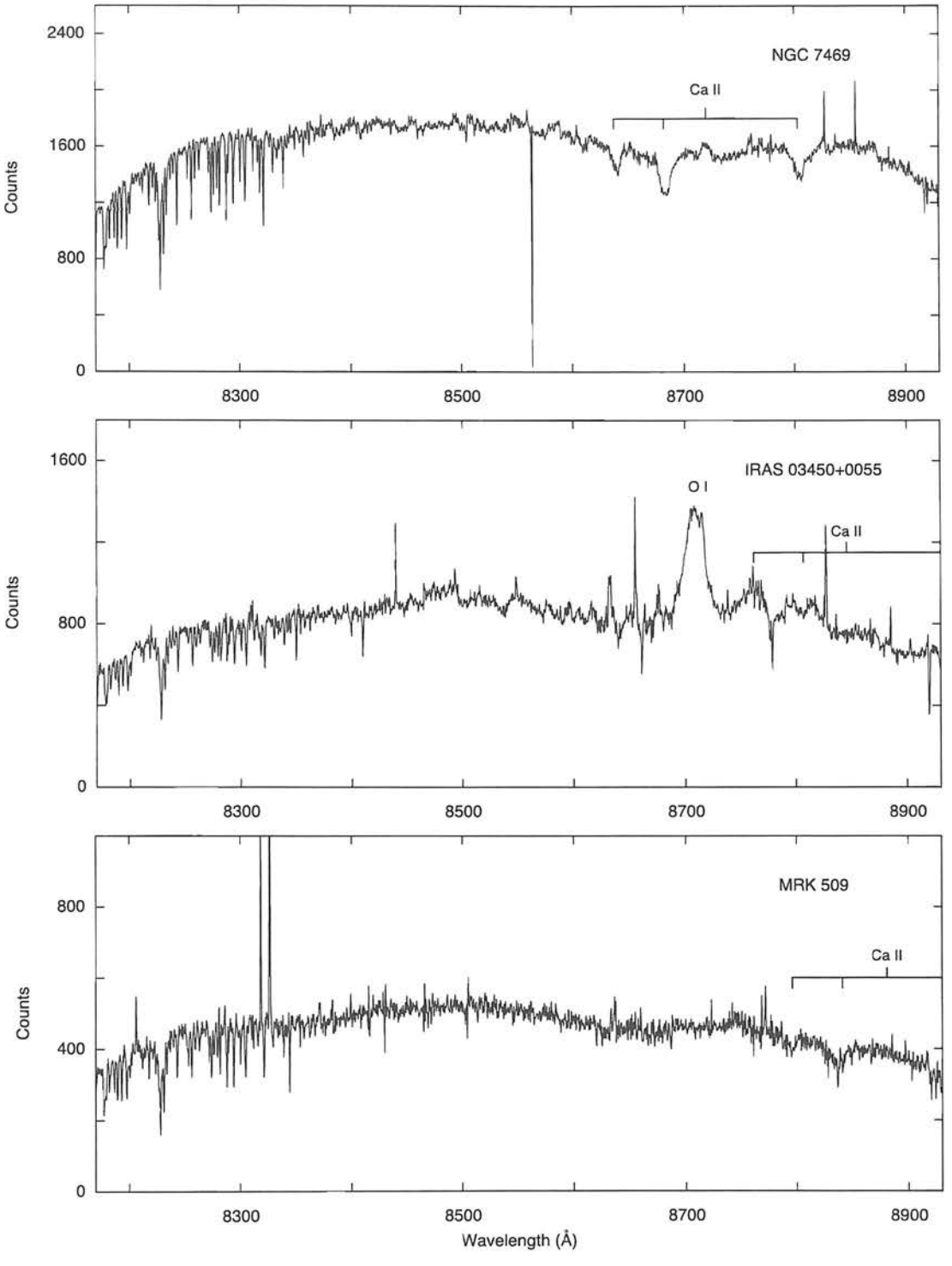

Figure 2.6: Red offset spectra for the BLS1 sample observed with the ISIS red-arm spectrograph. Spectra are shown in the observed frame and prominent emission/absorption lines are marked. Note the presence of significant sky absorption in the region of interest for the higher-redshift objects.

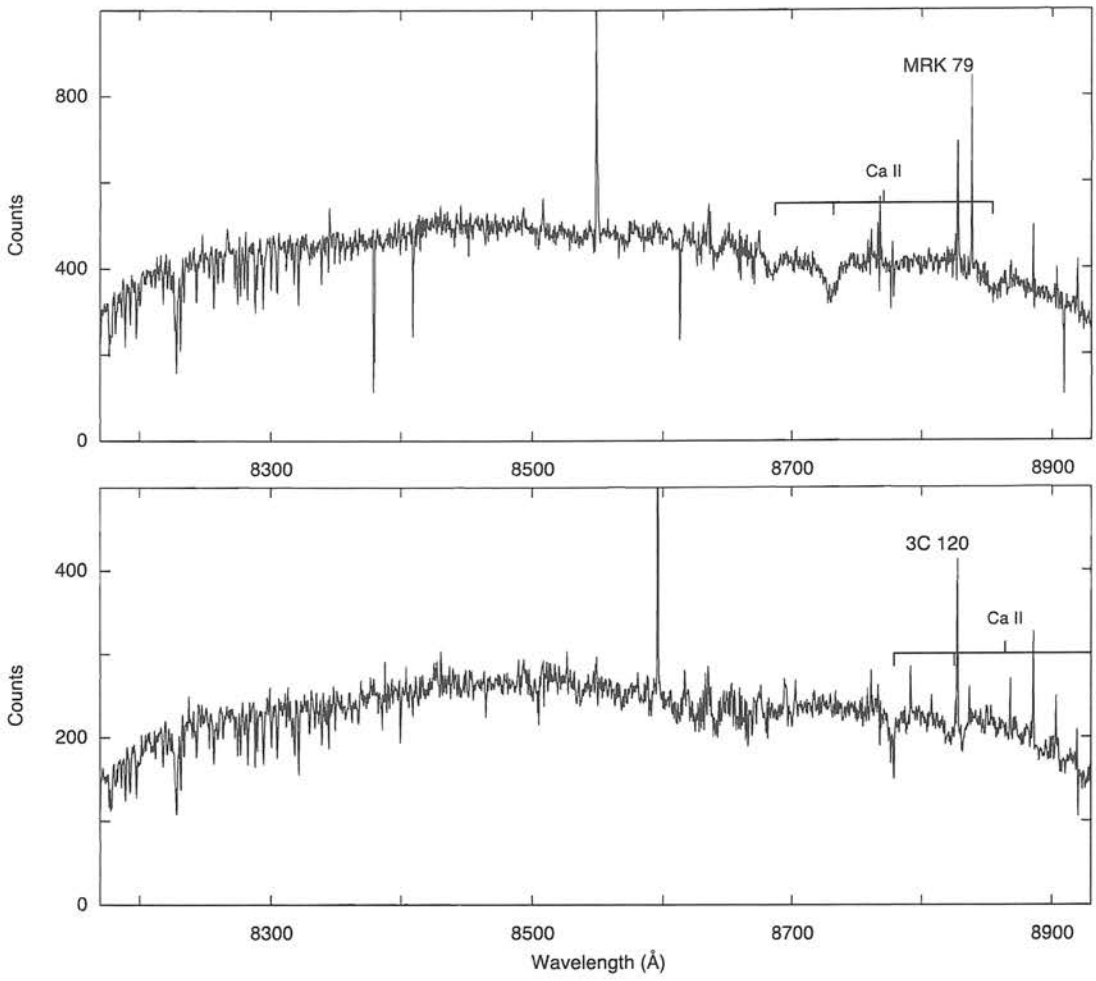

Figure 2.6: -*Continued*

spectrum. This continuum fit was subtracted off and the spectrum divided by the mean continuum level. The continuum-subtracted galaxy spectrum is assumed to be a convolution of the stellar template spectrum $S(x)$ with a broadening function $B(x)$

$$G(x) = B(x) * S(x) \tag{2.1}$$

where $B(x)$ relates to the line-of-sight velocity distribution, or line profile $L(v)$ according to

$$L(v) = B(v/c) \tag{2.2}$$

The fitting code assumed that the broadening function depends on a finite number of free parameters, which are found by minimizing the quantity

$$\chi^2 = \int [G(x) - B(x) * S(x)]^2 dx \tag{2.3}$$

This approach assumes that the line profiles are Gaussians where the free parameters are the line strength γ, the mean systemic velocity V and the velocity dispersion σ_*. The option to use the best-fitting Gaussian parameters to then determine deviations away from Gaussian in the line-profile was not possible in this case as this requires extremely high-S/N data.

Each galaxy spectrum was fitted using each of the eight stellar templates in Table 2.2. The acceptability of each fit was determined using the χ^2 values and visual inspection, and the average of the acceptable fits was adopted as the final stellar velocity dispersion. Some authors (e.g. Treu et al. 1999) used the line-ratio parameter γ as a measure of goodness-of-fit. Unfortunately, this is not possible for AGN spectra because the nuclear contribution causes a dilution and variation of the line strengths that is difficult to model. The results of the stellar velocity dispersion analysis are shown in Tables 2.3 and 2.4 for the NLS1 and BLS1 samples respectively. It was not possible to fit successfully all of the galaxy spectra. In some cases, particularly for the NLS1s, the residual nuclear emission was too strong to allow the much weaker stellar features to be resolved. In others the S/N of the spectra was not good enough for the fitting routine to be able to distinguish between features and noise. The spectra for which the fitting was not successful are shown in Figures 2.7 (ISIS blue-arm), 2.9 (ISIS red-arm) and 2.11 (EMMI). The successful fits are shown overplotted on the nuclear-subtracted galaxy spectra in Figures 2.8, 2.10 and 2.12.

There were three principal sources of error in the determination of σ_* using the method above: (1) the formal error of the fit $\Delta\sigma_f$, caused by fitting to a number of stellar absorption features, (2) errors due to template mismatches $\Delta\sigma_t$ and (3) a small but potentially significant uncertainty due to the continuum order chosen for the fit ($\Delta\sigma_c$). It is necessary to attempt to quantify all of these areas of uncertainty in the final error ϵ quoted with the velocity dispersions listed in Tables 2.3 and 2.4. The formal error was chosen to be the mean of the uncertainties of the fits using all of the acceptable templates for each object, and the error due to template mismatches was calculated to be the standard deviation of the σ_* values of the acceptable fits. The error resulting from the choice of continuum order was calculated by running the fitting code using a sample of continuum orders that gave acceptable fits while producing no

Table 2.3: Stellar velocity dispersions and nuclear properties of the NLS1 sample. Column (1) gives the object name. Stellar velocity dispersion is given in column (2). The nuclear property measurements: optical luminosity at 5100Å, FWHM Hβ, and [O III] 5007Å luminosity and FWHM are listed in columns (3), (4), (5) and (6).

Object	$\sigma_* \pm \epsilon$	Log $\lambda L_\lambda(5100\text{Å})$	FWHM Hβ	Log (L_{5007})	$\sigma_{\rm FWHM}$
	km s^{-1}	(W)	km s^{-1}	(W)	km s^{-1}
Mrk 335	110 ± 15	36.28	1833	34.02	137
I Zw 1	...	36.42	1337	34.07	605
Mrk 359	110 ± 7	35.78	1142	33.76	54
IRAS 13224	...	36.82	1353	34.52	364
MCG -6-30-15	112 ± 6	34.96	1885	32.77	67
Mrk 493	115 ± 11	36.44	1064	33.77	148
IRAS 17020	...	36.64	1101	34.78	116
Kaz 163	...	37.09	1496	35.11	192
Akn 564	...	36.62	1314	34.49	81

Table 2.4: Stellar velocity dispersions and nuclear properties of the BLS1 sample. Column (1) gives the object name. Stellar velocity dispersion is given in column (2). The nuclear property measurements: optical luminosity at 5100Å, FWHM Hβ, and [O III] 5007Å luminosity and FWHM are listed in columns (3), (4), (5) and (6).

Object	$\sigma_* \pm \epsilon$	Log $\lambda L_\lambda(5100\text{Å})$	FWHM Hβ	Log (L_{5007})	$\sigma_{\rm FWHM}$
	km s^{-1}	(W)	km s^{-1}	(W)	km s^{-1}
E12-G21	...	36.30	2517	33.60	194
NGC 526A	203 ± 14	35.48		33.75	111
IRAS 03450	...	36.25	2822	33.93	255
3C 120	162 ± 20[a]	37.20	2195	35.11	109
Mrk 79	141 ± 14	36.51	4379	33.95	156
E141-G55	166 ± 24	36.93	5195	34.58	150
NGC 6814	115 ± 18[a]	34.79	3379	32.69	85
NGC 6860	136 ± 7	35.65	5709	33.64	84
Mrk 509	169 ± 32	37.18	3600	35.06	209
PG 2130+099	...	37.63	2748	35.24	147
NGC 7213	212 ± 11	35.39	3878	32.98	430
3C 445	...	36.70	3278	35.30	127
NGC 7450	85 ± 25[a]	34.82	3668	33.01	58
NGC 7469	127 ± 10	36.49	2240	34.64	158

[a]Taken from Nelson & Whittle (1995).

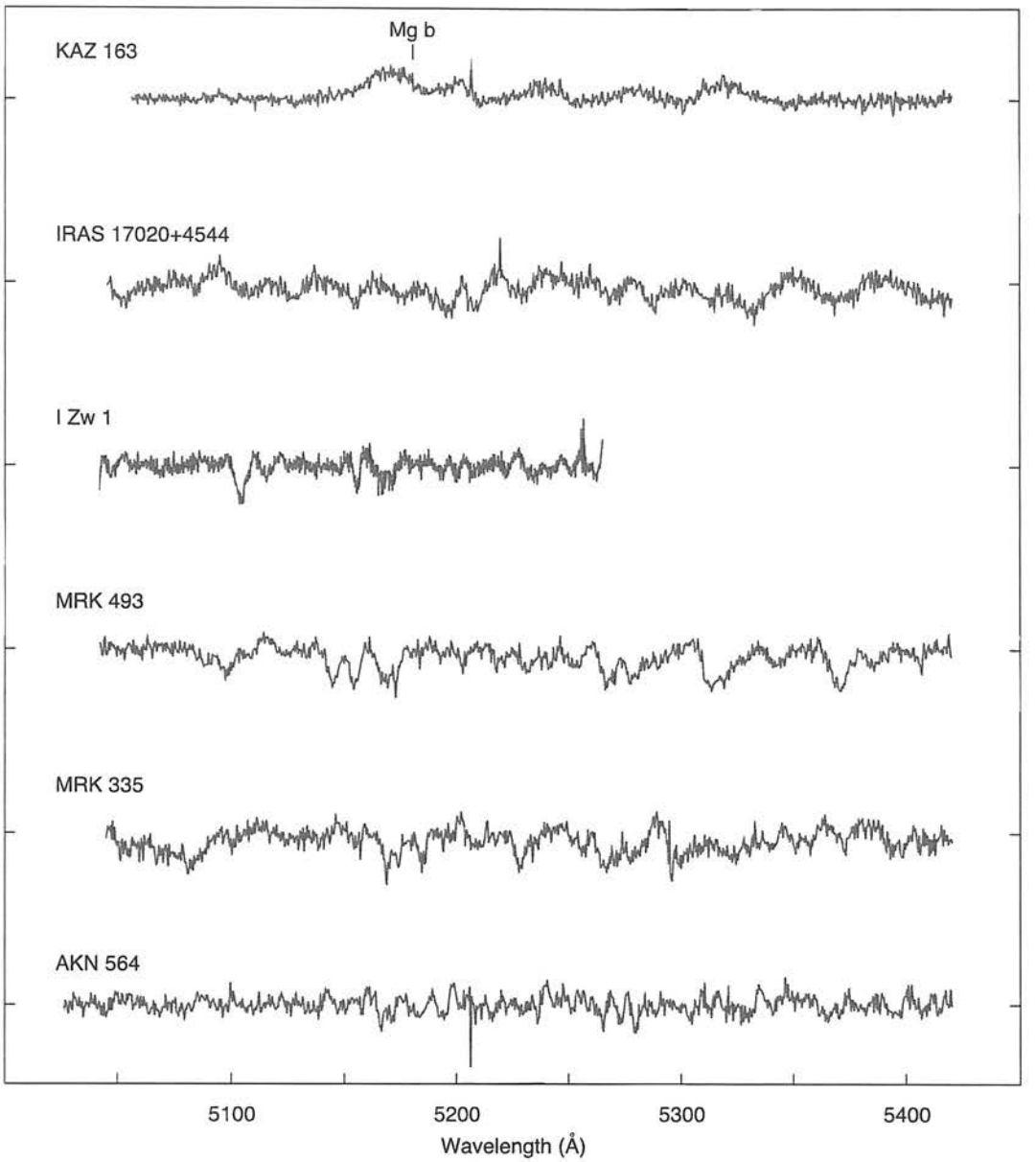

Figure 2.7: Normalized nuclear-subtracted spectra for the entire sample observed with the blue-arm ISIS spectrometer for which the velocity dispersion analysis was unsuccessful. The spectra have also been converted to the rest-frame of the AGN.

trends in the weighted residuals. The resulting uncertainty was quantified from the formal standard deviation in the mean σ_* for each continuum order. The final error ϵ was produced by adding $\Delta\sigma_f$, $\Delta\sigma_t$ and $\Delta\sigma_c$ in quadrature.

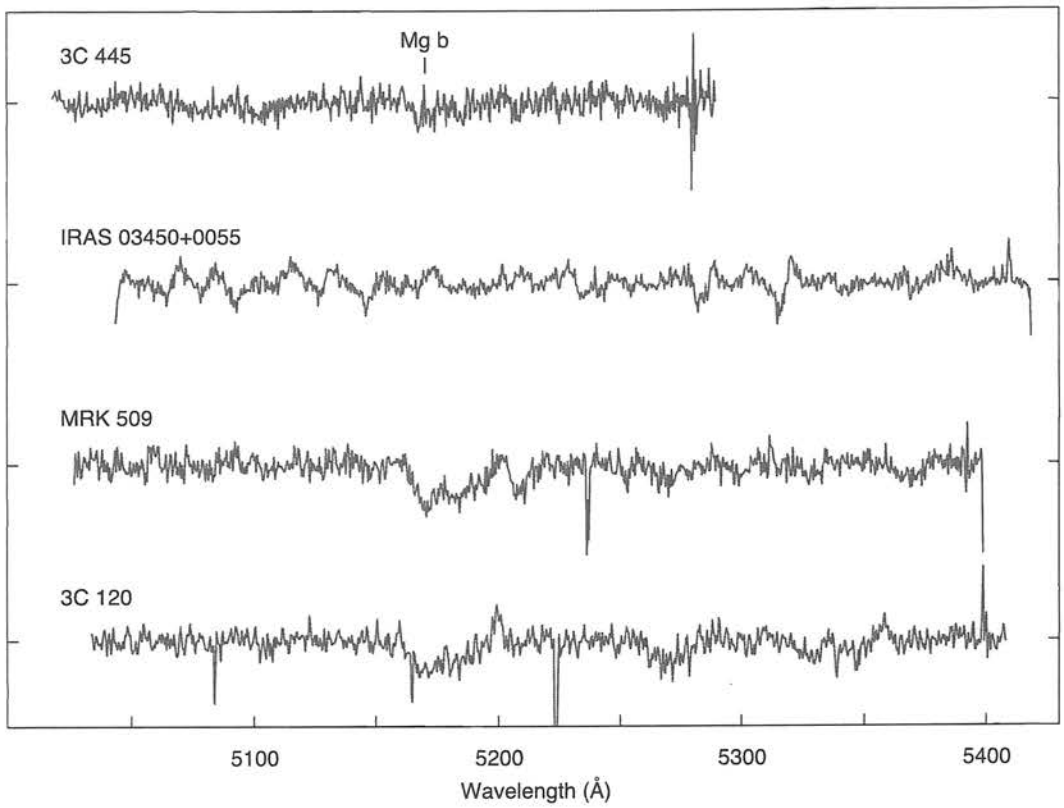

Figure 2.7: *-Continued*

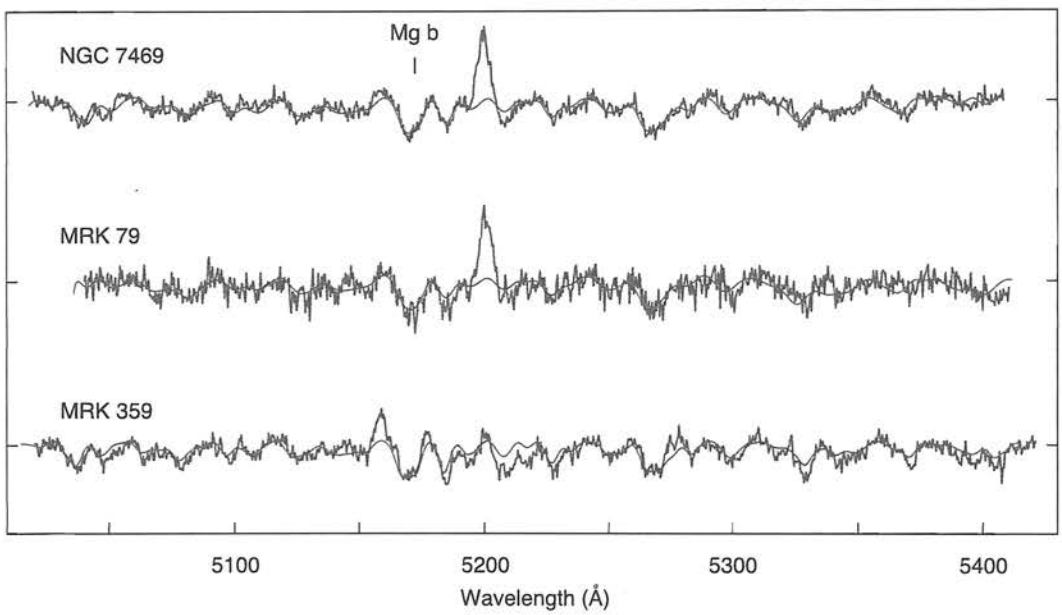

Figure 2.8: Normalized nuclear-subtracted spectra (black) and velocity dispersion fits (blue) for the sample observed with the ISIS blue-arm spectrograph for which the velocity dispersion analysis was successful. Spectra are shown in the AGN rest-frame.

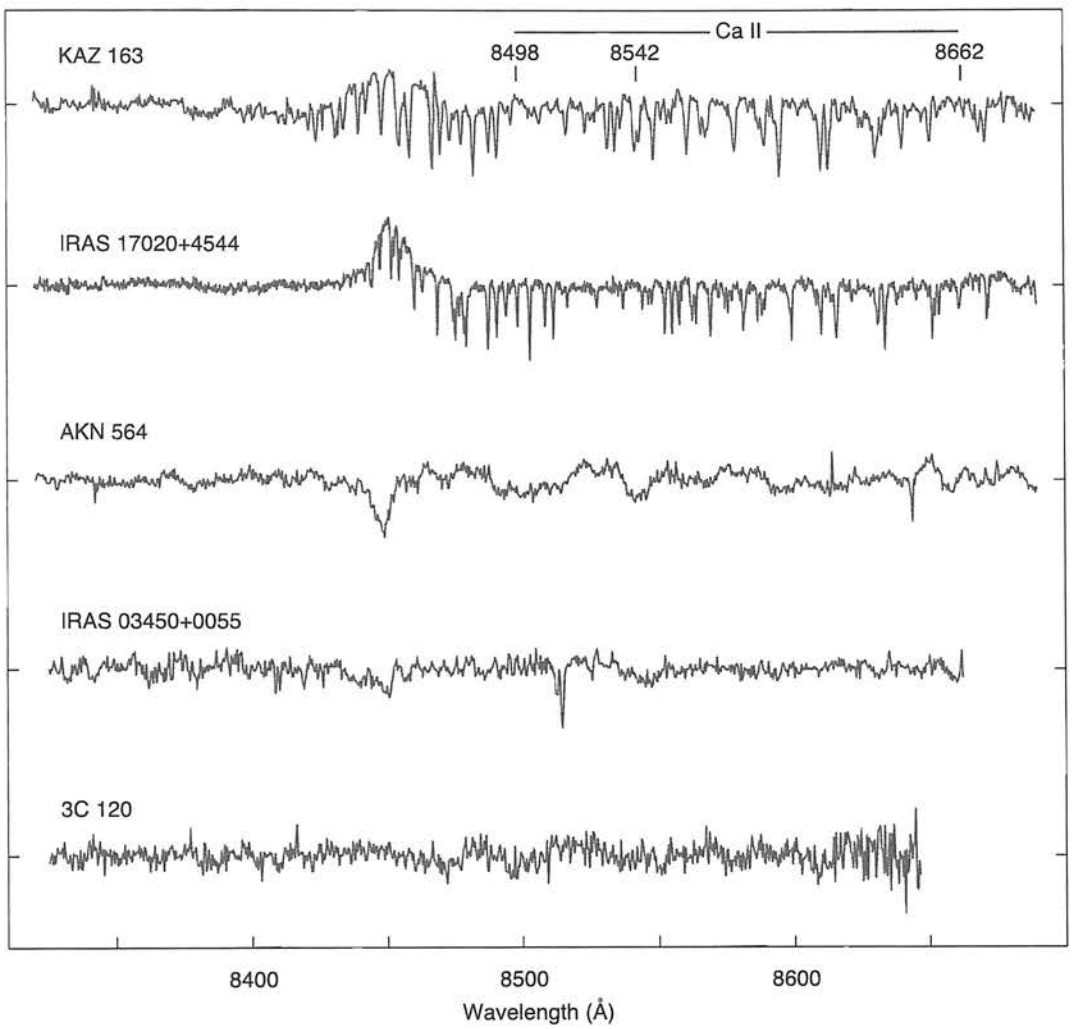

Figure 2.9: Normalized nuclear-subtracted spectra for the entire sample observed with the red-arm ISIS spectrograph for which the velocity dispersion analysis was unsuccessful. Spectra are shown in the AGN rest-frame.

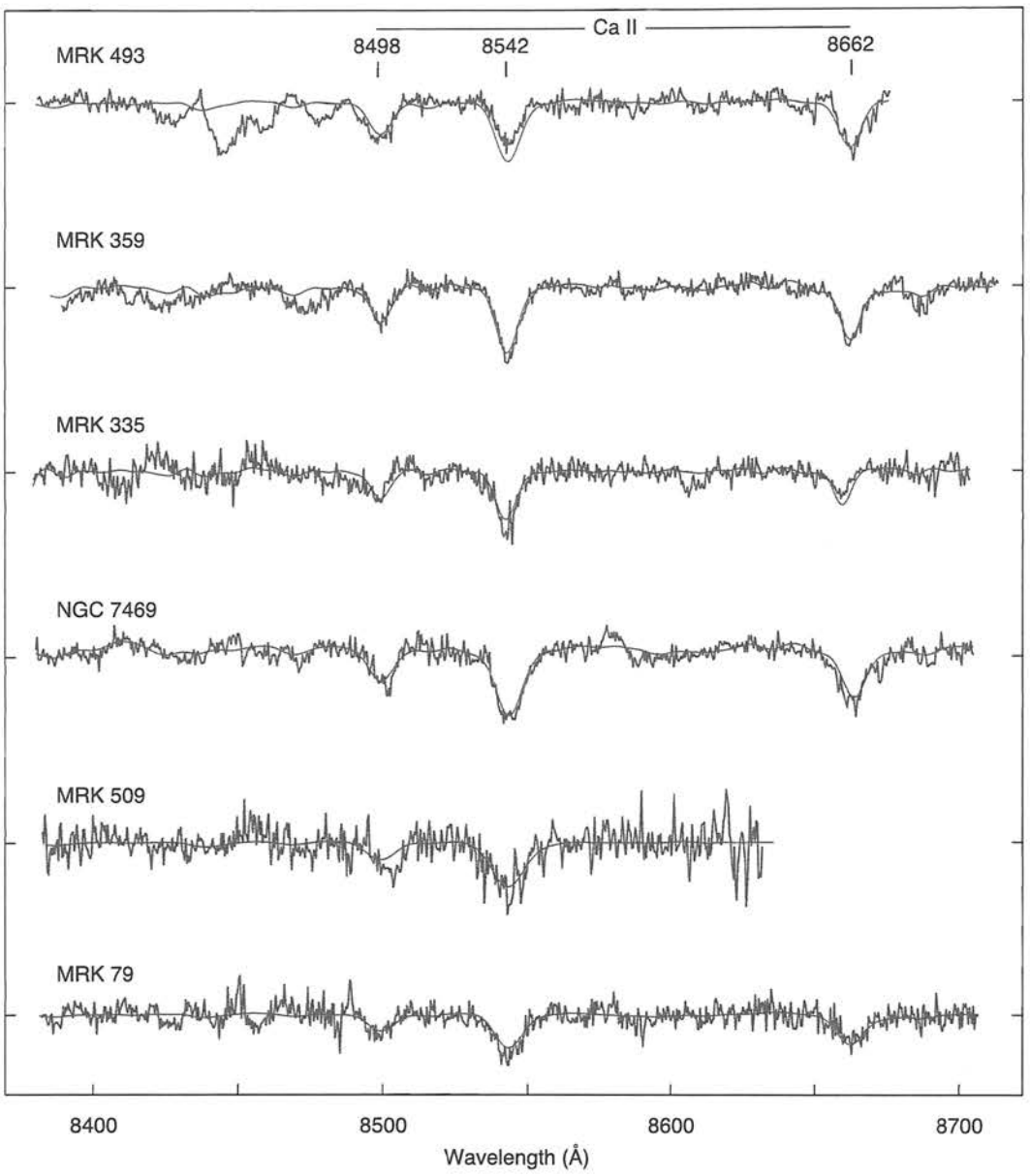

Figure 2.10: Normalized nuclear-subtracted spectra (black) and velocity dispersion fits (blue) for the sample observed with the ISIS red-arm spectrograph for which the velocity dispersion analysis was successful. Spectra are shown in the AGN rest-frame.

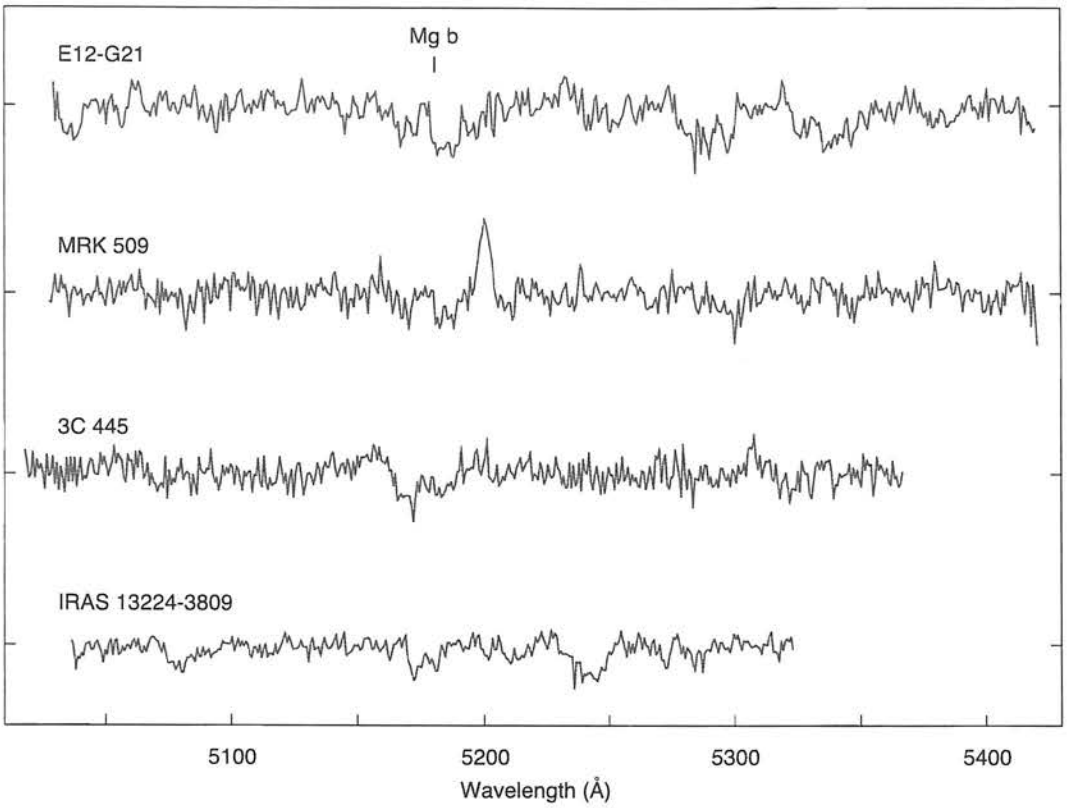

Figure 2.11: Normalized nuclear-subtracted spectra for the sample observed with the EMMI spectrograph for which the velocity dispersion analysis was unsuccessful. Spectra are shown in the AGN rest-frame.

2.6 Measuring the nuclear properties

The optical luminosity at 5100Å, the FWHM of the Hβ line and the luminosity and width of the [O III] 5007Å line were determined from the flux-calibrated nuclear spectra. The optical luminosity was determined by fitting a polynomial function to the nuclear continuum and measuring the flux F at 5100Å. This was then converted into a luminosity using the relation

$$L = 4\pi D_{\rm Eff}^2 (1+z)^3 F \tag{2.4}$$

where the effective distance $D_{\rm Eff}^2$ takes into account the deviation from a Euclidean geometry. The expansion of the universe has two principal effects upon emitted photons. Firstly, the frequency (and hence energy) of the photons is reduced by a factor of $(1+z)$ and secondly the cosmological time dilation reduces the arrival rate by another factor of $(1+z)$. The final $(1+z)$ factor in Equation 2.4 arises as a result of the band-

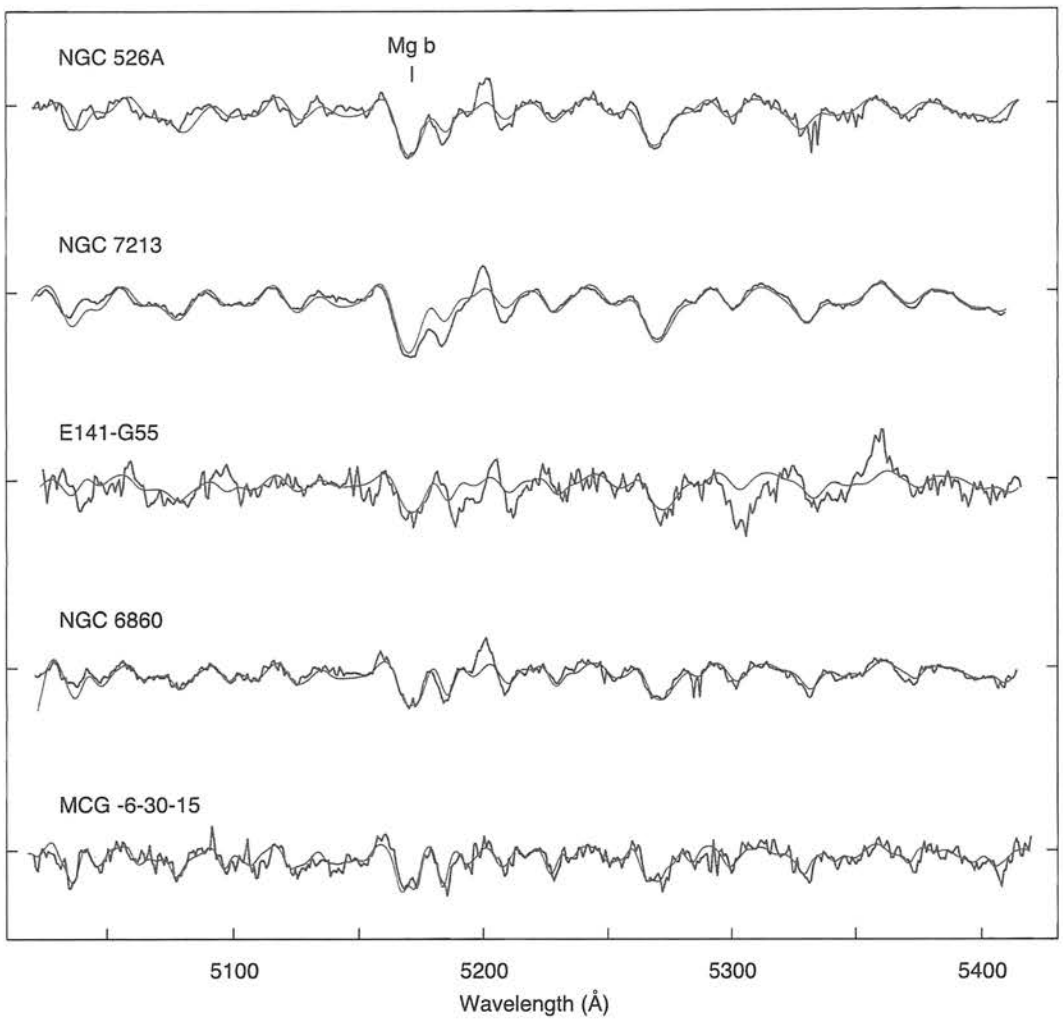

Figure 2.12: Normalized nuclear-subtracted spectra (black) and velocity dispersion fits (blue) for the sample observed with the EMMI spectrograph for which the velocity dispersion analysis was successful. Spectra are shown in the AGN rest-frame.

width increase $\Delta\nu$ that is also a function of time dilation (i.e., 1 Hz in the rest-frame of the emitting galaxy increases by a factor $(1 + z)$ upon arrival in the rest-frame of the observer). Cosmological parameter values of $H_0 = 70$ km s^{-1}Mpc^{-1}, $\Omega_m = 0.3$ and $\Omega_\Lambda = 0.7$ were used. The optical luminosities for each object are shown alongside the stellar velocity dispersion measurements in Tables 2.3 and 2.4.

To measure the [O III] line widths and fluxes, a similar procedure to that outlined in Greene & Ho (2005) was followed. The continuum fit used to determine the 5100Å flux was first subtracted from the nuclear spectrum. Gaussian profiles were then fitted to the [O III] lines at 4959Å and 5007Å. Although the parameters were measured using the 5007Å line alone, the 4959Å line was fitted also to ensure that the line separation and intensity ratio were constrained to be their theoretical values. In all but one case (MCG -6-30-15), two Gaussian components were required to give an acceptable fit to the 5007Å line. This is consistent with other studies, which have found that the [O III] lines often have a broad, low-intensity component that is shifted (often blueshifted) in relation to the narrow core (Heckman et al. 1981; de Robertis & Osterbrock 1984; Whittle 1985; Greene & Ho 2005). The fits to the [O III] lines for both the ISIS and EMMI samples are shown in Figures 2.13 and 2.14. In some cases the fits to the 4959Å and 5007Å lines were markedly different. This could be caused by the presence of other low-intensity narrow lines contaminating the fit. Good examples of this are shown in the fits to I Zw 1 and Mrk 493 (Figure 2.13).

To measure the line luminosities, the line fluxes were first calculated by summing the flux in the Gaussian component fits. These were then converted into luminosities using the relation

$$L = 4\pi D_{\rm Eff}^2 (1 + z)^2 F \tag{2.5}$$

which is similar to Equation 2.4, except that there is no factor of $(1 + z)$ arising from the increased bandwidth.

The widths of the line profiles were parametrized in three ways, in order to probe the NLR gas motions. The first was a simple cut across the line profile at the FWHM, which was then converted into a measurement of the gas dispersion using the relationship $\sigma_{\rm FWHM}$=[O III] FWHM/2.35. The observed linewidth σ_o is the convolution of the true line width σ with the instrumental response σ_i, and this was accounted for to

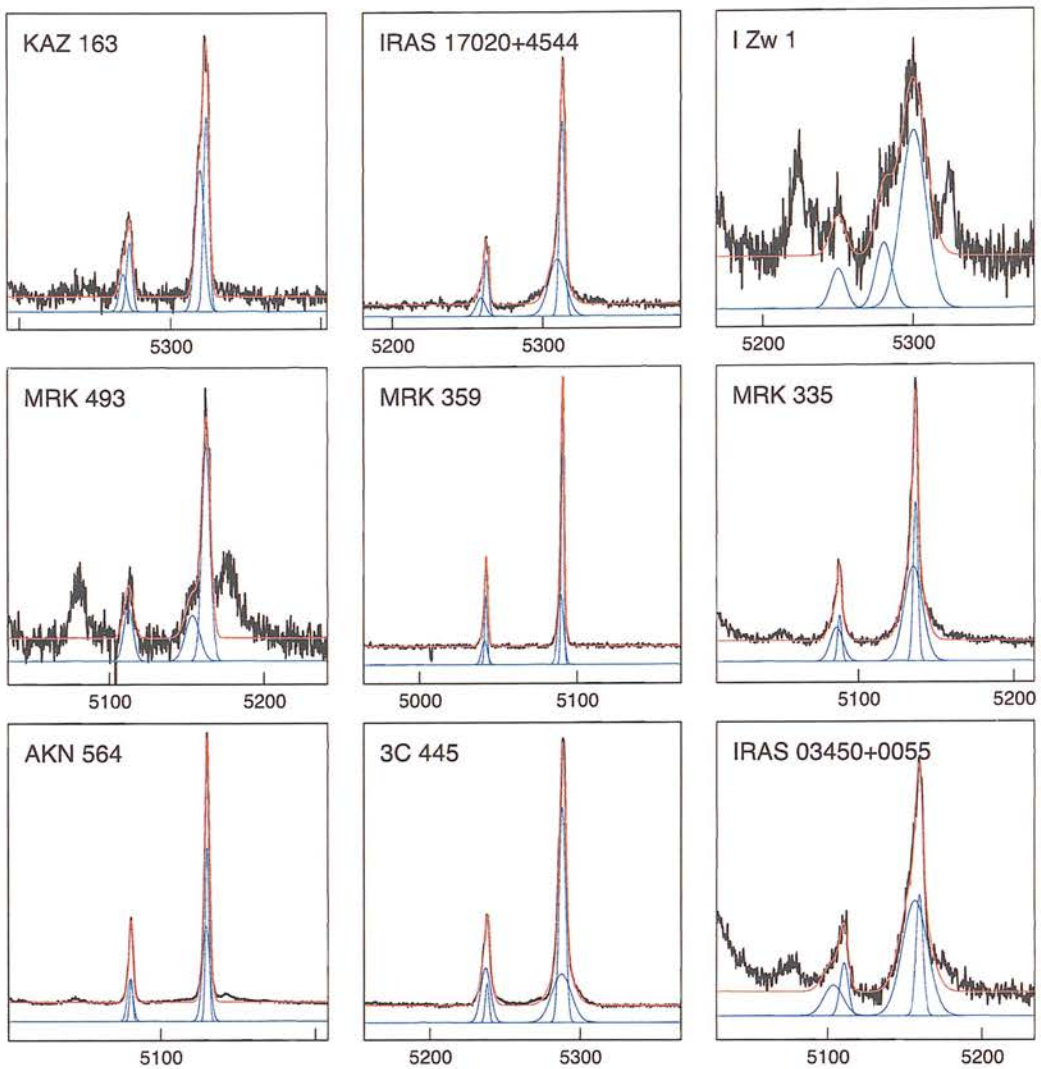

Figure 2.13: Fits to the [O III] lines for the sample of objects observed with ISIS. The individual Gaussian profiles (blue) and the composite profile (red) are shown plotted with the continuum-subtracted spectrum (black). The spectra are shown in the observed frame. The wavelength range for each object represents a velocity range of 12,000 km s^{-1} in the rest-frame of the AGN. Note the presence of low-intensity emission lines for some of the objects (I Zw 1, Mrk 493, IRAS 03450+0055) that could influence the fits.

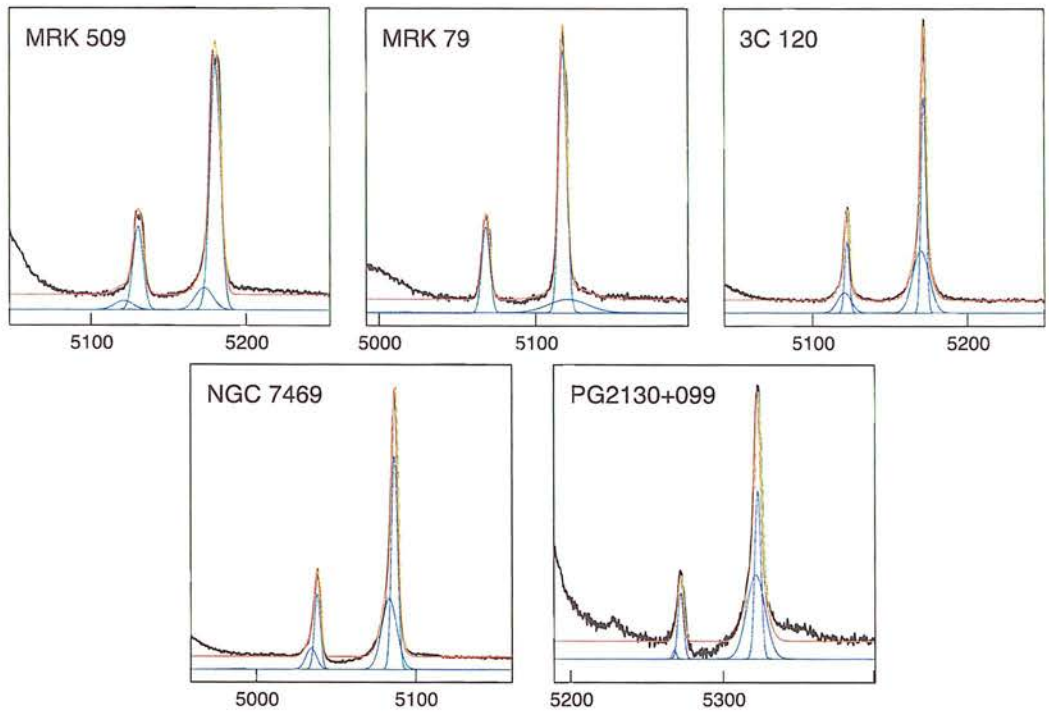

Figure 2.13: *-Continued*

first order using the relationship

$$\sigma = \sqrt{\sigma_{\rm o}^2 - \sigma_{\rm i}^2} \tag{2.6}$$

The second parametrization of the [O III] linewidths was to use the second moment of the line, defined as

$$\sigma_{\rm line}^2 = \left(\frac{c}{\lambda_c}\right)^2 \frac{\int(\lambda - \lambda_c)^2 f_\lambda d\lambda}{\int f_\lambda d\lambda} \tag{2.7}$$

where λ_c is the line centroid and f_λ is the flux-density in the line as measured from the continuum-subtracted spectrum. For a pure Gaussian line profile the second moment would obviously be equal to the dispersion. However, the second moment is sensitive to the presence of the wings and therefore provides a better diagnostic of the full line profile than the FWHM alone. The second moment of the [O III] 5007Å line was calculated numerically using the profile fits rather than the raw spectrum itself as the S/N of the nuclear spectrum varied from object-to-object. The final parameter used for the line-widths was to use the width $\sigma_{\rm core}$ of the core component of the fit only. This follows the analysis of Greene & Ho (2005), who found that the line core proved a much

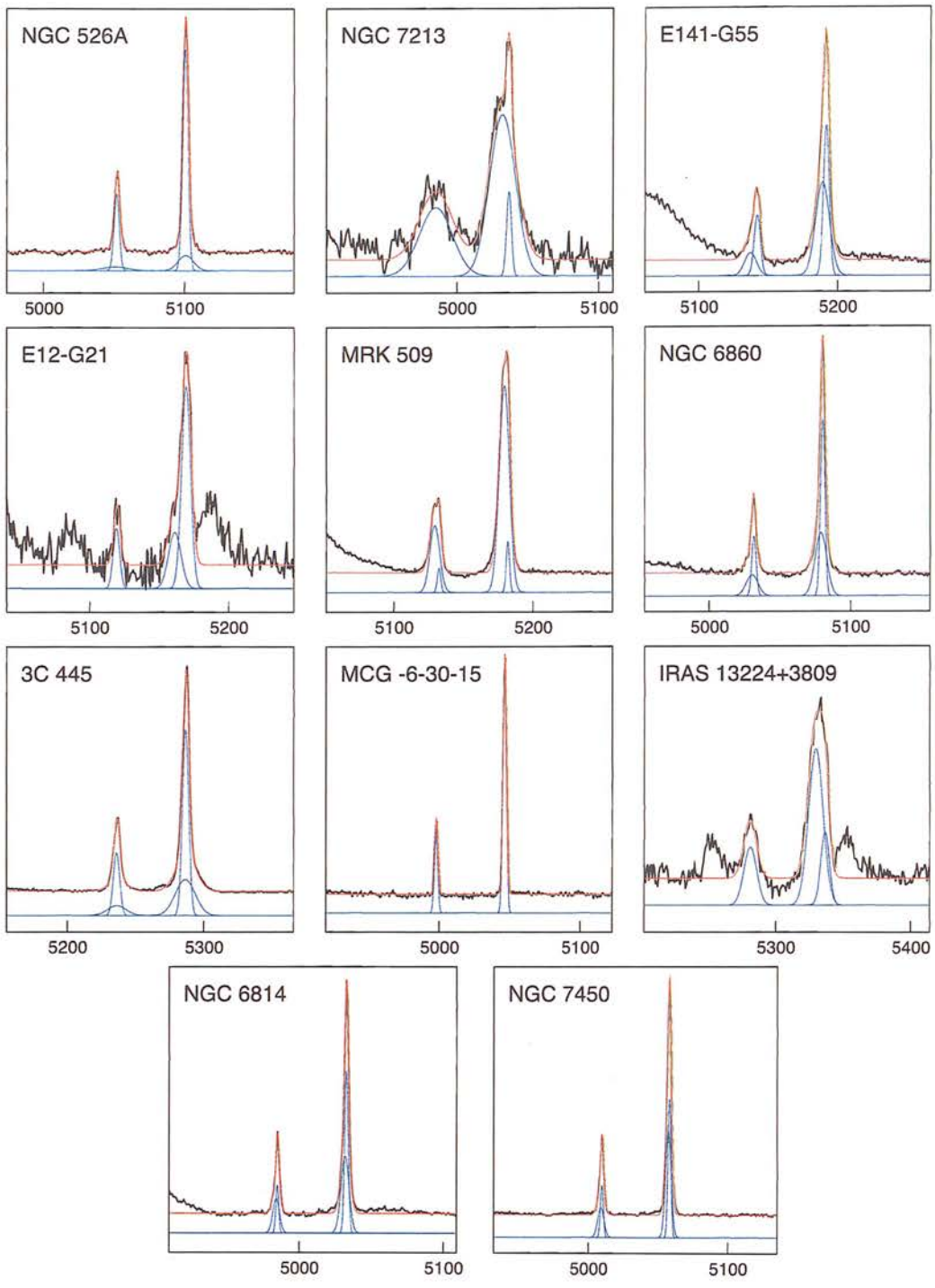

Figure 2.14: Fits to the [O III] lines for the sample of objects observed with EMMI. The individual Gaussian profiles (blue) and the composite profile (red) are shown plotted with the continuum-subtracted spectrum. The spectra are shown in the observed frame.

Table 2.5: The three parametrizations of the [O III] 5007Å line widths. Column (1) gives the object. Column (2) gives the [O III] FWHM derived directly from the line profile. Columns (3) and (4) list the second-moment $\sigma_{\rm line}$ and core component width $\sigma_{\rm core}$ as measured from the emission-line fits.

Object	$\sigma_{\rm FWHM}$ km s^{-1}	$\sigma_{\rm line}$ km s^{-1}	$\sigma_{\rm core}$ km s^{-1}
Mrk 335	137	298	89
I Zw 1	605	496	469
Mrk 359	54	92	46
IRAS 13224	364	442	173
MCG -6-30-15	64	50	50
Mrk 493	148	325	156
IRAS 17020	116	265	98
Kaz 163	192	227	103
Akn 564	81	116	63
E12-G21	194	318	177
NGC 526A	111	155	99
IRAS 03450	255	446	131
3C 120	109	233	90
Mrk 79	156	356	146
E141-G55	150	258	109
NGC 6814	85	124	50
NGC 6860	84	181	76
Mrk 509	209	263	193
PG 2130+099	147	185	113
NGC 7213	430	572	85
3C 445	127	252	119
NGC 7450	58	91	30
NGC 7469	158	242	112

better tracer of the stellar velocity dispersion then the second moment, although with large scatter (see their Table 1). The widths thus obtained using each of the linewidth parametrizations are given in Table 2.5. As the FWHM method is the most-common method used by other authors, the linewidths calculated from this are also given in Tables 2.3 and 2.4 alongside the other nuclear parameters.

The FWHM of the Hβ line was measured in a similar way to the [O III] linewidths using the continuum-subtracted spectra. Two Gaussian profiles were fitted to the line, one broad and one narrow whose FWHM was constrained to be the FWHM of the core

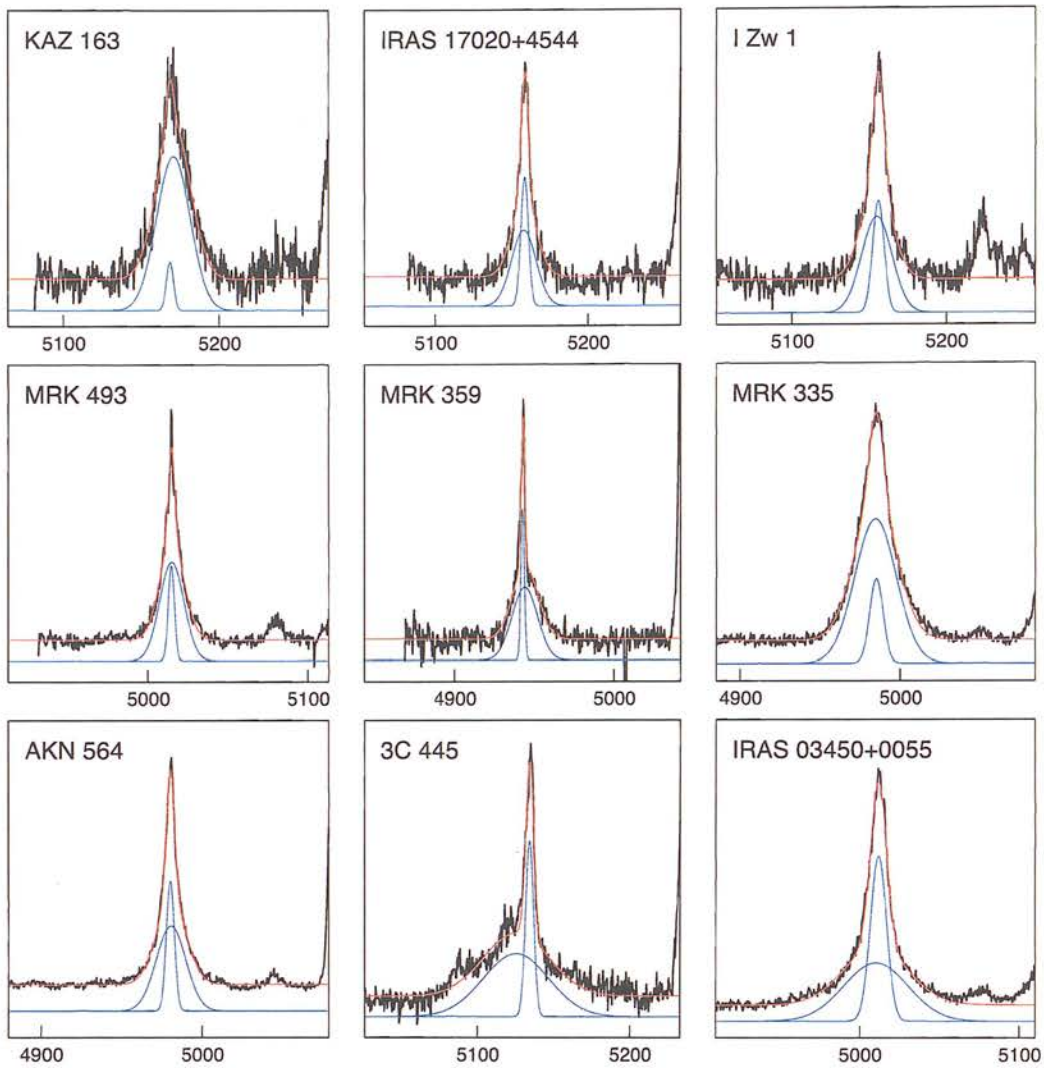

Figure 2.15: The Hβ line fits for the sample of ISIS objects. The spectra are shown in the observed frame. The wavelength range for each object represents a velocity range of 12,000 km s^{-1} in the rest-frame of the AGN so that linewidths can be visually compared.

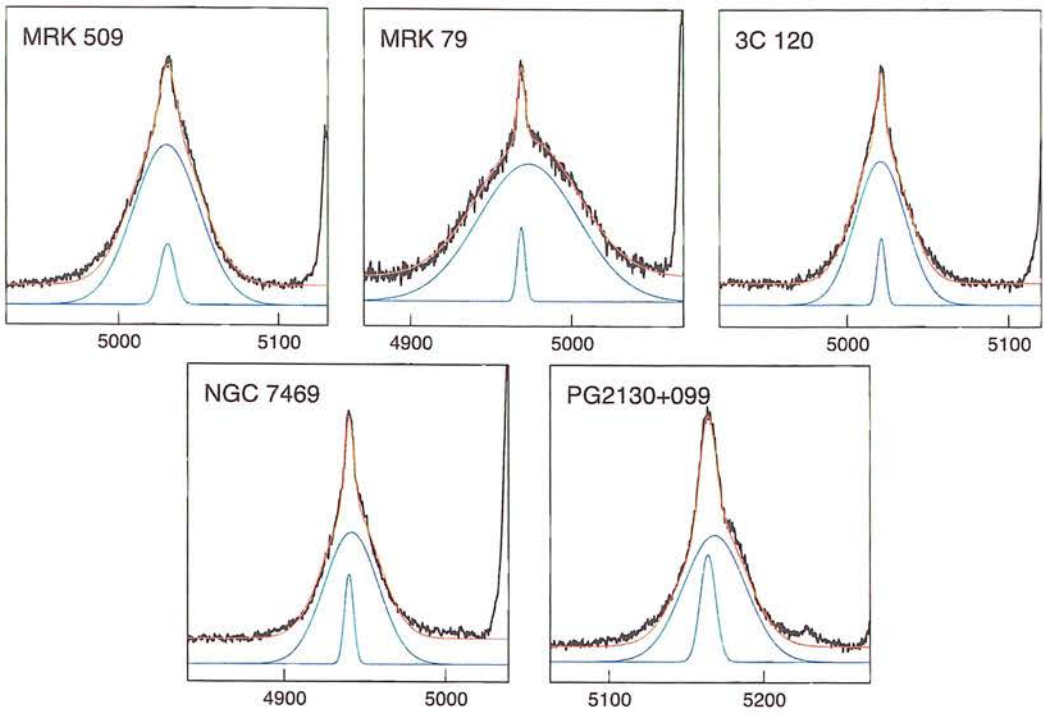

Figure 2.15: *-Continued*

component of the narrow lines. The FWHM was then measured using only the width $\Delta\lambda$ of the broad component, and converted into a velocity using the simple Doppler relation

$$v_{\rm FWHM} = \frac{\Delta\lambda}{\lambda}c \tag{2.8}$$

which is possible as even the broadest lines have widths that correspond to ~ 1 per cent of the speed of light and so relativistic effects are negligible. The FWHM velocities for all objects are shown in Tables 2.3 and 2.4. The Hβ line fits are shown in Figures 2.15 and 2.16 for the ISIS and EMMI objects respectively.

2.7 Notes on individual objects

Here I discuss the analysis of individual objects in the NLS1 and BLS1 samples, as well as briefly commenting on salient observational features. The objects are discussed in the order in which they are shown in Figures 2.2 and 2.3.

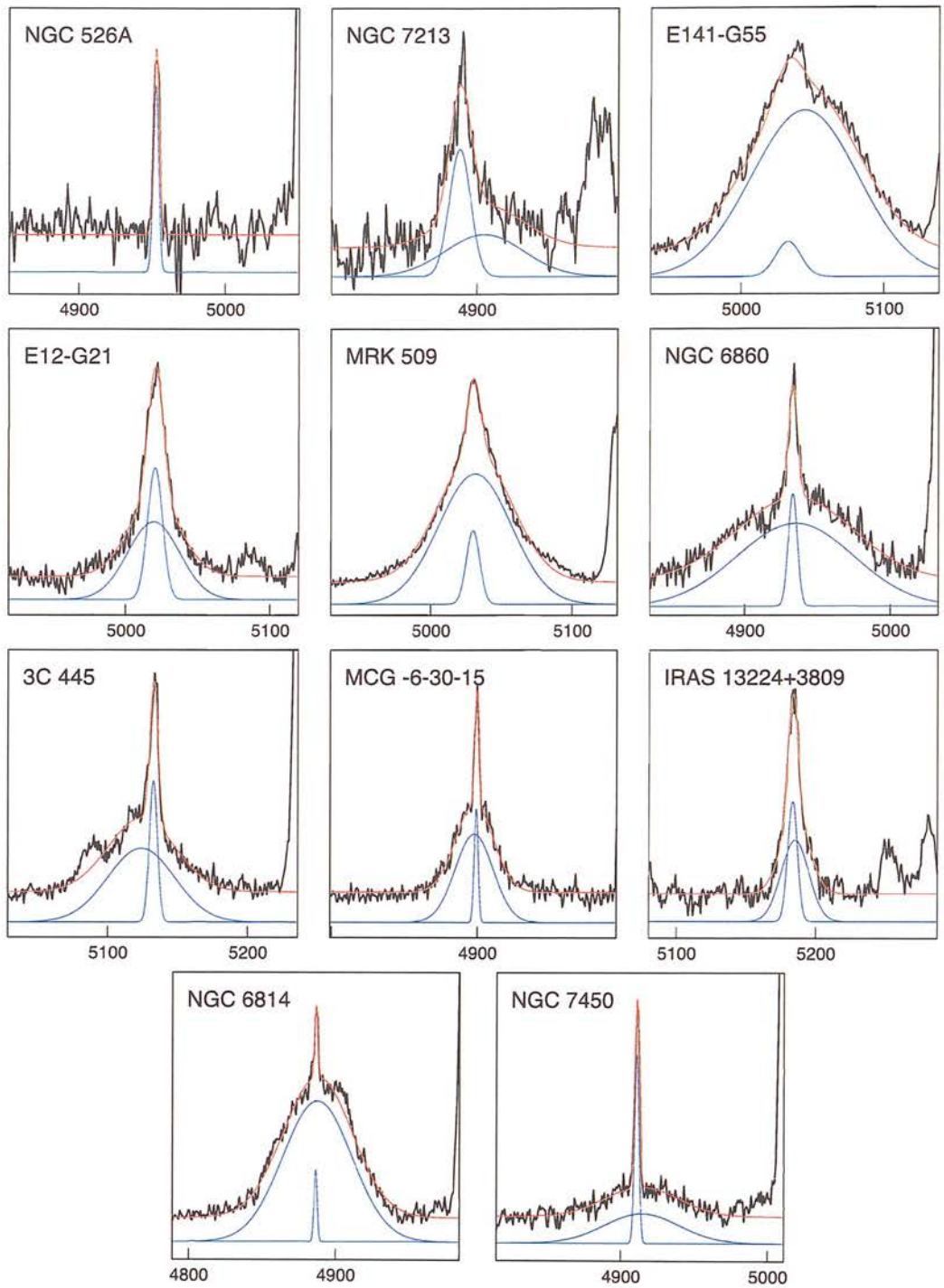

Figure 2.16: The Hβ line fits for the sample of EMMI objects. The spectra are shown in the observed frame. The wavelength range for each object represents a velocity range of 12,000 km s^{-1} in the rest-frame of the AGN so that linewidths can be visually compared.

Kaz 163. Kaz 163 is one of an interacting pair (Hutchings & Hickson 1988), and one of the higher redshift objects in this sample. The host galaxy is irregular, and is possibly undergoing a collision with a neighbouring elliptical. This is one of the NLS1s in the soft X-ray selected sample of Boller et al. (1996), and was also found to be variable in hard X-rays (Leighly 1999). The S/N in both the blue and red ISIS spectra is low, and no stellar features are visible in the spectrum even after nuclear subtraction. The red-arm spectrum was particularly problematic due to the strong atmospheric absorption features. No bulge velocity dispersion was consequently obtained for this object. The wing of the [O III] line is particularly strong for this object, reflected in the large discrepancy between $\sigma_{\rm line}$ and $\sigma_{\rm core}$ (Table 2.5).

IRAS 17020+4544. Another relatively high-redshift NLS1 ($z = 0.0604$), which was also found to be variable in X-rays in the study by Leighly (1999), IRAS 17020+4544 provided the same difficulties as Kaz 163, and no velocity dispersion information was obtained. The wing of [O III] 5007Å was found to be strongly blueshifted and heavily biased the $\sigma_{\rm line}$ determination. The Hβ line is shown to have only a weak broad component; see Figure 2.15.

I Zw 1. I Zw 1 exhibits very broad, low-intensity [O III] lines and very strong Fe II emission. One of the prototype NLS1s, it exhibits a steep soft X-ray spectrum and considerable variability in both soft and hard X-rays (Boller et al. 1996; Leighly 1999). Unfortunately the wavelength coverage of the October 2002 *WHT* observations was not sufficient to detect the Ca II triplet. The nuclear spectrum for this object proved extremely difficult to model, and it could not be confirmed that features in the nuclear-subtracted spectrum were not artifacts of incorrect scaling of the nuclear model. Therefore no velocity dispersion information was obtained for this object. [O III] 5007Å is extremely broad for this object (FWHM $= 600$ km s^{-1}), but in this case it is the core component that is broader than the blue wing.

Mrk 493. Mrk 493 shows strong emission in both the blue and red ISIS spectra. However the lower redshift of this object allowed a more accurate modelling of the nuclear spectrum. No velocity information was obtained from the Mg b region, but a measurement of the stellar velocity dispersion was obtained from the nuclear-subtracted Ca II lines. [O III] 5007Å exhibits a strongly-blueshifted component, but

also a component redward of the core that was not modelled during the analysis. The $\sigma_{\rm line}$ estimate for this object should therefore be viewed with some caution, as the NLR motions in this object are obviously complex.

Mrk 359. Both the Mg b and Ca II features were clearly visible in the offset spectrum prior to nuclear subtraction, and so two velocity dispersion estimates were obtained for this object. The two values obtained for the line-of-sight velocity dispersion were consistent (115 ± 8 km s^{-1} and 104 ± 7 km s^{-1}), and since the spectral regions used for fitting were of similar size the mean of the two values was adopted as σ_* and the standard error in the mean calculated using the weighted uncertainties. The [O III] lines were found to be extremely narrow for this object and all three parametrizations give smaller dispersions than the stellar lines. Mrk 359 is one of the soft X-ray selected NLS1s in Boller et al. (1996), but is only weakly variable over short time-scales. No hard X-ray variability data is available for this object.

Mrk 335. Mrk 335 has weak forbidden lines and Fe II emission, but it was not possible to fit to the stellar features even after nuclear subtraction using the blue spectrum. The Ca II lines were detected, however, and so a σ_* measurement was obtained. [O III] 5007Å has a very strong blue wing in this object, which heavily biases $\sigma_{\rm line}$. This is the only object in the NLS1 sample for which $\sigma_{\rm FWHM}$ and $\sigma_{\rm core}$ have similar widths to σ_*. Mrk 335 is included in the sample of Leighly (1999) and is weakly variable in hard X-rays.

Akn 564. The nuclear continuum was too strong in the offset spectra to obtain a reliable estimate of σ_*. Poor S/N in the red nuclear spectrum made modelling of the strong [Ca II] emission seen in Figure 2.2 too uncertain. Nuclear subtraction in the blue spectrum was more successful, but the resulting S/N of the stellar features was too poor for velocity profile fitting to give a convincing result. The [O III] lines are extremely strong in this object ([O III]/H$\beta \sim 3$) with fairly strong broad components but narrow cores. A very steep soft X-ray spectral index is found for this object ($\Gamma = 3.4$; Boller et al. 1996) and it is strongly variable in both soft and hard X-rays over short time-scales (Boller et al. 1996; Leighly 1999).

3C 445. 3C 445 is one of two radio-loud BLS1s in the sample, and also one of two objects to be included in both the *WHT* and *NTT* observing runs. As for I Zw 1, the

redshift of this object pushed the Ca II region out of the wavelength coverage of the ISIS red spectrum. Strong nuclear emission is seen in both offset spectra covering the Mg *b* region (Figures 2.3 and 2.4). Nuclear subtraction was performed in both cases, but the resulting S/N was too poor for Gaussian profile fitting. A very broad blue wing in the [O III] lines strongly biases the resulting $\sigma_{\rm line}$ determination by a factor of $\sim$2 in comparison to the $\sigma_{\rm FWHM}$ and $\sigma_{\rm core}$ widths.

IRAS 03450+0055. This object has previously been identified as a NLS1 (Véron-Cetty et al. 2001). However, profile fitting to the Hβ line (Figure 2.15) in this study found widths considerably greater than 2000 km s^{-1}. It is not clear whether this is due to poor continuum subtraction (either in this or previous studies) or possible profile variability. Strong nuclear emission in both blue and red ISIS spectra meant that no stellar lines were visible even after subtraction of a nuclear model and so no σ_* measurement was obtained. The [O III] lines in this object are very broad, and $\sigma_{\rm FWHM}$, $\sigma_{\rm line}$ and $\sigma_{\rm core}$ give widely-differing estimations of the width.

Mrk 509. Another object observed with both *WHT* and *NTT*, this object shows clear evidence of double-peaked narrow lines in the higher-resolution ISIS spectrum. The [O III] linewidths for this object were taken from the EMMI observations, but these should be viewed with some caution. Nuclear subtraction of the Mg *b* spectral region was not sufficient to detect the stellar features; however, two members of the Ca II triplet were clearly present allowing a determination of σ_*. The third member of the triplet lies outside the wavelength coverage of the spectrum. Hence, the relative accuracy of this measurement is somewhat poorer.

Mrk 79. One of several objects with σ_* measurements in the literature (Nelson et al. 2004), stellar features were visible in both the blue and red spectra, allowing two velocity determinations. The uncertainties for the blue spectrum were significant, due primarily to template mismatch, and so the value obtained from the Ca II region (141 ± 14 km s^{-1}) was adopted. This compares with 130 ± 12 km s^{-1} determined by Nelson et al. (2004). The two values are clearly consistent to within 1σ. [O III] 5007Å has a very broad, low-intensity wing that affects the $\sigma_{\rm line}$ measurement, exemplified by the fact that the widths obtained from $\sigma_{\rm FWHM}$ and $\sigma_{\rm core}$ are consistent within the expected errors.

3C 120. The other radio-loud object in the BLS1 sample, 3C 120 exhibited strong nuclear emission in the blue ISIS offset spectrum. The fringing in the red spectrum was difficult to remove due to the low S/N of the offset spectrum for this object. As a result, no velocity dispersion information was obtained, and so the value from Nelson & Whittle (1995) is given in Table 2.4. As for many of the other objects, $\sigma_{\rm line}$ is dominated by a strong wing component.

NGC 7469. NGC 7469 also has other σ_* determinations in the literature, and is another of the objects in this sample for which stellar features were clearly distinguishable in both blue and red offset spectra. As the S/N of the spectra is comparable, the mean of the resulting σ_* estimates was adopted for this object. The wing of the [O III] 5007Å line is strongly blueshifted for this object, and consequently the $\sigma_{\rm line}$ and $\sigma_{\rm core}$ parametrizations are significantly different.

PG 2130+099. The only high-luminosity Type-1 object in the sample, the observations of PG 2130+099 were affected by cloud midway through the integration, and so the S/N of the offset spectra was severely compromised. Therefore no σ_* determination was possible. The nuclear spectrum was not affected by the deterioration in observing conditions, allowing measurements of the AGN parameters. The forbidden lines for this object are complex, and not well fitted by the two-component Gaussian fits.

NGC 526A. Although designated a BLS1, no broad component of Hβ was detected in the nuclear observation of this object. This was not an artifact of the continuum subtraction, as could possibly be the case for IRAS 03450+0055. The wings of the [O III] lines were very weak, although they still bias the $\sigma_{\rm line}$ determination, but all three parametrizations are significantly lower than the derived velocity dispersion. Stellar absorption features were clearly visible in the spectrum and a σ_* measurement was obtained from the Mg *b* region.

NGC 7213. A BLS1 that exhibited very high S/N stellar features. The Mg *b* complex for this object was not fitted well by a single stellar template, as shown in Figure 2.12. The [O III] lines were almost double-peaked and very broad. The broad component of Hβ had very poor S/N, and so the FWHM measurement is highly uncertain.

E141-G55. This broad-line object exhibits a peculiarly asymmetric Hβ profile (see Figure 2.16). Stellar features were detected after subtraction of the nuclear continuum and a velocity dispersion measurement was made.

E12-G21. The S/N of the offset spectrum for this BLS1 was too poor to fit velocity profiles to even after nuclear subtraction, and so no velocity dispersion information was obtained. This is another object that exhibits very complex forbidden line profiles, with an apparent redshifted component in addition to the blue wing (Figure 2.14).

NGC 6860. Another BLS1 observed using EMMI for which stellar features are visible in even the raw spectrum with no nuclear subtraction, this object was successfully fitted with Gaussian velocity profiles.

MCG -6-30-15. This object has been designated as both NLS1 and BLS1. This study found FWHM Hβ < 2000 km s^{-1}, suggesting the former designation. Continuum subtraction was relatively simple in this case, suggesting that this is not a contributing factor. The stellar features were clear in this object, giving a velocity dispersion of 112 ± 6 km s^{-1}. This was the only object that did not require a two-component fit to [O III] 5007Å. The forbidden lines are extremely narrow (much narrower than the bulge features), and are only just resolved by the EMMI spectrograph.

IRAS 13224-3809. The NLS1 IRAS 13224-3809 shows extremely high-amplitude, fast variability in both soft and hard X-rays (Boller et al. 1997; Leighly 1999), and also exhibits an extremely steep soft X-ray photon index of $\Gamma = 4.4$ (Boller et al. 1996). Unfortunately it is also a very strong Fe II emitter, and no stellar features were visible even after careful nuclear subtraction. The [O III] lines were found to be complex, consisting of at least two strong components (Figure 2.14).

NGC 6814. The first of the two objects for which only a nuclear spectrum was obtained. Fits to [O III] and Hβ are shown in Figures 2.14 and 2.16.

NGC 7450. The other object including only a nuclear spectrum. The broad component of Hβ was weak for this object (see Figure 2.16), and so the FWHM measurement is somewhat uncertain.

CHAPTER 3

Properties of NLS1 Galaxies

The previous Chapter described in detail the determination of the stellar velocity dispersions and nuclear properties of the samples of NLS1s and BLS1s observed in this study. In order to make meaningful comparisons between the two types, these two samples have been bolstered using objects from previous studies in the literature. The following Section describes the selection criteria for these objects, and the remainder of this Chapter discusses the respective properties of NLS1s and BLS1s and the implications for the various NLS1 models.

3.1 Literature objects

A number of studies of both NLS1s and BLS1s have been conducted over the past few years, as the apparent ubiquity of black holes in the centres of nearby inactive galaxies spurred a renewed interest in methods for estimating the black hole masses in AGN. However, the difficulties associated with measuring the stellar velocity dispersion in AGN mean that the number of Type-1 AGN with measurements both of the nuclear properties investigated in this study and σ_* is still limited, such that it is not possible to compile a complete sample of either BLS1s or NLS1s. However, even with this proviso it is still possible to make meaningful comparisons between the two groups.

The majority of the BLS1 sample were chosen from the studies of Nelson & Whittle

(1995) and Nelson et al. (2004), as these had both reliable σ_* measurements and in the majority of cases also had measurements of the relevant nuclear parameters. In all cases it was required that the object have a σ_* estimate and tabulated values for at least two of the nuclear properties investigated in this study in order to be included in the sample. Many of the sample were also included in the reverberation mapping studies of Wandel et al. (1999), Kaspi et al. (2000) and Peterson et al. (2004). For these objects the 5100Å luminosity measurements from Kaspi et al. (2000) were used, after a correction for the differing cosmological parameters was applied, and FWHM Hβ measurements were taken to be the mean FWHM values tabulated in Wandel et al. (1999). The [O III] FWHM and luminosities were taken from Nelson & Whittle (1995). For NGC 5940, the σ_* estimate was drawn from the sample of Jiménez-Benito et al. (2000), while the [O III] FWHM and luminosity were taken from Nelson & Whittle (1995) and FWHM Hβ from Marziani et al. (2003). In the cases of Mrk 10 and Mrk 1040, σ_*, [O III] FWHM and luminosity were taken from the studies of Nelson & Whittle (1995) or Whittle (1992), while FWHM Hβ and the 5100Å luminosity came from Botte et al. (2004). For Mrk 1018, the parameters were taken either from Nelson & Whittle (1995) (σ_* and FWHM [O III]) or the earlier study by Whittle (1992) ([O III] luminosity). Finally, the parameters for UGC 3223 were taken from Nelson & Whittle (1995) and Crenshaw et al. (2003).

Most of the NLS1 σ_* measurements came from the studies of Botte et al. (2005) (Mrk 705, Mrk 766, Mrk 896 and IC 3599) and Barth et al. (2005). The latter study observed a sample of 19 putative NLS1s from the Sloan Digital Sky Survey (SDSS) First Data Release archive and 2 NLS1s from the SDSS Second Data Release with ESI on the *W. M. Keck-II* telescope, obtaining 15 new σ_* measurements. In the case of the SDSS objects, the virial masses were calculated using the Hα linewidths rather than the more commonly-used Hβ FWHM as the Hα lines in many cases had significantly better S/N allowing a more accurate decomposition of the broad and narrow components. FWHM Hα values and 5100Å luminosities were obtained from Barth et al. (2005), while the FWHM [O III] values (corrected for instrumental resolution) and [O III] 5007Å luminosities were taken from Greene & Ho (2004). For NGC 4051 and Mrk 110, the σ_* estimates were taken from Onken et al. (2004), while 5100Å luminosi-

ties came from Kaspi et al. (2000), Hβ FWHM from Wandel et al. (1999) and [O III] FWHM and luminosities from Whittle (1992). The broad-line and narrow-line objects for both this study and from the literature are listed in Tables 3.1 and 3.2 respectively.

3.2 Virial black hole masses

Black hole mass estimates from reverberation mapping were used instead of virial mass estimates for all objects where these measurements were available. These were obtained from the most recent compilation of 35 AGN by Peterson et al. (2004) (see also references therein). The rest were calculated using the relationship between the radius of the broad-line region $R_{\rm BLR}$ and the monochromatic luminosity at 5100Å described first by Kaspi et al. (2000). The study by Kaspi et al. (2000) combined the reverberation mapping measurements of 17 quasars with the sample of Seyfert 1 galaxies from Wandel et al. (1999) and determined $R_{\rm BLR}$ from the cross-correlation of the continuum and emission-line light-curves. The ionizing luminosity was estimated from the 5100Å luminosity. This was taken to have a power-law relationship to the ionizing luminosity, as determining the actual ionizing luminosity was impossible since it originates in the unobservable far-UV. These were then used to investigate relationships between the monochromatic luminosity at 5100Å with $R_{\rm BLR}$, the gas velocity (determined from the line FWHM), and the derived central masses. Relatively poor correlations were found for both FWHM–luminosity and mass–luminosity, as expected, but a better correlation was found between luminosity and $R_{\rm BLR}$, suggesting that luminosity is the principal parameter that determines the size of the BLR. Kaspi et al. (2000) found the best-fitting relationship between λL_λ and $R_{\rm BLR}$ to be

$$R_{\rm BLR} = (32.0^{+2.0}_{-1.9}) \left[\frac{\lambda L_\lambda(5100\text{Å})}{10^{37}\ \text{W}}\right]^{0.700\pm0.033} \quad \text{lt} - \text{days} \tag{3.1}$$

which is not consistent with the relationship $R_{\rm BLR} \propto \lambda L^{0.5}$ expected if all AGN are assumed to be characterised by the same ionization parameter (see Equation 1.11). These data were then re-analysed by Peterson et al. (2000), and they found $R_{\rm BLR} \propto \lambda L^{0.62\pm0.02}$ using a linear regression analysis and excluding NGC 4051 from the fit. The origin of the discrepancy between these two results is not clear, as both used the same data-sets in the analysis. Follow-up by work was performed by McLure

Table 3.1: Broad-line objects from this study and the literature. Column (1) gives the object name (objects from this study are listed first) and column (2) the redshift. Column (3) gives the stellar velocity dispersion where this is available. Columns (4-7) give the optical luminosity (in log W), FWHM of the Hβ broad component, [O III] 5007Å line luminosity and FWHM. Black hole mass is listed in column (8).

Object	z	$\sigma_* \pm \epsilon$ km s^{-1}	Log (λL_λ) (5100Å)	FWHM Hβ km s^{-1}	Log ($L_{[\mathrm{OIII}]}$) (W)	σ_{FWHM} km s^{-1}	$\log\left(\frac{M_{\mathrm{BH}}}{M_\odot}\right)$
E12-G21	0.0300	...	36.30	2517	33.60	194	7.05
NGC 526A	0.0191	203 ± 14	35.48		33.75	111	
IRAS 03450	0.0310	...	36.25	2822	33.93	255	7.12
3C 120	0.0330	162 ± 20[a]	37.20	2195	35.11	109	7.74[b]
Mrk 79	0.0222	141 ± 14	36.51	4379	33.95	156	7.71[b]
E141-G55	0.0360	166 ± 24	36.93	5195	34.58	150	8.06
NGC 6814	0.0052	115 ± 18[a]	34.79	3379	32.69	85	6.38
NGC 6860	0.0149	136 ± 7	35.65	5709	33.64	84	7.36
Mrk 509	0.0344	169 ± 32	37.18	3600	35.06	209	8.16[b]
PG 2130+099	0.0630	...	37.63	2748	35.24	147	8.66[b]
NGC 7213	0.0060	212 ± 11	35.39	3878	32.98	430	6.87
3C 445	0.0562	...	36.70	3278	35.30	127	7.52
NGC 7450	0.0106	85 ± 25[a]	34.82	3668	33.01	58	6.47
NGC 7469	0.0163	127 ± 10	36.49	2240	34.64	158	7.09[b]
NGC 3227	0.0039	136 ± 4[c]	35.37[d]	4920[e]	33.34[f]	206[f]	7.63[b]
NGC 3516	0.0088	181 ± 5[c]	35.95[d]	2700[b]	33.92[f]	106[f]	7.63[b]
NGC 4151	0.0033	97 ± 3[c]	35.92[d]	5910[e]	34.45[f]	180[f]	7.12[b]
NGC 4593	0.0090	135 ± 6[c]	36.16[b]	3720[b]	33.49[f]	108[f]	6.73[b]
NGC 5548	0.0172	201 ± 12[c]	36.50[d]	6300[e]	34.59[f]	174[f]	7.83[b]
NGC 5940	0.0339	103 ± 27[g]		5240[h]	33.97[a]	164[a]	
Mrk 10	0.0293	137 ± 38[a]	36.15[i]	3047[i]	34.44[f]	153[f]	7.12
Mrk 279	0.0305	197 ± 12[c]	36.96[d]	3410[e]	34.48[f]	246[f]	7.54[b]
Mrk 590	0.0264	189 ± 6[c]	36.78[d]	2470[e]	33.93[f]	170[f]	7.68[b]
Mrk 817	0.0315	120 ± 15[c]	36.80[d]	4490[e]	34.48[f]	140[f]	7.69[b]
Mrk 1018	0.0424	195 ± 25[a]			34.16[f]	140[f]	
Mrk 1040	0.0167	151 ± 32[a]	35.97[h]	4220[h]	33.91[f]	130[f]	6.57
Akn 120	0.0323	221 ± 17[c]	37.22[d]	5800[e]	34.35[f]	208[f]	8.18[b]
3C 390.3	0.0561	273 ± 16[c]	36.89[d]	10000[e]		217[h]	8.46[b]
UGC 3223	0.0156	106 ± 28[a]		4740[j]	33.42[a]	108[a]	

References (if no reference; this study):

[a] Nelson & Whittle (1995)
[b] Peterson et al. (2004)
[c] Nelson et al. (2004)
[d] Kaspi et al. (2000)
[e] Wandel et al. (1999)
[f] Whittle (1992)
[g] Jiménez-Benito et al. (2000)
[h] Marziani et al. (2003)
[i] Botte et al. (2004)
[j] Crenshaw et al. (2003)

Table 3.2: Narrow-line objects from both this study and the literature. Column listings are as for Table 3.1.

Object	z	$\sigma_* \pm \epsilon$ km s^{-1}	Log (λL_λ) (5100Å)	FWHM Hβ km s^{-1}	Log $(L_{[OIII]})$ (W)	σ_{FWHM} km s^{-1}	$\log\left(\frac{M_{BH}}{M_\odot}\right)$
Mrk 335	0.0258	110 ± 15	36.28	1833	34.02	137	7.15[a]
I Zw 1	0.0611	...	36.42	1337	34.07	605	6.57
Mrk 359	0.0178	115 ± 8	35.78	1142	33.76	54	6.04
IRAS 13224	0.0667	...	36.82	1353	34.52	364	6.82
MCG -6-30-15	0.0077	112 ± 6	34.96	1885	32.77	67	5.98
Mrk 493	0.0313	115 ± 11	36.44	1064	33.77	148	6.38
IRAS 17020	0.0604	...	36.64	1101	34.78	116	6.54
Kaz 163	0.0630	...	37.09	1496	35.11	192	7.08
Akn 564	0.0247	...	36.62	1314	34.49	81	6.68
NGC 4051	0.0023	84 ± 9[b]	34.78[c]	1170[d]	32.67[e]	81[e]	6.28[a]
Mrk 110	0.0342	86 ± 13[b]	36.66[c]	1430[d]	34.81[e]	123[e]	7.40[a]
Mrk 705	0.0287	82 ± 25[f]	37.54[g]	1790[h]	34.23[e]	159[e]	7.51
Mrk 766	0.0129	81 ± 17[f]		1630[h]	34.40[e]	76[e]	5.80
Mrk 896	0.0265	87 ± 11[f]	36.37[g]	1673[g]		130[f]	6.73
IC 3599	0.0224	85 ± 17[f]	35.07[g]	693[g]		107[f]	5.18
0107+1408	0.0768	35 ± 10[i]	36.06[j]	950[1 i]	33.72[j]	84[j]	6.05
0249-0815	0.0295	55 ± 9[i]	34.87[j]	690[1 i]	33.02[j]	85[j]	5.05
0325+0034	0.102	55 ± 6[i]	35.91[j]	820[1 i]	33.71[j]	47[j]	5.83
0809+4416	0.054	65 ± 4[i]	35.80[i]	1100[1 i]			6.02
0829+5006	0.0434	59 ± 8[i]	35.80[j]	760[1 i]	33.92[j]	72[j]	5.70
1011+0029	0.100	48 ± 7[i]	35.83[j]	1240[1 i]	33.42[j]	85[j]	6.15
1016-0007	0.0943	39 ± 6[i]	35.97[j]	1140[1 i]	34.01[j]	177[j]	6.16
1240-0029	0.0809	52 ± 11[i]	36.33[j]	720[1 i]	34.54[j]	81[j]	5.98
1250-0155	0.0814	63 ± 9[i]	36.22[j]	2110[1 i]	34.27[j]	55[j]	6.84
1434+0338	0.0281	54 ± 10[i]	34.92[j]	770[1 i]	32.99[j]	93[j]	5.18
1702+6028	0.0690	76 ± 10[i]	35.53[j]	1170[1 i]	33.48[j]	69[j]	5.91
1727+5421	0.0994	58 ± 7[i]	36.05[j]	930[1 i]	33.99[j]	69[j]	6.03
2156+1103	0.108	81 ± 8[i]	36.50[i]	780[1 i]			6.15
2321+0007	0.183	81 ± 9[i]	36.09[j]	1770[1 i]	33.67[j]	126[j]	6.61
2338-0028	0.0355	56 ± 6[i]	34.69[j]	1890[1 i]	33.87[j]	59[j]	5.82

[1] Broad-line widths measured from Hα

References (if no reference; this study):

[a] Peterson et al. (2004)

[b] Onken et al. (2004)

[c] Kaspi et al. (2000)

[d] Wandel et al. (1999)

[e] Whittle (1992)

[f] Botte et al. (2005)

[g] Botte et al. (2004)

[h] Crenshaw et al. (2003)

[i] Barth et al. (2005)

[j] Greene & Ho (2004)

& Jarvis (2002), designed to develop a similar relationship between $R_{\rm BLR}$ and the near-UV luminosity to allow high-redshift samples to be probed. For the $R_{\rm BLR} - \lambda L_{\lambda}$ relationship at 5100Å they found

$$R_{\rm BLR} = (26.4 \pm 4.4) \left[\frac{\lambda L_{\lambda}(5100\text{Å})}{10^{37}\ \rm W} \right]^{0.61 \pm 0.10} \quad {\rm lt-days} \tag{3.2}$$

after conversion of the Kaspi et al. (2000) luminosities to the slightly different cosmology adopted by the later study. The difference in cosmological parameters is the probable explanation for the slightly flatter best-fitting relation found by McLure & Jarvis (2002). This relationship was then used to derive a virial mass-estimation method that could be used for large samples of AGN (which would be unfeasible with a time-intensive method such as reverberation mapping), using the broad-line widths as an estimator for the BLR cloud velocities. The derived optical virial black hole mass ($M_{\rm BH}$) estimator was

$$\frac{M_{\rm BH}}{M_{\odot}} = 4.74 \left(\frac{\lambda L_{\lambda}(5100\text{Å})}{10^{37}\ \rm W} \right)^{0.61} \left[\frac{\rm FWHM\ H\beta}{\rm km\ s^{-1}} \right]^{2} \tag{3.3}$$

which was used to derive all the non-reverberation mapping black hole masses in column 8 of Tables 3.1 and 3.2. The black hole masses derived for the NLS1 sample of Barth et al. (2005) were derived in that study using the calibration between $M_{\rm BH}$ from virial masses and that calculated using reverberation mapping by Onken et al. (2004). However, to ensure as homogeneous a sample as possible, all black hole masses were recalculated using Equation 3.3. The black hole masses estimated using this relation were on average 0.17 dex lower than the virial masses adopted by Barth et al. (2005). Figure 3.1 shows the masses estimated using Equation 3.3 versus masses determined from reverberation mapping for all objects for which this is applicable. A linear fit taking into account errors on both parameters was performed, and the results consistent with a 1:1 relationship. Although the scatter is still significant, there is no evidence for a systematic bias arising from the use of the virial estimation method.

One potentially large source of error for black hole masses determined using Equation 3.3 is from variability in the Hβ FWHM. The broad emission lines have been observed to vary in width in a number of studies (Peterson 1988; Peterson et al. 1998, 1999). In some cases (e.g. NGC4151: Penston & Perez 1984; Peterson 1985) the broad component of Hβ has been observed to disappear almost completely only to reappear

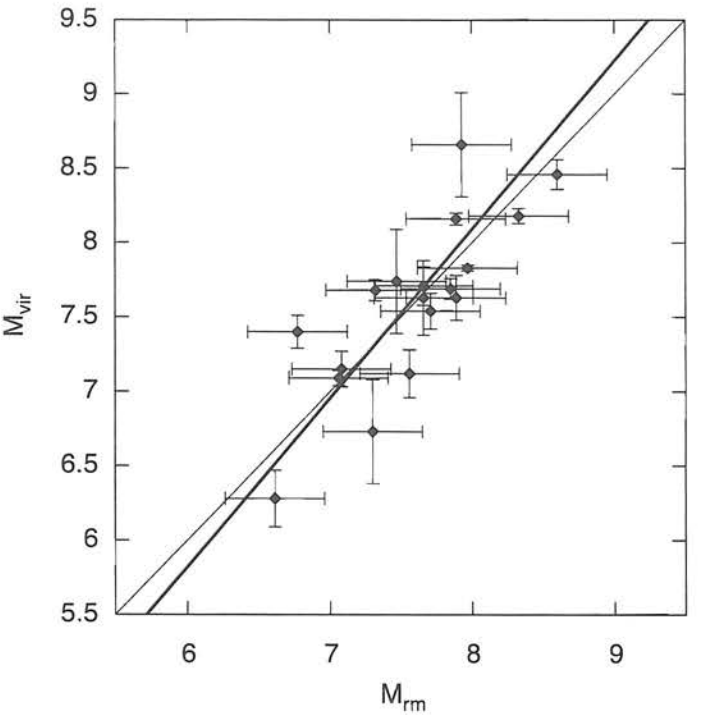

Figure 3.1: The masses determined from the virial method (Equation 3.3; $M_{\rm vir}$) versus masses from reverberation mapping ($M_{\rm rm}$). The 1:1 relation (thin line) and best-fitting relation (thick line) are also shown.

later. Given that the observations for this study encompass single epochs only, it is not possible to quantify the magnitude of the likely uncertainty from profile variability. However, it seems likely that this would increase scatter rather than including a bias, since any variability will be random.

3.3 Comparing the BLS1 and NLS1 samples

As neither the BLS1 nor NLS1 samples were complete, and therefore potentially subject to unknown selection effects, in order to make meaningful comparisons between them it was necessary to ensure that the two samples were drawn from similar populations in order to rule out effects due to either redshift or luminosity evolution. The distributions of 5100Å luminosity, [O III] luminosity and redshift for the BLS1 and NLS1 samples are shown in Figures 3.2, 3.3 and 3.4 respectively. To test that the two samples were drawn from similar parent populations, Kolmogorov-Smirnov (KS) tests

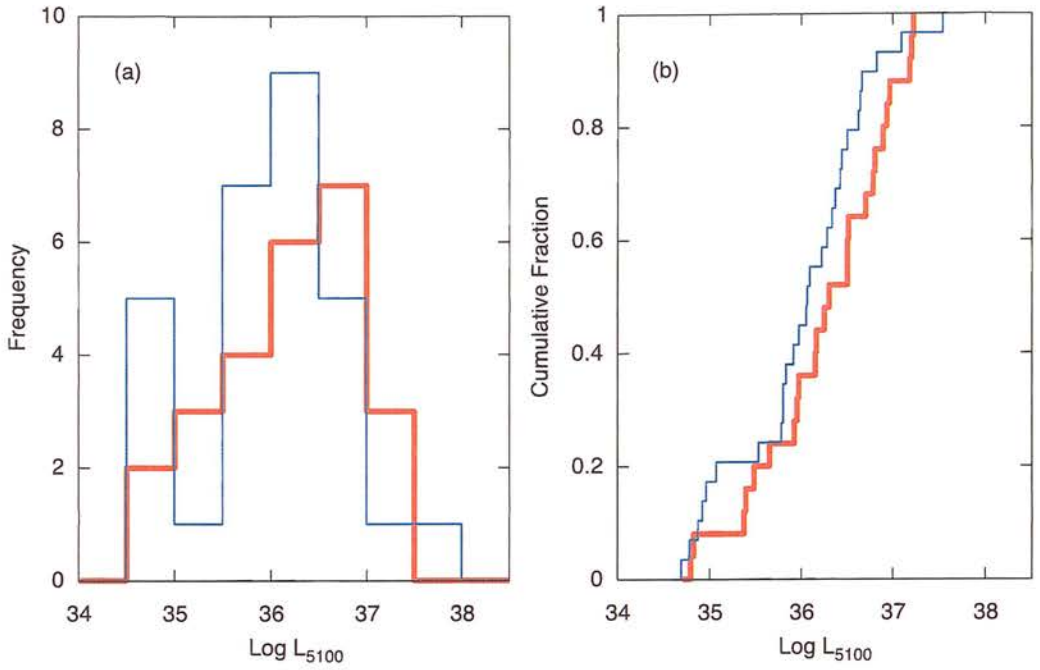

Figure 3.2: (a) The optical luminosity distributions of the NLS1 sample (blue, thin) and the BLS1 sample (red, thick). (b) The cumulative distributions of the two samples.

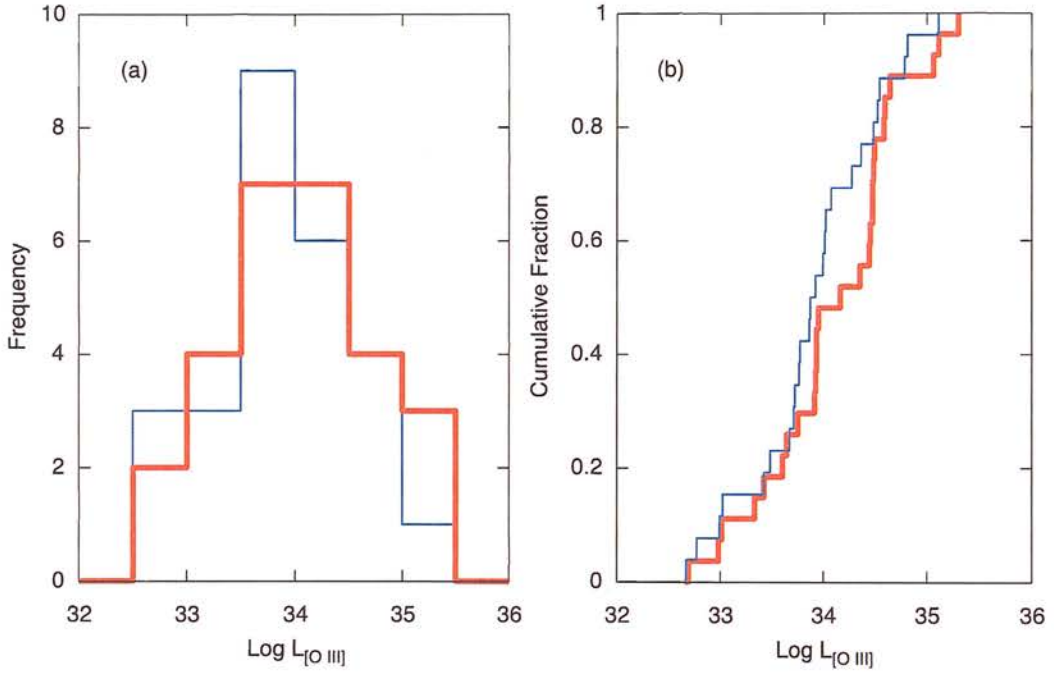

Figure 3.3: (a) The [O III] luminosity distributions of the NLS1 sample (blue, thin) and the BLS1 sample (red, thick). (b) The cumulative distributions of the two samples.

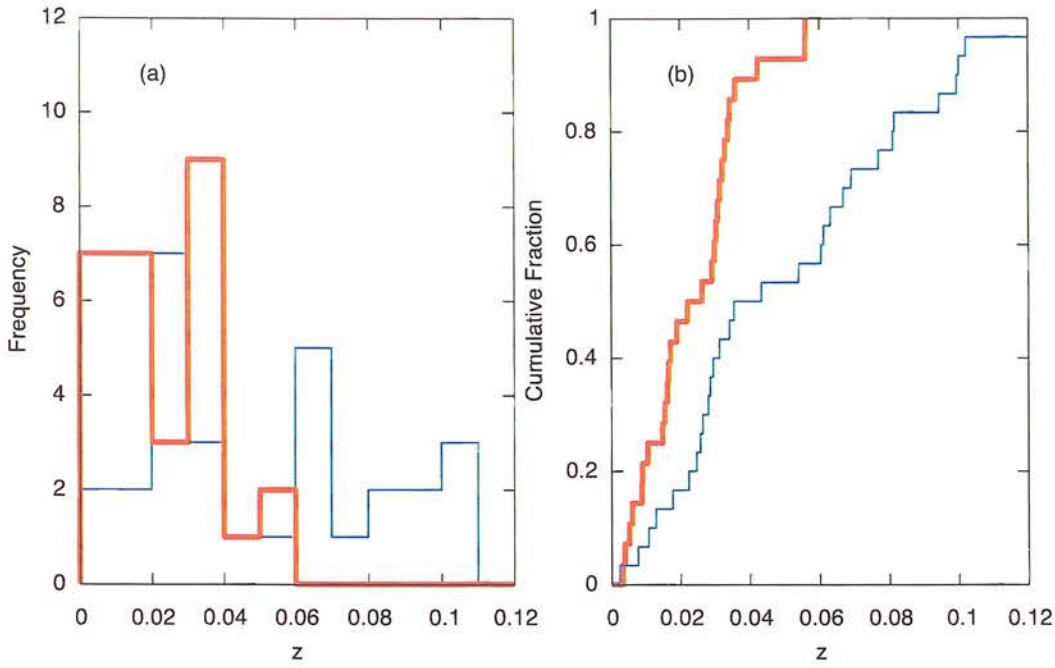

Figure 3.4: (a) The redshift distributions of the NLS1 sample (blue, thin) and the BLS1 sample (red, thick). (b) The cumulative distributions of the two samples.

were performed on the three cumulative distributions, also shown respectively in Figures 3.2, 3.3 and 3.4 for optical luminosity, [O III] luminosity and redshift. The KS test compares the cumulative distributions for the two samples and gives the probability that the two are consistent with being randomly sampled from the same parent population (Press et al. 1992). This is done by calculating the maximum absolute difference D between the two cumulative distributions. The D-statistic is expected to be normally distributed, which can then be used to determine the probability that the two samples are similar. As the two samples in this study are quite small, the KS test result was deemed to be acceptable if the probability of the two samples being different was less than 2σ (95 per cent). The probabilities that the 5100Å and [O III] luminosities were drawn from the same population were calculated to be 29.4 per cent and 52.8 per cent respectively, both well within the required limits. However the redshift distributions were significantly different (probability 0.6 per cent that the two are the same). Disregarding the four highest-redshift NLS1s improved the result significantly (to under 2σ). However, the likelihood of significant evolution of the two populations with redshift over the small ranges considered here is extremely small. It was therefore

decided to include all objects in the analysis.

An analogue to the KS test was also performed upon the two-dimensional distributions of 5100Å luminosity–redshift, [O III] luminosity–redshift and 5100Å luminosity–[O III] luminosity, in order to determine whether the two populations were significantly different when two of the relevant parameters were taken into account. In these cases, a slightly different approach was required, as it is difficult to define a cumulative distribution in more than one dimension. A method to overcome this difficulty was first proposed by Peacock (1983). In this generalisation, rather than considering only one ordering method for the cumulative distribution, the maximum difference between the two distributions is calculated for *all* possible ordering combinations. In the case of two data-sets (rather than one data-set and a theoretical prediction), for each point the plane is divided into four quadrants centred on the particular point in question. The fractional number of points from both data-sets is calculated in each quadrant, and the difference in each quadrant is then the difference between these two quantities. The point for which this difference is maximized (in one quandrant) is found by considering each data-set in turn, and D is calculated from the average of these (Press et al. 1992). The three two-dimensional distributions considered here are shown in Figure 3.5. The probabilities that the two samples were taken from the same parent populations were calculated to be 0.9, 4.2 and 49.2 per cent for the L_{5100}–z, $L_{[\mathrm{OIII}]}$–z and L_{5100}–$L_{[\mathrm{OIII}]}$ distributions respectively. Clearly, the redshift distributions of the two samples are different; however, the redshift ranges considered here are small and so this is not expected to be a problem. All objects are retained for the following analysis.

3.4 Is $\sigma_{[\mathrm{OIII}]}$ a proxy for σ_*?

Many previous studies of the M_{BH}–σ_* relation have used the width of the [O III] 5007Å line as a proxy for the true stellar velocity dispersion. Greene & Ho (2005) have shown for a large sample of AGN that $\sigma_{[\mathrm{OIII}]}$ overestimates σ_* by a factor of ∼30 per cent. However, the kinematics of low-ionization species were consistent with gravity-dominated dynamics, suggesting that the active nucleus has a direct effect on the motions of the [O III]-emitting gas. This appeared to contradict the earlier study by Nelson & Whittle

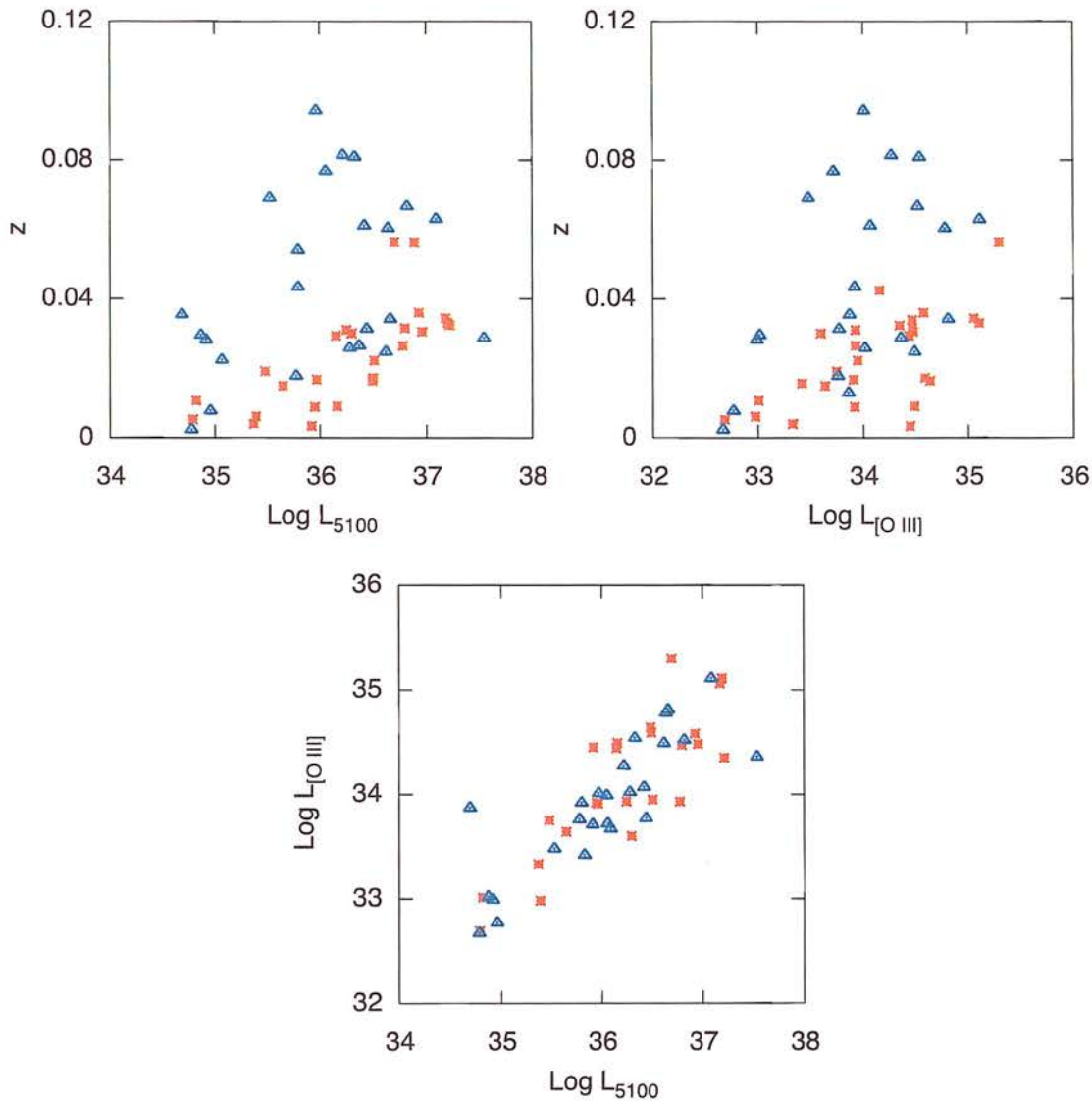

Figure 3.5: The two-dimensional distributions for the NLS1 and BLS1 samples. The panels show the distributions for L_{5100}–z (top left), $L_{[OIII]}$–z (top right) and L_{5100}–$L_{[OIII]}$ (bottom). Blue triangles are NLS1s, red stars are BLS1s.

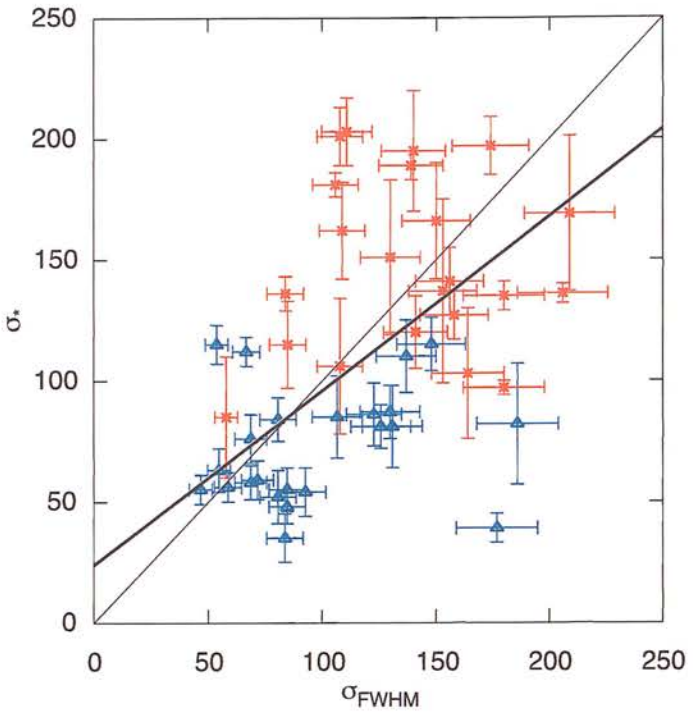

Figure 3.6: Stellar velocity dispersion σ_* versus the [O III] 5007Å linewidths $\sigma_{\rm FWHM}$ as measured from the FWHM of the emission line profile. Red stars are BLS1s and blue triangles are NLS1s. The thin line represents a 1:1 relation, while the thick line is the best-fitting relation determined from an unweighted least-squares fit.

(1995; 1996) who found a moderately good correlation between $\sigma_{\rm FWHM}$ and σ_*. This suggested that gravity played a key role in the dynamics of the NLR, although the intrinsic scatter was non-negligible and the gradient of the best-fitting relation was flatter than unity. Interestingly, Greene & Ho (2005) found that $\sigma_{\rm [OIII]}$ was a good tracer of σ_* if the width of only the core of the two-component fit was used.

This study provides for the first time an opportunity to investigate the correlation between $\sigma_{\rm [OIII]}$ and σ_* for both BLS1s and NLS1s. Previous studies have concentrated either on Seyfert galaxies as a monolithic group (Nelson & Whittle 1996), or on large samples of Type-2 AGN (Greene & Ho 2005). Greene & Ho (2005) noted that NLS1 studies that rely on $\sigma_{\rm [OIII]}$ probably overestimate the true stellar velocity dispersion by a factor that depends on the Eddington ratio, but were unable to make definitive statements about these objects as a group using their sample of Type-2 AGN.

The velocity dispersion derived from the [O III] 5007Å FWHM ($\sigma_{\rm FWHM}$ = [O III]

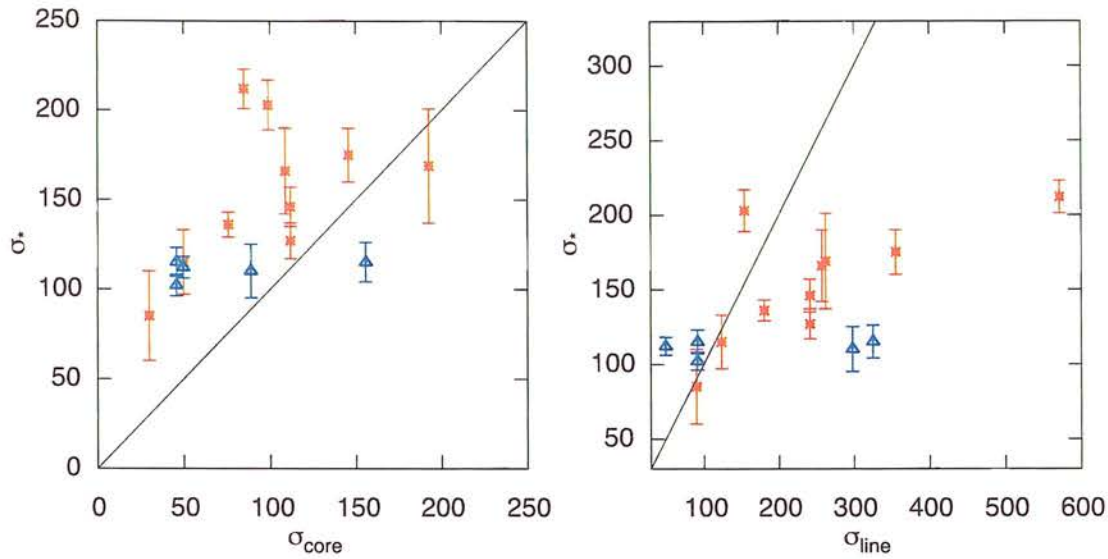

Figure 3.7: Stellar velocity dispersion σ_* versus the [O III] 5007Å linewidths σ_{core} measured from only the line core (left) and using the second moment σ_{line} (right). Again, red stars are the BLS1s and blue triangles are NLS1s and the solid line is the 1:1 relation.

FWHM/2.35) is shown plotted versus the velocity dispersion obtained from the stellar absorption features in Figure 3.6. An error of ~10 per cent was adopted for σ_{FWHM}. The 1:1 relation and the best-fitting relation are also shown. The correlation is moderately good, although with a large scatter. The Spearman rank-correlation coefficient for the two parameters is $r_s = 0.52$, with a probability of $P_{\mathrm{null}} = 1.6 \times 10^{-4}$ for the null hypothesis of no correlation. The slope of the best-fitting relationship determined from a least-squares fit taking into account the errors on both variables is 0.72 ± 0.05, although the χ^2 for this fit ($\chi^2/\mathrm{d.o.f} = 9.6$) is formally unsatisfactory. It is immediately noticeable that the NLS1s and BLS1s fall into two relatively well-defined groups on the plot, with the NLS1s having in general lower velocity dispersions than the BLS1s. This is discussed later in this Chapter. Considering either the BLS1 or NLS1 samples in isolation gives poor correlations, with ($r_s = 0.21$, $P_{\mathrm{null}} = 0.31$) and ($r_s = 0.15$, $P_{\mathrm{null}} = 0.50$) respectively.

The correlations between σ_* and the dispersion derived from the line core σ_{core} and second-moment σ_{line} are shown in Figure 3.7, for only the new objects presented in this study, as this information was generally not available for the literature objects. In both cases the two quantities show a moderate correlation ($r_s = 0.61$; $P_{\mathrm{null}} = 0.015$ for

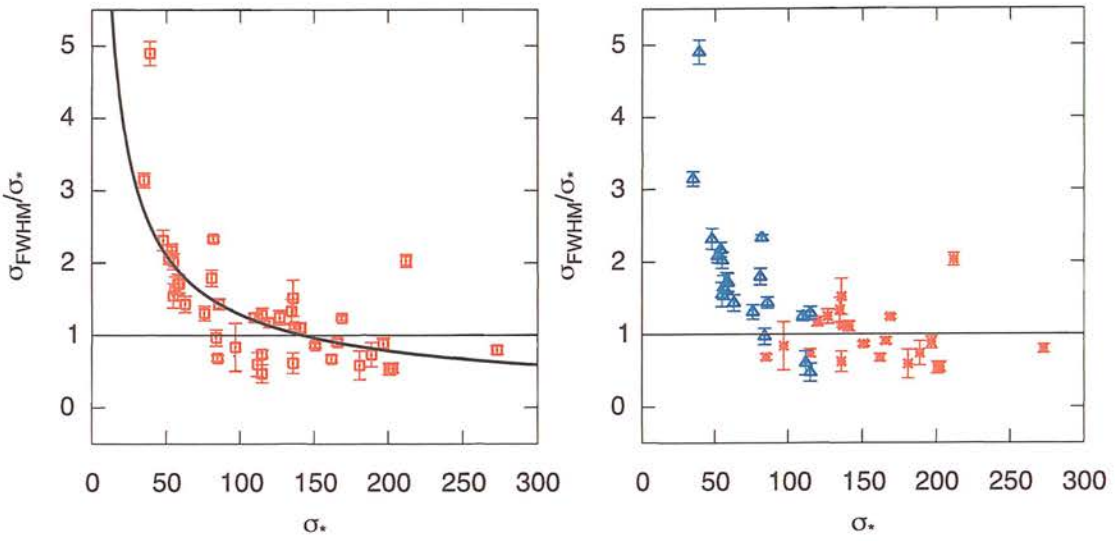

Figure 3.8: The ratio $\sigma_{\rm FWHM}/\sigma_*$ versus σ_* for the entire sample of objects. The left-hand panel shows all of the objects as a single sample, with the $\sigma_{\rm FWHM} = \sigma_*$ relation (thin line) and best-fitting power law relation (thick line). In the right-hand panel the sample is segregated into BLS1s (red stars) and NLS1s (blue triangles).

$\sigma_{\rm core}$ and $r_s = 0.64$; $P_{\rm null} = 0.010$ for $\sigma_{\rm line}$), but neither of them is formally consistent with a 1:1 relationship. The best-fitting relations for the $\sigma_{\rm core}$ and $\sigma_{\rm line}$ parameters have gradients of 0.50 and 0.20 respectively. These results are not in agreement with the findings of Greene & Ho (2005); however, the sample size in this study is small by comparison and so it is not clear what significance to attach to these findings. It does seem clear that the second-moment of the line profile significantly over-estimates the stellar velocity dispersion, but as this study contains only one object with both a σ_* measurement and a very large second-moment (NGC 7213) it is not clear how much this object is biasing the fit. It is certainly the case that the blueshifted wing is very strong for this object (see Figure 2.13), and since the second-moment measurement is sensitive to both the widths and intensities of the wings this could dramatically influence the results.

Figure 3.8 shows the ratio $\sigma_{\rm FWHM}/\sigma_*$ plotted against the stellar velocity dispersion σ_*. The samples are shown plotted as a single group (left-hand panel) and then segregated into NLS1s and BLS1s (right-hand panel). It is shown that NLS1s have systematically higher $\sigma_{\rm FWHM}/\sigma_*$ ratios than BLS1s, and that this ratio is negatively correlated

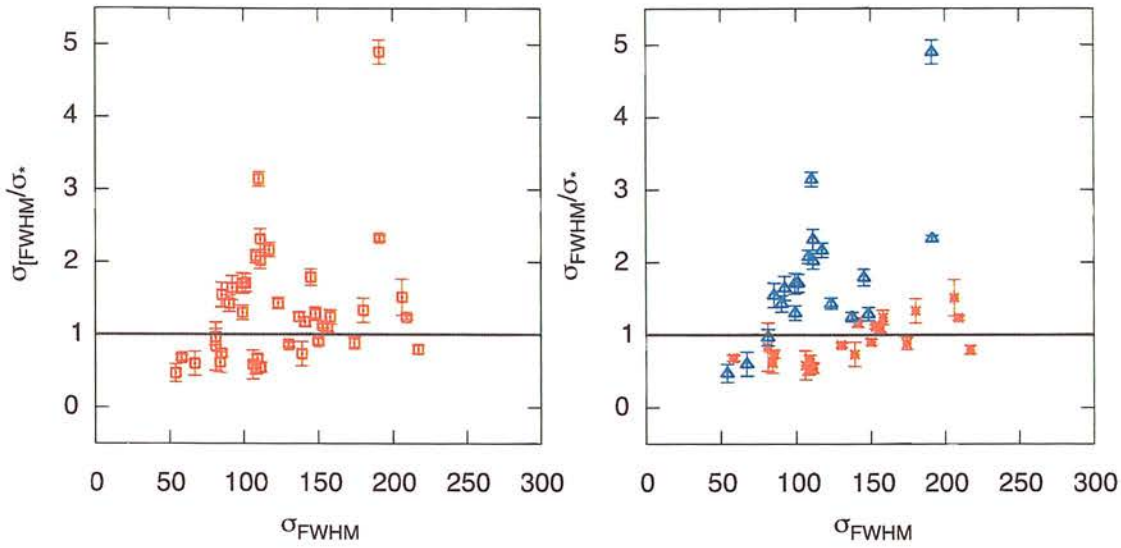

Figure 3.9: The ratio of $\sigma_{\mathrm{FWHM}}/\sigma_*$ versus σ_{FWHM} for the entire sample of objects. The left-hand panel shows all of the objects as a single sample, while in the right-hand panel the sample is segregated into BLS1s (red stars) and NLS1s (blue triangles).

with the stellar velocity dispersion itself and hence central black hole mass as a result of the M_{BH}–σ_* relation. This result is confirmed in the investigation by Greene & Ho (2005), who found the quantity $\Delta\sigma \equiv \log\sigma_{[\mathrm{OIII}]} - \log\sigma_*$ to be correlated with σ_*. A weighted least-squares fit to the data in Figure 3.8 gives a best-fitting relationship of

$$\log\left(\frac{\sigma_{\mathrm{FWHM}}}{\sigma_*}\right) = 1.53 - 0.72\log(\sigma_*) \tag{3.4}$$

which has $r_s = -0.69$ with a probability $P_{\mathrm{null}} = 4.8 \times 10^{-7}$ of no correlation. This is a somewhat-stronger correlation than that found by Greene & Ho (2005). This clearly illustrates the danger of using σ_{FWHM} as a proxy for σ_*, particularly in the case of NLS1s.

To attempt to discover the physical reason for the correlation in Figure 3.8, the ratio $\sigma_{\mathrm{FWHM}}/\sigma_*$ was investigated as a function of other physical parameters of the nucleus. Figures 3.9 and 3.10 show $\sigma_{\mathrm{FWHM}}/\sigma_*$ plotted against the [O III] width σ_{FWHM} and 5100Å luminosity respectively. Again, the parameters are shown plotted as a single ensemble and then split into BLS1s and NLS1s. The left panel of Figure 3.9 shows that $\sigma_{\mathrm{FWHM}}/\sigma_*$ is poorly correlated with the width of [O III] 5007Å ($r_s = 0.32$ with $P_{\mathrm{null}} = 0.04$). Interestingly, the right-hand panel appears to show that NLS1s are more strongly correlated with σ_{FWHM} than BLS1s. However, the scatter is still considerable.

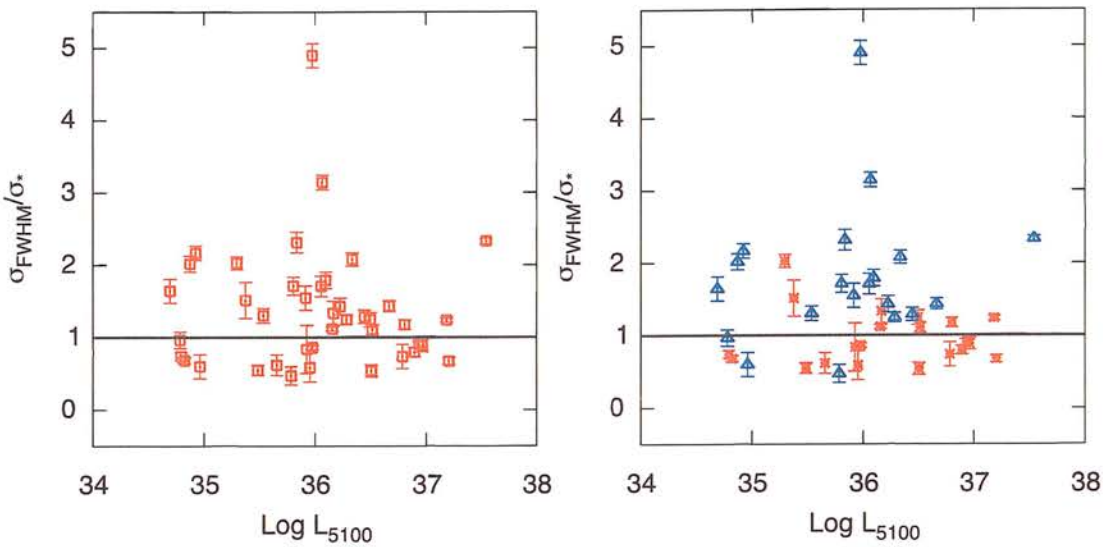

Figure 3.10: The ratio of $\sigma_{\rm FWHM}/\sigma_*$ versus the 5100Å luminosity for the entire sample of NLS1s and BLS1s.

Again, it is not clear what biasing effect the extreme points have in this case.

If the size of the NLR increases as a function of increasing luminosity, then higher-luminosity objects should have larger NLR radii which may prove more accurate tracers of the gravitational potential of the bulge. If this is the case then $\sigma_{\rm FWHM}$ should provide a more accurate estimate of the stellar velocity dispersion in higher-luminosity objects. Figure 3.10 shows $\sigma_{\rm FWHM}/\sigma_*$ plotted versus the optical luminosity. It is noticable from the right-hand panel of this Figure that NLS1s generally have a higher $\sigma_{\rm FWHM}/\sigma_*$ ratio than BLS1s at the same luminosity. The entire sample of objects (NLS1s and BLS1s) was divided into two luminosity bins ($\log L_{5100} < 36.00$ W and $\log L_{5100} > 36.00$ W). The mean and standard deviation of the $\sigma_{\rm FWHM}/\sigma_*$ ratio in each bin were calculated to be 1.40 and 1.00 for the low luminosity bin and 1.34 and 0.60 for the high-luminosity bin. Although this suggests that higher-luminosity objects may on average have $\sigma_{\rm FWHM}/\sigma_*$ ratios closer to unity with less scatter than the lower-luminosity objects, it is unlikely that source luminosity is the primary driver underlying the $\sigma_{\rm FWHM}/\sigma_* - \sigma_*$ correlation. A larger luminosity range would allow a more accurate determination of this.

Greene & Ho (2005) concluded from their study that the primary physical driver behind $\Delta\sigma$ was the quantity $L_{\rm Bol}/L_{\rm Edd}$, i.e. the Eddington ratio of the AGN. This

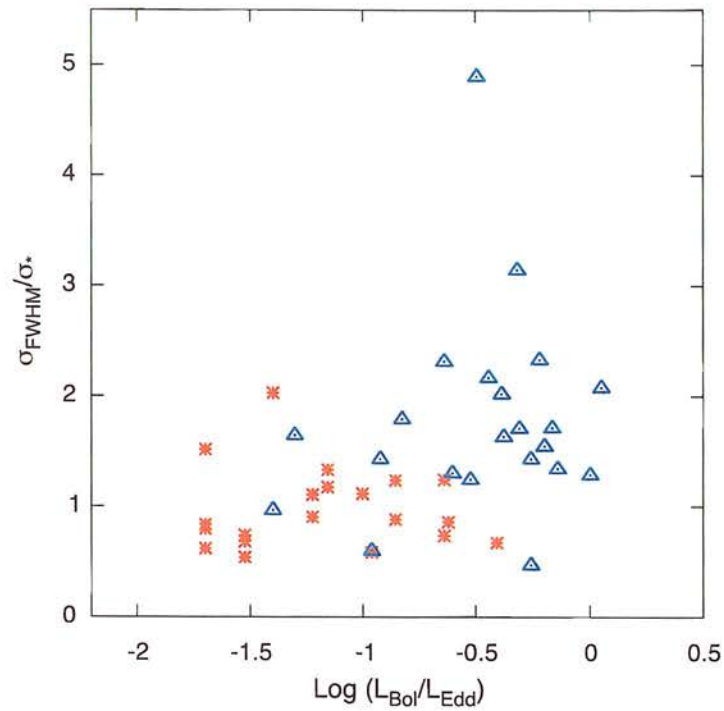

Figure 3.11: The ratio $\sigma_{\rm FWHM}/\sigma_*$ versus the Eddington ratio calculated using the optical luminosity at 5100Å. Red plusses are BLS1s, blue triangles are NLS1s.

might be expected since the higher the Eddington ratio, the higher the likelihood of non-virial motions as a result of increased radiation pressure. If NLS1s have systematically smaller black hole masses by comparison with their broad-line counterparts, then these AGN require higher accretion rates (and hence higher Eddington ratios) to explain their comparable luminosities. If higher Eddington luminosities lead directly to super-virial gas motions, then this could explain the correlation between $\sigma_{\rm FWHM}/\sigma_*$ and σ_*.

To calculate the Eddington ratios for the sources in this study, it was assumed that the bolometric luminosity was related to the optical luminosity via the relation $L_{\rm Bol} = 9.8\lambda L_{5100}$ (McLure & Dunlop 2004). This correction factor was derived using the bolometric correction factor determined at 2500Å by Elvis et al. (1994), and extrapolating this to 5100Å using the slope of the mean spectral energy distribution for quasars. The Eddington luminosity $L_{\rm Edd}$ was calculated for each object using the

masses listed in Tables 3.1 and 3.2, and is given by (c.f. Equation 1.2)

$$L_{\rm Edd} = \frac{4\pi G c m_{\rm p} M_{\rm BH}}{\sigma_{\rm e}} = 1.26 \times 10^{37} \left[\frac{M_{\rm BH}}{10^6 M_\odot}\right] \quad {\rm W}. \tag{3.5}$$

Figure 3.11 shows $\sigma_{\rm FWHM}/\sigma_*$ versus the Eddington ratio $L_{\rm Bol}/L_{\rm Edd}$ for all BLS1s and NLS1s in this study. It can be seen that the NLS1s (as expected) have generally higher Eddington ratios than the BLS1s, but the correlation between the two is fairly weak, with $r_s = 0.40$ and $P_{\rm null} = 0.01$. However, the estimated Eddington ratios are expected to be highly uncertain. In particular, it has not yet been confirmed that the relationship between optical and bolometric luminosities used above provides a good estimate in the case of NLS1s. In their study, Greene & Ho (2005) concluded from their large dataset that the Eddington ratio rather than black hole mass was the driving parameter underlying the correlation between $\sigma_{\rm FWHM}/\sigma_*$ and σ_*. The results of this study do not unambiguously confirm this conclusion; however, it cannot be ruled out due to the relatively small size of the sample of AGN investigated.

3.5 Comparing σ_* in NLS1s and BLS1s

One test of the pole-on model of NLS1s is to compare directly the stellar velocity dispersions in NLS1s and BLS1s. If the pole-on model is true, and the narrow permitted lines in NLS1s are entirely as a result of orientation, then the distribution of σ_* (which is not orientation dependent) for the population of NLS1s and BLS1s should be identical. Figure 3.12 shows the σ_* distributions for the two samples. A KS test gave a probability of 6×10^{-8} that the two samples were drawn from the same distribution. This confirms that NLS1s and BLS1s are two different populations of AGN and that the pole-on model is not valid. This conclusion is unlikely to be due to selection effects. As discussed in Section 3.3 the distributions of [O III] or 5100Å luminosities are not significantly different, and the redshift range too small, for selection bias to impact this result.

A further test of the orientation model was made using two different determinations of the black hole mass, the first from using the virial relationship in Equation 3.3, and the second using the stellar velocity dispersion and the $M_{\rm BH} - \sigma_*$ relationship. If the linewidths in NLS1s are orientation-dependent, then there should be a relation-

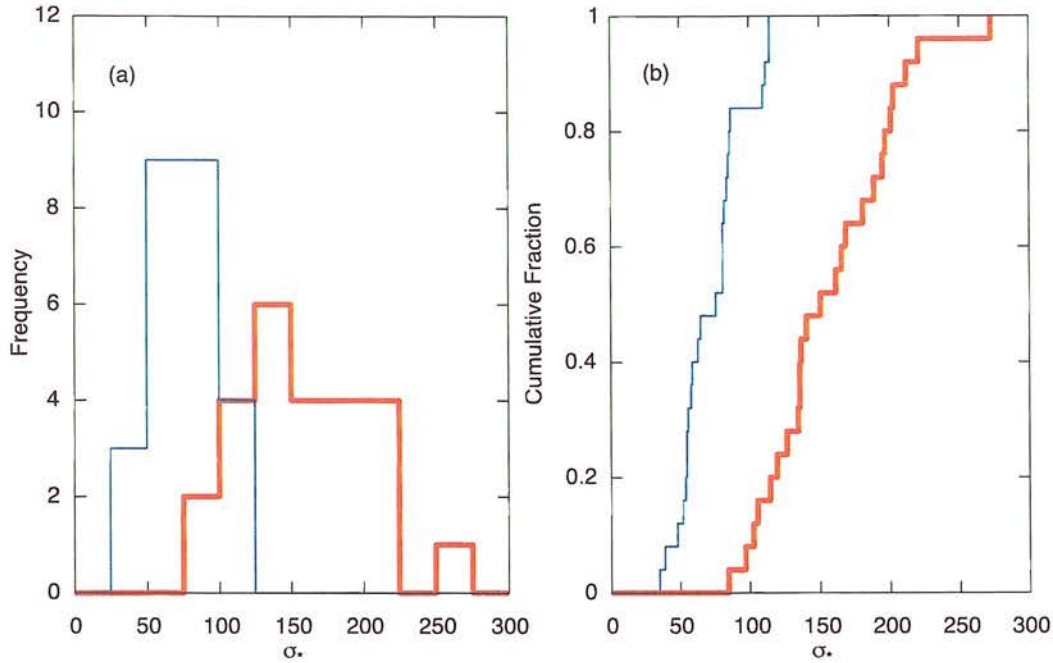

Figure 3.12: (a) The stellar velocity distributions of the NLS1 sample (blue, thin) and the BLS1 sample (red, thick). (b) The cumulative distributions of the two samples.

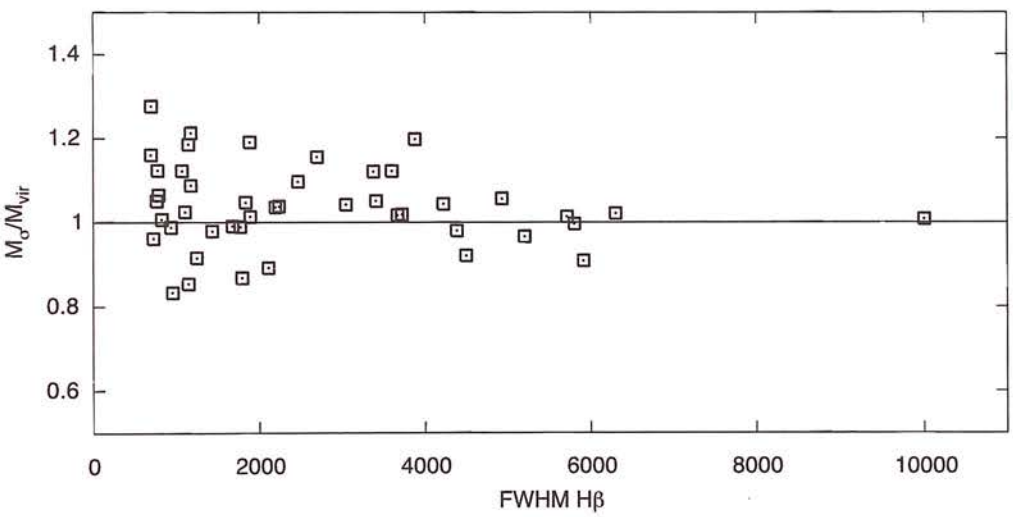

Figure 3.13: The ratio of $M_{\rm BH}$ determined from σ_* to $M_{\rm BH}$ determined from the virial relationship versus Hβ FWHM for the entire sample of NLS1s and BLS1s.

ship between the ratio of the two mass estimates and the linewidths that depends on the precise geometry of the BLR. Figure 3.13 shows the $M_\sigma/M_{\rm vir}$ ratio plotted against the FWHM of the Hβ broad component. A Spearman rank-correlation test between the two variables gives $r_s = -0.16$ and $P_{\rm null} = 0.28$, suggesting no correlation and confirming the previous conclusion that the pole-on model is not a sufficient explanation for the widths of the permitted lines in NLS1s.

3.6 NLS1s and the $M_{\rm BH}$–σ_* relation

It has not yet been confirmed whether NLS1s do lie on the $M_{\rm BH}-\sigma_*$ relation, or whether they have smaller black holes than their velocity dispersions (and hence bulge masses) would suggest. Mathur et al. (2001), Grupe & Mathur (2004) and Bian & Zhao (2004) have all found in studies that the latter conclusion appears to be true, adding weight to the hypothesis that the black holes in NLS1s are in an active growth phase and that they are analogous to the early evolution that should be occurring in high-redshift quasars. However, one thing that all of these studies have in common is their use of $\sigma_{\rm FWHM}$ as a proxy for σ_*, which is shown here to be a dangerous assumption. A study by Botte et al. (2005) that used velocity dispersions from stellar absorption lines found that NLS1s were consistent with the $M_{\rm BH} - \sigma_*$ relation, but that the scatter was significant. Barth et al. (2005) measured the stellar velocity dispersions and virial black hole masses of 15 probable NLS1s from the SDSS (see Table 3.2), and found that these also were consistent with the slope of the best-fitting $M_{\rm BH} - \sigma_*$ relation determined by Tremaine et al. (2002). Although their study did not deal specifically with NLS1s, Greene & Ho (2005) used the calibration derived between $L_{\rm Bol}/L_{\rm Edd}$ and $\sigma_{\rm FWHM}/\sigma_*$ to correct the [O III] line widths in the study by Grupe & Mathur (2004). It was found that the argument that NLS1s have systematically small black holes for their bulge masses was no longer statistically valid. The results of this study prompted Mathur & Grupe (2005) to re-examine their NLS1 data. They found that optically-selected NLS1s did in fact lie on the $M_{\rm BH} - \sigma_*$ relation, but that soft X-ray selected NLS1s were more likely to have super-Eddington accretion rates and that these did *not* lie on the relation. They concluded that if their σ_* estimates were correct, black holes in high accretion-rate, low-redshift AGN must grow quickly and thus approach the $M_{\rm BH} - \sigma_*$

relation asymptotically over the course of their active lifetimes.

The $M_{\rm BH} - \sigma_*$ relation for the objects studied here is shown in Figure 3.14. Also included are the inactive galaxies from the Tremaine et al. (2002) study and the low-luminosity Seyfert 1 galaxy NGC 4395 (see Chapter 4). The velocity dispersion for this object is taken from Filippenko & Ho (2003), and $M_{\rm BH}$ is taken from the recent reverberation mapping study by Peterson et al. (2005). The top panel of this Figure shows all objects (inactive, BLS1s and NLS1s) plotted without distinguishing between the different types. The best-fitting relation to only the inactive galaxy sample from Tremaine et al. (2002) is plotted, together with the best-fitting relation for all objects. The sample was fitted using an iterative fitting routine that takes into account uncertainties in both variables (FITEXY; see Press et al. 1992). An error of 0.4 dex was used as the uncertainty on the single-epoch virial mass estimates, and is that quoted in the McLure & Jarvis (2002) study. The slope of the best-fitting relation was 4.35 ± 0.25, slightly steeper than the 4.02 ± 0.3 found by Tremaine et al. (2002), but the two are clearly consistent within the uncertainties. The bottom-left panel of Figure 3.14 shows that the samples from the three sources do not show systematic offsets with respect to each other. The bottom-right panel shows the objects separated according to AGN type. There is no evidence from this Figure that NLS1s lie systematically below the $M_{\rm BH} - \sigma_*$ relationship. The objects observed for this study were specifically selected to include a number of (low redshift) soft X-ray selected NLS1s from the *ROSAT* sample of Boller et al. (1996). It was only possible to extract stellar velocity dispersion information for two of these (Mrk 359 and Mrk 493), but two others (Mrk 766 and Mrk 896) were available from the literature. The mean photon index for these objects (from Boller et al. 1996) is 2.55. Only one of these objects (Mrk 359) lies more than 2σ from the best-fitting relationship; however, it is not clear whether these objects represent the high Eddington-ratio objects sampled by Mathur & Grupe (2005).

3.6.1 The scatter in the $M_{\rm BH} - \sigma_*$ relation

The two AGN samples show a larger scatter around the $M_{\rm BH} - \sigma_*$ relation than the inactive galaxies. One probable source of this is the relative inaccuracy of $M_{\rm BH}$ measurements for AGN by comparison with nearby inactive galaxies, for which detailed

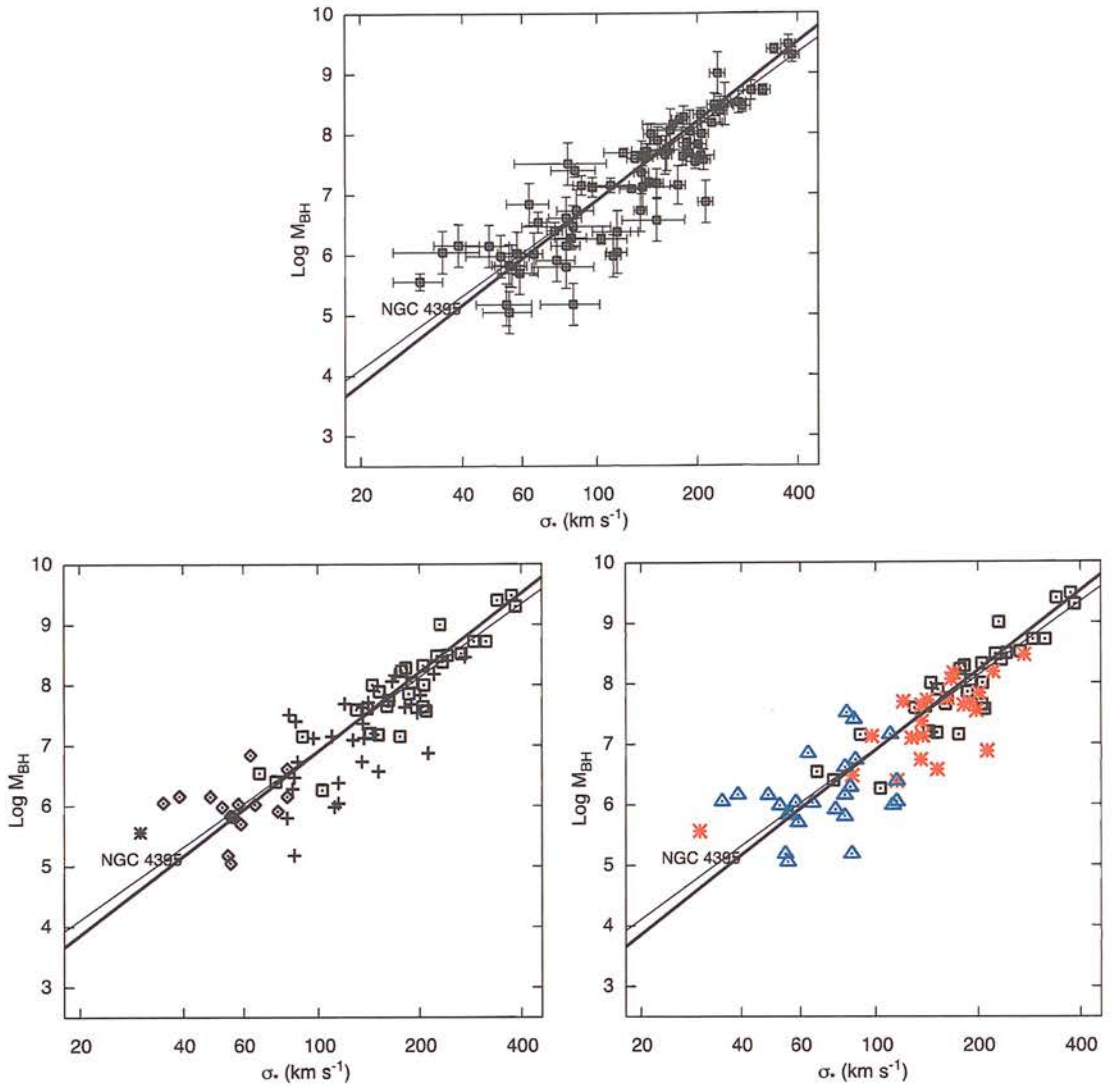

Figure 3.14: Stellar velocity dispersion σ_* versus $M_{\rm BH}$ measurements from either reverberation mapping or virial methods. The top panel shows the results for all objects collected from the literature, together with their uncertainties. The bottom left panel shows the inactive galaxies from Tremaine et al. (2002) (open boxes), the NLS1s from Barth et al. (2005) (open diamonds) and the samples of NLS1s and BLS1s listed in Tables 3.1 and 3.2 (plusses). The bottom right-hand panel shows these split into inactive galaxies (black, open boxes), BLS1s (red, stars) and NLS1s (blue, open triangles). The errorbars have been left out in the latter two cases to allow the different samples to be more easily distinguished. The best-fitting relation found by Tremaine et al. (2002) (thin line) and this study (thick line) are also plotted in each panel.

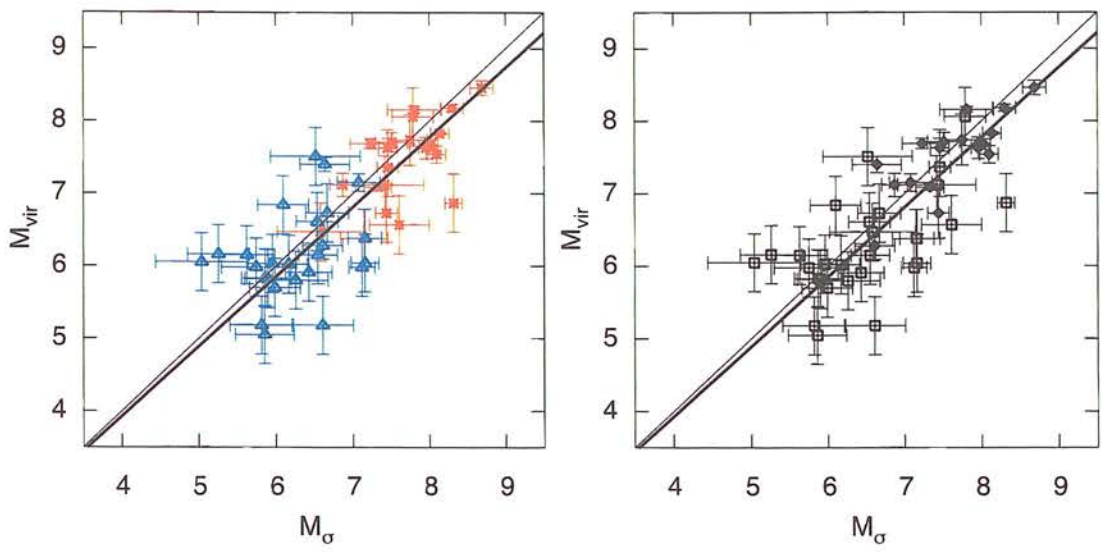

Figure 3.15: Masses calculated using the $M_{\rm BH}$–σ_* relation (M_σ) versus masses calculated using the virial relationship from McLure & Jarvis (2002) ($M_{\rm vir}$). (Left panel) $M_{\rm vir}$ vs M_σ for BLS1s (red stars) and NLS1s (blue triangles). (Right panel) The $M_{\rm vir}$ vs M_σ relation for virial masses determined from reverberation mapping (diamonds) and single-epoch measurements (boxes). The two solid lines are the 1:1 relation (thin) and best fit (thick).

dynamical modelling is possible. Many of the AGN estimates used here came from single-epoch virial measurements using the relationship from Equation 3.3, which is known to include significant uncertainties when used for small samples of objects. The stellar velocity dispersion was used to calculate the black hole mass using the best-fitting relationship from Tremaine et al. (2002), which is shown plotted against the virial masses from either reverberation mapping or Equation 3.3. The two quantities are strongly correlated, with $r_s = 0.79$ and $P_{\rm null} < 10^{-10}$. The best-fitting linear relation, taking into account uncertainties in both variables, gave a slope of 0.96 ± 0.06 with $\chi^2/{\rm d.o.f} = 1.9$. The left-hand panel of Figure 3.15 seems to indicate that NLS1s show a larger scatter than BLS1s. Single-epoch measurements were used for a larger fraction of the NLS1 sample, however, so the two groups were then split according to the method used to estimate $M_{\rm BH}$ (Figure 3.15, right panel). This shows that the scatter resulting from single-epoch measurements could account for much of the scatter in the $M_{\rm BH} - \sigma_*$ relation.

CHAPTER 4

The Optical Variability of NGC 4395

4.1 Introduction

NGC 4395 is a nearby, late-type spiral galaxy of morphological type Sd III-IV. It exhibits a very low surface-brightness disc, with almost no central bulge and loose spiral arms showing some isolated regions of star formation. Optical spectra of the faint, star-like nucleus reveal strong, narrow forbidden emission lines from a wide range of species and ionization, as well as weak broad wings on permitted lines. Filippenko & Sargent (1989) interpreted these observations as an indication that NGC 4395 harboured an extremely low-luminosity Seyfert 1 nucleus. Subsequent multiwavelength observations (Sramek 1992; Filippenko et al. 1993) confirmed this classification and convincingly argued against other origins for the observed non-stellar emission. With an absolute blue magnitude of ~ -11, the nucleus of NGC 4395 has a lower luminosity than the brightest supergiant stars, and is a factor of $\sim 10^4$ fainter than even low-luminosity classical Seyfert 1s such as NGC 4051, making it the least-luminous Seyfert 1 discovered to date.

There are two likely possibilities for the very low luminosity nucleus in NGC 4395. One is a low accretion rate, in line with other low-luminosity AGN (Ptak et al. 1998). The other is that the central supermassive black hole is significantly smaller than in more luminous AGN, with a relative accretion rate that is more typical of classical

Seyferts giving rise to the observed properties of NGC 4395. Given that NGC 4395 is a small late-type spiral with a very low-luminosity bulge component, a small central black hole is consistent with the observed correlation between bulge mass and black hole mass (Ferrarese & Merritt 2000; Gebhardt et al. 2000a). Several estimates of the black hole mass in NGC 4395 have been made. A firm upper limit of $6.2 \times 10^6 M_\odot$ has been placed by Filippenko & Ho (2003) using velocity dispersion analysis of the Ca II near-IR triplet. However, this is a measure of the virial mass of the entire nuclear stellar cluster and the mass of the actual black hole could be considerably smaller. Estimates using photoionization modelling of the broad-line region (Kraemer et al. 1999) and from power-law fitting to the fluctuation power density spectrum (Shih et al. 2003) give consistent estimates in the region $10^4 - 10^5 M_\odot$. These values are lower by several orders of magnitude than those found in other typical Seyfert galaxies, and while neither of these methods is particularly accurate, it is encouraging that the estimates are consistent with one another.

One test of the size of the central engine in NGC 4395 is fast multiwavelength variability. Smaller scale-lengths imply that the light- and sound-crossing time-scales should be shorter, leading to variability on short time-scales. An early optical monitoring campaign over several years by Shields & Filippenko (1992) reported that NGC 4395 showed no variability in either the broad lines or the continuum. However, a subsequent spectroscopic study by Lira et al. (1999) found continuum variability over a time-scale of 6 months of factors of order 2 and 1.3 in the blue and red respectively. Variability in the broad lines was also found, although with a smaller amplitude than that seen in the continuum. Lira et al. (1999) also analysed broadband photometric images (B and I bands) and detected variability of order 20 per cent between nights. Optical spectroscopic data on NGC 4395 had also been obtained over a number of years at Lick Observatory (Kraemer et al. 1999). When these data were investigated to determine whether they showed variability similar to that seen by Lira et al. (1999), they found no evidence of the factor of 2 variations but more modest variability could not be ruled out (Moran et al. 1999).

A well-studied correlation is seen to exist between the amplitude of the variability in X-rays and the intrinsic luminosity of the nucleus for local AGN (Nandra et al. 1997;

Turner et al. 1999; Almaini et al. 2000; Manners et al. 2002), showing that higher luminosity AGN exhibit lower amplitude variability. In contrast, many low-luminosity AGN (typical X-ray luminosity $0.4 - 60 \times 10^{33}$ W) in nearby large galaxies show very little variability in X-rays, which has been interpreted as evidence for an inefficient accretion process such as an advection-dominated accretion flow (Ptak et al. 1998). NGC 4395 has been well studied at X-ray wavelengths and fast, large amplitude variability has been observed in this object. Lira et al. (1999) found variability of about a factor of 2 over a time-scale of 15 days from *ROSAT* PSPC (0.1-2.4 keV) data. Such variability is not particularly fast for Seyfert 1 AGN. However, subsequent variability studies with better sensitivity and time resolution in the harder 2-10 keV band using *ASCA* found X-ray flux changes on time-scales of about 100 seconds to 12 hours, with the shortest doubling time-scale found to be of order 100 s (Iwasawa et al. 2000). Follow-up *ASCA* observations (Shih et al. 2003) confirmed the earlier findings and estimated the power density spectrum in the 1.2-10 keV and 2-10 keV bands, with the possible detection of a break in the best-fitting power-law. These findings suggest that, while other dwarf Seyferts may have normal-size central engines but radiatively inefficient accretion processes, NGC 4395 is accreting at a normal fraction of the Eddington limit but genuinely contains a small central engine when compared to other classical Seyfert 1s.

To test the hypothesis that the Seyfert nucleus in NGC 4395 contains a small central black hole, optical spectroscopic observations of NGC 4395 were undertaken with the aim of monitoring the nuclear region every ~30 minutes for several consecutive nights. The motives for this study were several; firstly, it was important to check whether the short time-scale variability observed in the broadband optical observations of Lira et al. (1999) was characteristic of NGC 4395 or a freak event, and secondly it was necessary to determine whether the variability seen in NGC 4395 had different characteristics to classical Seyfert 1s, in both amplitude and time-scale. Although the absolute flux calibration of spectroscopic observations is often less accurate than for broadband photometry, a careful observing procedure can reduce the uncertainties and allow quantitative statements to be made. The spectroscopic observations had two advantages; if rapid continuum variability was observed, it could be determined (1) whether there was a corresponding colour change and (2) whether any simultane-

ous variability was seen in the broad lines. If broad line variability was seen, it was hoped that the time sampling of the observations would allow any lag between the continuum and line variations to be estimated, thus determining whether the size of the broad-line region scales with luminosity (Peterson et al. 2000). In this Chapter the reduction and analysis of the spectroscopic data are discussed and the detection of optical variability on time-scales of $\sim$8 hours is reported. In the following two Sections the observations and reduction of the optical spectra are presented. Following this the analysis procedure and checks that were carried out to determine whether the observed variability was due to systematic or atmospheric effects are discussed in detail. The results are discussed with respect to other well-studied AGN and the implications for models of nuclear regions in active galaxies are also included.

4.2 Observations

The observations for the NGC 4395 monitoring project were undertaken prior to the assumption of this PhD research studentship by A. Lawrence. Here I give a description of the procedure that was followed. Spectra of the nuclear region of NGC 4395 were obtained on 1998 March 17-20 using the 2.5-m *Isaac Newton Telescope* (*INT*) at the Roque de los Muchachos Observatory. A TEK 1024 $\times$ 1024 CCD was used together with a R300V grating. The CCD was windowed to give a scale of 0.7 arcsec pixel^{-1} in the spatial direction and the central wavelength of the observations was 5135Å, giving a dispersion of 3.32Å pixel^{-1} over a wavelength range of $\sim$3500 $-$ 6900Å.

In order to detect spectral variations of the order of 20 per cent, a meticulous observing strategy was required, since the standard procedure rarely results in better than 30 per cent accuracy in the absolute flux calibration. The aim of this study was for an accuracy of $\sim$5 per cent, and to realise this the following procedure was implemented.

NGC 4395 was visible at an elevation of $> 30^{o}$ for the entirety of the four nights. Conditions were cloudless for 3 of the 4 nights. The data from night 4 were affected by the presence of high cirrus for part of the night and were later scrapped. The slit width was alternated between 2 and 8 arcseconds, giving separate interleaved sets of observations of NGC 4395, with a sampling interval of approximately 30 minutes in

both cases. In all observations the slit was positioned at the parallactic angle to prevent light losses due to differential refraction through the atmosphere. The use of two slit widths allowed a number of systematic effects to be corrected for or eliminated entirely. The 2 arcsec slit was used to reduce the contribution of the host galaxy starlight in each spectrum, while the 8 arcsec slit was used to minimize aperture effects due to variable seeing conditions, poor centring of the object in the slit and the possibility that the narrow-line region was resolved. This last point is unlikely; analysis of *HST* images by both Filippenko et al. (1993) and Lira et al. (1999) found that the nucleus of NGC 4395 had an intrinsic FWHM of less than 0.05 arcsec. Seeing conditions were never better than 1 arcsec during these observations, and so the resolution of the NLR was not a serious consideration in this case. Each NGC 4395 observation was bracketed by observations of photometric standard stars (each observed using both slits at all times). These allowed any variations in both the seeing conditions and atmospheric extinction to be quantified and if necessary corrected for. Bias frames, tungsten flats and twilight sky flats were taken at the beginning and end of each night. A log of the NGC 4395 observations is given in Table 4.1.

4.3 Data reduction

The first section of the data reduction was performed by A. Pappa, between March 1998 and September 2002. Special care was taken to remove all vignetting effects and other illumination problems from the spectra to obtain the best possible accuracy during the flux calibration. Therefore I first describe the stages performed prior to my involvement as these are crucial to this project.

The data were reduced using IRAF software routines, and bias correction was performed in the standard way described in Chapter 2. Pixel-to-pixel gain variations were removed using tungsten lamp spectra, which were observed to contain vignetting effects. It was decided to correct these effects using spectra of the twilight sky, as the optical light path for these frames was the same as for the spectra of NGC 4395 itself. Therefore the tungsten spectrum was first smoothed using a median filter designed to smooth the gain variations but preserve the vignetting features. The unsmoothed flat was then divided through by the smoothed version to produce a flat field that con-

Table 4.1: Journal of NGC 4395 observations. Column (1) gives the Julian Date, column (2) the slit width (in arcsec) and column (3) the exposure time. Column (4) gives the parallactic angle in degrees and column (5) the airmass at the midpoint of each observation.

JD +2450800	SW	Exp (s)	PA	Airmass	JD +2450800	SW	Exp (s)	PA	Airmass
		Night 1					Night 2, Continued		
90.3959	2	500	104.5	1.791	91.6016	2	1000	121.5	1.012
90.4022	2	500	103.6	1.711	91.6116	8	200	111.1	1.021
90.4090	8	100	102.6	1.633	91.6256	2	1000	103.4	1.039
90.4233	2	1000	100.4	1.496	91.6337	8	200	100.0	1.051
90.4312	8	200	99.2	1.431	91.6474	2	1000	95.8	1.079
90.4453	2	1000	97.0	1.335	91.6552	8	200	93.7	1.098
90.4544	8	200	95.6	1.283	91.6684	2	1000	90.8	1.137
90.4681	2	1000	93.2	1.216	91.6762	8	200	89.2	1.163
90.4761	8	200	91.8	1.183	91.6891	2	1000	86.8	1.215
90.4896	2	1000	89.2	1.135	91.6969	8	200	85.5	1.250
90.4995	8	200	87.0	1.106	91.7025	2	1000	83.4	1.319
90.5125	2	1000	83.6	1.074	91.7175	8	200	82.2	1.368
90.5204	8	200	81.3	1.058	91.7293	2	1000	80.4	1.454
90.5336	2	1000	75.9	1.036	91.7370	8	200	79.2	1.519
90.5429	8	200	71.0	1.024	91.7503	2	1000	77.2	1.652
90.5562	2	1000	58.3	1.012	91.7581	8	200	77.2	1.744
90.5642	8	200	47.3	1.007	91.7676	2	1000	74.6	1.875
90.5763	2	1000	12.8	1.004	91.7725	8	200	73.9	1.952
90.5842	8	200	165.1	1.004					
90.5972	2	1000	132.5	1.008			Night 3		
90.6053	8	200	119.3	1.013					
90.6765	2	500	89.7	1.154	92.4082	2	1000	101.9	1.586
90.6828	2	500	88.5	1.177	92.4262	8	200	99.1	1.428
90.6880	8	200	87.5	1.198	92.4438	2	1000	96.4	1.312
90.7000	2	1000	85.4	1.253	92.4516	8	200	95.1	1.269
90.7080	8	200	84.1	1.294	92.4644	2	1000	92.9	1.209
90.7200	2	1000	82.2	1.368	92.4724	8	200	91.5	1.176
90.7279	8	200	81.0	1.422	92.4856	2	1000	88.8	1.131
90.7398	2	1000	79.2	1.520	92.4934	8	200	87.2	1.107
90.7475	8	200	78.0	1.592	92.5086	2	1000	83.2	1.071
90.7565	2	500	76.7	1.691	92.5164	8	200	80.8	1.055
90.7628	2	500	75.8	1.769	92.5301	2	1000	74.9	1.033
90.7677	8	150	75.0	1.835	92.5381	8	200	70.6	1.023
90.7701	2	100	74.7	1.870	92.5513	2	1000	57.6	1.012
					92.5592	8	200	46.4	1.007
		Night 2			92.5735	2	1000	4.2	1.004
					92.5813	8	200	156.5	1.004
91.3987	2	1000	103.7	1.721	92.5939	2	1000	128.8	1.009
91.4065	8	200	102.5	1.630	92.6016	8	200	117.5	1.014
91.4235	2	1000	100.0	1.471	92.6145	2	1000	107.9	1.027
91.4313	8	200	98.8	1.410	92.6222	8	200	103.5	1.037
91.4455	2	1000	96.6	1.318	92.6363	2	1000	98.3	1.061
91.4534	8	200	95.3	1.274	92.6441	8	200	95.9	1.078
91.4667	2	1000	93.0	1.211	92.6573	2	1000	92.6	1.111
91.4746	8	200	91.6	1.178	92.6650	8	200	90.9	1.134
91.4918	2	1000	88.1	1.120	92.6792	2	1000	88.1	1.185
91.4998	8	200	86.3	1.098	92.6870	8	200	86.7	1.217
91.5203	2	1000	80.3	1.053	92.7002	2	1000	84.5	1.282
91.5284	8	200	77.2	1.039	92.7079	8	200	83.2	1.325
91.5421	2	1000	69.3	1.022	92.7245	2	1000	80.7	1.439
91.5499	8	200	63.3	1.015	92.7324	8	200	79.5	1.502
91.5623	2	1000	43.8	1.007	92.7452	2	1000	77.6	1.626
91.5701	8	200	25.9	1.004	92.7531	8	200	76.4	1.716
91.5822	2	1000	164.4	1.004	92.7661	2	1000	74.4	1.895
91.5900	8	200	140.0	1.006	92.7723	8	200	73.5	1.994

tained information about the pixel-to-pixel variations but no information about the vignetting. Each twilight sky and NGC 4395 spectrum was divided through by this frame. The vignetting effects were then removed from the NGC 4395 spectrum by dividing through by the processed twilight sky frame that containing the vignetting information.

For wavelength calibration, a low-order polynomial function was fitted to strong lines in a copper-argon comparison spectrum. The precision of the fit was improved by including intermediate lines once a rough determination of the dispersion solution had been found. Dispersion solutions were found every 35 arcsec (50 pixels) along the slit and 6th-order Chebyshev polynomials were fitted to these solutions to correct any geometrical distortions. To remove the sky background, a low-order cubic spline function was fitted along the spatial axis of each spectrum and then subtracted. One-dimensional spectra were extracted using a $\sim$5 arcsec aperture designed to minimize any contributions from the host galaxy, including nearby H II regions. Lira et al. (1999) estimated the contamination from host galaxy starlight to be at most 10 per cent from measurements of the equivalent width of the ultraviolet Ca II line.

Flux calibration of the extracted NGC 4395 spectra was initially performed in the standard way by Dr. Pappa. Spectrophotometric standard stars were used to determine the sensitivity of the detector over the entire wavelength range. The standard stars used were Feige 34, G191-B2B and HZ44 from Massey et al. (1988), together with BD75+325 and HZ21 from Oke (1990). The standard extinction curve for the Roque de los Muchachos observatory was used to perform the extinction correction[1]. For each NGC 4395 observation the sensitivity function was constructed using the standard star observations closest in time and using the same slit width. Since a $\sim$5 per cent accuracy was desired, in order to ensure that the extinction correction had been applied correctly I then applied the standard extinction correction to each standard star observation, and then measured the counts sec^{-1} Jy^{-1} at 5500Å (Johnson V). Significant variations were seen in the derived calibration both within a night and on a night-to-night basis. To correct for the night-to-night variations, a grey shift correction was applied to all spectra (including both spectrophotometric standards and NGC 4395

[1]See http://www.ing.iac.es/Astronomy/observing/ manuals/ps/tech_notes/tn031.pdf

observations) based on measurements made on-site by the *Carlsberg Meridian Telescope* (*CMT*). The grey shifts for the three nights were 0.30, 0.20 and 0.13 magnitudes respectively.

To correct for atmospheric variations within each night, the following procedure was implemented. First, the standard star observations taken with the 8 arcsec slit width were corrected to first order using the data from the CMT and the counts sec^{-1} Jy^{-1} for each observation were measured. This was done at several different wavelengths to check that any intra-night variations were grey, as shown in Figure 4.1. The mean of all measurements (at one wavelength) was found and the magnitude shift required to bring each observation to the mean value calculated. The 8 arcsec slit data was used for this purpose because due to the large slit width it was likely that any variations seen were solely due to variations in atmospheric transparency and *not* due to other effects such as seeing changes. The magnitude shifts required to apply the same second-order correction to the NGC 4395 data (both 2 and 8 arcsec slit widths) were then calculated by interpolating between the 8 arcsec standard star observations, and individual extinction curves were constructed for each observation. The flux calibration was then repeated using a global sensitivity function calculated for each night and the separate extinction curves. The procedure followed here assumes that the transparency trends seen in the standard stars are also followed by NGC 4395. The smoothness of the trends suggests this is correct. Any remaining small time-scale transparency fluctuations could produce errors in the derived light curves of NGC 4395. The magnitude of these uncertainties was estimated by fitting straight lines to the data for each night in Figure 4.1, and then calculating the residual variations. This showed that any such short time-scale transparency variations are less than 5 per cent (2σ).

The combined spectrum using the 2 arcsec data is shown in Figure 4.2. This has extremely high signal-to-noise and many weak lines can be clearly seen. Most of the structure visible in the lower panel of Figure 4.2 is real rather than noise.

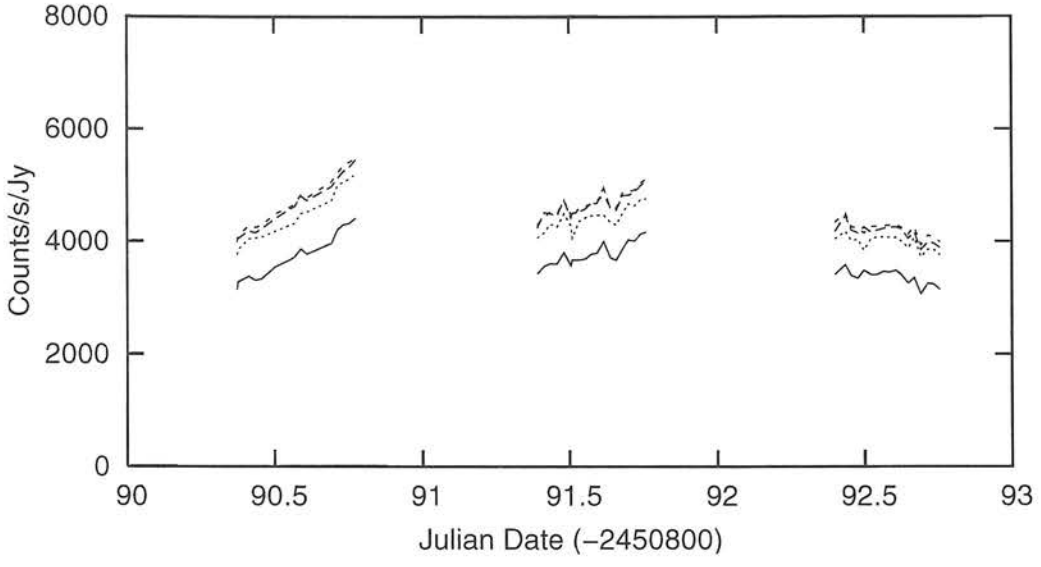

Figure 4.1: The variation in counts sec^{-1} Jy^{-1} over the three photometric nights for the standard stars observed using the 8 arcsec slit. To ensure that any variations were grey, measurements were made at four wavelengths: 4000Å (solid line), 4500Å (short dashes), 5500Å (long dashes) and 6200Å (dotted).

4.4 Analysis and Results

4.4.1 Procedure

The continuum variability of NGC 4395 has been examined in two ways. First, using the absolute flux calibration described above, including the second-order transparency corrections, and second, by measuring the equivalent widths of narrow lines, which is expected to be particularly reliable. If the size of the narrow-line region is of order ~10 pc (Filippenko et al. 1993), this gives a light-crossing time in excess of 30 years, and so significant variability in the narrow lines would not be expected on time-scales of hours or days. If this is the case, then measurements of the narrow line equivalent widths give a direct measurement of any continuum variability. A further advantage of this technique is that in the absence of systematic effects the EQW is independent of the absolute flux calibration, and so the principal sources of uncertainty will be the accuracies to which it is possible to measure the relative line and continuum fluxes. Possible sources of systematic errors and aperture effects in the NGC 4395 data have been investigated and are discussed in the next Section.

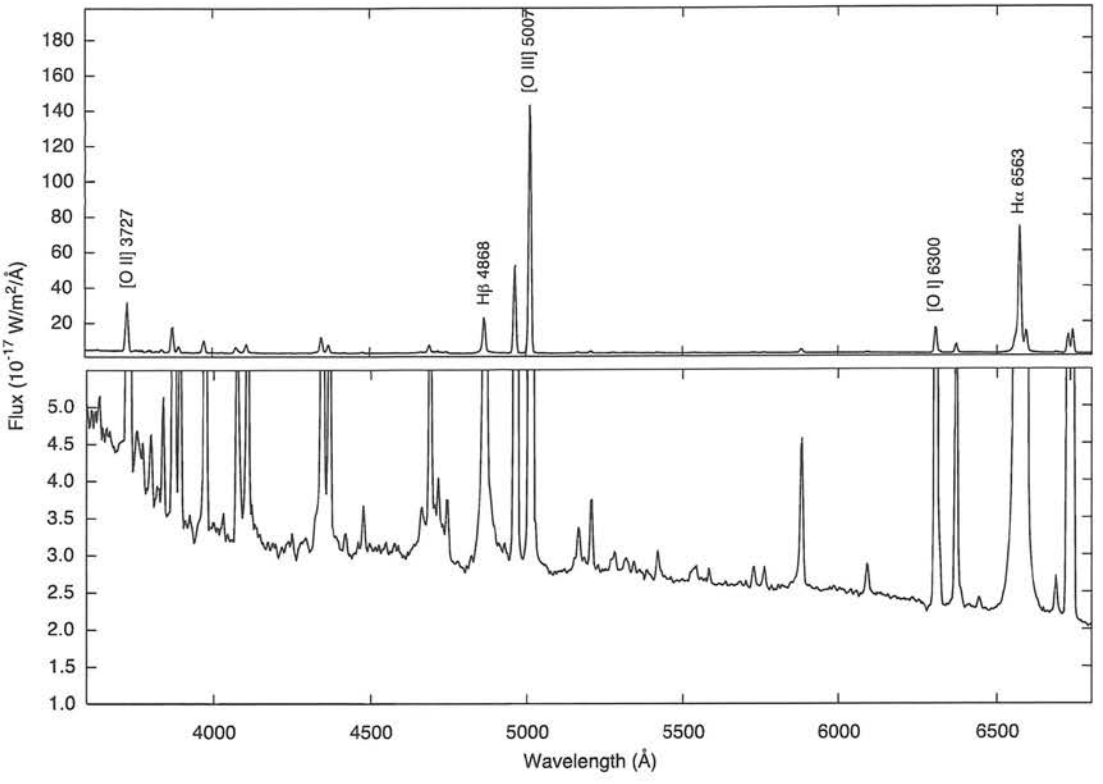

Figure 4.2: Averaged spectrum for all observations taken using the 2 arcsec slit. The bottom panel has an expanded flux scale showing the low S/N lines.

The equivalent widths were obtained by fitting low-order polynomial functions to the continuum region under the emission lines, and then fitting Gaussian profiles to the emission lines themselves. The emission lines selected were [O II] 3727Å, [O III] 5007Å and [O I] 6300Å. These lines were selected because they were the strongest unblended lines in the blue, green and red regions of the spectrum. Several wavelength regions were required to allow differences in variability with colour to be quantified. To measure the continuum flux, co-ordinate ranges close to the relevant emission line were selected that would result in the least contamination of the fit by low signal-to-noise emission lines, and a polynomial of order zero or one was fitted to these co-ordinate ranges. The actual fitting order to be used was determined by eye. A Gaussian function was then fitted to the emission line to obtain the narrow line flux and hence the equivalent width.

The largest uncertainty in the equivalent widths arises from the continuum flux

measurement, particularly for the [O II] 3727Å line which has the poorest signal-to-noise ratio in both the 2 arcsec and 8 arcsec slit data-sets. Two methods were used to quantify this error. First, the continuum fit was manually constrained to lie some distance away from the actual best-fitting value, and the effect upon the equivalent width measurement observed. Secondly, the co-ordinate ranges used for the fitting were changed by small amounts, thus varying the contribution from any low signal-to-noise emission lines, and again the effect upon the equivalent widths was determined. The actual uncertainty in the measurement is likely to lie somewhere between these two values, with the fractional error being slightly larger for the [O II] 3727Å line than either of the other two lines.

Table 4.2 gives 51 measurements for the equivalent widths and the continuum and line fluxes for the [O III] 5007Å and [O I] 6300Å emission lines, as measured from the 2 arcsec slit data. There are only 50 measurements for the [O II] 3727Å line, since the signal-to-noise ratio of the last observation on night 1 was too poor in the blue end to allow the measurements to be made. Table 4.3 contains the measurements made using data from the 8 arcsec slit measurements. There are 48 measurements for both the [O III] 5007Å and [O I] 6300Å lines, but similarly only 47 for the [O II] 3727Å line. The final light curves produced from these data are shown in Figures 4.3 (2 arcsec slit) and 4.4 (8 arcsec slit). To allow the measurements from the different emission lines to be compared directly, all light curves have been scaled using the mean equivalent width for each line.

Measurements of the Hβ line flux were also carried out, and a similar procedure to that described in Lira et al. (1999) was followed. First, the zero and slope of the continuum region under the Hβ line were determined by eye, and then these parameters were fixed during the fitting process. The line itself was fitted using two Gaussians. The narrow component of the line was fitted using a Gaussian of fixed instrumental width determined from the nearby narrow lines, with the amplitude and centre as free parameters. The broad component was fitted using a Gaussian in which the amplitude, width and centre were all free parameters. This procedure was only possible for the 2 arcsec slit data, since the poorer signal-to-noise of the 8 arcsec slit data due to starlight contamination from the host galaxy meant that it was difficult to distinguish

the weak broad wings on the Hβ line from the continuum. The measured narrow- and broad-component fluxes are given in columns (11) and (12) of Table 4.2. An example fit and residuals is shown in Figure 4.5. The measured FWHM for the narrow and broad components were $\sim$250 km s^{-1} (fixed using the instrumental resolution) and $\sim$1800 km s^{-1} respectively. Previous studies give values of $\lesssim$ 50 km s^{-1} for the narrow component using high-resolution spectroscopy (Filippenko & Sargent 1989), and $\sim$1500 km s^{-1}for the broad component (Kraemer et al. 1999).

4.4.2 Diagnostic Checks

Figures 4.3 and 4.4 show short time-scale variations of the nucleus of NGC 4395 throughout all 3 nights. In order to determine whether these variations were real intrinsic variations of the source or due to aperture or systematic effects a number of diagnostic checks were implemented.

Although NGC 4395 is a very low surface-brightness galaxy, it nonetheless shows a number of isolated knots of star formation and H II regions. Since the slit was positioned always at the parallactic angle, this resulted in the position angle of the slit relative to the galaxy rotating over the course of the night's observations. Over the course of the observations, therefore, the inclusion and exclusion of any host galaxy features within the slit would have varied. To combat this, a narrow aperture was used during the extraction procedure, rather than performing an optimal extraction using a weighted function over the entire spatial axis. To check whether any emission from extended regions had been inadvertently included in the extraction aperture in spite of the precautions that were taken, a small ($\sim$20 pixels) section of the spectral axis covering the [O III] 5007Å line of each 2-dimensional spectrum was summed and then checked to see whether there had been any contamination by nearby features such as H II regions. No variable contamination was found.

To double-check this, the equivalent widths, line fluxes and continuum fluxes were plotted versus the slit PA to check for correlations (Figure 4.6). No correlations are seen with any of these variables, and so we are confident that any observed variability does not arise from variable contributions from H II or star-forming regions. The lack of correlations *also* rules out variability resulting from changing ellipticity of the host

Table 4.2: Equivalent width, line flux and continuum flux measurements for the 2 arcsec slit data.

JD	[O II] λ3727Å			[O III] λ5007Å			[O I] λ6300Å			Hβ	
+2450800	EQW	Line[1]	Cont[2]	EQW	Line	Cont	EQW	Line	Cont	Narrow	Broad
90.3959311	58.6	4.558	7.775	469	22.80	4.861	57.7	2.325	4.027	1.827	0.935
90.4022447	64.8	4.946	7.637	463	23.95	5.168	58.7	2.487	4.235	2.005	0.910
90.4233443	63.8	5.726	8.974	468	28.42	6.075	59.8	2.914	4.869	2.400	1.002
90.4453813	66.3	5.463	8.243	461	25.60	5.551	61.8	2.538	4.108	2.085	1.071
90.4681417	61.7	5.674	9.195	456	27.15	5.957	57.5	2.823	4.912	2.189	0.949
90.4896174	53.0	5.645	10.65	444	29.69	6.694	57.5	3.156	5.491	2.424	1.058
90.5125167	49.0	5.326	10.86	400	26.81	6.703	57.1	3.111	5.451	2.485	1.054
90.5336336	50.8	4.950	9.738	422	26.82	6.359	57.5	3.007	5.232	2.440	0.980
90.5562956	57.3	5.374	9.374	441	28.37	6.426	59.4	3.189	5.366	2.505	1.066
90.5763477	57.8	5.267	9.105	435	26.73	6.147	58.3	2.979	5.110	2.401	0.980
90.5972456	63.6	4.924	7.748	482	26.67	5.533	61.0	3.116	5.111	2.276	0.965
90.6765387	67.0	6.263	9.353	483	27.74	5.748	63.6	2.864	4.500	2.363	0.951
90.6828755	68.4	5.857	8.559	493	27.23	5.527	62.1	2.745	4.421	2.181	1.103
90.7000862	62.7	5.737	9.152	490	28.36	5.788	64.0	2.932	4.584	2.426	1.008
90.7200977	59.0	5.479	9.280	485	29.07	5.994	63.3	2.927	4.625	2.471	1.110
90.7398720	63.8	5.763	9.030	460	27.22	5.915	59.9	2.828	4.725	2.225	1.093
90.7565387	63.9	5.343	8.362	441	23.49	5.329	58.7	2.462	4.195	1.889	0.991
90.7628350	56.0	5.432	9.693	459	24.89	5.419	59.8	2.606	4.360	1.950	1.032
90.7701035				435	23.33	5.386	55.2	2.416	4.373		
91.3987031	61.0	3.997	6.556	402	19.84	4.937	55.9	2.429	4.343	1.815	0.935
91.4235642	57.9	5.038	8.708	442	25.25	5.716	57.7	2.699	4.674	2.122	1.018
91.4455433	57.8	5.008	8.670	447	24.99	5.592	60.0	2.581	4.304	2.230	1.001
91.4667008	49.8	4.504	9.042	437	25.82	5.906	57.4	2.628	4.593	2.246	1.058
91.4918165	47.4	4.521	9.543	411	24.81	6.042	58.2	2.705	4.646	2.294	1.041
91.5203003	57.6	5.430	9.421	432	26.20	6.066	55.9	2.704	4.840	2.259	1.083
91.5421116	50.4	4.608	9.140	418	24.06	5.758	54.3	2.396	4.415	2.221	1.083
91.5623142	55.8	5.045	9.048	437	24.82	5.679	57.6	2.450	4.256	2.246	1.038
91.5822621	52.9	4.834	9.141	466	27.06	5.810	60.5	2.711	4.481	2.433	0.946
91.6016718	55.1	4.786	8.692	452	25.34	5.603	60.2	2.865	4.757	2.227	1.001
91.6256822	58.2	4.885	8.390	435	24.74	5.692	61.5	2.898	4.715	2.196	1.045
91.6474646	54.4	4.824	8.861	428	23.29	5.443	59.3	2.619	4.417	2.215	1.030
91.6684774	57.1	5.483	9.601	478	29.28	6.121	61.5	3.029	4.923	2.564	1.080
91.6891660	58.8	5.159	8.769	485	26.28	5.417	64.2	2.802	4.362	2.239	1.024
91.7096753	66.8	4.850	7.263	476	23.58	4.957	64.3	2.568	3.995	2.011	0.983
91.7293165	62.3	5.259	8.436	472	27.07	5.736	64.8	3.065	4.733	2.205	1.138
91.7503119	58.5	4.916	8.399	462	24.80	5.368	59.1	2.599	4.399	2.097	0.957
92.4082054	60.1	5.293	8.799	439	26.54	6.049	54.1	2.827	5.223	2.232	1.075
92.4438362	57.2	5.267	9.203	437	26.89	6.152	58.3	2.944	5.049	2.513	1.103
92.4644959	52.1	5.063	9.714	461	28.51	6.181	62.6	2.999	4.792	2.633	1.216
92.4856764	56.2	5.014	8.914	487	27.28	5.598	61.4	2.848	4.636	2.513	1.072
92.5086510	56.3	4.930	8.763	500	27.79	5.563	65.0	2.946	4.531	2.556	1.086
92.5301961	62.7	5.185	8.275	523	28.85	5.514	65.6	2.905	4.431	2.549	1.045
92.5513535	65.0	5.152	7.929	546	29.13	5.334	64.7	2.827	4.372	2.690	1.081
92.5735642	72.8	5.080	6.979	555	26.85	4.752	68.6	2.700	3.934	2.360	1.006
92.5939288	69.1	5.268	7.627	573	29.02	5.065	67.9	2.860	4.214	2.476	1.041
92.6145017	71.8	5.686	7.918	579	29.87	5.157	73.0	3.036	4.161	2.504	1.043
92.6363651	80.9	6.584	8.140	559	31.49	5.635	71.4	3.232	4.524	2.682	1.092
92.6573258	87.1	6.006	6.893	574	27.40	4.843	69.9	2.777	3.974	2.224	0.973
92.6792123	84.9	7.328	8.634	562	32.68	5.814	70.4	3.390	4.817	2.713	1.045
92.7002193	81.0	7.207	8.893	534	32.69	6.120	70.1	3.563	5.085	2.588	1.111
92.7452077	80.1	5.399	6.742	541	26.84	4.960	69.2	2.794	4.038	2.130	0.983

[1]Line fluxes in units of 10^{-17} W m^{-2}

[2]Continuum fluxes in units of 10^{-19} W m^{-2}Å^{-1}

Table 4.3: Equivalent widths, continuum and line flux measurements for 8 arcsec slit observations.

JD	[O II] λ3727Å			[O III] λ5007Å			[O I] λ6300Å		
+2450800	EQW	Line[1]	Cont[2]	EQW	Line	Cont	EQW	Line	Cont
90.4090040	77.9	7.020	9.015	411	27.39	6.660	56.4	3.031	5.376
90.4312551	72.0	6.254	8.685	439	27.60	6.291	56.3	3.011	5.351
90.4544959	66.8	6.492	9.719	394	27.29	6.921	54.8	3.212	5.861
90.4761452	56.8	5.800	10.21	411	29.15	7.098	48.6	3.144	6.471
90.4995480	60.4	6.721	11.12	390	29.10	7.454	49.7	3.111	6.263
90.5204855	65.7	6.812	10.37	400	29.74	7.433	50.5	3.200	6.339
90.5429507	73.9	7.468	10.11	389	28.58	7.343	53.2	3.291	6.184
90.5642586	64.1	6.410	10.00	408	28.22	6.924	54.4	3.147	5.782
90.5842470	65.8	6.561	9.976	405	28.04	6.920	51.4	3.025	5.880
90.6053176	67.6	6.286	9.292	425	29.37	6.907	56.8	3.348	5.894
90.6880549	80.4	6.263	7.793	442	27.90	6.316	55.5	3.102	5.590
90.7080896	70.2	6.074	8.650	444	27.59	6.208	56.5	3.126	5.529
90.7279623	72.6	6.462	8.896	426	27.79	6.522	55.0	3.013	5.475
90.7475341	71.9	6.593	9.166	401	28.49	7.107	51.4	3.123	6.076
90.7677135				402	27.71	6.887	51.2	2.987	5.838
91.4065966	64.4	6.564	10.19	390	27.12	6.948	51.4	2.968	5.778
91.4313883	62.0	5.565	8.971	410	25.63	6.246	54.1	2.791	5.159
91.4534484	65.1	6.215	9.551	405	27.55	6.802	53.7	2.966	5.520
91.4746001	57.9	6.084	10.50	404	26.93	6.665	49.6	2.817	5.685
91.4998489	60.0	6.286	10.48	381	27.22	7.146	51.3	2.929	5.705
91.5284947	64.4	5.978	9.282	410	27.43	6.683	50.0	2.902	5.809
91.5499415	57.5	5.632	9.789	407	27.06	6.652	51.0	2.904	5.692
91.5701730	69.1	6.534	9.450	429	26.85	6.255	55.0	2.995	5.444
91.5900283	70.6	6.198	8.779	439	26.88	6.118	54.6	2.945	5.392
91.6116892	69.6	6.429	9.234	431	27.18	6.300	56.0	3.020	5.391
91.6337262	61.5	5.822	9.463	430	26.88	6.254	53.5	2.846	5.319
91.6552135	62.0	5.940	9.580	425	26.95	6.340	54.5	3.078	5.651
91.6762725	70.4	5.612	7.977	449	25.98	5.780	56.1	2.827	5.041
91.6969612	82.6	6.332	7.667	456	26.55	5.821	59.9	3.030	5.223
91.7175572	78.2	6.221	7.959	466	26.04	5.583	56.6	2.827	4.997
91.7370827	72.0	6.132	8.514	418	27.33	6.535	50.7	2.890	5.701
91.7581764	59.9	6.266	10.46	399	28.19	7.061	50.5	3.007	5.949
92.4262725	67.7	5.688	8.400	411	26.05	6.345	52.2	2.707	5.185
92.4516776	63.5	6.100	9.610	428	27.80	6.494	54.9	2.833	5.160
92.4724531	63.2	6.223	9.844	446	28.63	6.413	56.7	2.905	5.120
92.4934542	66.9	6.119	9.142	447	29.16	6.521	54.2	2.873	5.304
92.5164461	68.2	6.082	8.921	453	29.54	6.522	55.1	2.878	5.226
92.5381012	74.5	6.409	8.602	470	29.49	6.270	58.0	3.007	5.181
92.5592702	79.1	5.986	7.563	470	27.75	5.901	58.2	2.797	4.808
92.5813998	82.3	6.382	7.751	520	27.68	5.318	65.5	2.824	4.311
92.6016660	94.5	6.392	6.762	524	27.22	5.198	66.3	2.729	4.115
92.6222563	93.0	6.451	6.933	510	28.06	5.499	65.1	2.842	4.365
92.6441545	89.3	6.687	7.485	505	27.66	5.479	64.6	2.933	4.537
92.6650746	89.8	5.994	6.672	518	25.71	4.959	66.6	2.701	4.058
92.6870017	85.8	6.848	7.983	476	28.52	5.987	56.2	2.721	4.841
92.7079970	80.8	5.447	6.742	503	25.41	5.054	57.5	2.464	4.287
92.7324183	76.7	5.171	6.740	487	24.54	5.044	66.3	2.643	3.987
92.7531591				490	26.29	5.364	61.2	2.710	4.425

[1]Line fluxes in units of 10^{-17} W m^{-2}

[2]Continuum fluxes in units of 10^{-19} W m^{-2}Å^{-1}

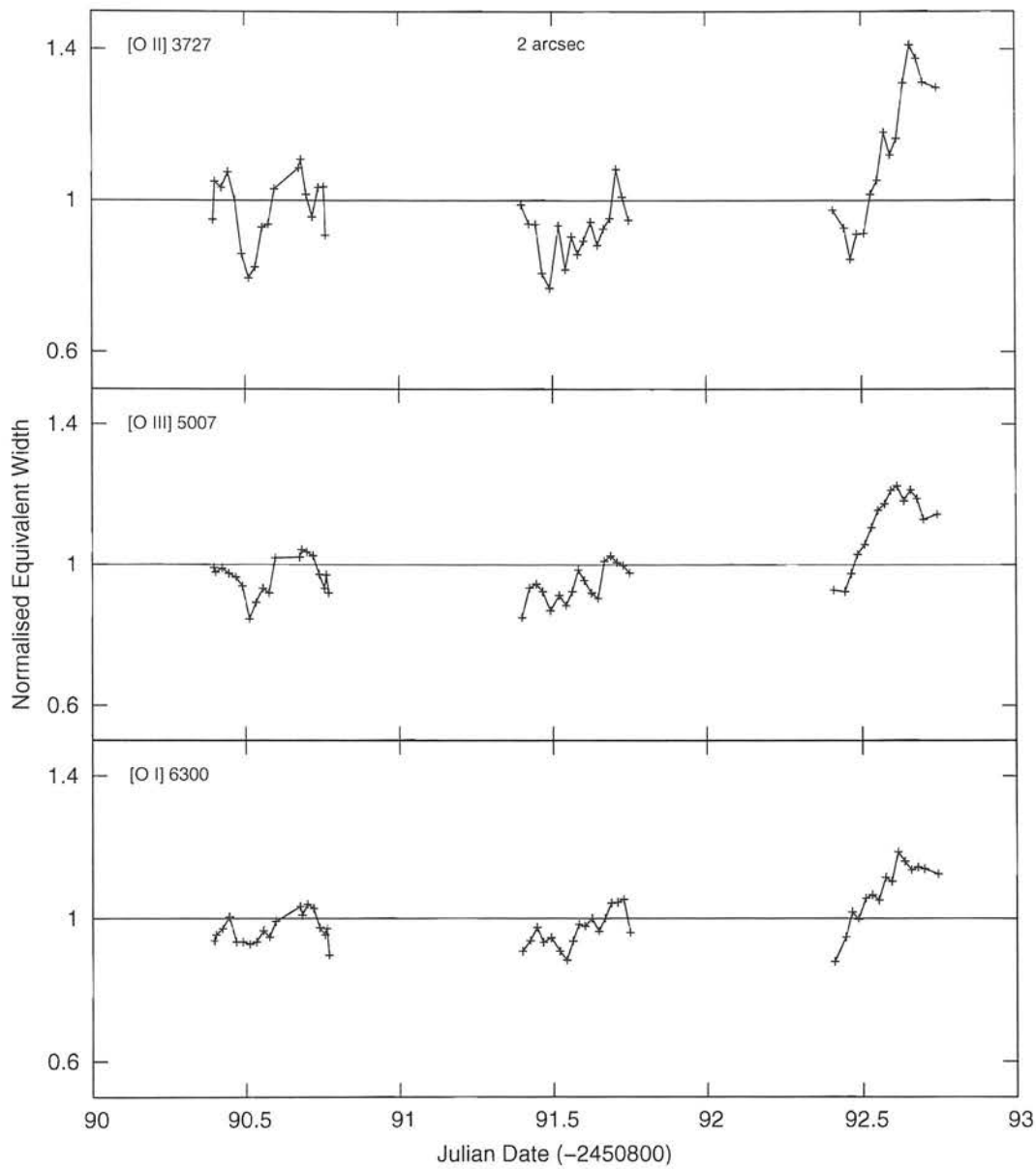

Figure 4.3: Equivalent widths (scaled using mean equivalent width) versus JD for the [O II] 3727Å (top panel), [O III] 5007Å (middle) and [O I] 6300Å (bottom) lines measured using from the 2 arcsec slit spectra.

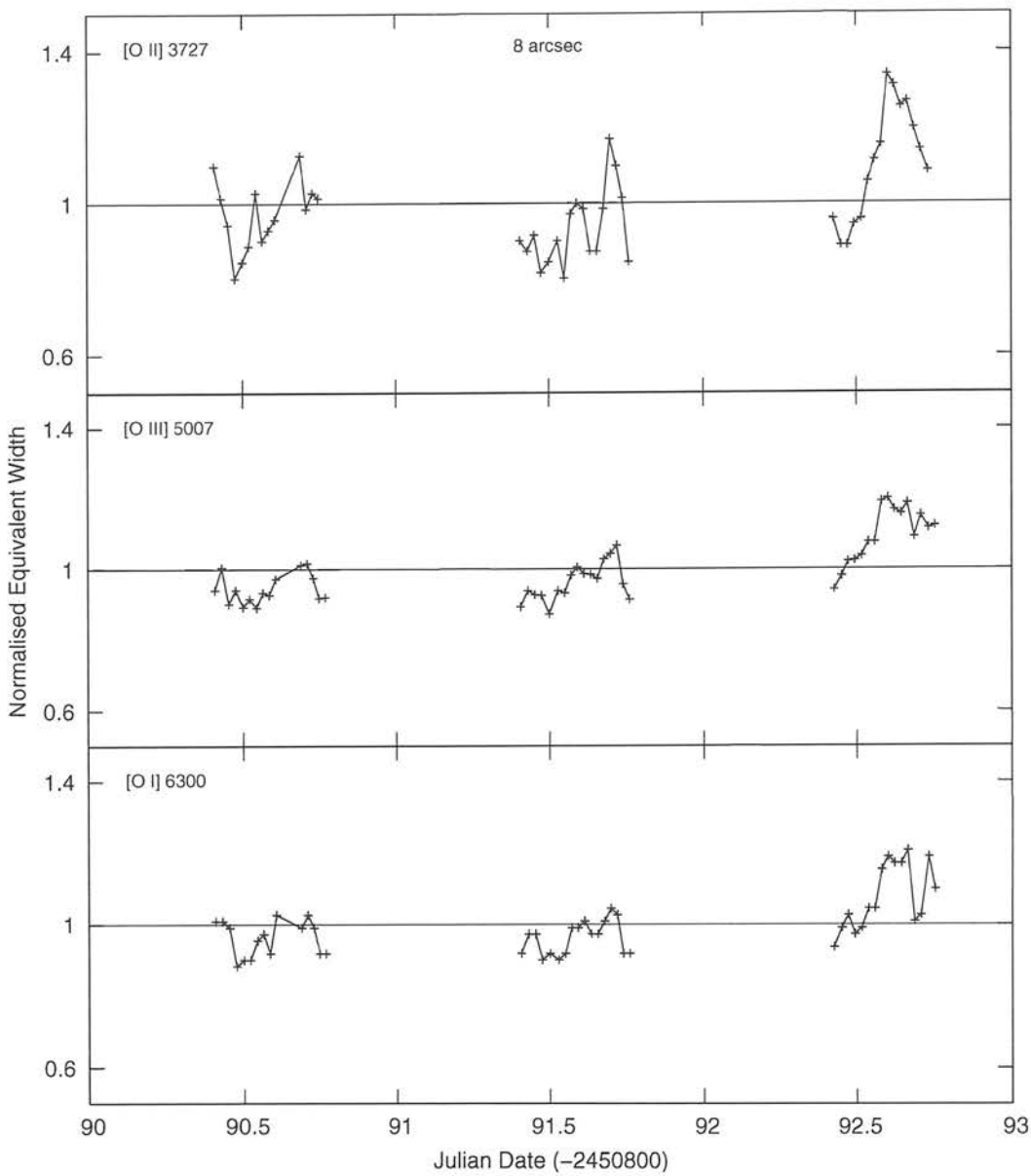

Figure 4.4: Equivalent widths (scaled using mean equivalent width) versus JD for the [O II] 3727Å (top panel), [O III] 5007Å (middle) and [O I] 6300Å (bottom) lines measured using from the 8 arcsec slit spectra.

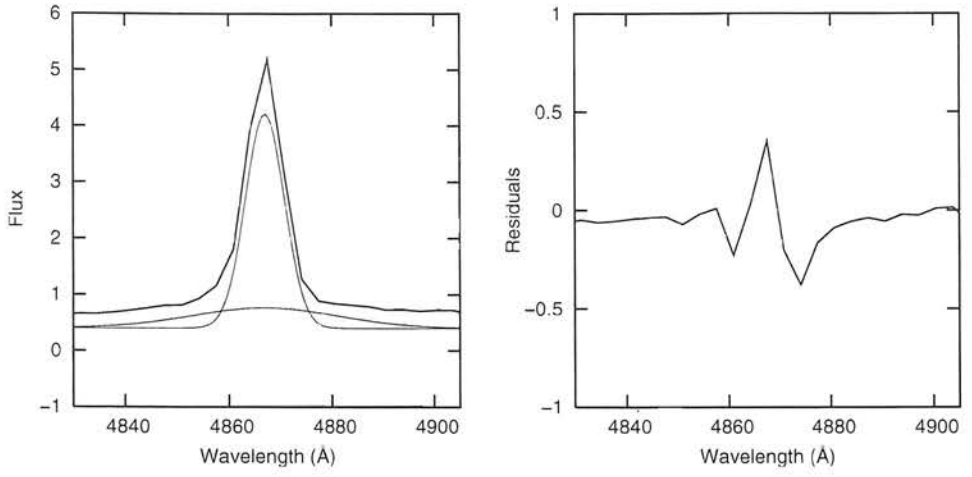

Figure 4.5: Example Gaussian fit to Hβ. The width of the narrow component had a fixed instrumental width measured from other lines, while the width of the broad component varied as a free parameter. All fluxes are in units of 10^{-18} W m^{-2} Å^{-1}.

galaxy core in the slit.

Poor centring either of the slit on the galaxy or of the extraction aperture during the data reduction could lead to variations in flux density. The use of two slits was intended primarily to take the former point into account; if the observed variability in the 2 arcsec slit data was due solely to mis-centring of the galaxy in the slit, this would not be expected to be as significant a problem in the wider 8 arcsec slit data. Since the variability has similar shape and amplitude for both slits, this can be confidently ruled out as the source of variability. Also, as mentioned above, the extraction aperture used during the data reduction was checked and no evidence that the aperture failed to collect all the light from the Seyfert nucleus or that the host galaxy contribution varied significantly was found.

The next check investigated whether any variations could be due to changes in seeing conditions during the observations. Three possibilities are considered here: (1) the variations are entirely due to seeing changes, (2) the source has some small intrinsic variability, but this is exaggerated by changes in flux brought about by changes in seeing, and (3) the relative sizes of the NLR and continuum-emitting regions change depending on the seeing conditions. The first possibility can again be discounted by looking at the variations seen in both the 2 arcsec and 8 arcsec slit data. If the variability is entirely due to seeing changes, one would expect that any variations seen in

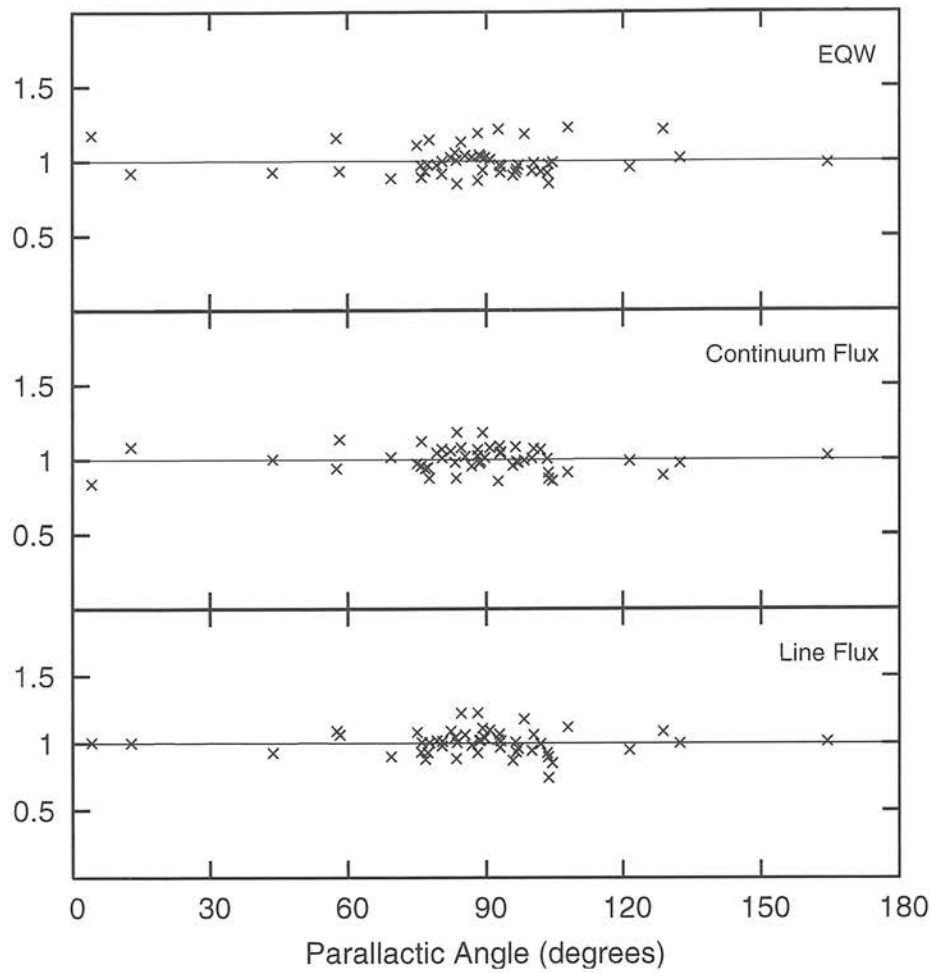

Figure 4.6: Normalised equivalent width (top panel), continuum flux (middle panel) and line flux (bottom panel) versus parallactic angle for the [O III] 5007Å line as measured from the 2 arcsec slit data.

the 2 arcsec slit data would get 'washed out' and be of considerably lower amplitude in the 8 arcsec slit data because even with poor seeing all of the nuclear light should pass through the wider slit. Also, since the equivalent width is a measure of the ratio between line and continuum flux, if all the variations in the line and continuum fluxes are entirely artificial and from the same source, it would be expected that there were *no* changes in the equivalent widths. In fact the amplitude of variability in both data sets is similar and so changes in equivalent width cannot be due entirely to changes in seeing.

It should be possible to determine whether any intrinsic source variations are exacerbated by variations due to poor seeing by investigating whether there is a cor-

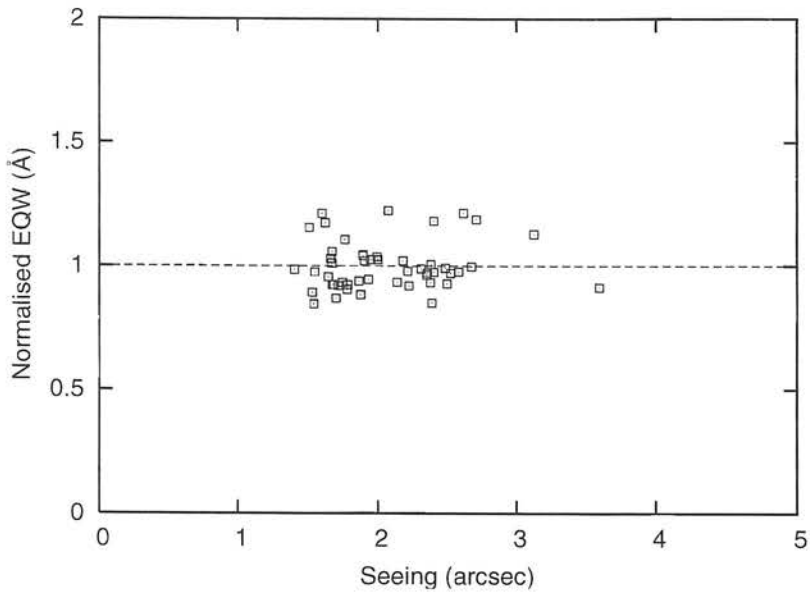

Figure 4.7: Normalised equivalent width versus the FWHM of the seeing disc. The EQW and FWHM measurements were made using the [O III] 5007Å line from spectra taken using the 2 arcsec slit width.

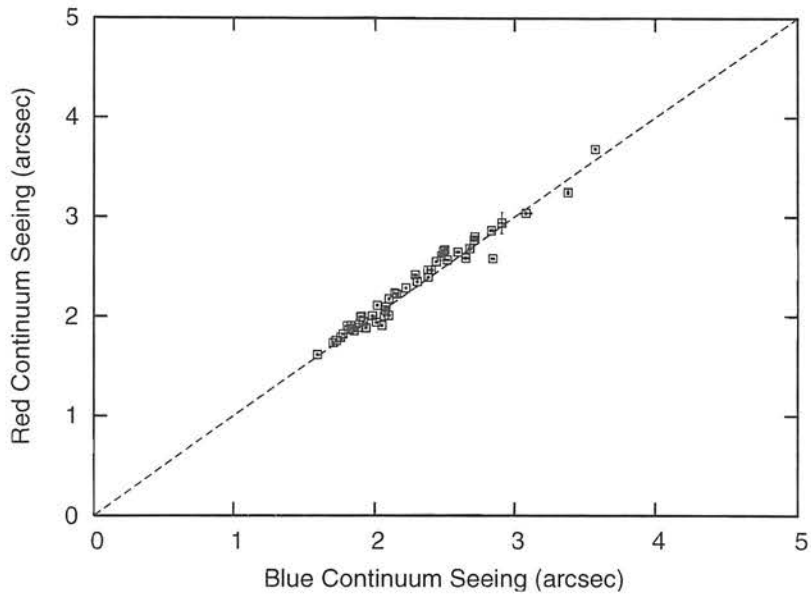

Figure 4.8: FWHM of the cross-dispersive profiles measured for the red continuum region against that of the blue continuum region, from the 2 arcsec slit spectra. Also shown is the 1:1 line for comparison.

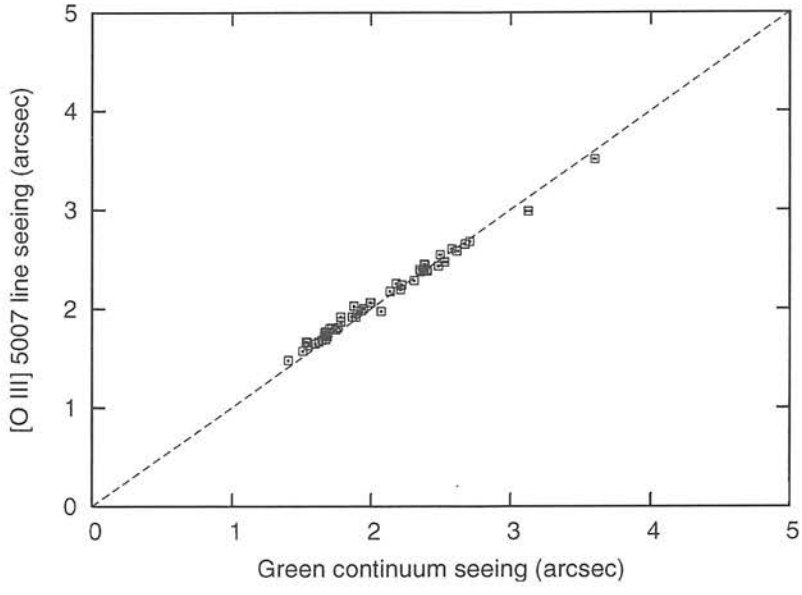

Figure 4.9: FWHM of the cross-dispersive profiles measured for the [O III] 5007Å line and nearby continuum region. Again the 1:1 line is shown for comparison.

relation between the size of the seeing disc and the equivalent width measurement, since it might reasonably be expected that the magnitude of any effect would be directly related to the quality of the seeing at the time. To measure the size of the seeing disc directly, a narrow section of each NGC 4395 spectrum close to the [O III] 5007Å emission line was extracted along the dispersion axis, and a single Gaussian fit to the resulting spatial profile. The FWHM of this fit was then used as a direct measurement of the seeing throughout each night. The equivalent width measurements for the [O III] 5007Å line are shown plotted versus FWHM in Figure 4.7. No correlation between the parameters is seen. Since any effect should be most readily observed in the 2 arcsec slit data (shown here), this is discounted as the source of the NGC 4395 variability.

In addition to the [O III] 5007Å line, continuum sections close to the [O II] 3727Å and [O I] 6300Å lines were extracted and similar Gaussian fits applied to the spatial profiles. The same procedure was also applied to the spectral regions containing the lines themselves. Since the AGN core will be a blue point source whereas any host galaxy contamination will be from diffuse and relatively red starlight, comparing the FWHM of the blue and red continuum regions checks whether changes in the quality

of the seeing affect the seeing disc for emission arising from different parts of the nuclear region in different ways. The FWHM for the red and blue continuum regions are shown plotted against one another in Figure 4.8, together with the 1:1 line for comparison. Similarly, changes in seeing could affect emission from the continuum-emitting source differently to emission from the NLR, which could be partially resolved under good conditions (although as mentioned in earlier this is unlikely). To test this, the FWHM for the extracted regions containing the [O III] 5007Å emission line and nearby continuum region are shown plotted in Figure 4.9, again with the 1:1 comparison line. There is no evidence in either Figure 4.8 or 4.9 for significant deviations from the 1:1 correlation, so the seeing changes have not had a significant differential effect on emission from different regions and hence this unlikely to be the source of the variability. The conclusion drawn from Figure 4.9 is that the NLR is not resolved in any of the observations and so this is not likely to cause spurious variability.

The last remaining likely systematic error is a result of atmospheric transparency variations. As discussed in Section 4.3 , although standard star observations were used to correct trends, short time-scale variations could remain at the level of a few per cent. In the next Section, it is shown that the scatter in measured line fluxes is consistent with this effect, whereas continuum fluxes show a larger scatter. Overall then, the diagnostic checks discussed here suggest that the continuum variations represent real intrinsic variability of the nuclear source.

4.4.3 Variability Analysis

Figure 4.10 shows the mean-normalized line and continuum fluxes for the [O III] 5007Å line measured from the 8 arcsec slit data. The absolute flux calibration accuracy achieved for the wider slit is ~4 per cent for all 3 nights, based on the deviation of the [O III] 5007Å line fluxes from the absolute flux calibration. The accuracy for the 2 arcsec slit data is somewhat lower because these data suffered from additional fluctuations attributed to changes in seeing across each night. The mean absolute line and continuum fluxes and fractional variation (defined as the ratio of the standard deviation and the mean flux) for the three narrow lines for which the equivalent widths were determined are given in Table 4.4. The Figures for the 8 arcsec data clearly show

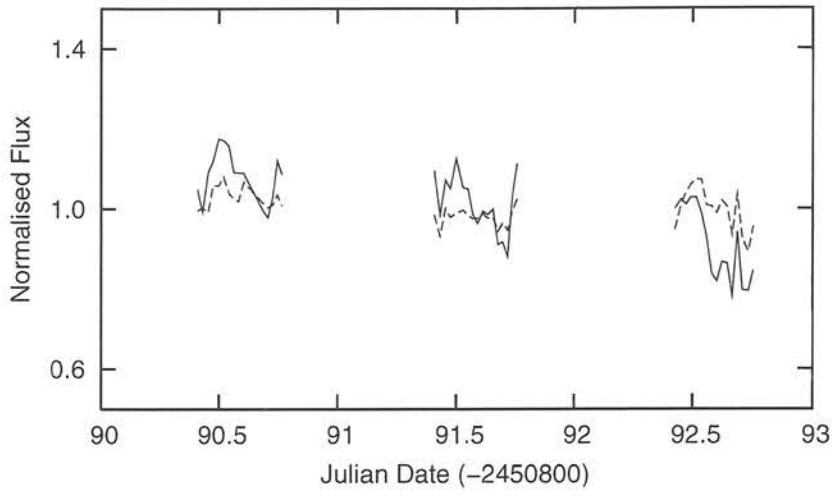

Figure 4.10: Mean-normalized [O III] 5007Å line flux (dashed line) and continuum flux (solid line) for the 8 arcsecond slit.

larger variances in the continuum fluxes than in the line fluxes, suggesting intrinsic source variability. Figure 4.11 shows the continuum and line fluxes plotted against one another. This not only shows the greater continuum variability, but also shows a correlation between the absolute flux measurements that suggests some small uncorrected systematic errors remain. This suggests the EQW will give the most accurate determination of intrinsic variability.

The optical light curves constructed using the EQW measurements in Tables 4.2 and 4.3 are shown in Figures 4.3 and 4.4 respectively, while the fractional variation in EQW for the three narrow lines and both slits are given in Table 4.5. The average sampling interval was 31.6 min and 33.0 min for the 2 arcsec and 8 arcsec slit data respectively, and the large gaps in the light curve represent daylight periods. The light curves show that the nucleus in NGC 4395 varied significantly during the observing campaign, including over short (< 8 hr) time-scales, with the changes similar in shape for all three lines and for both slit widths. The largest variability occurs on night 3, with a $\sim$50 per cent increase in equivalent width (at [O II] 3727Å) occurring over a time-scale of 5 hours, corresponding to a *decrease* in continuum luminosity of 35 per cent. Similar variability, but with smaller amplitude, is also seen in the green and red continuum regions. Small amplitude ($\sim$ few per cent) variability is seen over time-scales as short as the sampling interval, but given the measurement errors this is likely

Table 4.4: Line and continuum variability parameters. Column (1) gives the emission line studied and column (2) the observing night. Columns (3-6) give the line flux, continuum flux, fractional continuum variability and fractional line variability for the 2 arcsec data. Columns (7-10) list the same information for the 8 arcsec data.

Band	Night	2 arcsec slit				8 arcsec slit			
Å		$\bar{F}_l$ [a]	$\bar{F}_c$ [b]	σ_l / $\bar{F}_l$	σ_c / $\bar{F}_c$	$\bar{F}_l$ [a]	$\bar{F}_c$ [b]	σ_l / $\bar{F}_l$	σ_c / $\bar{F}_c$
[O II] 3727	1	5.429	9.040	0.073	0.096	6.515	9.500	0.061	0.088
	2	4.091	8.687	0.086	0.087	6.106	9.285	0.049	0.093
	3	5.611	8.228	0.136	0.104	6.132	7.943	0.067	0.133
	All	5.297	8.667	0.114	0.103	6.239	8.913	0.067	0.129
[O III] 5007	1	26.54	5.820	0.074	0.085	28.26	6.866	0.027	0.056
	2	25.13	5.638	0.077	0.058	26.93	6.423	0.022	0.068
	3	28.79	5.516	0.070	0.085	27.47	5.782	0.053	0.100
	All	26.72	5.670	0.091	0.080	27.53	6.348	0.041	0.102
[O I] 6300	1	2.812	4.721	0.093	0.097	3.125	5.861	0.033	0.058
	2	2.692	4.521	0.070	0.052	2.926	5.497	0.028	0.050
	3	2.977	4.519	0.078	0.089	2.785	4.686	0.046	0.096
	All	2.820	4.595	0.091	0.085	2.941	5.341	0.059	0.113

[a] Line fluxes in units of 10^{-17} W m^{-2}

[b] Continuum fluxes in units of 10^{-19} W m^{-2}Å^{-1}

to be of only marginal significance.

To test whether there was any difference in the variability with colour, the EQW measurements for the [O II] 3727Å and [O I] 6300Å line were plotted against each other, as shown in Figure 4.12. A least-squares fit was then performed in the usual way to determine the best-fitting straight line. The best-fitting solutions have gradients of 1.54 and 1.33 for the 2 arcsec and 8 arcsec data respectively, although a 1:1 relation gave a poorer fit (χ^2/d.o.f = 5.92 for the 2 arcsec slit data) but could not entirely be ruled out. This suggests that there was greater variability in the [O II] 3727Å EQW than the [O I] 6300Å EQW, which is consistent with the findings of Clavel et al. (1991) that the spectra of AGN harden as they brighten. The effect could potentially be caused by starlight contamination. However, the surface brightness of the host galaxy bulge is low, arguing against a large degree of contamination. The difference between the two lines is larger for the 2 arcsec data than the 8 arcsec data, which is consistent with

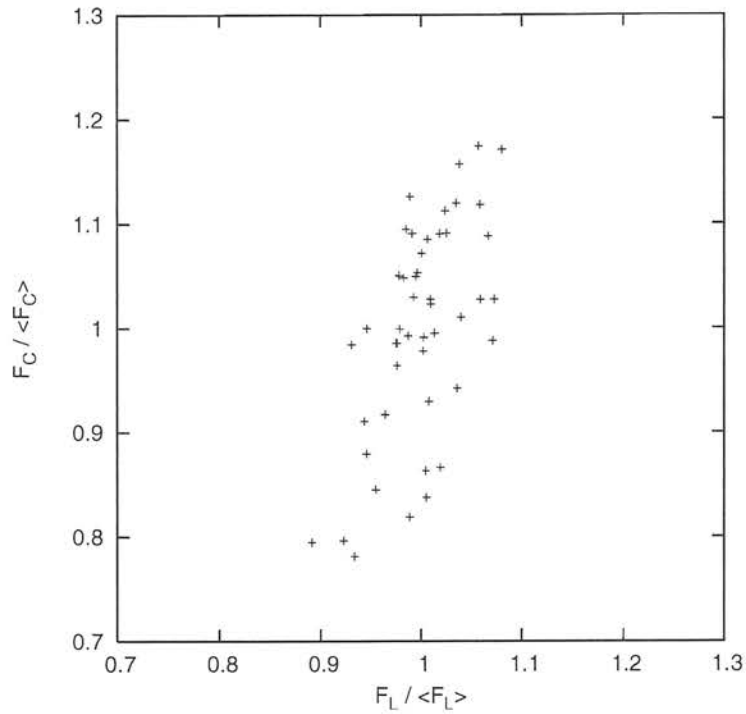

Figure 4.11: Normalized continuum flux versus normalized narrow line flux for the [O III] 5007Å line measured from the 8 arcsec slit data.

Table 4.5: Fractional variation in the EQW measurements for the three narrow lines.

Band	Night	2 arcsec slit	8 arcsec slit
Å		$\sigma_{EQW}/E\bar{Q}W$	$\sigma_{EQW}/E\bar{Q}W$
[O II] 3727	1	0.090	0.091
	2	0.081	0.104
	3	0.162	0.133
	All	0.147	0.135
[O III] 5007	1	0.053	0.043
	2	0.053	0.054
	3	0.090	0.070
	All	0.099	0.089
[O I] 6300	1	0.040	0.050
	2	0.050	0.047
	3	0.077	0.081
	All	0.075	0.083

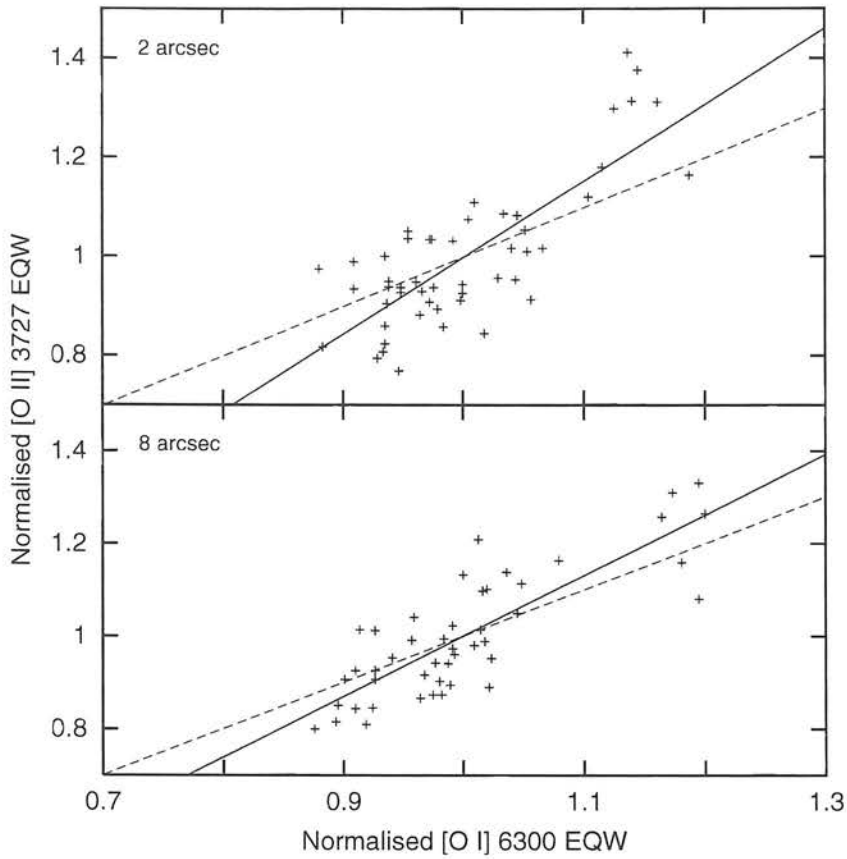

Figure 4.12: [O II] 3727Å normalized equivalent width versus [O I] 6300Å normalized equivalent width for both the 2 arcsec slit (top) and 8 arcsecond slit (bottom). In both cases the solid line represents the best-fitting straight line through the points and the dashed line represents the 1:1 gradient correlation. The gradients of the best-fitfing lines are 1.54 and 1.33 for the 2 arcsec and 8 arcsec slit data respectively.

the 8 arcsec data being affected more by contamination from the host galaxy starlight, suggesting a small but real residual colour effect.

No significant variability in the broad Hβ flux was observed. If the variability in NGC 4395 is qualitatively the same as that in other Seyfert 1s such as NGC 5548 (see Section 4.5.1), then roughly the same variations in the Hβ line as the nearby continuum would be expected, with a lag induced by the light travel time between the accretion disc and broad-line region (Peterson et al. 1992). However, the signal-to-noise ratio of the broad component is poor and proved difficult to fit a Gaussian profile to, so it is difficult to make quantitative statements. Figure 4.13 shows the mean-normalized continuum flux measured for the [O III] 5007Å line plotted against that for the Hβ

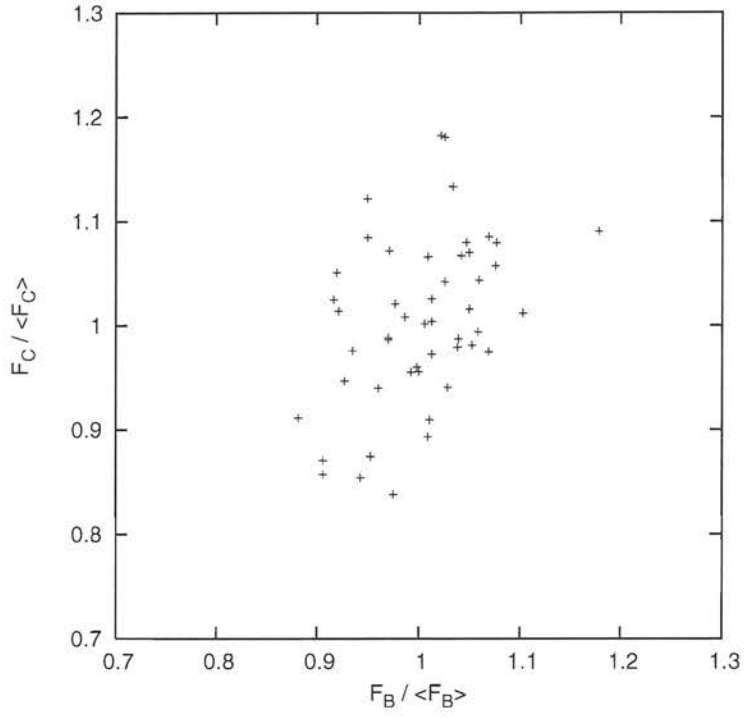

Figure 4.13: Normalized continuum flux measured under the [O III] 5007Å line (using a low-order polynomial fit to the continuum) versus the normalized flux measured for the broad component of the Hβ line. Measured using the 2 arcsec slit data.

broad component. The scatter is greater than that seen in Figure 4.11, but there is still greater variance in the continuum flux than the broad Hβ flux. Figure 4.14 shows the mean-normalized broad Hβ flux against the mean-normalized flux for the narrow component. The scatter is considerable for both parameters - the fractional variation over all 3 nights for the broad and narrow components is 5.9 and 9.5 per cent respectively. The apparent correlation is expected and is a result of allowing the amplitude of both fitted Gaussians to vary as free parameters.

4.5 Discussion

4.5.1 Comparison with NGC 5548

The short time-scale optical variability seen in NGC 4395 (shown in Figures 4.3 and 4.4) is unprecedented in Seyfert galaxies. This suggests that NGC 4395 does indeed have a small black hole rather than an extremely low accretion rate. Simultaneous

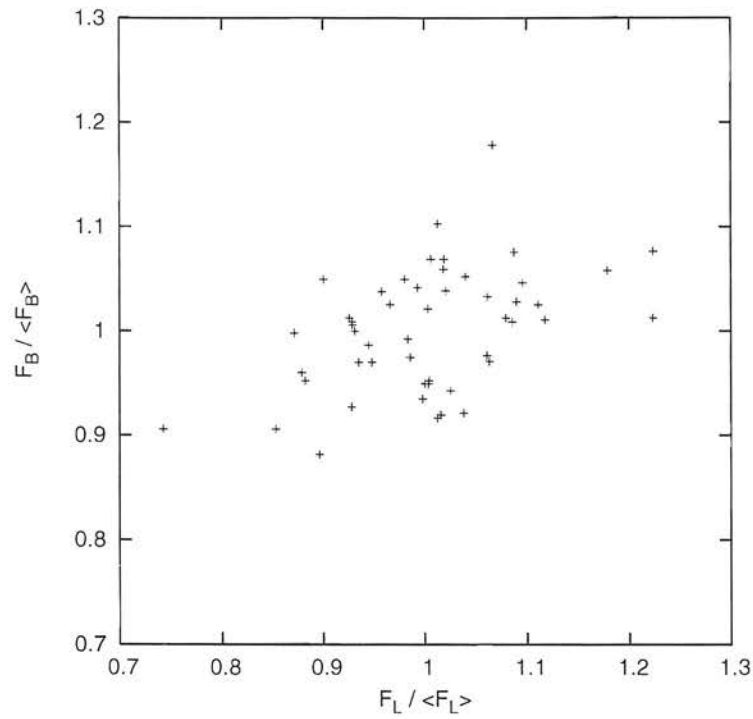

Figure 4.14: Normalized flux for the broad component of the Hβ line versus line flux measured for the [OIII] 5007Å line. Measured using the 2 arcsec slit data.

X-ray and optical observations of another low-luminosity Seyfert 1, NGC 4051 (Done et al. 1990) found no evidence for significant optical variability during a 6-day period in which the X-ray flux varied by up to a factor of 2. The total variability in the B-band over the entire observing period was just 1.4 per cent, with the optical flux remaining constant to within 1 per cent during the periods of highest X-ray variability.

The variability of both continuum and emission lines in the Seyfert 1 galaxy NGC 5548 has been well-studied at both UV and optical wavelengths in order to determine the structure of the unresolved emission line regions. NGC 5548 was monitored in the UV every 4 days for a total of 8 months using *IUE* (Clavel et al. 1991) and every few days over a period of 10 months using a number of telescopes in the optical (Peterson et al. 1991). The large quantity of variability data at these wavelengths makes it an ideal object to use as a comparison with NGC 4395.

To compare NGC 4395 and NGC 5548, the variability power density spectrum (PDS) for NGC 5548 for the UV light curve was obtained from Krolik et al. (1991). The stochastic nature of the variability in AGN means that the PDS is the best way to

probe the distribution of variability amplitude with time-scale. Given that the effect of red-noise means that the variability amplitude depends on the observation length, the PDS slope must be known before the fractional variability of two objects can be compared. Here we assume that the slopes of the PDS for NGC 5548 and NGC 4395 are the same and that the difference in black hole mass changes the frequency scaling, resulting in a change in the PDS normalization at a given frequency. This is consistent with the recent results of Vaughan et al. (2005), who suggest that the large X-ray variability amplitudes seen in both NGC 4051 and NGC 4395 could be the result of the power spectra in these objects being shifted to higher frequencies in comparison with AGN with more massive black holes.

A power-law of the form $P(\nu) = K\nu^{-\alpha}$ was fitted to the NGC 5548 PDS. The final few points are noisy due to the 4-day sampling interval and so these were excluded from the fit. The best-fitting solution gave a power-law index of $\alpha = 2.8$, which was used to extend the PDS to the higher frequencies sampled by the NGC 4395 light curves discussed here. Since the UV fluctuations for NGC 5548 have larger amplitude than the optical fluctuations, the normalization of the UV PDS was scaled using the ratio between the fractional variations for the UV and optical light curves calculated using the data from Clavel et al. (1991) and Peterson et al. (1991) respectively. To avoid the effects of red-noise on the variances, data sets of the same length were used for this.

The scaled PDS was used to calculate the expected variances in the optical light curves for NGC 5548 over time-scales of 8 and 72 hours. The expected fractional variations over these time-scales were calculated to be 0.04 per cent and 0.3 per cent respectively. The process was repeated, this time using the original UV PDS and the expected fractional variations in the UV for NGC 5548 were calculated to be 0.09 per cent (8 hr) and 0.7 per cent (72 hr). Neither the expected optical or UV fractional variability for NGC 5548 is consistent with the mean 6-13 per cent variation observed in the continuum flux for NGC 4395. This analysis confirms that NGC 4395 has larger short time-scale variability than other Seyfert galaxies. A similar result holds in X-rays (Iwasawa et al. 2000; Shih et al. 2003). It seems plausible that this is because the black hole is smaller and so time-scales are shorter. In the next section this question is addressed quantitatively.

4.5.2 Does variability scale with black hole mass?

The precise relationship between variability and black hole mass is dependent upon the precise origin of the variability. If the time-scales for variability are dictated principally by the light travel time across the accretion disc, then one might expect a direct scaling between variability time-scale and black hole mass. Considering a more detailed model in which the time-scale for variability at different wavelengths is dictated by the sound-crossing time-scale gives a different answer; this is discussed below.

To investigate direct scaling between black hole mass and variability it is assumed that the *slope* of the variability power spectra for both NGC 4395 and NGC 5548 are the same, and that the different black hole masses result in a simple translation of the power spectrum along the frequency axis. Then the black hole mass ratio can be used to predict the variability that would be observed in NGC 4395 using the NGC 5548 variability for which the power spectrum is already known. Black hole masses of $10^5 M_\odot$ (Kraemer et al. 1999; Shih et al. 2003) and $6.1 \times 10^7 M_\odot$ (Wandel et al. 1999) are used for NGC 4395 and NGC 5548 respectively. This implies that a time-scale of 200 days in NGC 5548 should correspond to a time-scale of 8 hours in NGC 4395. Using the UV power spectrum for NGC 5548, variability of 29 per cent is expected over this time-scale. This is much larger than the variability seen for NGC 4395 over an 8-hour period for any optical wavelength. If however we consider the optical variability of NGC 5548 over 200 days, we expect variability of order 12 per cent, which is much closer to that seen in NGC 4395. It is unclear at present whether a direct scaling of the two power spectra is valid. Consequently a more detailed model was investigated in which some of the properties of the accretion disc are taken into account.

The central engine of NGC 4395 was modelled using a simple accretion disc for which the emitted spectrum is a sum of blackbodies. Considering the release of thermal binding energy at a radius R gives a blackbody effective temperature of

$$T(R) = \left(\frac{G M_{\rm BH} \dot{m}}{8 \pi R^3 \sigma} \right)^{\frac{1}{4}} \tag{4.1}$$

where $M_{\rm BH}$ is the mass of the central black hole, $\dot{m}$ is the accretion rate, σ is the Stefan-Boltzmann constant and all other symbols take their usual definitions. Obviously the precise formula for $T(R)$ depends on the specific model adopted, but the

binding energy formula should be good enough for the approximate scaling calculation below. If it is assumed that the nucleus is time-steady and has an accretion rate $\dot{m} = (6.32 M_{\rm BH}/\eta c^2)(L/L_{\rm Edd})$ (in SI units), where $L_{\rm Edd}$ is the Eddington luminosity, the above temperature relation then gives

$$R^3 \propto \frac{M_{\rm BH}^2}{T^4}\left(\frac{L}{L_{\rm Edd}}\right) \tag{4.2}$$

If the size of the emitting region and the variability time-scale scales with black hole mass, then it should be possible to calculate the scaling factor for NGC 4395 and NGC 5548. An accretion rate of $0.0035 L_{\rm Edd}$ (Lira et al. 1999) is used for NGC 4395 (this value is slightly different to that adopted by Lira et al. (1999), and reflects the different value of $M_{\rm BH}$ adopted here), and an accretion rate of $0.015 L_{\rm Edd}$ for NGC 5548 (Wandel et al. 1999). From Equation 4.2, for a fixed wavelength (and hence temperature) the time-scales for variability for the two objects should scale by a factor $(6.1 \times 10^7/10^5)^{2/3}(0.015/0.0035)^{1/3} = 117$. So a time-scale of 8 hours in NGC 4395 (i.e. one observing night) should correspond to about 40 nights for NGC 5548. A randomly-selected sample of 10 sections of 40 days from the optical flux values given in Table 9 of Peterson et al. (1991) gives an average fractional deviation of 10.2 per cent. This value agrees well with the average fractional deviation of 10.0 per cent in the [O II] 3727Å EQW measurements for NGC 4395 over time-scales of 1 night. This shows that the anomalous variability of NGC 4395 is quantitatively consistent with that expected for a small central black hole.

4.5.3 Absolute variability time-scales

Above it was shown that the relative variability of NGC 4395 is consistent with simple accretion disc models. However there are problems when the absolute variability time-scales are considered. Estimating the light- and sound-crossing time-scales for a particular black hole mass gives lower and upper limits on the time-scales for variability using $R \propto {M_{\rm BH}}^{2/3} \propto \Delta t$. If the mass of the central engine in NGC 4395 is of the order $10^5 M_\odot$ and the temperature of order 10^4K, then using a value of 10^4 ms^{-1} for the sound speed gives a light-crossing time-scale of 28 min and sound-crossing time-scale of 1.6 years for the time-steady, Eddington-limited case if the optical emission is emitted at $1720 R_S$. This radius was calculated using Equation 4.1, rearranged to find

R and using the typical temperature for optical emission (10^4K) and assuming that the accretion is Eddington-limited. A more realistic estimate (Lira et al. 1999) puts the accretion rate at $\sim 10^{-3} L_{\rm Edd}$, giving light- and sound-crossing time-scales of 2.8 min and 59 days respectively. Instabilities in the disc would be expected to propagate at the sound speed, and therefore variability on time-scales shorter than this would not be expected. This shows that variability time-scale is therefore a problem for NGC 4395 as it is for other Seyfert galaxies.

Addendum: A reverberation mapping study of NGC 4395

The investigation described in this Chapter was submitted and accepted for publication prior to the submission of this thesis (Skelton et al. 2005). Since that time, a reverberation mapping study has been completed using *HST* (Peterson et al. 2005). This study successfully determined the time-lag between variability in the continuum and emission lines and yielded a black hole mass measurement of $(3.6 \pm 1.1) \times 10^5 M_{\odot}$. This is clearly consistent with the conclusions of the work discussed here. This mass estimate is used in all subsequent discussions involving this object.

CHAPTER 5

X-Ray Variability in AGN

The origin and nature of X-ray variability from AGN is a continuing problem for AGN models. As outlined in Chapter 1, a good correlation in seen between the amplitude of the X-ray variability in the 2-10 keV band and the X-ray luminosity for local broad-line Seyfert 1s (Lawrence & Papadakis 1993; Nandra et al. 1997; Turner et al. 1999). However, other classes of AGN such as narrow-line Seyfert 1s (e.g. Turner et al. 1999; Leighly 1999) and low-luminosity AGN do not follow this correlation (Ptak et al. 1998). NLS1s as a group commonly show rapid short time-scale variability (Boller et al. 1996), while in some objects persistent giant-amplitude variability (factor $\sim 50-60$) is seen in the softer 0.4-2 keV band (e.g. IRAS 13224-3809: Boller et al. 1997). LLAGN generally show little evidence of variability over either short or long time-scales (Ptak et al. 1998; Terashima et al. 2002). This suggests that an alternative parameter is driving the variability in X-rays.

One possibility is that it is the mass of the black hole that is the fundamental parameter driving the variability amplitude. If the size of the X-ray emitting region scales directly with $M_{\rm BH}$, then a small black hole implies a small emitting region and hence faster variability. If this is the case then it is the normalization of the power spectrum that changes with black hole mass. This then results in larger amplitude variability for low-mass black holes compared with high-mass black holes over the same time-

scale. Therefore it would be expected that NLS1s, which this study has shown appear to contain systematically smaller black holes, should show high-amplitude variability. By contrast, the lack of short-term variability in LLAGN implies that these objects should contain very massive black holes.

Several studies have already been performed to investigate this possibility. Lu & Yu (2001) calculated the normalized excess variance ($\sigma^2_{\rm NXS}$) for *ASCA* observations of a sample including BLS1s, NLS1s and LLAGN. Many of these had $M_{\rm BH}$ estimates from the reverberation mapping studies of Wandel et al. (1999) and Kaspi et al. (2000). A correlation between $\sigma^2_{\rm NXS}$ and $M_{\rm BH}$ was observed, which was consistent with a linear relationship although the scatter was considerable. Bian & Zhao (2003) performed a similar analysis on 41 *ASCA*-observed AGN with either reverberation-mapped or virial $M_{\rm BH}$ measurements (no LLAGN were included in this sample). This study confirmed that the $M_{\rm BH} - \sigma^2_{\rm NXS}$ correlation found by Lu & Yu (2001) was still valid when a larger group of objects was considered, but with a poorer correlation coefficient. They also investigated possible links between $\sigma^2_{\rm NXS}$ and the Eddington ratio $L_{\rm Bol}/L_{\rm Edd}$, but found only a possible weak correlation. More recently, a similar analysis was performed by O'Neill et al. (2005) on a sample of AGN (again observed using *ASCA*) with black hole masses determined from a variety of methods. This sample included several NLS1s but no LLAGN and attempted to investigate the $M_{\rm BH} - \sigma^2_{\rm NXS}$ relation while taking into account possible measurement errors and uncertainties arising from sampling and the steep power spectrum slope. A strong correlation between $M_{\rm BH}$ and $\sigma^2_{\rm NXS}$ was found, but the scatter was larger than that expected to arise from uncertainties in $\sigma^2_{\rm NXS}$ alone. It was, however, consistent with the expected level of uncertainty in the $M_{\rm BH}$ measurements. Unlike the studies by Lu & Yu (2001) and Bian & Zhao (2003), a linear fit to the data was found to be formally unacceptable, so a model universal power spectrum with low- and high-frequency breaks was fitted to the data. The relationship between $\sigma^2_{\rm NXS}$ and $L_{\rm X}$ was also investigated. It was found that the $\sigma^2_{\rm NXS} - L_{\rm X}$ correlation no longer held when the dependence on $M_{\rm BH}$ was removed, which was taken to indicate that $M_{\rm BH}$ was the primary physical driver and that the correlation with luminosity was principally a result of the relationship with mass.

This study extends the previous work performed by O'Neill et al. (2005). First, the

$M_{\rm BH} - \sigma^2_{\rm NXS}$ and $L_{\rm X} - \sigma^2_{\rm NXS}$ correlations are investigated for only those objects whose mass estimates are thought to be most reliable (i.e. those from reverberation mapping or stellar velocity dispersions). This includes the new mass estimates from this study (where relevant) and new reverberation mapping measurements for objects such as NGC 4395 that have become available since the O'Neill study was published. Secondly, the correlations are tested with the inclusion of extreme accretion rate objects, in this case NLS1s and LLAGN. The motivation for this was to include as many of the large-amplitude variability NLS1s from the studies by Turner et al. (1999) and Leighly (1999) as possible, as these had not been taken into consideration in the O'Neill et al. (2005) study. Also included are those LLAGN from Ptak et al. (1998) with relatively reliable black hole masses, primarily calculated from σ_* measurements from the literature. Unique to this study, principal components analyses are performed upon the data-sets in order to provide a quantitative test of the relative strengths of the correlations.

5.1 Objects with secure mass estimates

The objects from O'Neill et al. (2005) with mass estimates from either reverberation mapping or the $M_{\rm BH} - \sigma_*$ relation are listed in Table 5.1. Listed are the black hole mass, 2-10 keV X-ray luminosity and the excess variance as measured by O'Neill et al. (2005) from the *ASCA* data. The velocity dispersion data from Botte et al. (2005) has been used to recalculate $M_{\rm BH}$ for Mrk 766, resulting in a higher mass estimate than that obtained using the single epoch virial data in Chapter 3. Figure 5.1 shows the relationship between $M_{\rm BH}$ and $\sigma^2_{\rm NXS}$ for these objects. The correlation between these variables is strong, with Spearman rank correlation coefficient $r_s = -0.62$ and $P_{\rm null} = 3.3 \times 10^{-3}$ for the probability of no correlation. Also shown is an unweighted least-squares fit to the data, taking into account errors in both $\sigma^2_{\rm NXS}$ and $M_{\rm BH}$ of the form $\sigma^2_{\rm NXS} \propto M^{-\alpha}_{\rm BH}$. This gave $\alpha = 1.03 \pm 0.09$ with $\chi^2/{\rm d.o.f} = 2.74$. The upper panel of Figure 5.1 shows the quantity $\log(L_{\rm X}\sigma^2_{\rm NXS})$ against $M_{\rm BH}$.

Figure 5.2 shows the correlation between $\sigma^2_{\rm NXS}$ and $L_{\rm X}$ for the objects in Table 5.1. The correlation is slightly stronger than that between $\sigma^2_{\rm NXS}$ and $M_{\rm BH}$, with $r_s = -0.85$ and $P_{\rm null} = 2\times10^{-6}$; however, given that the $M_{\rm BH}$ measurement errors are considerable

Table 5.1: Objects from O'Neill et al. (2005) with reverberation-mapped mass estimates or estimates from stellar absorption features. Column (1) lists the objects and column (2) gives the Seyfert type. Column (3) gives $M_{\rm BH}$, column (4) gives the X-ray luminosity in the 2-10 keV band (in log W) and column (5) the normalized excess variance $\sigma^2_{\rm NXS}$ and its associated uncertainty ϵ. The mass estimation method (R=reverberation mapping, S=stellar velocity dispersion) and reference are given in column (6).

Object	Seyfert Type	$\log\left(\frac{M_{\rm BH}}{M_\odot}\right)$	$\log L_{\rm X}$ (W)	$\log \sigma^2_{\rm NXS} \pm \epsilon$	Refs.
Mrk 335	NLS1	7.15	36.07	-2.51 ± 0.41	R:1
PG 0026+129	BLS1	8.59	37.53	-2.88 ± 0.66	R:1
Fairall 9	BLS1	8.41	36.91	-3.46 ± 0.70	R:1
Mrk 1040	BLS1	7.61	35.40	-1.92 ± 0.40	S:2
Akn 120	BLS1	8.18	36.88	-3.42 ± 0.91	R:1
NGC 3227	BLS1	7.63	34.66	-1.62 ± 0.16	R:1
NGC 3516	BLS1	7.63	36.08	-2.43 ± 0.10	R:1
NGC 3783	BLS1	7.47	35.90	-2.41 ± 0.13	R:1
NGC 4051	NLS1	6.28	34.21	-1.06 ± 0.09	R:1
NGC 4151	BLS1	7.12	35.62	-2.55 ± 0.07	R:1
Mrk 766	NLS1	6.53	35.73	-1.40 ± 0.16	S:3
NGC 4395	BLS1	5.56	32.99	-0.95 ± 0.10	R:4
NGC 4593	BLS1	6.73	35.98	-1.85 ± 0.33	R:1
MCG -6-30-15	NLS1	7.12	35.72	-1.38 ± 0.03	S:5
IC 4329A	BLS1	7.00	36.59	-3.63 ± 0.47	R:1
Mrk 279	BLS1	7.54	36.66	-2.63 ± 0.36	R:1
NGC 5506	S2	7.94	35.73	-1.97 ± 0.23	S:6
NGC 5548	BLS1	7.83	36.41	-3.03 ± 0.14	R:1
Mrk 509	BLS1	8.16	37.02	-3.24 ± 0.59	R:1
NGC 7469	BLS1	7.09	36.25	-2.33 ± 0.27	R:1

References:

(1) Peterson et al. (2004)

(2) Nelson & Whittle (1995)

(3) Botte et al. (2005)

(4) Peterson et al. (2005)

(5) This work.

(6) Papadakis (2004)

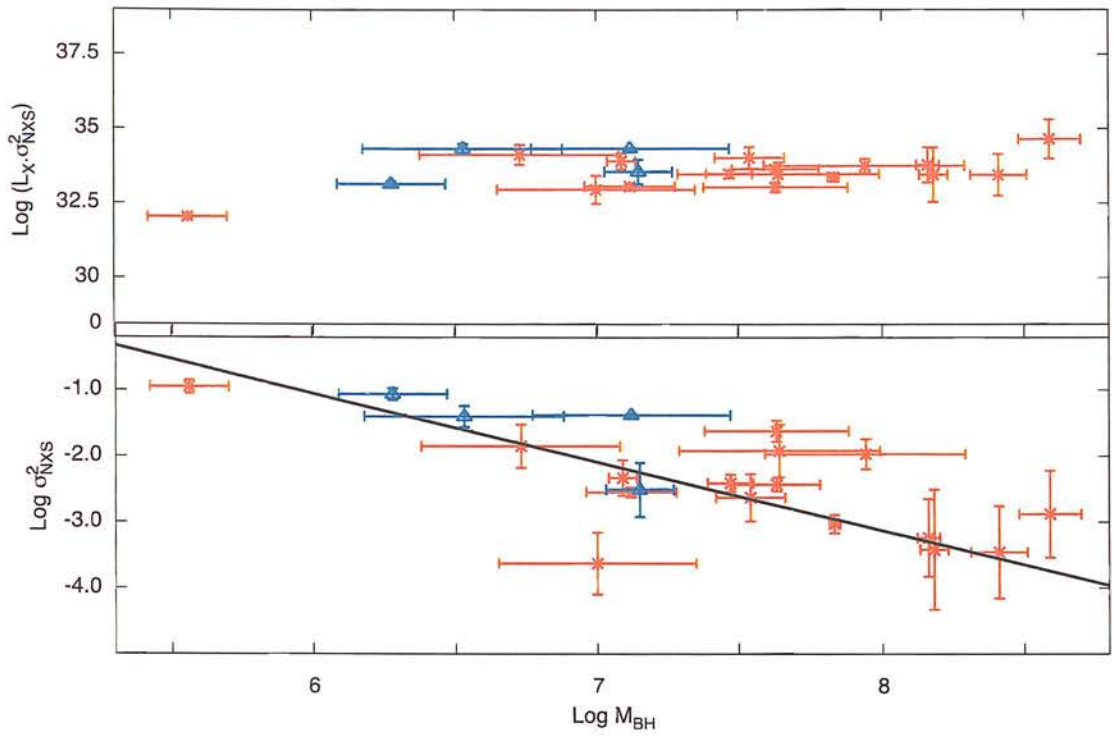

Figure 5.1: The relationship between black hole mass and X-ray variability for the objects from the O'Neill et al. (2005) study that have reliable black hole masses from either reverberation mapping studies or from the stellar velocity dispersion. The thin and thick solid lines are respectively weighted and unweighted fits to the data. Red stars are BLS1s, blue triangles are NLS1s.

one might expect the $M_{\rm BH} - \sigma^2_{\rm NXS}$ correlation measurement to be significantly weaker if both correlations are instrinsically the same strength. Weighted and unweighted linear fits ($\sigma^2_{\rm NXS} \propto L_{\rm X}^{-\beta}$) give $\beta = 0.38 \pm 0.03$ and $\beta = -0.64 \pm 0.10$ respectively, with χ^2/d.o.f $= 24.4$ for the weighted fit and χ^2/d.o.f $= 3.9$ for the unweighted fit. Following the analysis of O'Neill et al. (2005), the top panel of Figure 5.2 shows the quantity $\log(M_{\rm BH}\sigma^2_{\rm NXS})$ against $L_{\rm X}$.

Figures 5.1 and 5.2 appear to show that the correlations between $L_{\rm X}$ and $\sigma^2_{\rm NXS}$ and between $M_{\rm BH}$ and $\sigma^2_{\rm NXS}$ are very similar in strength. However, caution is advised as this sample does not include the NLS1s from the sample of Leighly (1999) that are known to exhibit large-amplitude variability over short time-scales. Unfortunately none of these has yet been the subject of a reverberation mapping study. A number were included in the observations described in Chapter 2, but in all cases the stellar

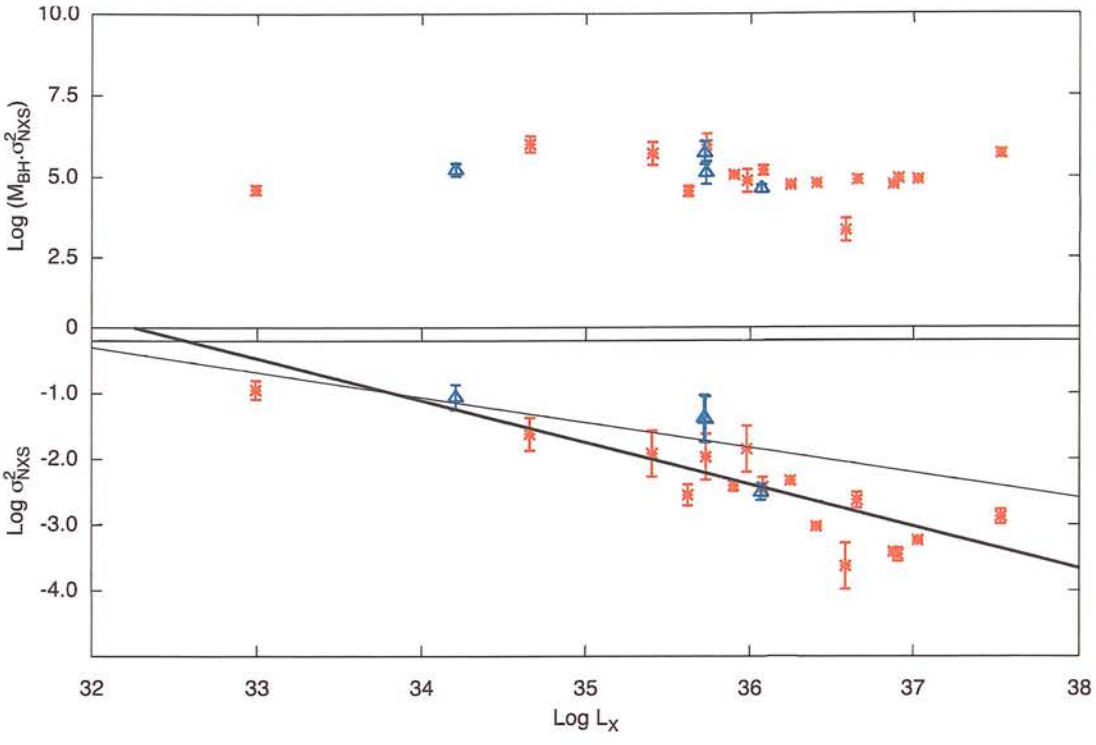

Figure 5.2: The relationship between X-ray luminosity and variability for the objects from the O'Neill et al. (2005) study that have reliable black hole masses. The thin and thick solid lines are respectively weighted and unweighted fits to the data. Red stars are BLS1s, blue triangles are NLS1s.

absorption features were not distinguishable from the nuclear continuum and therefore no velocity information was obtained. Single-epoch virial mass measurements were available allowing an estimate of $M_{\rm BH}$ to be obtained. These objects are therefore discussed in the following Section owing to the expected larger uncertainties.

O'Neill et al. (2005) used the results for NGC 4395 to suggest that the relationship between $\sigma^2_{\rm NXS}$ and $M_{\rm BH}$ that they found was non-linear. However, the $M_{\rm BH}$ estimate that was used was taken from Filippenko & Ho (2003), where the luminosity-$R_{\rm BLR}$ relationship was used to provide a mass estimate of $1.3 \times 10^4 M_{\odot}$. The recent reverberation mapping study by Peterson et al. (2005) has now increased that estimate by an order of magnitude. Using this estimate instead significantly reduces the apparent non-linearity of the correlation.

To attempt to determine which correlation ($\sigma^2_{\rm NXS} - M_{\rm BH}$ or $\sigma^2_{\rm NXS} - L_{\rm X}$) was stronger, a principal components analysis (PCA) was performed on the data. This was done

Table 5.2: Results of the principal components analysis for the objects with reliable masses only. Columns (1) and (2) give the eigenvalues of the covariance matrix expressed both as magnitudes and percentages. Columns (3), (4) and (5) give the components of the eigenvectors defined with respect to the original parameter axes.

Eigenvalue	As Percentage	$M_{\rm BH}$	$L_{\rm X}$	$\sigma^2_{\rm NXS}$
2.54	84.6	-0.56	-0.59	0.58
0.30	10.2	-0.78	0.16	-0.60
0.16	5.3	0.26	-0.79	-0.56

using the PCA routine in the ASTROLIB library of astronomical routines with the Interactive Data Language (IDL). The PCA is performed in several stages. First, the covariance matrix for the mean-normalised data-set is derived. In this case, there are three parameters ($M_{\rm BH}$, $L_{\rm X}$ and $\sigma^2_{\rm NXS}$), giving a 3×3 covariance matrix. The eigenvalues and eigenvectors of the covariance matrix are then calculated; the eigenvector with the largest eigenvalue is the first principal component of the data-set, the second-largest eigenvalue gives the second principal component, etc. Table 5.2 gives the eigenvalues (expressed as both magnitudes and percentages; columns 1 and 2) for the three principal components for the data-set containing only those objects with reliable masses. Also given are the eigenvectors (columns 3, 4 and 5) expressed as unit vectors in terms of the original parameters.

The PCA results show that the bulk of the variance (and hence the strongest correlation) is given by the first principal component, which states that $\sigma^2_{\rm NXS}$ is negatively correlated with both $M_{\rm BH}$ and $L_{\rm X}$, as expected. The $M_{\rm BH} - \sigma^2_{\rm NXS}$ and $L_{\rm X} - \sigma^2_{\rm NXS}$ correlations are similar in strength, and it is not easy from these data alone to determine whether $M_{\rm BH}$ or $L_{\rm X}$ is the driving parameter. This is due to the strong correlation between $M_{\rm BH}$ and $L_{\rm X}$, which arises as a result of including only this small subset of objects (primarily BLS1s).

In addition to providing the principal components, the PCA analysis also derives new values for all of the datapoints in terms of the new axes, determined by the orthogonal eigenvectors. Figure 5.3 shows the results of this transformation for each pair of axes. This Figure shows, as expected, that the bulk of the variance derives from the principal component, with significant scatter. The data-set is separated into BLS1 and

NLS1 objects; there is no evidence that NLS1s alone have a significant effect on the magnitude of the scatter for any of the projections. However, as before there are not very many objects, and so this conclusion is somewhat tenuous.

5.2 Investigating extreme accretion-rate objects

The study of O'Neill et al. (2005) looked at predominantly broad-line Seyfert 1s, with only a few purportedly high accretion-rate objects (NLS1s) and no extreme low-accretion rate LLAGN. By including these objects, it may be possible to determine whether the black hole mass truly is the principal parameter driving the X-ray variability, or whether it is necessary to consider alternative hypotheses.

The LLAGN sample was taken from the study by Ptak et al. (1998) and is listed in Table 5.3. Many of the sample have bulge velocity dispersions from either Nelson & Whittle (1995) or the updated catalogue of central velocity dispersions by McElroy (1994). The uncertainties on the σ_* measurements in the latter study are conservative, although it is possible that σ_* could be over-estimated if the black hole has a significant effect on the stellar kinematics of the central region. The σ_* measurements and corresponding $M_{\rm BH}$ estimates are given in columns (2) and (3). The mass estimate for NGC 4258 is taken from the most recent investigation of Herrnstein et al. (2005). The $\sigma^2_{\rm NXS}$ measurements are from Ptak et al. (1998) with the exception of NGC 3031, NGC 4258 and NGC 4579, which are taken from the more recent study of Lu & Yu (2001). Some of the excess variances are negative, indicating that no variability above the measurement uncertainty was detected. In these cases, 2σ upper limits have been calculated.

The NLS1s (and other BLS1s without reverberation-mapped masses) are shown in Table 5.4. In the case of the Leighly (1999) and Turner et al. (1999) $\sigma^2_{\rm NXS}$ measurements, these were corrected to the $\sim$40 ks time-scale used by O'Neill et al. (2005) using the following prescription. Lawrence & Papadakis (1993) analysed long-look X-ray light curves from *EXOSAT* for a sample of 11 AGN. The slopes derived for the power density spectrum (PDS) were consistent with all objects having a common power-law spectral index of $\alpha = 1.55$, with the variation in variability amplitude between objects resulting from the differing normalizations of the PDS. The excess variance for each

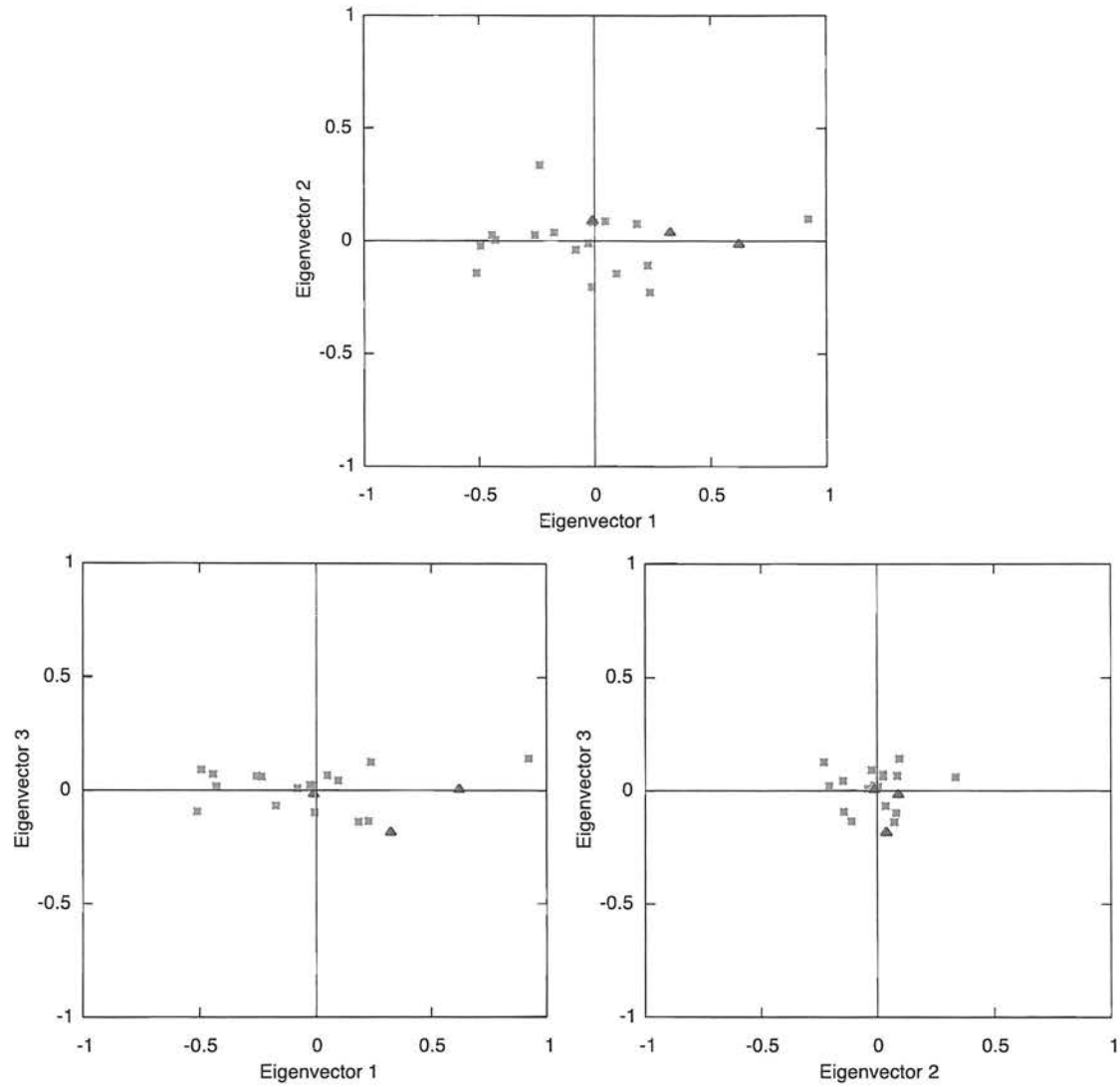

Figure 5.3: PCA results for objects with reliable masses only, expressed in terms of projections along the new axes determined by the 3 eigenvectors. The panels show (anti-clockwise from top): second principal components vs first principal component, third principal component vs first principal component, third principal component vs second principal component. Red stars are BLS1s and blue triangles are NLS1s.

Table 5.3: Low-luminosity AGN from Ptak et al. (1998). Object name and AGN type are listed in columns (1) and (2). Velocity dispersion measurements (where these are available) are given in column (3) and the mass estimates in column (4). Columns (5) and (6) give the X-ray luminosity (in W) and excess variance respectively. References for either σ_* or $M_{\rm BH}$ are listed finally in column (7).

Object	Type	$\sigma_* \pm \epsilon$ (km s^{-1})	$\log\left(\frac{M_{\rm BH}}{M_\odot}\right)$	$\log L_{\rm X}$ (W)	$\sigma^2_{\rm NXS} \pm \epsilon$ (10^{-3})	Refs.
NGC 3031 (M81)	LINER/S1.8	167 ± 8	7.82	32.60	1.3 ± 0.5	1
NGC 3031 (M81)				33.41	5.0 ± 1.6	
NGC 3031 (M81)				33.52	2.0 ± 1.9	
NGC 3079	LINER/S2	150 ± 20	7.63	34.60	340 ± 490	2
NGC 3147	S2	268 ± 20	8.64	34.81	-13 ± 14	2
NGC 3628	LINER	175 ± 20	7.90	33.37	-42 ± 17	2
NGC 3998	LINER/S1	319 ± 15	8.95	34.75	-6.0 ± 4.0	1
NGC 4258	LINER/S1.9		7.58	33.90	0.75 ± 2.0	3
NGC 4258					6.4 ± 1.8	
NGC 4258					8.0 ± 1.9	
NGC 4258					5.7 ± 1.8	
NGC 4579	LINER/S1.9	170 ± 18	7.85	34.37	6.1 ± 1.7	1
NGC 4594	LINER/S1.9	283 ± 20	8.74	34.18	-13 ± 16	4
NGC 5194	S2	102 ± 25	6.95	33.40	66 ± 61	1
NGC 5194				33.43	-18 ± 26	

References:

(1) Nelson & Whittle (1995)

(2) McElroy (1994)

(3) Herrnstein et al. (2005)

(4) Oliva et al. (1999)

of the objects in the two samples was corrected to a 40-ks time-scale by taking this to be true for the objects considered here. For each object the normalization constant was calculated using the time-scale and excess variance tabulated in Tables 1 and 2 of Leighly (1999), and this was used to derive the expected excess variance over a 40 ks observation. This analysis assumes that the light curve for each object is stationary; i.e. it does not matter when the observation was taken. The uncertainty on $\sigma^2_{\rm NXS}$ for these objects was calculated using the prescription given in O'Neill et al. (2005) (their Equation 2), although no estimation of the 'bootstrap uncertainty' was possible in this case.

The correlation between $\sigma^2_{\rm NXS}$ and $L_{\rm X}$ is shown for all objects in Figure 5.4. As

Table 5.4: BLS1s and NLS1s with single-epoch mass measurements. Object and Seyfert type are listed in columns (1) and (2), $M_{\rm BH}$ in column (3) and X-ray luminosity in column (4). The excess variance is give in column (5) and the references in column (6). (References are listed as $M_{\rm BH}$ source: $\sigma^2_{\rm NXS}$ source).

Object	Type	$M_{\rm BH}$	$\log L_{\rm X}$ (W)	$\log \sigma^2_{\rm NXS} \pm \epsilon$	Refs.
I Zw 1	NLS1	6.57	36.35	-1.73 ± 0.39	1:2
Ton S180	NLS1	6.81	36.58	-1.80 ± 0.07	3:2
Mrk 586	NLS1	8.03	37.07	-1.59 ± 0.22	4:2
NGC 985	BLS1	8.05	36.50	-2.46 ± 0.32	3:2
Fairall 303	BLS1	6.37	36.03	-2.17 ± 0.44	3:2
3C 120	BLS1	7.74	37.03	-2.81 ± 0.32	5:6
Mrk 142	NLS1	6.79	36.17	-1.34 ± 0.34	3:2
HE 1029-1401	BLS1	9.55	37.44	-2.99 ± 0.56	4:2
KUG 1031+398	NLS1	5.86	35.43	-1.81 ± 0.33	3:7
PG 1211+143	NLS1	8.16	36.62	-2.09 ± 0.31	5:7
PG 1244+026	NLS1	6.12	36.03	-1.59 ± 0.18	3:2
IRAS 13224-3809	NLS1	6.82	35.59	-0.52 ± 0.18	1:7
IRAS 13349+2438	NLS1	7.96	37.12	-1.42 ± 0.25	3:7
IRAS 13349+2438				-2.06 ± 0.29	
PG 1404+226	NLS1	6.85	36.05	-0.78 ± 0.17	8,9:7
Mrk 478	NLS1	7.38	36.50	-2.21 ± 0.35	3:2
Mrk 841	BLS1	8.10	36.54	-2.94 ± 0.38	10:2
Mrk 290	BLS1	7.05	36.22	-2.39 ± 0.32	11:2
IRAS 17020+4544	NLS1	6.54	36.73	-2.26 ± 0.28	1:2
KAZ 163	NLS1	7.08	36.19	-1.79 ± 0.84	1:7
Mrk 507	NLS1	6.97	35.62	-1.77 ± 0.92	12:7
Akn 564	NLS1	6.68	36.38	-1.27 ± 0.03	1:2

References:

(1) This study
(2) O'Neill et al. (2005)
(3) Grupe et al. (2004)
(4) McLure & Dunlop (2001)
(5) Peterson et al. (2004)
(6) Turner et al. (1999)
(7) Leighly (1999)
(8) Kaspi et al. (2000)
(9) Marziani et al. (2003)
(10) Woo & Urry (2002)
(11) Bian & Zhao (2003)
(12) Botte et al. (2004)

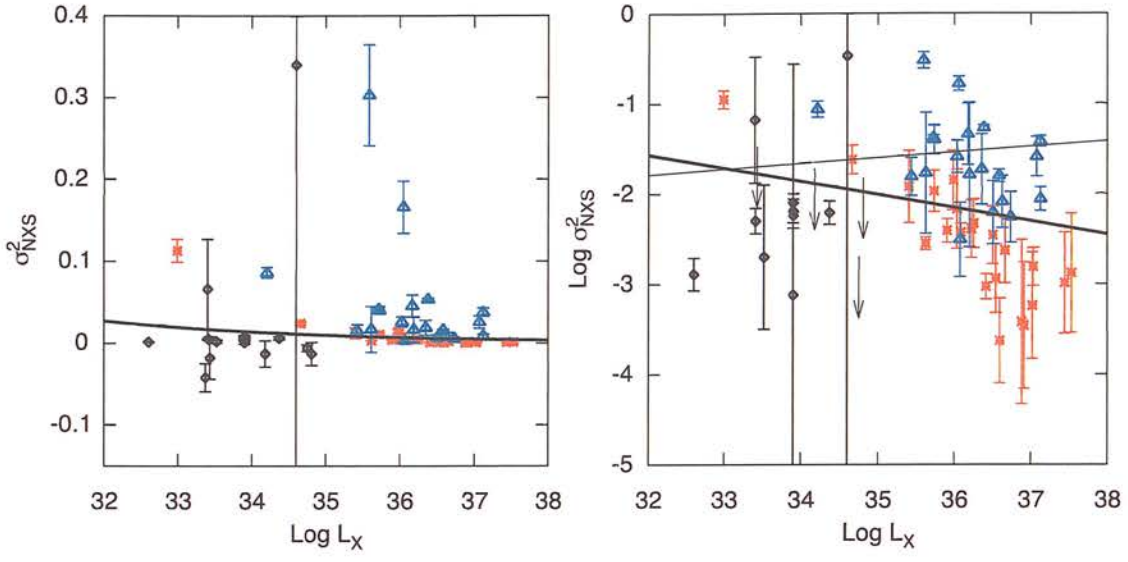

Figure 5.4: The $\sigma^2_{\rm NXS} - L_{\rm X}$ relationship for the entire sample of NLS1s, BLS1s and LLAGN obtained from the literature. The two panels show the X-ray variability in linear (left) and logarithmic space (right). Red stars are BLS1s, blue triangles are NLS1s and black diamonds are LLAGN.

expected, the correlation is poor when the extreme accretion rate objects are included, with $r_s = -0.32$ and $P_{\rm null} = 0.02$. An unweighted least-squares fit to the data results in a power-law index $\beta = -0.14$ with $\chi^2/{\rm d.o.f} = 26.5$. This is consistent with the findings of earlier studies. The correlation between $\sigma^2_{\rm NXS}$ and $M_{\rm BH}$ for all objects is shown in Figure 5.5. The correlation is still strong, although with significant scatter. The correlation coefficient is $r_s = -0.56$ with $P_{\rm null} = 1.5 \times 10^{-5}$. An unweighted least-squares fit (again, taking into account errors in both parameters) gives a power-law index of $\alpha = 1.09 \pm 0.08$, although the χ^2 for this fit is formally unacceptable at $\chi^2/{\rm d.o.f} = 2.72$.

As before, a principal components analysis was performed, this time on the data-set including all objects. The PCA results are given in Table 5.5. Again, the principal component shows a negative correlation between $\sigma^2_{\rm NXS}$ with both $M_{\rm BH}$ and $L_{\rm X}$, although the strength of this correlation is somewhat lower. The $\sigma^2_{\rm NXS} - M_{\rm BH}$ correlation is slightly stronger than that between $\sigma^2_{\rm NXS}$ and $L_{\rm X}$. However, this result is marginal. The second principal component suggests $\sigma^2_{\rm NXS}$ and $L_{\rm X}$ are positively correlated, suggesting that the correlation with $M_{\rm BH}$ is indeed intrinsically stronger.

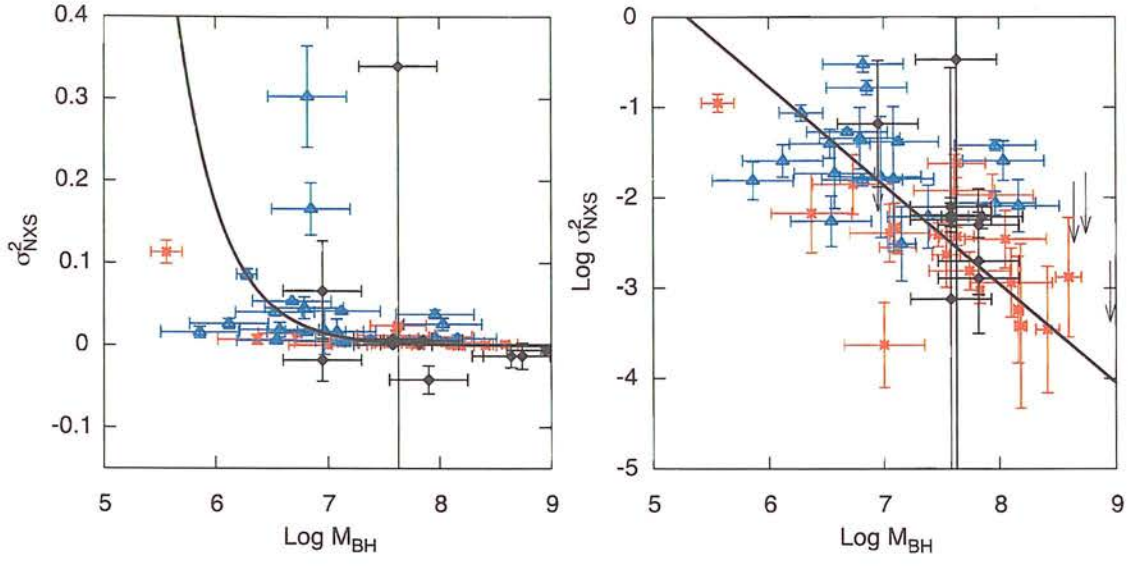

Figure 5.5: The $\sigma^2_{\rm NXS} - M_{\rm BH}$ relationship for the entire sample of NLS1s, BLS1s and LLAGN obtained from the literature. The two panels show the X-ray variability in linear (left) and logarithmic space (right). Red stars are BLS1s, blue triangles are NLS1s and black diamonds are LLAGN. Weighted and unweighted linear fits are shown as thin and thick solid lines respectively (for clarity, only the unweighted fit is shown in the left-hand panel).

Table 5.5: Results of the principal components analysis for all objects. Columns (1) and (2) give the eigenvalues of the covariance matrix expressed both as magnitudes and percentages. Columns (3), (4) and (5) give the components of the eigenvectors defined with respect to the original parameter axes.

Eigenvalue	As Percentage	$M_{\rm BH}$	$L_{\rm X}$	$\sigma^2_{\rm NXS}$
1.90	63.2	-0.60	-0.53	0.61
0.66	21.8	-0.42	0.85	0.32
0.45	15.0	0.69	0.07	0.73

Figure 5.6 shows the transformation of the data-set onto the new axes defined by the PCA eigenvectors. The top panel of this Figure shows that the three classes of AGN defined here (BLS1, NLS1 and LLAGN) appear to sit in fairly well-defined regions of the parameter space. In particular, the LLAGN introduce a large scatter, and are likely to be primarily responsible for the weak positive correlation between $\sigma^2_{\rm NXS}$ and $L_{\rm X}$. NLS1s seem to sit primarily above the EV2 $= 0$ line, suggesting residual scatter in the mass-variance relationship, whereas the BLS1 scatter about this line appears evenly distributed. The bottom right panel, showing the third versus second principal components, shows that the second principal component is well correlated with the different AGN classes. The first principal component is driven primarily by the best-fitting relationship for the largest (BLS1) sample, with the second principal component giving the scatter away from this caused by including the extreme accretion rate objects. That this scatter is correlated with the different samples could imply that there is an intrinsic difference between the different classes.

5.3 Physical models of the emitting region

In principle the relationships between $\sigma^2_{\rm NXS}$ with either mass or luminosity can provide information on the size of the emitting region and the origin of the X-ray variability itself. A correlation between mass and variability valid for all types of AGN poses problems for ADAF models of low-luminosity AGN. Such models imply a fundamental difference in the structures of the central regions of LLAGN and Seyfert galaxies with 'normal' luminosities. However, there is no evidence here that the LLAGN lie away from the mass-variability relationship found for other AGN (although, admittedly the uncertainties are considerable). This suggests that there is in fact *no* difference in the variability properties of LLAGN and that the observed variability is consistent with the estimated central masses of these objects.

In this Section the implications of the results presented here are discussed with respect to broad models in which the variability is due either to stochastic events (such as flares) or global changes in the emitting region. In the former case, the variability arises as a result of a number of stochastic events either in the accretion disc or its immediate surroundings. If the variability scales with either the luminosity or central

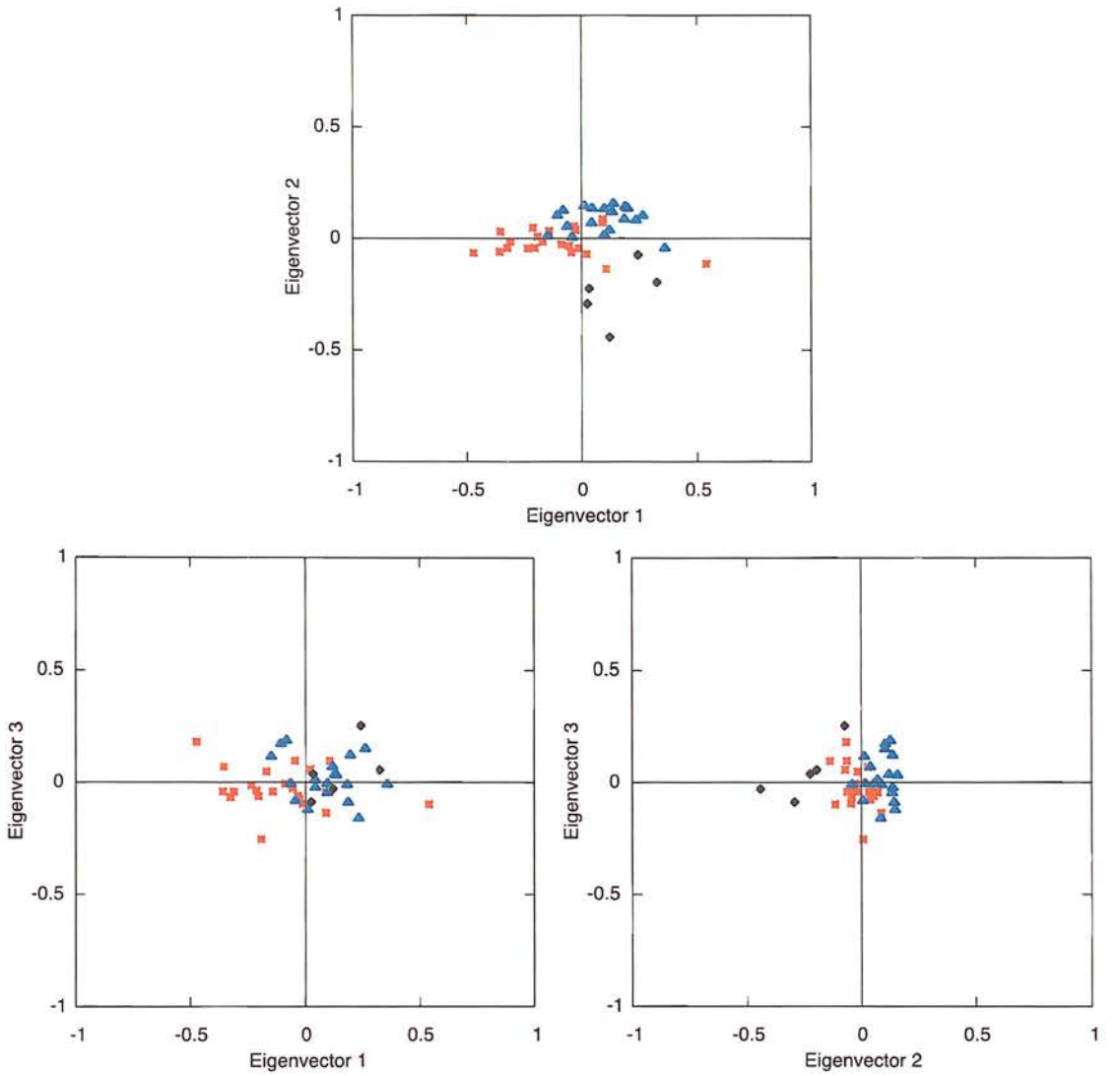

Figure 5.6: PCA results for all objects, expressed in terms of projections along the new axes determined by the 3 eigenvectors. The panels show (anti-clockwise from top): second principal components vs first principal component, third principal component vs first principal component, third principal component vs second principal component. Red stars are BLS1s, blue triangles are NLS1s and black diamonds are LLAGN.

mass, the scaling is likely to be with the amplitude of the variability (i.e. a translation of the PDS along the variance axis). In the latter set of models, where the variability arises as a result of coherent changes in the emitting region as a whole, a scaling relationship is likely to be primarily driven by the size-scale of the region. This would directly affect the time-scale of the variability and hence a self-similar scaling of the PDS would result in a translation along the frequency axis. Therefore sampling a single frequency or narrow band of frequencies changes the observed variability amplitude, with the total integrated power remaining the same.

If the primary driver of the X-ray variability is the mass and not the luminosity, then this has implications for models in which the X-ray variability is due to independent flaring events in a corona surrounding the accretion disc. A correlation with luminosity is expected in this case, as more luminous sources are predicted to have more flares. If all the flares are of similar magnitude and duration, then a larger number of flares will reduce the rms fluctuations seen by a distant observer. So more luminous sources would exhibit lower-amplitude variability than less-luminous sources, which fitted well with the original observations of local Seyfert 1s. It is not obvious that this model predicts a clear correlation with mass, unless the size of the flaring region is strongly constrained by black hole mass. If the corona of X-ray emitting particles is heated and flares as a direct result of radiation from the accretion disc, then it could be that the size of the flaring region is a consequence of the temperature of the disc, in which case a relationship with mass would seem reasonable.

Another possible model is that of the 'single coherent oscillator', in which the X-ray variability is due to global changes in the emitting region. If it is assumed that the X-ray emission is emitted at a fixed number of Schwarzschild radii from the central source, then this radius, and hence the variability time-scale will be directly proportional to $M_{\rm BH}$. This implies that the variability PDS in sources with larger central masses will be shifted towards lower frequencies. The variability σ^2 is obtained from the PDS $P(\nu)$ by

$$\sigma^2 = \int_{\nu_1}^{\nu_2} P(\nu) d\nu \tag{5.1}$$

and since $P(\nu) \propto \nu^{-\alpha}$ with $\alpha \simeq 1.55$, as found by Lawrence & Papadakis (1993), then

assuming a universal power spectrum for all objects this implies that

$$\sigma^2 \propto \nu^{1-\alpha} \propto R^{1-\alpha} \tag{5.2}$$

provided that $\nu_1 \ll \nu_2$. The precise relationship between σ and $M_{\rm BH}$ then depends on the relationship between R and $M_{\rm BH}$, which is dependent upon the geometry of the emitting region. This is currently unknown, and so it is parametrized here generally as $R \propto M_{\rm BH}^{\beta}$. Substituting this into the above gives

$$\sigma^2 \propto M_{\rm BH}^{(1-\alpha)\beta} \tag{5.3}$$

The best-fitting relationship between $\sigma^2_{\rm NXS}$ and $M_{\rm BH}$ has a slope of -0.55, which implies a relationship between $M_{\rm BH}$ and R of

$$R \propto M_{\rm BH}^{1.98\pm0.15} \tag{5.4}$$

where the error on this relation has been calculated by adding the uncertainties on the universal PDS slope and best-fitting $\sigma^2_{\rm NXS} - M_{\rm BH}$ relation in quadrature.

The final model considered here is one in which the X-ray variability arises as a result of shocked gas in an outflow or jet. In the absence of detailed models, it is reasonable to assume that the shock radius scales directly with black hole mass. In this case, the same analysis applied above to the single coherent oscillator model is relevant here.

It is clear from this study that any detailed models for X-ray variability will have to replicate the observed correlation between $M_{\rm BH}$ and $\sigma^2_{\rm NXS}$. This should provide valuable constraints on models of the emitting region, which have previously been lacking as a result of the lack of resolution of the central source.

CHAPTER 6

Conclusions and Future Work

6.1 Velocity dispersions in narrow-line Seyfert 1s

Medium-resolution spectroscopic observations of a sample of broad- and narrow-line Seyfert 1 galaxies are presented in Chapter 2. Information on the stellar velocity dispersion of the host galaxy was only obtained for 11 out of 21 objects, with three other galaxies in the sample having tabulated values in the literature that were used. This reinforces the conclusion that very high signal-to-noise spectra of the nuclear emission are required in order to reliably obtain this information, particularly in the cases of NLS1s where strong emission lines in the regions of interest are frequently observed. Measurements of nuclear parameters (optical luminosity at 5100Å, [O III] 5007Å linewidth and luminosity and Hβ FWHM) were also made using the nuclear spectra.

These results were augmented with objects taken from previous studies in the literature. The 5100Å optical luminosities and Hβ FWHM were used to obtain virial mass measurements using an empirical formula determined from reverberation mapping studies. A detailed investigation into the suitability of the [O III] 5007Å FWHM as a proxy for the true stellar velocity dispersion revealed that $\sigma_{\rm FWHM}$ only provided a good estimate of σ_* for galaxies with very massive bulges. Moreover, the ratio $\sigma_{\rm FWHM}/\sigma_*$ was strongly correlated with σ_*, so that the [O III] 5007Å FWHM was found to over-

estimate σ_* by a factor $2-3$ in the case of NLS1s, which had systematically smaller velocity dispersions than BLS1s. This finding calls into doubt the validity of the conclusions of previous studies that have used this method.

The velocity dispersions of NLS1s and BLS1s as groups were not consistent with the two samples being drawn from the same parent population. This argues against the optical properties of the two groups being a result of orientation alone, since the stellar velocity dispersion should be independent of viewing angle. The relationship between the Hβ FWHM and the ratio of the virial mass (determined from the Hβ linewidth) to the mass determined from the stellar velocity dispersion was investigated and no correlation was found, and this confirmed this conclusion.

It was investigated whether or not NLS1 AGN lie on the $M_{\rm BH}-\sigma_*$ relationship that has been confirmed for inactive galaxies and broad-line AGN. No evidence was found that suggested that NLS1s are systematically offset from the best-fitting correlation, and the scatter was consistent with the expected mass measurement uncertainties from the virial method. There was also no evidence, as had been suggested by some authors, that soft X-ray selected NLS1s lay preferentially off the relationship.

6.2 Variability and black hole mass in NGC 4395

In Chapter 4 optical spectroscopic data is presented for the least-luminous Seyfert 1, NGC 4395, covering three nights during which the nucleus was observed approximately every 30 minutes. Two slit widths were used, enabling any systematic errors and aperture effects to be minimized or quantified, giving an absolute flux calibration accuracy of 5-10 per cent. To reduce the effect of any remaining systematic errors, equivalent width measurements of three narrow lines in the blue, green and red regions of the spectrum were used to quantify the continuum variability, while absolute measurements of the broad-component flux of the Hβ line were used to constrain variability in the broad lines.

The continuum in NGC 4395 was variable over all three nights, with the greatest amplitude of variability occurring during night 3. The variability appeared to be simultaneous for all three continuum regions, with greater variability seen in the continuum flux under the [O II] 3727Å line than the continuum under the [O I] 6300Å

line. The observed hardening of the spectrum with increasing luminosity is consistent with the findings of Clavel et al. (1991), although contamination by starlight cannot be completely ruled out. No measurable variability was detected in the broad Hβ flux.

The nucleus in NGC 4395 was compared with another well-studied Seyfert 1, NGC 5548. NGC 4395 was found to vary with greater amplitude over shorter time-scales than NGC 5548. A simple accretion disc model was used to calculate the expected scaling between NGC 4395 and NGC 5548 if the time-scale for variability scaled with the mass of the central black hole, and the results were consistent with the observed optical variability for NGC 5548 if NGC 4395 has a black hole with a mass approximately two orders of magnitude smaller than that for NGC 5548. The observed variability was not consistent with the expected absolute time-scales for variability if instabilities propagate through the accretion disc at sound speed.

6.3 The correlations between $\sigma^2_{\rm NXS}$, $L_{\rm X}$ and $M_{\rm BH}$

The relationships between the hard X-ray variability ($\sigma^2_{\rm NXS}$), X-ray luminosity ($L_{\rm X}$) and black hole mass ($M_{\rm BH}$) were investigated in Chapter 5. First, the relationships were discussed only for those objects that were thought to have the most secure mass measurements, i.e. those from reverberation mapping. The $\sigma^2_{\rm NXS} - L_{\rm X}$ and $\sigma^2_{\rm NXS} - M_{\rm BH}$ correlations were found to be equally strong, and it was not possible using just these objects to determine whether it was $L_{\rm X}$ or $M_{\rm BH}$ that was the driving parameter behind the observed variability. However, when objects spanning the entire range of accretion rates were included, the correlation with $L_{\rm X}$ was poor, while the $\sigma^2_{\rm NXS} - M_{\rm BH}$ correlation was still good. From this it was concluded that the central mass is likely to be the primary driver of the X-ray variability amplitude.

6.4 The Bigger Picture

The results of the work undertaken in this thesis clearly imply that the principal parameter driving many of the observable properties of AGN is the mass of the central black hole. Perhaps this is not very surprising, given the apparent close relationship between supermassive black holes and host galaxies. However, this work explored for

the first time the relations between σ_* and $\sigma_{[\mathrm{OIII}]}$ for galaxies with very low stellar velocity dispersions, casting doubt on the conclusions of previous studies that have used $\sigma_{[\mathrm{OIII}]}$ in the absence of σ_* information. In addition, this work increases the number of AGN (particularly narrow-line objects) for which there is stellar velocity dispersion information by a significant percentage. There appear to be clear correlations not just between M_{BH} and variability amplitude in X-rays, but also between M_{BH} and variability time-scale for optical flux. It is not clear though, at the moment, whether the scatter in the $M_{\mathrm{BH}} - \sigma^2_{\mathrm{NXS}}$ correlation can be fully explained using only measurement uncertainties. An intensive monitoring campaign is proposed in the following Section to help explore this question.

6.5 Future work

This study has raised several specific questions whose answers are required before AGN models can be considered to be entirely convincing. Clearly it is important to obtain reliable black hole mass estimates for those NLS1s that exhibit large-amplitude X-ray variability and steep soft X-ray spectral indices. There are two principal reasons for this; firstly it is necessary to determine where these AGN lie on the $M_{\mathrm{BH}} - \sigma_*$ relationship in order to confirm or refute the hypothesis that these have rapidly-growing central engines and therefore lie away from the correlation confirmed here for both active and quiescent galaxies. Secondly, reliable mass estimates will help to constrain the $\sigma^2_{\mathrm{NXS}} - M_{\mathrm{BH}}$ correlation. Currently it is not clear whether the scatter in this relationship is due to uncertainties in the mass estimates or the effect of a further unidentified parameter.

More generally, it is clear that current AGN models do not explain the observed optical variability adequately. As the optical variability is expected to originate from the accretion disc, this then proves problematic for the accretion disc–black hole model. A detailed study of the optical variability of AGN with low-mass black holes (i.e. NLS1s) would allow the general optical variability properties (rather than for specific AGN) to be determined in a similar manner to that already achieved using X-ray observations. Low-mass AGN would be ideal for this purpose, partly because it will probe a sparsely-investigated region of the AGN parameter-space, but also because if, as ex-

pected, these AGN show variability on short time-scales then monitoring campaigns can be conducted over shorter time periods than required for high-mass AGN. Monitoring campaigns using robotic telescopes such as the recently-commissioned *Liverpool Telescope* would then be far less labour- or time-intensive, areas that have traditionally proven problematic for large-scale AGN monitoring campaigns.

Bibliography

Abramowicz M.A., Chen X., Kato S., Lasota J., Regev O., 1995, Astrophys. J. Letters, 438, L37

Almaini O., et al., 2000, Mon. Not. R. Astr. Soc., 315, 325

Antonucci R.R.J., 1983, Nature, 303, 158

Arnaud K.A., et al., 1985, Mon. Not. R. Astr. Soc., 217, 105

Awaki H., 1991, PhD. Thesis

Barth A.J., Greene J.E., Ho L.C., 2005, Astrophys. J. Letters, 619, L151

Bechtold J., Czerny B., Elvis M., Fabbiano G., Green R.F., 1987, Astrophys. J., 314, 699

Bian W., Zhao Y., 2003, Mon. Not. R. Astr. Soc., 343, 164

Bian W., Zhao Y., 2004, MNRAS, 347, 607

Binney J., 1978, Mon. Not. R. Astr. Soc., 183, 501

Blandford R.D., McKee C.F., 1982, Astrophys. J., 255, 419

Boller T., Brandt W.N., Fink H., 1996, Astron. Astrophys., 305, 53

Boller T., Brandt W.N., Fabian A.C., Fink H.H., 1997, Mon. Not. R. Astr. Soc., 289, 393

Botte V., Ciroi S., Rafanelli P., Di Mille F., 2004, Astron. J., 127, 3168

Botte V., Ciroi S., di Mille F., Rafanelli P., Romano A., 2005, Mon. Not. R. Astr. Soc., 356, 789

Clavel J., et al., 1991, Astrophys. J., 366, 64

Clavel J., et al., 1992, Astrophys. J., 393, 113

Crenshaw D.M., Kraemer S.B., Gabel J.R., 2003, Astron. J., 126, 1690

Czerny B., Elvis M., 1987, Astrophys. J., 321, 305

Danese L., Franceschini A., de Zotti G., Fasano G., 1986, Astron. Astrophys., 161, 1

Davidson K., Kinman T.D., 1978, Astrophys. J., 225, 776

de Robertis M.M., Osterbrock D.E., 1984, Astrophys. J., 286, 171

Done C., Krolik J.H., 1996, Astrophys. J., 463, 144

Done C., Ward M.J., Fabian A.C., Kunieda H., Tsuruta S., Lawrence A., Smith M.G., Wamsteker W., 1990, Mon. Not. R. Astr. Soc., 243, 713

Dressler A., Richstone D.O., 1988, Astrophys. J., 324, 701

Duncan M.J., Wheeler J.C., 1980, Astrophys. J. Letters, 237, L27

Edelson R., Vaughan S., Warwick R., Puchnarewicz E., George I., 1999, Mon. Not. R. Astr. Soc., 307, 91

Elvis M., et al., 1994, Astrophys. J. Suppl., 95, 1

Fabbiano G., Fassnacht C., Trinchieri G., 1994, Astrophys. J., 434, 67

Fabian A.C., Nandra K., Reynolds C.S., Brandt W.N., Otani C., Tanaka Y., Inoue H., Iwasawa K., 1995, Mon. Not. R. Astr. Soc., 277, L11

Fabian A.C., et al., 1994, Publ. Astron. Soc. Japan, 46, L59

Ferrarese L., Merritt D., 2000, Astrophys. J. Letters, 539, L9

Filippenko A.V., Ho L.C., 2003, Astrophys. J. Letters, 588, L13

Filippenko A.V., Sargent W.L.W., 1989, Astrophys. J. Letters, 342, L11

Filippenko A.V., Ho L.C., Sargent W.L.W., 1993, Astrophys. J. Letters, 410, L75

Fischer J.U., Hasinger G., Schwope A.D., Brunner H., Boller T., Trumper J., Voges W., Neizvestny S., 1998, Astr. Nachrichten, 319, 347

Fitch W.S., Pacholczyk A.G., Weymann R.J., 1967, Astrophys. J. Letters, 150, L67+

Gebhardt K., et al., 2000a, Astrophys. J. Letters, 539, L13

Gebhardt K., et al., 2000b, Astrophys. J. Letters, 543, L5

George I.M., Fabian A.C., 1991, Mon. Not. R. Astr. Soc., 249, 352

Gezari S., Ghez A.M., Becklin E.E., Larkin J., McLean I.S., Morris M., 2002, Astrophys. J., 576, 790

Ghez A.M., 1998, Bull. AAS. , 30, 847

Ghez A.M., Salim S., Hornstein S.D., Tanner A., Lu J.R., Morris M., Becklin E.E., Duchêne G., 2005, Astrophys. J., 620, 744

Greene J.E., Ho L.C., 2004, Astrophys. J., 610, 722

Greene J.E., Ho L.C., 2005, Astrophys. J., 627, 721

Gregory S., Ptak R., Stoner R., 1982, Astrophys. J., 261, 30

Grupe D., Mathur S., 2004, Astrophys. J. Letters, 606, L41

Grupe D., Beuermann K., Thomas H.C., Mannheim K., Fink H.H., 1998, Astron. Astrophys., 330, 25

Grupe D., Beuermann K., Mannheim K., Thomas H.C., 1999, Astron. Astrophys., 350, 805

Grupe D., Wills B.J., Leighly K.M., Meusinger H., 2004, Astron. J., 127, 156

Guilbert P.W., Rees M.J., 1988, Mon. Not. R. Astr. Soc., 233, 475

Harms R.J., et al., 1994, Astrophys. J. Letters, 435, L35

Heckman T.M., Miley G.K., van Breugel W.J.M., Butcher H.R., 1981, Astrophys. J., 247, 403

Herrnstein J.R., Greenhill L.J., Moran J.M., 1996, Astrophys. J. Letters, 468, L17+

Herrnstein J.R., Moran J.M., Greenhill L.J., Trotter A.S., 2005, Astrophys. J., 629, 719

Horne K., Welsh W.F., Peterson B.M., 1991, Astrophys. J. Letters, 367, L5

Hutchings J.B., Hickson P., 1988, Astron. J., 95, 1363

Illingworth G., 1977, Astrophys. J. Letters, 218, L43

Iwasawa K., Fabian A.C., Almaini O., Lira P., Lawrence A., Hayashida K., Inoue H., 2000, Mon. Not. R. Astr. Soc., 318, 879

Jiménez-Benito L., Díaz A.I., Terlevich R., Terlevich E., 2000, Mon. Not. R. Astr. Soc., 317, 907

Kaspi S., Smith P.S., Netzer H., Maoz D., Jannuzi B.T., Giveon U., 2000, Astrophys. J., 533, 631

Korista K.T., et al., 1995, Astrophys. J. Suppl., 97, 285

Kormendy J., 1988a, Astrophys. J., 325, 128

Kormendy J., 1988b, Astrophys. J., 335, 40

Kormendy J., 2003, In Carnegie Obs. Astr. Series, Vol 1

Kormendy J., Gebhardt K., 2001, In AIP Conf. Proc. 586: 20th Texas Symposium on relativistic astrophysics, pp. 363–+

Kormendy J., McClure R.D., 1993, Astron. J., 105, 1793

Kormendy J., Richstone D., 1995, Annu. Rev. Astron. Astrophys., 33, 581

Kraemer S.B., Ho L.C., Crenshaw D.M., Shields J.C., Filippenko A.V., 1999, Astrophys. J., 520, 564

Krolik J.H., 2001, Astrophys. J., 551, 72

Krolik J.H., Horne K., Kallman T.R., Malkan M.A., Edelson R.A., Kriss G.A., 1991, Astrophys. J., 371, 541

Laor A., 2001, Astrophys. J., 553, 677

Laor A., Netzer H., 1989, Mon. Not. R. Astr. Soc., 238, 897

Lauer T.R., et al., 1991, Astrophys. J. Letters, 369, L45

Lawrence A., 1991, Mon. Not. R. Astr. Soc., 252, 586

Lawrence A., Elvis M., 1982, Astrophys. J., 256, 410

Lawrence A., Papadakis I., 1993, Astrophys. J. Letters, 414, L85

Lawrence A., Watson M.G., Pounds K.A., Elvis M., 1987, Nature, 325, 694

Leighly K.M., 1999, Astrophys. J. Suppl., 125, 297

Lira P., Lawrence A., O'Brien P., Johnson R.A., Terlevich R., Bannister N., 1999, Mon. Not. R. Astr. Soc., 305, 109

Lo K.Y., Schilizzi R.T., Cohen M.H., Ross H.N., 1975, Astrophys. J. Letters, 202, L63

Lu Y., Yu Q., 2001, Mon. Not. R. Astr. Soc., 324, 653

Lynden-Bell D., 1978, Physica Scripta, 17, 185

Madau P., 1988, Astrophys. J., 327, 116

Magorrian J., et al., 1998, Astron. J., 115, 2285

Malkan M.A., 1983, Astrophys. J., 268, 582

Manners J., Almaini O., Lawrence A., 2002, Mon. Not. R. Astr. Soc., 330, 390

Maoz E., 1995, Astrophys. J. Letters, 447, L91+

Maoz E., 1998, Astrophys. J. Letters, 494, L181+

Marziani P., Sulentic J.W., Zamanov R., Calvani M., Dultzin-Hacyan D., Bachev R., Zwitter T., 2003, Astrophys. J. Suppl., 145, 199

Massey P., Strobel K., Barnes J.V., Anderson E., 1988, Astrophys. J., 328, 315

Mathur S., 2000, Mon. Not. R. Astr. Soc., 314, L17

Mathur S., Grupe D., 2005, astro-ph/0507624

Mathur S., Kuraszkiewicz J., Czerny B., 2001, New Astronomy, 6

Matthews T.A., Sandage A.R., 1963, Astrophys. J., 138, 30

McElroy D.B., 1994, Bull. AAS. , 26, 1498

McLure R.J., Dunlop J.S., 2001, Mon. Not. R. Astr. Soc., 327, 199

McLure R.J., Dunlop J.S., 2002, Mon. Not. R. Astr. Soc., 331, 795

McLure R.J., Dunlop J.S., 2004, Mon. Not. R. Astr. Soc., 352, 1390

McLure R.J., Jarvis M.J., 2002, Mon. Not. R. Astr. Soc., 337, 109

Miyoshi M., Moran J., Herrnstein J., Greenhill L., Nakai N., Diamond P., Inoue M., 1995, Nature, 373, 127

Moran E.C., Halpern J.P., Helfand D.J., 1996, Astrophys. J. Suppl., 106, 341

Moran E.C., Filippenko A.V., Ho L.C., Shields J.C., Belloni T., Comastri A., Snowden S.L., Sramek R.A., 1999, Publs. Astr. Soc. Pacif., 111, 801

Mushotzky R.F., Done C., Pounds K.A., 1993, Annu. Rev. Astron. Astrophys., 31, 717

Nandra K., Pounds K.A., Stewart G.C., Fabian A.C., Rees M.J., 1989, Mon. Not. R. Astr. Soc., 236, 39P

Nandra K., Pounds K.A., Stewart G.C., George I.M., Hayashida K., Makino F., Ohashi T., 1991, Mon. Not. R. Astr. Soc., 248, 760

Nandra K., George I.M., Mushotzky R.F., Turner T.J., Yaqoob T., 1997, Astrophys. J., 476, 70

Narayan R., Yi I., 1995, Astrophys. J., 452, 710

Nelson C.H., Whittle M., 1995, Astrophys. J. Suppl., 99, 67

Nelson C.H., Whittle M., 1996, Astrophys. J., 465, 96

Nelson C.H., Green R.F., Bower G., Gebhardt K., Weistrop D., 2004, Astrophys. J., 615, 652

Netzer H., 1989, In IAU Symp. 134: Active Galactic Nuclei, pp. 69–+

Oke J.B., 1990, Astron. J., 99, 1621

Oliva E., Origlia L., Maiolino R., Moorwood A.F.M., 1999, Astron. Astrophys., 350, 9

O'Neill P.M., Nandra K., Papadakis I.E., Turner T.J., 2005, Mon. Not. R. Astr. Soc., 358, 1405

Onken C.A., Ferrarese L., Merritt D., Peterson B.M., Pogge R.W., Vestergaard M., Wandel A., 2004, Astrophys. J., 615, 645

Osterbrock D.E., Pogge R.W., 1985, Astrophys. J., 297, 166

Osterbrock D.E., Pogge R.W., 1987, Astrophys. J., 323, 108

Papadakis I.E., 2004, Mon. Not. R. Astr. Soc., 348, 207

Peacock J.A., 1983, Mon. Not. R. Astr. Soc., 202, 615

Penston M.V., Perez E., 1984, Mon. Not. R. Astr. Soc., 211, 33P

Peterson B.M., 1985, IAU Circ., 4036, 1

Peterson B.M., 1988, Publs. Astr. Soc. Pacif., 100, 18

Peterson B.M., 1993, Publs. Astr. Soc. Pacif., 105, 247

Peterson B.M., 2001, In Advanced Lectures on the Starburst-AGN, pp. 3–+

Peterson B.M., Korista K.T., Wagner R.M., Reichert G.A., 1990, Astrophys. J., 352, 68

Peterson B.M., Ali B., Horne K., Bertram R., Lame N.J., Pogge R.W., Wagner R.M., 1993, Astrophys. J., 402, 469

Peterson B.M., Wanders I., Bertram R., Hunley J.F., Pogge R.W., Wagner R.M., 1998, Astrophys. J., 501, 82

Peterson B.M., Pogge R.W., Wanders I., 1999, In ASP Conf. Ser. 175: Structure and Kinematics of Quasar Broad Line Regions, pp. 41+

Peterson B.M., et al., 1991, Astrophys. J., 368, 119

Peterson B.M., et al., 1992, Astrophys. J., 392, 470

Peterson B.M., et al., 2000, Astrophys. J., 542, 161

Peterson B.M., et al., 2002, Astrophys. J., 581, 197

Peterson B.M., et al., 2004, Astrophys. J., 613, 682

Peterson B.M., et al., 2005, Astrophys. J., 632, 799

Pounds K.A., Turner T.J., Warwick R.S., 1986, Mon. Not. R. Astr. Soc., 221, 7P

Pounds K.A., Stanger V.J., Turner T.J., King A.R., Czerny B., 1987, Mon. Not. R. Astr. Soc., 224, 443

Pounds K.A., Nandra K., Stewart G.C., Leighly K., 1989, Mon. Not. R. Astr. Soc., 240, 769

Pounds K.A., Nandra K., Stewart G.C., George I.M., Fabian A.C., 1990, Nature, 344, 132

Press W.H., Teukolsky S.A., Vetterling W.T., Flannery B.P., 1992, Numerical recipes in FORTRAN. The art of scientific computing. Cambridge: University Press, —c1992, 2nd ed.

Ptak A., Yaqoob T., Mushotzky R., Serlemitsos P., Griffiths R., 1998, Astrophys. J. Letters, 501, L37+

Rees M.J., Phinney E.S., Begelman M.C., Blandford R.D., 1982, nat, 295, 17

Salpeter E.E., 1964, Astrophys. J., 140, 796

Sargent W.L.W., Young P.J., Lynds C.R., Boksenberg A., Shortridge K., Hartwick F.D.A., 1978, Astrophys. J., 221, 731

Schlegel D.J., Finkbeiner D.P., Davis M., 1998, Astrophys. J., 500, 525

Shakura N.I., Sunyaev R.A., 1973, Astron. Astrophys., 24, 337

Shields J.C., Filippenko A.V., 1992, In ASP Conf. Ser. 31: Relationships Between Active Galactic Nuclei and Starburst Galaxies, pp. 267–+

Shih D.C., Iwasawa K., Fabian A.C., 2003, Mon. Not. R. Astr. Soc., 341, 973

Skelton J.E., Lawrence A., Pappa A., Lira P., Almaini O., 2005, Mon. Not. R. Astr. Soc., 358, 781

Smith H.J., Hoffleit D., 1963, Nature, 198, 650

Smith J.E., Young S., Robinson A., Corbett E.A., Giannuzzo M.E., Axon D.J., Hough J.H., 2002, Mon. Not. R. Astr. Soc., 335, 773

Sramek R., 1992, In ASP Conf. Ser. 31: Relationships Between Active Galactic Nuclei and Starburst Galaxies, pp. 273–+

Tanaka Y., et al., 1995, Nature, 375, 659

Terashima Y., Iyomoto N., Ho L.C., Ptak A.F., 2002, Astrophys. J. Suppl., 139, 1

Tremaine S., et al., 2002, Astrophys. J., 574, 740

Treu T., Stiavelli M., Casertano S., Møller P., Bertin G., 1999, Mon. Not. R. Astr. Soc., 308, 1037

Treu T., Malkan M.A., Blandford R.D., 2004, Astrophys. J. Letters, 615, L97

Turner T.J., George I.M., Nandra K., Turcan D., 1999, Astrophys. J., 524, 667

Ulrich M.H., Horne K., 1996, Mon. Not. R. Astr. Soc., 283, 748

Véron-Cetty M.P., Véron P., Gonçalves A.C., 2001, Astron. Astrophys., 372, 730

van der Marel R.P., 1994, Mon. Not. R. Astr. Soc., 270, 271

Vaughan S., Iwasawa K., Fabian A.C., Hayashida K., 2005, Mon. Not. R. Astr. Soc., 356, 524

Wandel A., 1999, Astrophys. J. Letters, 519, L39

Wandel A., 2002, Astrophys. J., 565, 762

Wandel A., Peterson B.M., Malkan M.A., 1999, Astrophys. J., 526, 579

Wang T., Lu Y., 2001, Astron. Astrophys., 377, 52

Ward M., Elvis M., Fabbiano G., Carleton N.P., Willner S.P., Lawrence A., 1987, Astrophys. J., 315, 74

Whittle M., 1985, Mon. Not. R. Astr. Soc., 213, 1

Whittle M., 1992, Astrophys. J. Suppl., 79, 49

Wilkes B.J., Elvis M., 1987, Astrophys. J., 323, 243

Witt H.J., Czerny B., Zycki P.T., 1997, Mon. Not. R. Astr. Soc., 286, 848

Woo J.H., Urry C.M., 2002, Astrophys. J., 579, 530

Yaqoob T., Edelson R., Weaver K.A., Warwick R.S., Mushotzky R.F., Serlemitsos P.J., Holt S.S., 1995, Astrophys. J. Letters, 453, L81+

Young P.J., Westphal J.A., Kristian J., Wilson C.P., Landauer F.P., 1978, Astrophys. J., 221, 721